



HAL
open science

Refroidissement laser simultané des deux isotopes bosonique et fermionique du Lithium sur les raies D1

Gentle Dash

► **To cite this version:**

Gentle Dash. Refroidissement laser simultané des deux isotopes bosonique et fermionique du Lithium sur les raies D1. Quantum Physics [quant-ph]. Université Paris sciences et lettres, 2022. English. NNT : 2022UPSLE039 . tel-04579344

HAL Id: tel-04579344

<https://theses.hal.science/tel-04579344v1>

Submitted on 17 May 2024

HAL is a multi-disciplinary open access archive for the deposit and dissemination of scientific research documents, whether they are published or not. The documents may come from teaching and research institutions in France or abroad, or from public or private research centers.

L'archive ouverte pluridisciplinaire **HAL**, est destinée au dépôt et à la diffusion de documents scientifiques de niveau recherche, publiés ou non, émanant des établissements d'enseignement et de recherche français ou étrangers, des laboratoires publics ou privés.

THÈSE DE DOCTORAT
DE L'UNIVERSITÉ PSL

Préparée à Ecole normale supérieure

Simultaneous D1 laser cooling of Bose-Fermi Lithium isotopes

Soutenue par

Gentle DASH

Le 13 juin 2022

École doctorale n°564

Physique en Île-de-France

Spécialité

Physique Quantique

Composition du jury :

Florian Schreck Professeur, Université de Amsterdam	<i>Président</i>
Bruno Laburthe-Tolra Directeur de recherche au CNRS, Laboratoire de Physique des lasers	<i>Rapporteur</i>
Thomas Bourdel Charge de recherche au CNRS, Institut d'Optique, Palaiseau	<i>Rapporteur</i>
Juliette Billy Maitre de Conférences, Université Paul Sabatier, Toulouse	<i>Examineur</i>
Michel Brune Directeur de recherche au CNRS, Laboratoire Kastler Brossel, Ecole nor- male supérieure et Collège de France	<i>Examineur</i>
Christophe Salomon Directeur de recherche au CNRS, Laboratoire Kastler Brossel, Ecole Nor- male supérieure,	<i>Directeur de thèse</i>

Dedicated to

my teachers

who have taught me many valuable lessons in my life.

This page intentionally left blank

Abstract

This thesis reports on the construction of a new generation Bose-Fermi quantum gas experiment. We implement simultaneous D1 sub-Doppler cooling on ${}^6\text{Li}$ and ${}^7\text{Li}$ isotopes. We operate D1 molasses on ${}^7\text{Li}$ $|F_g = 2\rangle \rightarrow |F_e = 1\rangle$ and on ${}^6\text{Li}$ $|F_g = 3/2\rangle \rightarrow |F_e = 3/2\rangle$ which display dark states. Using a novel pulsed sequence we cool both isotopes from a magneto optical trap (MOT) temperature of ~ 1 mK to less than $100 \mu\text{K}$ in 3 ms. We discuss the optimization of the pulsed cooling sequence.

We also provide a detailed description of the experimental set-up focusing in particular on the all-diode laser system, the magnetic field coil design and the new computer control system.

After D1 cooling, the obtained phase space densities of $\sim 2 \times 10^{-6}$ are suitable for directly loading a far detuned optical dipole trap with $\sim 7 \times 10^5$ atoms where evaporative cooling to dual quantum degeneracy could be performed. Our results pave the way towards the study of Bose-Fermi quantum many-body physics at low temperature.

This page intentionally left blank

Résumé

Cette thèse porte sur la construction d'une expérience de nouvelle génération sur un mélange de gaz quantiques bosons-fermions. Nous implémentons un refroidissement sub-Doppler D1 simultané sur les isotopes ${}^6\text{Li}$ et ${}^7\text{Li}$ de l'atome de lithium. Nous opérons une mélasse D1 sur la transition $|F_g = 2\rangle \rightarrow |F_e = 1\rangle$ du ${}^7\text{Li}$ et la transition $|F_g = 3/2\rangle \rightarrow |F_e = 3/2\rangle$ du ${}^6\text{Li}$ qui présentent des états noirs. En utilisant une nouvelle séquence pulsée, nous refroidissons les deux isotopes à partir d'une température de piège magnéto-optique (MOT) de ~ 1 mK à moins de $100 \mu\text{K}$ en 3 ms. Nous discutons de l'optimisation de la séquence de refroidissement pulsé.

Nous fournissons également une description détaillée du montage expérimental en nous concentrant en particulier sur le système de diode lasers, la conception des bobines de champ magnétique et le nouveau contrôle informatique de l'expérience.

Après refroidissement par mélasses grises, les densités dans l'espace des phases obtenues, de $\sim 2 \times 10^{-6}$ pour les deux isotopes, sont adaptées au chargement direct d'un piège dipolaire fortement désaccordé avec $\sim 7 \times 10^5$ atomes où un refroidissement par évaporation jusqu'à la double dégénérescence quantique pourrait être effectué. Nos résultats ouvrent la voie à l'étude des propriétés quantiques des mélanges Bose-Fermi à très basse température.

This page intentionally left blank

Contents

1	Introduction	1
1.1	Quantum gases	4
1.2	Ultracold Bose and Fermi mixtures	6
1.3	Context: construction of a next generation Bose-Fermi quantum gas machine	9
1.3.1	Magnetic vs optical trap	9
1.3.2	The subject of my thesis	10
1.4	Outline of my thesis	11
2	Experiment set-up	13
2.1	Experimental chamber	15
2.1.1	Atomic beam and details of the Oven	16
2.1.2	Main chamber	20
2.2	Zeeman slower	20
2.3	Magneto-optical trap	21
2.3.1	MOT and Feshbach coils	21
2.3.2	Electrical circuit	24
2.4	Laser systems	29
2.4.1	Master laser system	30
2.4.2	Lithium spectroscopy and frequency locking	33
2.4.3	Injection locking and slave lasers	37
2.4.4	Zeeman slowing beams	39
2.4.5	D1 cooling setup	40
2.4.6	Probe beams	43
2.4.7	Beam mixing	44
2.5	Experiment control and data acquisition	45
2.5.1	Experiment control	45
2.5.2	Data acquisition	47
2.6	Detection system	48
2.6.1	Fluorescence detection	48
2.6.2	Absorption imaging technique	49
2.7	Summary of chapter 2	55

3	Overview of Laser cooling methods	57
3.1	Doppler cooling	58
3.2	Sub-Doppler cooling	60
3.3	Sub-recoil cooling techniques	62
3.4	Gray molasses cooling	66
3.5	Summary of chapter 3	68
4	Simultaneous D1 sub-Doppler cooling of ^6Li and ^7Li isotopes	71
4.1	Experiment sequence	72
4.2	D2 molasses results	75
4.3	Individual D1 molasses in CW mode	78
4.4	The problem of simultaneous D1 cooling	79
	4.4.1 Estimate of the differential light shifts of ^6Li ground states	80
	4.4.2 Off-resonant excitation estimate	81
4.5	Pulsed D1 scheme	83
4.6	Model for D1 molasses cooling and heating	86
4.7	Optimization of pulsed sequence	88
	4.7.1 D1 molasses in the optimized pulse sequence	89
4.8	Lifetime measurements	92
4.9	Molasses center of mass drift	93
4.10	TOF peak drift	94
4.11	Data Analysis method and error estimates	95
4.12	Improvements	98
5	Perspectives	101
A	Oven operation and unclogging procedure	109
B	Hybrid trap	111
C	Abbreviations	113
D	Publication	114
	Acknowledgements	123
	Bibliography	127

List of Figures

1.1	bosons and fermions at $T=0$	2
1.2	Phase diagram of BEC-BCS cross over and s-wave scattering length (a_s) as a function of magnetic field	4
2.1	Diagram of the vacuum chamber	15
2.2	Diagram of the Lithium oven.	16
2.3	Oven temperature at different parts of the oven.	17
2.4	Vacuum setup for oven replacement procedure.	18
2.5	Sketch of the MOT coil assembly.	22
2.6	Cross section view of MOT and Feshbach coil assembly.	23
2.7	Switch-off time of different coils.	26
2.8	Electrical connections for the coils.	27
2.9	Circuit diagram for the electrical connections.	28
2.10	Energy level diagram for ${}^6\text{Li}$ and ${}^7\text{Li}$ atoms	30
2.11	Setup for ${}^7\text{Li}$ master laser system.	31
2.12	Setup for ${}^6\text{Li}$ master laser system.	32
2.13	Doppler free saturation spectroscopy setup for locking the master lasers.	33
2.14	Beat note of the two Toptica master lasers.	34
2.15	Spectroscopy signal for ${}^7\text{Li}$ master laser system.	35
2.16	Spectroscopy signal for ${}^6\text{Li}$ master laser.	36
2.17	Principle of injection locking.	37
2.18	Slave laser systems for different MOT beams.	38
2.19	Energy diagram scheme for generation of ${}^7\text{Li}$ D1 beams from ${}^6\text{Li}$ D2 MOT beam	40
2.20	${}^7\text{Li}$ D1 laser setup.	41
2.21	${}^6\text{Li}$ D1 laser setup.	42
2.22	Imaging beam setup.	43
2.23	Setup for beam mixing.	44
2.24	Overview of the hardware control.	46
2.25	Double shutter mode for Pixelfly camera	47
2.26	Fluorescence image of the MOT.	48
2.27	Schematic representation of imaging process.	49

2.28	Setup for absorption imaging.	50
2.29	Absorption imaging technique.	51
2.30	Electric dipole transition matrix element for ${}^6\text{Li}$ on the D2 transition line from $ 2S_{1/2}, F = 3/2\rangle \rightarrow 2P_{3/2}, F' = 5/2\rangle$	52
2.31	Electric dipole transition matrix element for ${}^7\text{Li}$ on the D2 transition line from $ 2S_{1/2}, F = 2\rangle \rightarrow 2P_{3/2}, F' = 3\rangle$	53
3.1	Schematic representation of optical molasses in 1D.	58
3.2	Force vs velocity for a laser detuning $\delta = -\Gamma$	59
3.3	Schematics of low intensity Sisyphus cooling	61
3.4	Random walk process in momentum space and the photon scattering rate as a function of momentum.	62
3.5	Schematics of a three level system and the Raman resonance condition.	63
3.6	Schematic representation of VSCPT.	65
3.7	Schematics of Raman resonance cooling.	66
3.8	Schematics of gray molasses cooling.	67
3.9	Temperature limit associated with various cooling techniques.	68
4.1	A typical experiment sequence.	74
4.2	TOF images of ${}^6\text{Li}$ and ${}^7\text{Li}$ for $500\ \mu\text{s}$ D2 molasses.	75
4.3	Temperature and atom number measurement of ${}^6\text{Li}$ after $500\ \mu\text{s}$ of D2 molasses	76
4.4	Temperature and atom number measurement of ${}^7\text{Li}$ after $500\ \mu\text{s}$ of D2 molasses	76
4.5	Displacement of center of mass of the ${}^6\text{Li}$ and ${}^7\text{Li}$ atomic clouds as a function of TOF	77
4.6	TOF images of ${}^6\text{Li}$ and ${}^7\text{Li}$ for D1 molasses in the continuous mode for 1 ms.	78
4.7	Energy level diagrams and relevant transitions for D1 cooling of ${}^6\text{Li}$ and ${}^7\text{Li}$	79
4.8	Off-resonant photon scattering of $ S_{1/2}, F = 1/2\rangle$ and $ S_{1/2}, F = 3/2\rangle$ due to the ${}^7\text{Li}$ D1 beams.	82
4.9	Pulse sequence for the operation of ${}^6\text{Li}$ and ${}^7\text{Li}$ dual D1 molasses.	83
4.10	Temperature decay of ${}^6\text{Li}$ and ${}^7\text{Li}$ from D2 molasses temperature to sub-Doppler temperatures as function of time.	84
4.11	Atom number as a function of TOF for ${}^6\text{Li}$ and ${}^7\text{Li}$ for the dual D1 molasses of 1.6 ms.	84
4.12	Atom number as a function of TOF for 3 ms of dual D1 molasses.	85
4.13	Temperature of D1 molasses as a function of number of pulses.	86
4.14	Schematic representation of cooling and heating cycle for ${}^6\text{Li}$ isotope during pulsed D1 molasses scheme	87
4.15	Optimized pulse sequence for the operation of ${}^6\text{Li}$ D1 and ${}^7\text{Li}$ D1 molasses.	88

4.16	OD profile of ${}^6\text{Li}$ and ${}^7\text{Li}$ at different TOF in the optimized pulse sequence.	89
4.17	${}^6\text{Li}$ temperature (a) and atom number (b) measurement in the optimized dual D1 molasses sequence of 13 pulses (1.95 ms).	90
4.18	${}^7\text{Li}$ temperature (a) and atom number (b) measurement in the optimized dual D1 molasses sequence of 13 pulses (1.95 ms).	90
4.19	Temperature of ${}^6\text{Li}$ and ${}^7\text{Li}$ as a function of number pulses of in the optimised cooling sequence	91
4.20	D1 molasses lifetime in the optimized pulse sequence	93
4.21	Center of mass drift during the pulsed dual D1 molasses.	94
4.22	Center of mass drift as a function of TOF after 1.9 ms of D1 molasses.	94
4.23	Gaussian fits on OD profile corresponding to different baseline corrections.	95
4.24	Relative tilt on the baseline along x and y axis as a function of TOF for ${}^6\text{Li}$	96
4.25	Error in temperature measurement corresponding to different baseline on the Gaussian fit.	96
4.26	Lifetime of ${}^6\text{Li}$ and ${}^7\text{Li}$ D1 molasses after the optimization of D1 beams.	98
4.27	Temperature of ${}^6\text{Li}$ and ${}^7\text{Li}$ as function of pulse duration.	99
4.28	Temperature ${}^6\text{Li}$ and ${}^7\text{Li}$ obtained by different cooling strategies.	99
5.1	Scattering length for ${}^6\text{Li}$, ${}^7\text{Li}$ and ${}^6\text{Li}+{}^7\text{Li}$ as a function of magnetic field.	106
B.1	Energy levels as a function of the magnetic field for the hyperfine ground states of ${}^6\text{Li}$ and ${}^7\text{Li}$	111
B.2	Magnetic field variation along the axial direction in a hybrid trap	112

This page intentionally left blank

List of Tables

1.1	Examples of Bose-Fermi mixtures studied around the globe.	7
2.1	Rate of water flow and the resistance of the coils.	22
2.2	Detuning and output power of the Zeeman slave lasers with respect to the corresponding main transitions as shown in figure 2.10.	39
2.3	Values of different parameters used for ^6Li and ^7Li absorption imaging.	53
4.1	Magnetic field gradient and detuning of the laser beams.	73
4.2	Parameters of D1 beams for simultaneous D1 molasses of ^6Li and ^7Li	80
4.3	Comparison between the symmetric and asymmetric pulse modes.	88
4.4	Heating rate and comparison between the predicted and measured temperatures for symmetric and asymmetric pulse modes.	92
4.5	Temperature measurements corresponding to different baseline corrections in the Gaussian fits.	97
4.6	Gain in PSD from D2 to D1 molasses.	100
5.1	Initial collision rate for Lithium isotopes.	106

This page intentionally left blank

Chapter 1

Introduction

Contents

1.1 Quantum gases	4
1.2 Ultracold Bose and Fermi mixtures	6
1.3 Context: construction of a next generation Bose-Fermi quantum gas machine	9
1.3.1 Magnetic vs optical trap	9
1.3.2 The subject of my thesis	10
1.4 Outline of my thesis	11

The formulation of Maxwell's equation puts forth the foundation for radiation pressure exerted by electromagnetic radiation, which was demonstrated by Nichols, Hull and Lebedew[1] in early 1900. The experimental realization is now widespread since the availability of multiple laser sources. The invent of Lasers in 1957 was a major paradigm shift in the field of atomic physics. Apart from probing the atoms, it has asserted a more significant role in controlling the internal as well as external degrees of freedom of the atoms and thus led to development of several laser cooling techniques during mid 70s[2] and their experimental realizations happened in the 80s.

These cooling techniques reduce the kinetic energy of the atoms through spontaneous emission processes and cool them to very low temperatures. The collective quantum properties of the atoms is revealed at low temperatures where the wave nature of the particles becomes prominent. When the de Broglie wavelength $\lambda_{dB} = \sqrt{\frac{2\pi\hbar^2}{mk_B T}}$ becomes comparable to the inter particle distance, the quantum statistics plays a dominant role.

Among many fundamental properties, each particle can be characterized by its intrinsic angular momentum, its spin[3]. Based on its spin it is categorized in two distinct groups and is identified as a boson or fermion. The bosons have an integer spin and follow Bose-Einstein statistics. At sufficiently low temperature they undergo a phase transition (see figure 1.1) and occupy a single quantum state at $T=0$. This phenomenon of phase transition is called the Bose-Einstein Condensation (BEC) and was predicted by Albert Einstein[4] based on Satyendra Nath Bose's theory[5].

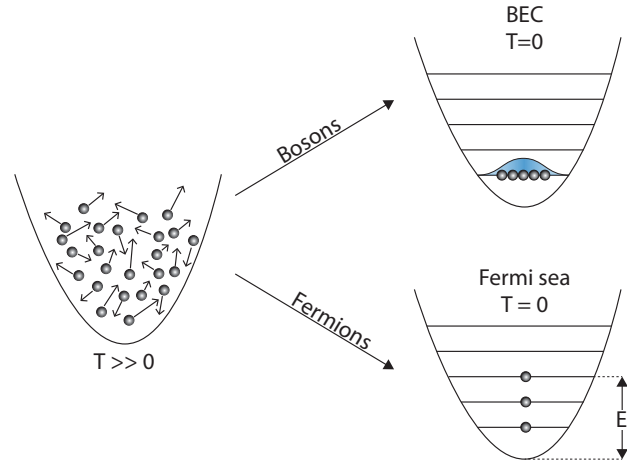


Figure 1.1: In a trapped harmonic potential, at low enough temperature bosons undergo a phase transition to a Bose Einstein condensate, with a macroscopic occupation of the trap ground state. In contrast to bosons, fermions on the other hand obey Pauli exclusion principle and fill-up in the lowest energy states up to the Fermi energy. The energy of the highest energy fermion is called the Fermi energy and is denoted by (E_F).

The fermionic systems behave in a very different manner from bosonic systems. The fermions have half-integer spin and they follow Pauli exclusion principle, which prevents two identical fermions to occupy the same quantum state. So at $T = 0$ temperature, fermions fill up the lowest energy levels one by one up to the Fermi energy and thus constitute the Fermi sea (see fig. 1.1). This situation was first described theoretically by E. Fermi in 1926[6]. The energy of the highest occupied single particle eigen state is called the Fermi energy (E_F) and the corresponding temperature is denoted by $T_F = E_F/k_B$.

While the thermodynamic behaviour of a non-interacting gas is completely governed by its quantum statistics, the real systems are also characterized by the interactions between the constituent particles.

Examples of quantum collective effects for bosons and fermions

Liquid Helium

In 1937, Kapitza[7], Allen and Misener[8] discovered that the viscosity of ^4He below the phase transition temperature of 2.2 K was exactly zero. This was interpreted[9]–[12] as the condensation predicted by Bose and Einstein of bosonic ^4He . Years later, in 1972, ^3He was also found to undergo a phase transition, at a temperature of 2.6 mK, below which it was superfluid[13], [14]. Here, the superfluidity was interpreted as resulting from the formation of pairs of fermionic ^3He [15].

Superconductivity

Unlike Bose-Einstein condensates degenerate fermionic systems are more common in nature. For instance at low temperature metals undergo a phase transition towards a superconducting state. This phenomenon involves interacting electrons (two spin states in weak attraction) and is described by the Bardeen-Cooper-Schrieffer (BCS) theory[16], [17]. The superfluid character of the Cooper pairs leads to the observed absence of electric resistance.

Neutron stars

Degenerate fermions are also found in neutron stars. Neutrons are spin 1/2 particles. The Fermi pressure counterbalances the attractive gravitational pull and thus stabilizes the star. The typical temperature in a neutron star is in the order of $T = 10^9\text{K}$ and density of $n = 10^{38}$ atoms/cm³. The Fermi temperature of this system is on the order of $T_F = 10^{11}\text{K}$ and thus the degeneracy parameter is on the order of $T/T_F = 0.01$ which is very similar to the T/T_F produced in the cold atom labs but with huge differences in temperature and density.

1.1 Quantum gases

History of Quantum gases

Although the first experiments related to BEC were performed with liquid ^4He [18], the rapid progress of the laser cooling[19]–[21] and trapping[22]–[24] techniques for neutral atoms in vacuum paved the way of dilute quantum degenerate gases to become a unique platform for the study and simulation of quantum many body systems. Indeed the first observation of BEC[25]–[27] in 1995 and degenerate Fermi gas[28] in 1999 demonstrated that cold atoms are indeed suitable candidates for studying the quantum many-body properties.

Since the production of the first Bose-Einstein condensates, a huge number of experiments have been performed, examining different aspects of the physics of BEC. A few important observations are briefly mentioned here. Measurement of energy and ground state occupation of BEC investigated the BEC phase transition[29]. Matter-wave interference between two Bose condensates confirmed the coherence of BEC[30]. The atom laser was produced[31], [32]. Many more ground breaking results were obtained such as evidence of critical velocity for superfluidity[33], Mott insulator transition[34] Anderson localization of matter waves[35], [36], observation of quantized vortices in rotating clouds[37]–[39] as well as dark and bright solitons[40], [41].

Tunable Fermi gases, BEC-BCS crossover and Feshbach resonances

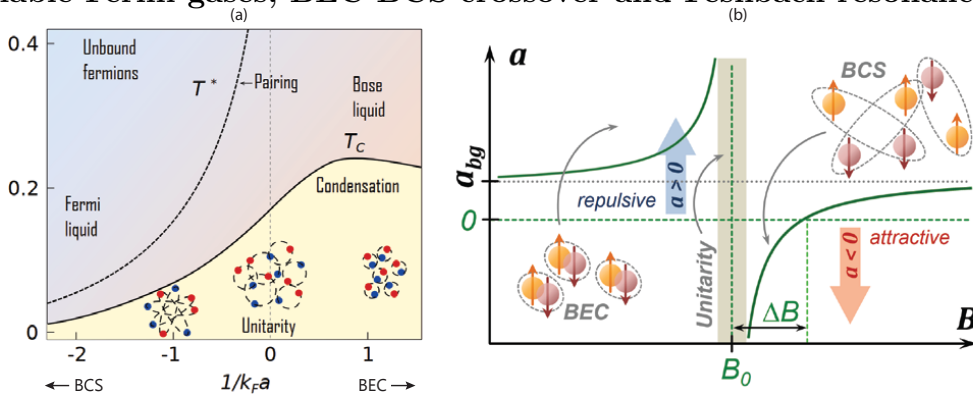


Figure 1.2: (a) Phase diagram of BEC-BCS cross over as a function of $1/k_F a_s$. Picture adapted from[42]. (b) s-wave scattering length (a_s) as a function of magnetic field.

Nowadays, one of the most important tool in quantum gas experiments are Feshbach resonances[43]. At a Feshbach resonance the colliding atoms couple to a molecular bound state, which results in an increase of the scattering length and therefore stronger interactions among the atoms. The energy level of the molecular bound state with respect to the relative energy of the colliding atoms can be tuned, by changing the magnetic field.

While Pauli exclusion principle forbids s-wave interaction between fermions having the same internal state, interactions are allowed in a two-component Fermi gas (for instance, atoms in two different spin-states denoted by \uparrow and \downarrow). These two fermionic species may interact with each other, and interactions are characterized by the scattering length a_s and the interaction strength $k_F a_s$ where k_F is the Fermi momentum given by $k_F = \sqrt{2m\hbar E_F}$. Using a Feshbach resonance between the two spin states \uparrow and \downarrow , we have full control over the sign and magnitude of the scattering length (see figure 1.2 (b)). Based on the value of the quantity $1/k_F a_s$ the system can be classified between two limiting cases, the BEC regime and the BCS regime. For $1/k_F a_s \gg 1$ fermions form tightly bound pairs that display bosonic character and undergo Bose-Einstein condensation. This regime is called BEC regime. Whereas on the other side $1/k_F a_s \ll -1$ fermions form Cooper pairs[16]. This regime is called the BCS regime of weakly attractive fermions (see figure 1.2 (a)). In between, the situation $1/k_F a_s \rightarrow 0$ is called the unitary limit and the system is said to be strongly interacting in this region. Thus by changing the scattering length one can tune the system from the BEC regime to a BCS regime[44]–[49].

High-temperature superfluidity

Superfluidity is possible in the whole BEC-BCS crossover but it is particularly robust in the unitary limit. While on the weakly attractive BCS side the superfluid transition temperature scales exponentially with the inverse interaction parameter, increasing $k_F a$ increases considerably the superfluid temperature. The transition temperature T_c for superfluidity at unitarity and for a homogeneous gas is $T_c = 0.167(13) T_F$ [50].

Equation of state

The thermodynamic equation of state is a key quantity for the macroscopic description of ultracold Fermi gases. It is convenient to express the equation of state in the grand-canonical ensemble. The equation of state relates pressure (P), chemical potential (μ_1, μ_2) and temperature (T), where μ_1 and μ_2 are the chemical potential of spin up and spin down particles respectively. In general this equation of state depends on scattering length a . At unitarity and for spin balanced gas the equation of state depends only on μ/T and is universal[48], [51].

Spin imbalance Fermi gases

As described above, the equation of state in the fermionic system is a function of three parameters: temperature[48], [50], [52], interaction strength[49], [53], and the ratio between the two spin-populations. In the case of a spin-imbalanced gases, the superfluidity is lost above certain population imbalance. This threshold is known as the Chandrasekhar-Clogston limit[54], [55], and has been investigated both theoretically[56], [57] and experimentally by the group at MIT, Rice and Paris[48], [49], [58], [59]. The three groups revealed that a spin-imbalanced harmonic trapped gas exhibits three regions I) superfluid core where atoms are paired and densities are thus equal for both spin states, and II) surrounding the core a partially polarized normal phase and III) an outer fully polarized Ideal Fermi gas of the majority spin component.

The phase diagram of spin-imbalanced Fermi gases is very rich. Exotic phases are predicted to be stable, the most famous one being the Fulde-Ferrell-Larkin-Ovchinnikov (FFLO)[60], [61] states in which the order parameter is modulated in space and pairs have finite momentum. However this state is expected to occupy a very small part of the phase diagram and their observation may require substantial experimental efforts. The ongoing development of uniform trapping potentials is a promising route for the observation of FFLO phases.

1.2 Ultracold Bose and Fermi mixtures

After the observation of BEC and degenerate Fermi gases, experimentalists have simultaneously cooled mixtures of bosonic and fermionic isotopes close to the quantum degeneracy¹[62], [63]. In fact the first observation of a mixture of BEC with a Fermi sea was obtained in the ultracold Fermi gases team at ENS[64]. A variety of Bose-Fermi mixtures have been produced in the cold atom community and table 1.1 provides a list of such experimental realizations.

Mixtures of bosons and fermions present us a unique platform to study interesting open problems such as the polaron problem, double superfluidity, appearance of vortices, the Kondo effect and many more.

¹It is also interesting to note that the first methods to cool fermions was via sympathetic cooling with bosons.

bosons	fermions	Reference	Type of trap
^7Li	^6Li	Schreck et.al.,2001[64]	Magnetic trap
^7Li	^6Li	Ferrier-Barbut et al., 2014[65]	Hybrid trap
^7Li	^6Li	Truscott et al., 2001[63]	Magnetic trap
^{23}Na	^6Li	Hadzibabic et al., 2002[66]	Magnetic trap
^{87}Rb	^{40}K	Roati et al., 2002[67]	Magnetic trap
^{87}Rb	^6Li	Silber et al., 2005[68]	Magnetic trap
$^4\text{He}^*$	$^3\text{He}^*$	McNamara et al., 2006[69]	Magnetic trap
^{87}Rb	$^6\text{Li}, ^{40}\text{K}$	Taglieber et al., 2008[70]	Magnetic trap
^{87}Rb	^6Li	Deh et al., 2008[71]	Magnetic trap
^{85}Rb	^6Li	Deh et al., 2010[72]	Optical trap
^{84}Sr	^{87}Sr	Tey et al., 2010[73]	Optical trap
$^{84,86,88}\text{Sr}$	^{87}Sr	Stellmer et al., 2013[74]	Optical trap
^{174}Yb	^6Li	Hara et al., 2011[75]	Optical trap
^{174}Yb	^6Li	Hansen et al., 2011[76]	Optical trap
$^{170,174}\text{Yb}$	^{173}Yb	Sugawa et al., 2011[77]	Optical trap
^{41}K	$^{40}\text{K}, ^6\text{Li}$	Wu et al., 2011[78]	Hybrid trap
^{162}Dy	^{161}Dy	Lu et al., 2012[79]	Hybrid trap
^{23}Na	^{40}K	Park et al., 2012[80]	Hybrid trap
^{133}Cs	^6Li	Repp et al., 2013[81]	Optical trap
^{52}Cr	^{53}Cr	Naylor et al., 2015[82]	Optical trap
^{23}Na	^{40}K	Yan et al., 2020[83]	Optical trap

Table 1.1: Examples of Bose-Fermi mixtures studied around the globe. Hybrid traps are a combination of magnetic and optical traps.

Polaron problem

Polarons are one of the most studied interdisciplinary research topics in physics, chemistry and material science. In condensed matter, a polaron is a quasi particle made of an electron dressed by a cloud of phonons. The study of this electron-phonon interaction and polaron dynamics have been shown to be relevant in active research topics such as semiconductors and polymer physics.

Ultracold Bose-Fermi mixtures provide a clean and controllable system to investigate the properties of polarons [84]. In quantum gases an impurity interacting with a BEC or with a two component Fermi gas leads to a dressing of the impurity that is called a polaron. As an example, the Fermi energy of ultracold Fermi gases being in the $1 \mu\text{K}$ range makes the dynamics of polaron formation in the μs domain easily accessible experimentally [85]. Using Feshbach resonances the interaction strength between a Fermi superfluid (or a BEC) and the impurity can be tuned. Fermi polaron properties have been studied in the strongly interacting regime for both attractive and repulsive polarons [48], [86]–[88].

Double superfluidity

Our group has measured the critical velocity of a BEC oscillating inside a superfluid Fermi gas. The critical velocity at which damping occurs was found remarkably high[89], [90].

Quantized vortices

Quantized vortices are the topological defects in the angular momentum of a rotating superfluid. Ever since the experimental realization of BEC many theoretical and experimental studies are conducted for characterization of the quantized vortices which enriches our understanding of the superfluid phenomena. Observation of vortices in a mixture of Bose-Fermi double superfluid[91] has opened up new avenues of exploration of many static and dynamic properties of Bose-Fermi superfluid mixture such as the inter species vortex interactions. With a wide range of tunable parameters such as the population imbalance or the interaction strength as a result of Feshbach resonances the exploration of such rotating systems is very rich.

Kondo effect

Kondo effect is one of the interesting many-body effect in condensed matter physics. It is a non-trivial transport interaction between the fermions in the presence of a magnetic impurity (boson in this case). At low temperature this impurity forms a spin singlet many-body bound state with the Fermi sea and magnetically screen the other fermion. This Kondo effect describes the change in electrical resistivity as a function of temperature in the presence of magnetic impurities in semiconductors[92] and it is also observed in quantum dots[93]. Given its importance in condensed matter it is natural to consider to implement the Kondo model with a mixture of ultracold Bose and Fermi gases. Several models have been proposed[94]–[97] but the experimental realizations are still elusive.

In summary the physics of Bose and Fermi mixture is very rich. When the mass of bosons and fermions are nearly equal the physics is somewhat simpler. In our laboratory at LKB we focus on the study of mixture of ^6Li (fermion) and ^7Li (boson). During my PhD my goal was to build a next generation machine for addressing some of the interesting open problems on Bose-Fermi mixtures.

1.3 Context: construction of a next generation Bose-Fermi quantum gas machine

The work I am presenting in the PhD manuscript has been carried out in between October 2017 and September 2021 on the Lithium 1 experiment in the Fermi gas group at ENS under the supervision of Christophe Salomon. I have also been helped and guided by Tarik Yefsah throughout my PhD. Tim de Jongh, a postdoc working on Lithium 3 (the experiment led by Tarik Yefsah), helped me on my experiment from mid June until beginning of September 2021, when I stopped working on the machine for writing my PhD manuscript. The first signals of simultaneous D1 cooling of ^6Li and ^7Li were obtained during this period.

Before I joined the Fermi gas group at ENS in October 2017 we had an experiment working with lithium isotopes confined in a magnetic trap for evaporation followed by a confinement in an optical dipole trap to enable trapping of arbitrary spin states. This machine was build more than 20 years ago and the last major upgrades were done about 10 years ago. As a result a couple of magnetic coils such as Ioffe bars and Feshbach coils had deteriorated over time and developed leaks which stopped the experiment. So we took this opportunity to explore an all-optical trapping route towards Bose-Fermi quantum degeneracy removing the need of evaporation in a magnetic trap.

1.3.1 Magnetic vs optical trap

Magnetic traps make use of electromagnets or permanent magnets to create the appropriate magnetic fields to trap the atoms in appropriate spin states. The trapping extension of magnetic traps are given by the dimension of the magnets, typically on the macroscopic scales, i.e. several centimeters. Together with the usual experimental curvature or gradient values, they give rise to a large trap depth typically several hundreds of millikelvins. With these huge trap depth and large spatial extension it is possible to load the atoms from a MOT into a magnetic trap with 100% efficiency. However operation of a magnetic trap relies on the internal Zeeman states of the atoms and requires the atoms to be in low field seeking Zeeman states.

On the other hand an optical dipole trap (ODT)[\[98\]](#) uses the dipole force of a far detuned laser beam on the atoms and its operation does not depend on the inner state of the atoms. However the size of the optical dipole trap is limited by the laser beam waist, which is usually one order of magnitude less than the size of a typical MOT atomic cloud. Also to reduce the trap heating due to spontaneous emission, large detunings are used and the trap depth is correspondingly low compared to a magnetic trap and is only up to a few millikelvins. Thus it requires high optical power on the order of ~ 100 W.

Despite having a disadvantage for its capture volume over the magnetic traps, the optical dipole traps provide very good trapping frequencies in the strongly confining direction on the order of a few kHz as compared to the magnetic traps (few hundred Hz) in the strongly confining direction. High trapping frequency is very useful in evaporative cooling as it provides strong confinement resulting in high collision rate of the atoms in the trap. Further increase in trapping frequency can be achieved by crossing two optical dipole traps. Even at the low optical power, the trapping frequencies are typically several hundreds of Hertz, which is still larger than the typical magnetic trapping frequencies. The other key advantage of optical dipole traps are the ability to trap atoms in arbitrary internal states which is not possible in a magnetic trap.

1.3.2 The subject of my thesis

This thesis presents the construction of a next generation Bose-Fermi machine and a novel technique to cool ${}^6\text{Li}$ and ${}^7\text{Li}$ simultaneously to sub-Doppler temperatures using gray molasses cooling on D1 lines. Gray molasses cooling has been applied to most alkali atoms[99]–[103]. Although ${}^6\text{Li}$ and ${}^7\text{Li}$ have been separately cooled to sub-Doppler temperatures using gray molasses in the past[65], [99], [101], [104], [105], they have never been cooled simultaneously before.

D1 cooling involves the existence of dark states and operates on $|g, J\rangle \rightarrow |e, J\rangle$ or $|g, J\rangle \rightarrow |e, J-1\rangle$ transitions with respectively one or two dark states. Because of the accidental near coincidence of ${}^6\text{Li}$ D2 line with ${}^7\text{Li}$ D1 optical transition lines, it is not immediately obvious that the D1 cooling of ${}^6\text{Li}$ in the presence of ${}^7\text{Li}$ will work efficiently. As we show in this thesis when the ${}^7\text{Li}$ D1 beams are tuned to $|F=2\rangle \rightarrow |F'=1\rangle$ transition we find that the ${}^6\text{Li}$ D1 molasses does not work. Therefore we have developed a novel pulsed cooling scheme to circumvent the above mentioned problem and we achieved temperatures below $100\ \mu\text{K}$ for both isotopes.

We were initially thinking to operate D1 cooling for ${}^7\text{Li}$ on the $|F=2\rangle \rightarrow |F'=2\rangle$ transition as in previous D1 cooling demonstrations[65], [101]. After I stopped working on the machine to write my PhD manuscript, Tim de Jongh carried on with the project together with Maxime Dixmerias (PhD student on Lithium 3) under the supervision of Tarik Yefsah until the beginning of March 2022. Their work led to improved experiments and allowed us to acquire a better understanding of the physics at play. In particular, they understood that the destruction of the ${}^6\text{Li}$ cloud in the presence of ${}^7\text{Li}$ D1 light was due to the fact that we were accidentally operating ${}^7\text{Li}$ D1 cooling on the $|F=2\rangle \rightarrow |F'=1\rangle$ transition which is only 17 MHz away ($\sim -3\ \Gamma$) from the ${}^6\text{Li}$ D2 $|F=1/2\rangle \rightarrow |F'=3/2\rangle$ transition. They also showed that when operating the ${}^7\text{Li}$ D1 on the $|F=2\rangle \rightarrow |F'=2\rangle$ transition, continuous simultaneous D1 cooling yields good results for both isotopes.

The complete description of experiments on both the $|F = 2\rangle \rightarrow |F' = 1\rangle$ described in this thesis and the $|F = 2\rangle \rightarrow |F' = 2\rangle$ transition, is the subject of the publication [106] (see appendix D). These combined experiments show the robustness of D1 cooling using dark states and the usability of simultaneous sub-Doppler cooling of Lithium isotopes. I will also briefly report in section 4.12 on some of the improvements made.

Along this program we have upgraded the laser system and redesigned the magnetic field coil assembly to perform evaporation near the ${}^6\text{Li}$ Feshbach resonances. We have implemented a new computer control system of the experiment which is now running on Cicero[107]. With National Instruments analog and digital cards, the program is now more user friendly and allows one to control experimental sequence with ease. With the current upgrade we now have been able to reduce the cooling cycle time to a temperature of $100\ \mu\text{K}$ from 2 min to 10 sec. These upgrades are essential and play a key role in smooth operation of the experiment. These upgrades will be discussed in detail in subsequent chapters.

In this all-optical trapping route a major step has been the simultaneous D1 laser cooling of ${}^6\text{Li}$ and ${}^7\text{Li}$ isotopes to below $100\ \mu\text{K}$ which forms the core of my PhD work. Atoms with $100\ \mu\text{K}$ temperature can be efficiently loaded in an optical dipole trap (ODT)[98] having sufficient trap depth and capture volume to proceed towards quantum degeneracy by evaporative cooling.

1.4 Outline of my thesis

This thesis is divided into five chapters and it is structured as follows. After the introduction, Chapter 2 describes the experimental setup and the upgrades that were made on the existing setup. In Chapter 3 we briefly recall the basics of laser cooling and describe several cooling methods currently in use. In chapter 4 we describe the experimental D1 cooling scheme to achieve simultaneous sub-Doppler temperature on both lithium isotopes and present the results. In chapter 5 we discuss perspectives of the experiment.

Chapter 2 - Experimental setup

This chapter has three parts. In the first part of the chapter we describe the various parts of the machine and the upgrades we made on the oven and the magnetic coils such as the replacement of the oven for producing lithium atoms having both isotopes; design, fabrication and assembly of the magnetic coils required for producing magnetic gradient and bias at specific time in the experimental sequence; implementation of a new electrical circuit required to drive the magnetic coils and its characterizations.

In the second part of the chapter we describe the newly implemented laser system in details. This upgrade includes the replacement of the home made master

laser sources with the commercial Toptica lasers; replacement of the slave lasers with slave lasers in Thorlabs mounts for better stability and power; implementation of optical setup for generating laser frequencies at the required frequencies necessary for D1 cooling of both isotopes.

And lastly in the third part of this chapter we discuss the newly implemented computer control of different components in order to manipulate and control the sequence. We also upgraded the imaging system which will also be discussed in this chapter.

Chapter 3 - Overview of laser cooling methods

We start our chapter by recalling the Doppler cooling technique. Then we discuss the sub-Doppler cooling techniques such as polarization gradient cooling. We briefly discuss the velocity selective coherent population trapping (VSCPT) and Raman cooling techniques which lead to sub-recoil temperatures. Later in this chapter we present the gray molasses cooling technique which we have used in our experiment to achieve temperatures on the order of $\sim 100 \mu\text{K}$ on both lithium isotopes.

Chapter 4 - Simultaneous D1 sub-Doppler cooling

After describing our experiment apparatus and the underlying theory in the previous chapters this chapter begins with a typical experiment sequence. Then we present the results obtained by the D2 molasses and subsequently individual D1 molasses in the CW mode. Later we address the problem of simultaneous D1 cooling, we present an explanation why we think the simultaneous D1 cooling of ${}^6\text{Li}$ and ${}^7\text{Li}$ isotopes does not work on the ${}^7\text{Li}$ transition $|F = 2\rangle \rightarrow |F' = 1\rangle$. We then introduce a novel pulsed D1 scheme as a solution to the above mentioned problem and we present the various results obtained with such cooling method. Then we discuss the uncertainties and errors in our measurements. Lastly we present the improvements made by my successors in the pulsed D1 cooling scheme.

Chapter 5 - Perspectives

This chapter talks about future perspectives of the experiment. After D1 cooling we intend to load the atoms into an optical dipole trap (ODT) In this chapter we have estimated the loading efficiency of the ODT, trapping frequencies and the collision rate in the ODT.

We finally conclude the thesis with further directions and some possible applications of this technique.

Chapter 2

Experiment set-up

Contents

2.1	Experimental chamber	15
2.1.1	Atomic beam and details of the Oven	16
2.1.2	Main chamber	20
2.2	Zeeman slower	20
2.3	Magneto-optical trap	21
2.3.1	MOT and Feshbach coils	21
2.3.2	Electrical circuit	24
2.4	Laser systems	29
2.4.1	Master laser system	30
2.4.2	Lithium spectroscopy and frequency locking	33
2.4.3	Injection locking and slave lasers	37
2.4.4	Zeeman slowing beams	39
2.4.5	D1 cooling setup	40
2.4.6	Probe beams	43
2.4.7	Beam mixing	44
2.5	Experiment control and data acquisition	45
2.5.1	Experiment control	45
2.5.2	Data acquisition	47
2.6	Detection system	48
2.6.1	Fluorescence detection	48
2.6.2	Absorption imaging technique	49
2.7	Summary of chapter 2	55

In this chapter we describe different parts of the lithium machine on which I have worked, with a brief overview of the experimental workflow. This machine was the first ultracold Bose-Fermi mixture experiment developed in our group. The detailed description of the construction of the vacuum system and the Zeeman slower can be found in the previous thesis of Lithium 1 group[108]–[111].

Very briefly, a lithium gas jet is produced in a vacuum chamber by heating lithium in an oven and letting the gas escape through a small tube. The atomic beam is slowed down by counter-propagating laser beams in a Zeeman slower configuration. Slow atoms are collected and cooled in a magneto-optical trap (MOT). In the next phase these atoms are transferred into a quadruple trap, where the first stage of evaporative cooling is performed. The atoms are then transferred into a strongly confining Ioffe-Pritchard trap where evaporation to quantum degeneracy has been achieved[64]. Bose and Fermi lithium isotopes can be transferred around $50\ \mu\text{K}$ from the Ioffe-Pritchard trap to an optical dipole trap for taking advantage of Feshbach resonances in ^7Li [41] and ^6Li [45], [65]. Most measurements were performed by absorption imaging method either in-situ[48], [49] or after time of flight.

In this chapter, I will describe how the complex magnetic trapping stages could be removed by implementing simultaneous D1 cooling of Bose-Fermi lithium isotopes. Reaching temperatures of the order of $100\ \mu\text{K}$ or below will enable us to directly load a high power optical dipole trap where evaporative cooling near the ^6Li Feshbach resonance at 832G is highly efficient. In this program we have conducted a major upgrade of the laser systems and of the magnetic coils that I will describe in this chapter.

This chapter is organized as follows. First, I give the detailed description of the lithium oven and the newly fabricated magnetic coils which have multi-purpose uses for the experiment. We then describe the major upgrades of the laser bench which is solely relying on diode laser systems. We describe in detail how the laser beams are produced for different stages of the experiment. And finally we conclude the chapter with a brief description of the absorption imaging technique used in our experiment to detect the atoms and measure the temperature of the atomic cloud.

2.1 Experimental chamber

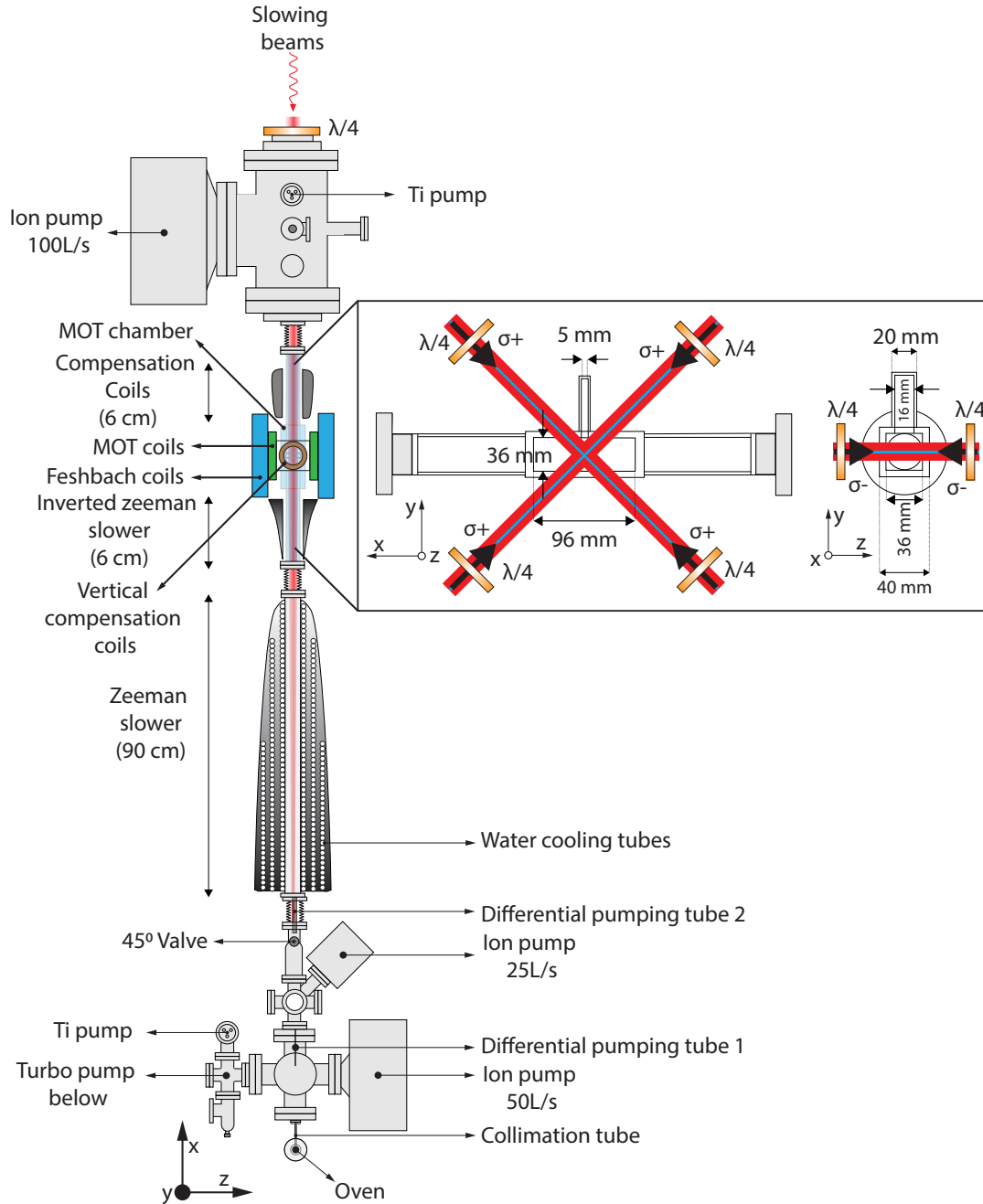


Figure 2.1: Diagram of the vacuum chamber. In the inset the transverse view of the glass cell is represented with the MOT and D1 beams intersecting each other perpendicularly and forming a capture volume at the center of the glass cell. D1 molasses beams are superimposed onto the MOT beams. The approximate $1/e^2$ waist radius of MOT beams and D1 beams are 12.5 mm and 3 mm respectively.

In this section we briefly present different subsystems of the vacuum setup. The vacuum system consists of two chambers, the oven chamber and the main chamber see figure 2.1. Each chamber is independently pumped by its own ion pump, the oven chamber by a 50 l/s ion pump¹ and the main chamber by a 100 l/s ion pump². In addition one titanium sublimation pump is installed in each vacuum chamber though these pumps are rarely used at the moment. We also have a turbo pump³ attached to the oven chamber which is used only in some specific cases for example replacing the oven (which we had to do in February 2021. Normally this change is made only once or twice over a period of 10 years). These two vacuum chambers are connected by the Zeeman slower and differential pumping tubes (see section 2.2).

2.1.1 Atomic beam and details of the Oven

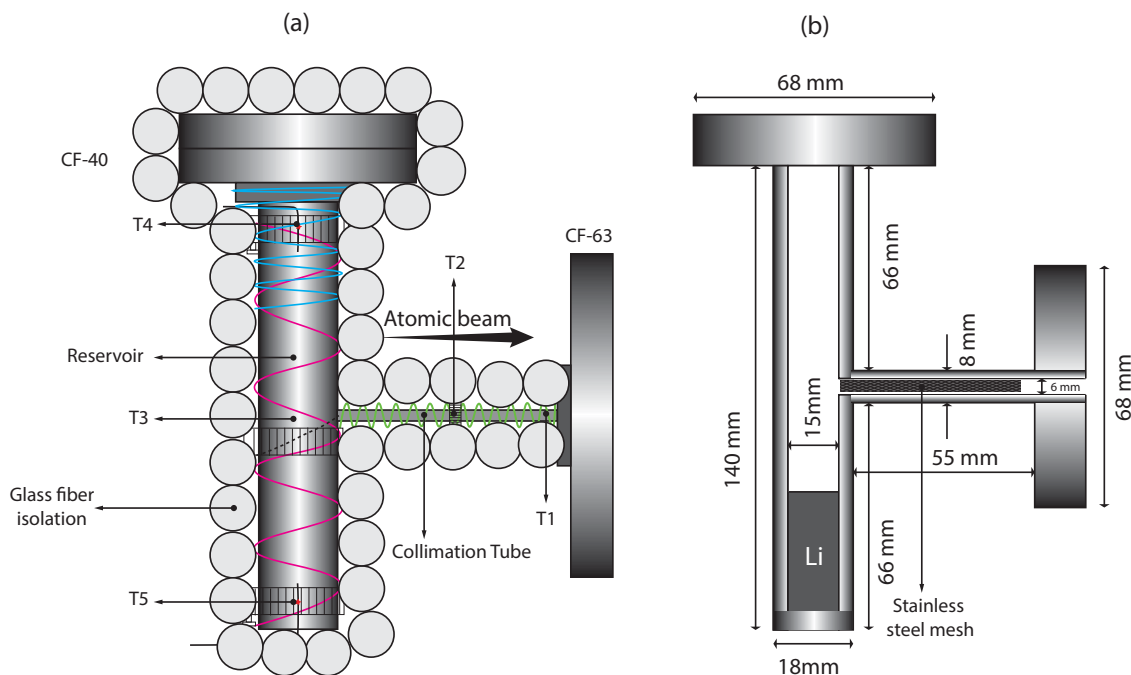


Figure 2.2: Diagram of the Lithium oven. The heating coil and temperature sensor positions are shown in fig (a). The heating coils are represented by cyan, magenta and green curly lines. The exterior is covered with glass fiber in order to provide better thermal isolation. The internal dimensions of the oven are shown in fig (b). Inside the collimation tube a stainless steel cylindrical mesh of thickness $130 \mu\text{m}$ is inserted in order to increase the capillary action of lithium, recycling the Li liquid towards the oven.

¹ MECA 2000 PID 50 N

² MECA 2000 PID 100 N

³ Pfeiffer Hi Pace 80

There are two stable lithium isotopes, the bosonic ${}^7\text{Li}$ and the fermionic ${}^6\text{Li}$. The natural abundance of ${}^6\text{Li}$ is rather high, 7.5%. A natural source is sufficient to deliver both fermionic and bosonic isotopes, which is very useful for sympathetic cooling. In addition it is easy to obtain enriched ${}^6\text{Li}$, because of the high 16% mass difference between ${}^6\text{Li}$ and ${}^7\text{Li}$. In addition ${}^6\text{Li}$ is produced in vast quantities in nuclear reactors. In the latest oven upgrade which is described below, enriched ${}^6\text{Li}$ is put in the oven to balance the mixture of ${}^6\text{Li}$ and ${}^7\text{Li}$ to 50%-50%.

During my PhD, the lithium oven got clogged, we had to build a new one. In this section I present some details on the procedure and operating conditions. The oven is made of a vertical steel cylinder of 18 mm outer diameter and 140 mm length with an extension tube in the middle of the cylinder. A sketch of the structure of the oven is shown in figure 2.2. The top part of the oven is used to fill Lithium inside the reservoir. There are 4 heating element⁴ and 5 temperature sensors⁵ (T1 - T5) wrapped around different parts of the oven as shown in the figure 2.2. The extension tube from the midpoint of the reservoir is called the collimation tube (see figure 2.2). The atoms exiting the oven have high thermal velocity ($\sim 1000\text{m/s}$ and much of the atoms collide to the inner surface of the collimation tube. These atoms need to be recycled back into the reservoir otherwise it develops a clog in the collimation tube. In order to transport back the atoms into the reservoir we maintain a temperature gradient along the collimation tube which results in a capillary force on the atoms which forces the atoms to move back into the reservoir [112]. This process is facilitated by increasing the inner surface area of the collimation tube by inserting a thin cylindrical stainless steel mesh into the tube. The oven is attached to a cubic chamber through the CF63 flange with a nickel gasket. Finally the oven is wrapped with glass fiber and a lot of aluminium foil for better thermal isolation.

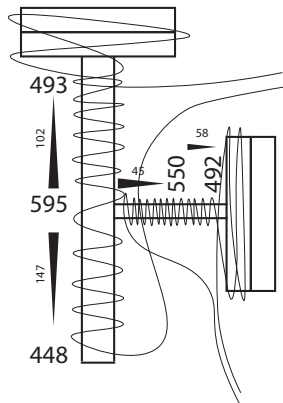


Figure 2.3: The temperature at different parts of the oven is represented in this figure where the solid triangles indicate the temperature gradients.

⁴ Thermocoax SEI 10/50-25/2x CM10

⁵ Omega XICB-K-1-1-3

Lithium has a very low vapor pressure at room temperature, thus it is necessary to heat the oven above 400 °C in order to have a decent atomic flux. At present the temperature at the bottom of the oven (T5) is set at 430 °C and it is controlled by a temperature controller⁶. The middle part of the oven is always at higher temperature and thus it provides the temperature gradient for the lithium recycling process. A typical temperature setup for the oven is shown in the figure 2.3.

The oven chamber is connected to the Zeeman slower through a differential pumping tube. There have been several instance where due to incorrect temperature gradient the collimation tube got partially clogged and the flux of atoms got reduced. In those situation an oven unclogging procedure is followed for getting rid of these partial clogs inside the collimation tube (see appendix A).

Oven bake-out and outgassing procedure

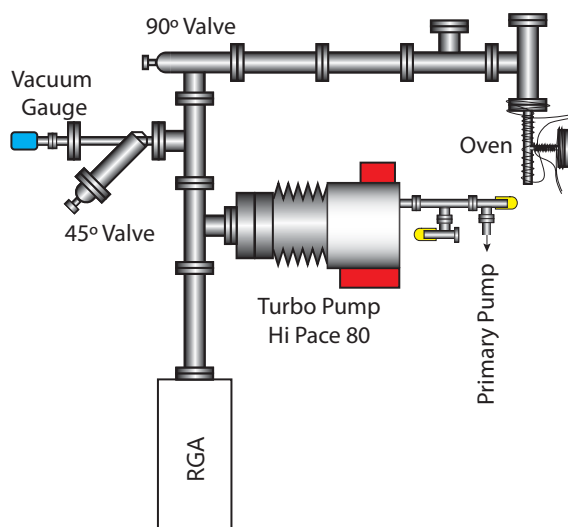


Figure 2.4: Vacuum setup for oven replacement procedure. The oven is heated with thermocoax heating coils. A turbo pump is used to remove the out-gassed impurities. The Residual Gas Analyzer (RGA) is used to monitor the partial pressure of the constituent gas molecules. The total vacuum pressure is measured by the vacuum gauge.

The old oven in the experiment had a good run of 10 years. During my PhD the collimation tube of the oven started to clog more frequently. Though I was able to unclog the tube and make it operational it was never fully unclogged. We were partially unclogging the tube and perhaps while doing so we were shifting the clog position from one position to another and making the inner diameter of the

⁶ Temperature controller Omega CN76133

tube smaller by each iteration. This process one day led to the ultimate clog of the oven and we were no longer able to unclog the oven by heating the collimation tube anymore. Thus we decided to change the oven since it had been working for more than 10 years.

In order to use a new oven we need to clean the oven to get rid of all the impurities inside it. So the oven was first cleaned with an ultra sonic cleaner to remove the dirt and oils from the surface. It was then connected to the setup shown in fig 2.4 so that it can be heated and the gaseous impurities adsorbed in the stainless steel surface can be removed. The oven was heated slowly upto 650° C for a period of 9 to 10 hours each day without the lithium inside, and this process was repeated for 3 days. A turbo pump⁷ is used to suck out all the gaseous impurities released from the oven in this out gassing process. A residual gas analyzer (RGA)⁸ is used to monitor various components of this gaseous impurities.

After we removed the impurities from the empty oven we then inserted Lithium (in the form of solid chunks) which contains both naturally obtained Li and enriched ⁶Li. The oven is then again subjugated to the out-gassing process in order to remove the unwanted chemical impurities from the Lithium chunks. Please note that the melting point of Lithium is $\sim 180^{\circ}\text{C}$. We started heating the oven from room temperature and progressively increased the temperature until the partial pressure of Hydrogen was kept under 1×10^{-4} Torr and allowed the turbo pump to remove these impurities. This way we ensured there is no damage to the RGA by Lithium outgassing process. We continued this process 5-6 hours each day for several days with progressively increasing the temperature of the oven as compared to the previous day. In this way we evaporated the LiH and other oxides from the Lithium sample. After one week of outgassing we were able to out-gas most of the impurities. In the final day of outgassing we measured the Hydrogen partial pressure of $\sim 5 \times 10^{-5}$ Torr with the oven at 600 °C temperature. This temperature is well above our standard operating temperature ($\sim 400^{\circ}\text{C}$) for the oven in the experiment. The $\sim 5 \times 10^{-5}$ Torr partial pressure of Hydrogen at 600 °C indicates that we have sufficiently out-gassed the impurities from our Lithium sample.

After this process is done we then filled it with Argon and we replaced the old oven in the main experiment by the new one. With the help of a turbo pump and the ion pump we were able to reach sufficient vacuum in the oven chamber. The typical operating temperature and pressure can be found in appendix A. For a 430°C in the oven we have 130 μA current in the 50L/s ion pump corresponding to a pressure of $\sim 2 \times 10^{-7}$ mBar⁹ in the chamber immediately after the collimation tube and $\sim 3.5 \times 10^{-4}$ mBar¹⁰ inside the oven chamber.

⁷ Pfeiffer Hi Pace 80

⁸ SRS RGA series

⁹ See [MECA 2000 Ion pumps manual](#)

¹⁰ See [Lithium NIST data](#)

2.1.2 Main chamber

The other end of the Zeeman tube is connected to a glass vacuum chamber. This is the central part of the experiment where the atoms are trapped after travelling through the Zeeman slower. The glass chamber has two components: MOT chamber and an appendix chamber. The structure and dimensions of these chambers are shown in the figure 2.1. The glass chamber is connected at both ends with the steel chamber using glass-metal connections. At the far end of the vacuum chamber a T shaped chamber is attached. The chamber is closed by a view port window which allows the Zeeman slowing beams to enter inside the Zeeman tube. The lithium atoms which could not be slowed by the Zeeman beam gets deposited on this window. Since lithium chemically reacts with glass it forms an opaque deposit on this glass window thus reducing the transmitted intensity of the Zeeman beams. In order to prevent this chemical reaction the window is constantly heated to 60 °C and water cooled on the sides.

2.2 Zeeman slower

At the exit of the oven the atoms have a thermal velocity $\sqrt{k_B T/m}$ of about 1000 m/s. But the capture velocity of a lithium magneto-optical trap (MOT) is about 50 m/s. So it is necessary to slow down the atoms for capturing them in the MOT. This is done by using radiation pressure of counter propagating beams on the atoms inside a one meter long Zeeman slower[21]. With each absorption the momentum of the atom is reduced by the momentum of the photon $\hbar k$. But due to Doppler effect as soon as the atoms are slowed they get out of the resonance from the counter propagating light by Doppler shift ($\Delta\nu = \nu_0 v/c$). Using the principles of Zeeman effect we compensate this frequency shift ($\Delta\nu(z) = \mu_B B(z)$). The Zeeman slower creates a varying magnetic along the motion of the atoms, z , which ensures the atoms are always in resonance throughout the length of the Zeeman slower.

In our lab we use a spin flip Zeeman slower which consists of two coils producing magnetic fields in the opposite direction (see fig. 2.1). The magnetic field varies from +800 G to -200 G. This is called spin flip zeeman slower because initially the spin of the atom is parallel to the magnetic field and after it crosses the zero crossing the spin of the atom is anti-parallel to the magnetic field direction. This Zeeman slower has a capture velocity of 1000 m/s. There are a couple of advantages of using a spin-flip zeeman slower.

- The laser beams used in the Zeeman slower will be off resonant for the atoms in the Magneto-optical trap (MOT).
- Power consumption for the coils is less and hence it produces less heat in the coils.

2.3 Magneto-optical trap

2.3.1 MOT and Feshbach coils

A 3D diagram of the MOT coil assembly is given in figure 2.5. The atoms are trapped in the MOT inside the vacuum glass cell. This glass cell has two chambers namely the upper appendix and the lower MOT chamber. Around this glass cell we have various electromagnetic coils which serve different purposes in our experiment. The most important coils are the MOT coils and Feshbach coils which are defined by their roles in the experiment. The MOT coils are used to provide magnetic field gradient in the MOT, and the Feshbach coils are used to provide magnetic field bias for the Feshbach resonances. The other coils are used for magnetic field compensation in different stages of the experimental sequence.

We have constructed a new set of MOT coils and Feshbach coils used to tune the s-wave scattering length between lithium spin states through the Feshbach resonance mechanism. These coils are made with winding a hollow copper wire¹¹ of 4 mm x 4 mm. The MOT coils consist of 4 turns and 4 layers, whereas the Feshbach coils have 10 turns and 9 layers. A schematic of the MOT and Feshbach coils is shown in figure 2.6. During the MOT phase 20 A current flows in the MOT coils in opposite direction, it provides a gradient of 20G/cm. The MOT coils have other usability. First they are also used as a compensation coils in order to cancel the residual magnetic field along z direction during the D1 molasses phase. They can also be used as a curvature coil to provide axial confinement (19 Hz for 50 A) along the z direction for the hybrid magnetic¹² / optical dipole trap used for evaporation to quantum degeneracy at large magnetic field near 832 G. The Feshbach coils together with the MOT coils in parallel current configuration are designed to produce a magnetic field of 832 G at the center of the glass cell with the Feshbach coils operating at 390 A and the MOT coils at 190 A. They will be used to tune the interactions between the $\pm 1/2$ spin states around the Lithium Feshbach resonances at 832 G.

The total power consumed by the coils can be as high as 20 kW. This power is dissipated as electrical heat produced in the coils. In the absence of a cooling system this would lead to disastrous consequences resulting in the destruction of coils and glass chamber. Thus a proper water cooling system is installed. Various temperature sensors are installed on each of the coils to measure the coil temperature. Water flows inside both MOT coils and Feshbach coils in order to cool down the electrical heat produced by these coils. We have measured the water flow rate in both the coils which are presented in the table below. Since the Feshbach coil is having more turns and layers than the MOT coils the rate of water flow in these coils at 4 bar is less. This 4 bar pressure is not sufficient enough for the Feshbach

¹¹ S&W wire company, SPEC NO. MW53C

¹² See Appendix B

coils to dissipate heat in to the water. A pressurized water flow at 20 bar is required for the Feshbach coils to transfer heat efficiently. A water pump is installed in order to produce these kind of pressure for the Feshbach coils. We also use high pressure resistant water tubes for the Feshbach water cooling circuit.

Coil name	Water flow rate (L/min)	Resistance (m Ω)
MOT 1	1.13	6.8
MOT 2	1.10	6.8
Feshbach 1	0.78	22.4
Feshbach 2	0.91	20.9

Table 2.1: Rate of water flow in the coils are measured at 4 bar pressure. The resistance of the coil includes the intrinsic resistance of the coils and the contact resistance of the connectors for testing of resistance. It does not take into account the resistance of the water-cooling copper tubes and the long copper wires from the power supplies to the coils. The contact resistance of the IGBTs are also not taken into account in this measurement.

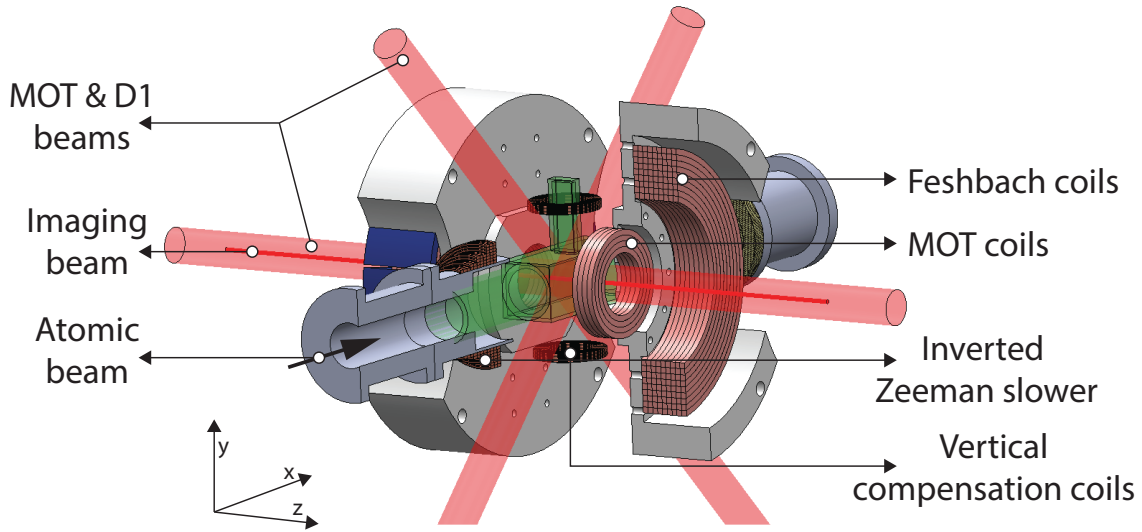


Figure 2.5: This is a cross sectional view of the MOT coil assembly. The glass chamber is represented in green. The red cylinders represent the laser beams which include MOT beams and the D1 beams. All laser beams and the magnetic coils are centered around the geometrical center of the MOT chamber. The slowed atomic beam enters the MOT chamber and is captured by the MOT beams. The cloud is imaged by a probe beam axial to the MOT coil direction. The compensation coils are used to compensate the residual magnetic field during D2 and D1 molasses phases.

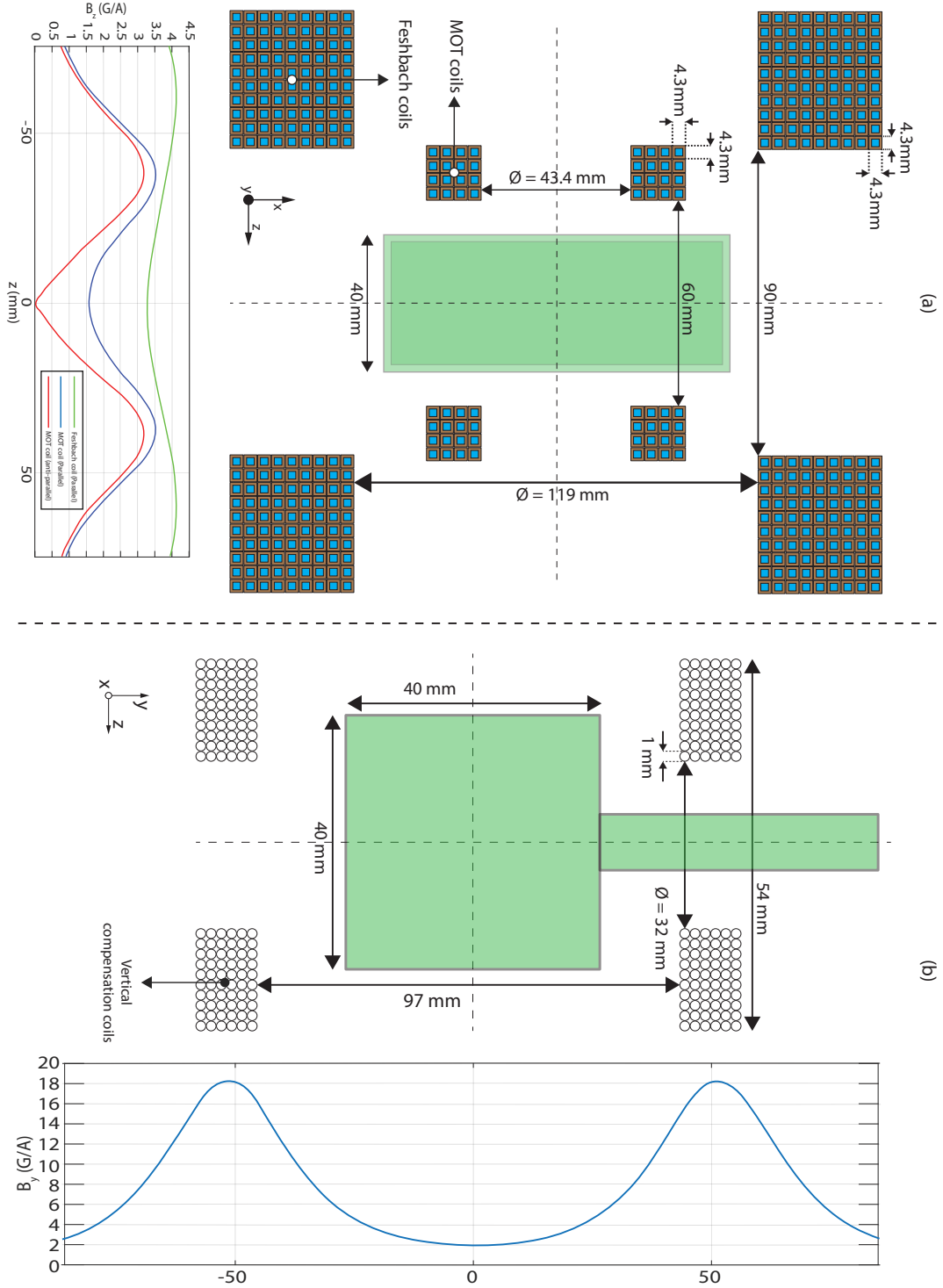


Figure 2.6: (a) Top view of the MOT and Feshbach coil assembly. Here the MOT and Feshbach coils are represented with their dimensions. The modulus of magnetic field per Ampere along the z direction is shown on the top left plot. During the MOT phase the current in the MOT coils flow in anti-parallel direction and provide the magnetic field gradient for the MOT (red curve). In the parallel current configuration the MOT coils produce a field (blue curve) that could add or subtract to the field produced by the Feshbach coils along the z direction (green curve). (b) Side view of the MOT chamber. In this diagram the vertical compensation coils are represented. Magnetic field strength of the compensation coils along the vertical direction (y axis) is plotted in the bottom graph.

2.3.2 Electrical circuit

The electrical connections for the coils and its circuit diagrams are shown in Fig. 2.8 and Fig. 2.9 respectively. The coils use high current power supplies. The MOT coils are connected to a Delta power supply ¹³ which can provide 70 V and 45 A.

IGBT¹⁴ switches, diodes and H-bridge¹⁵ are used to configure the circuit and switch the currents off quickly. These IGBT switches are controlled by opto-isolated drivers which provide ± 15 V to switch on and off the IGBTs in less than $10 \mu s$. Fast switching time for IGBTs are essentially important, since the IGBT junction will behave as a load for the current when the IGBT gate is not saturated, and heat up until destruction.

A typical structure of IGBT is given in 2.8 legend. A diode is usually integrated inside the IGBT module. An IGBT module is a Field effect transistor (FET) which blocks current only in one direction thus this integrated diode bypasses the current in the opposite direction. Therefore an IGBT is used as an one directional switch. Diodes are added in series with IGBTs to the circuit. They are conducting in the sense of operation of the IGBT and block current in the opposite direction. These diodes also protect the transfer and the MOT power supplies against currents in counter direction. The IGBTs, diodes and the H-bridges are mounted on a water cooled breadboard to prevent it from overheating (see Fig. 2.8).

The MOT coils are connected to the power supplies with the help of a H-Bridge. The H-bridge consists of two components (H-bridge A and B). The H-bridge components are nothing but a combination of intrinsic IGBT modules (see Fig. 2.9). The H-bridge is particularly useful in changing the direction of current flow in one of the coils while keeping the other unchanged. By switching the internal IGBT modules we can alter the current direction in one of the coils. This way we can produce parallel magnetic field or cancelling magnetic fields in each of the MOT coils.

The MOT coils can be operated in several configurations. During the MOT phase the currents flow in opposite directions leading to a magnetic zero and a magnetic field gradient at the center between the axis of the two coils (see Fig. 2.6 (a) red curve). These coils can also be operated with current flowing in the same direction in both the coils leading to a magnetic minima and a curvature. The MOT coils operating in such configuration can be used as a curvature coil and in combination with the optical dipole trap (ODT) these coils provide enough curvature to trap the atoms in the axial direction.

¹³ Delta Elektronika SM 45-70 D

¹⁴ Powerex CM600HA-24H

¹⁵ Powerex

The Feshbach coils are the bulkiest of all the coils. The electrical circuit is very simple (see Fig. 2.9). We use two 40V and 500A power supplies¹⁶ in parallel providing us 1000A current available for the coils. An IGBT is connected in series in order to be able to switch on and off the coils rapidly. In addition to an IGBT a diode is also connected to prevent current flow produced by the induced magnetic field in the opposite direction during the switch offs.

The gray molasses D1 cooling is known to work best when there is zero magnetic field in the vicinity of the atoms. There are several sources which produces a small net residual magnetic field around the center of the atomic clouds. These residual magnetic field can be due to the earth's magnetic field or to any other source such as the ion pumps. For efficient gray molasses cooling we need to cancel these residual magnetic fields. There are compensation coils installed along the 3 perpendicular direction around the glass cell. A pair of newly wound coils¹⁷ are installed along the vertical direction to compensate the vertical component of the residual magnetic field. The MOT coils can also act as a compensation coil when used in the parallel current mode¹⁸. These coils can cancel the z component of the residual magnetic field when tuned to appropriate current. The previously installed compensation coils along x axis cancels the x component of the residual magnetic field. The vertical compensation coils are connected to a (15 V, 10 A) power supply as shown in figure 2.9.

Switch-off

The switch-off time of the coils needs to be fast. The residual magnetic field for the D2 and D1 molasses phase should be as small as possible as the presence of magnetic field degrades the temperature. The use of a glass cell and magnetic coils at short distance around the cell is very favourable for fast switch-off. There is very little inductive coupling to the surrounding magnetic structure.

The switch off time is dependent upon the induced voltage during the switch off of the coils $U_{induced} = -LdI/dt$, where L is the inductance of the coils. This voltage accumulates at the junction of the switches (i.e IGBTs). We choose IGBTs which can support 1200 V before breaking down thus allowing us a rapid switch off time. Varistors are connected to IGBTs in parallel. These varistors become conducting at a voltage of 800V and protect the IGBTs from burning. The magnetic energy stored in the coils are thus dissipated in the varistors during switch-offs. See figure 2.7 for the switch off time of the Feshbach coils and the MOT coils.

¹⁶ Sorensen Sga 40-500 40V, 500A, 20Kw, Dc Power Supply

¹⁷ See figure 2.6 for its dimensions and spatial magnetic field gradients

¹⁸ Thanks to the H-Bridge connections for the MOT coils

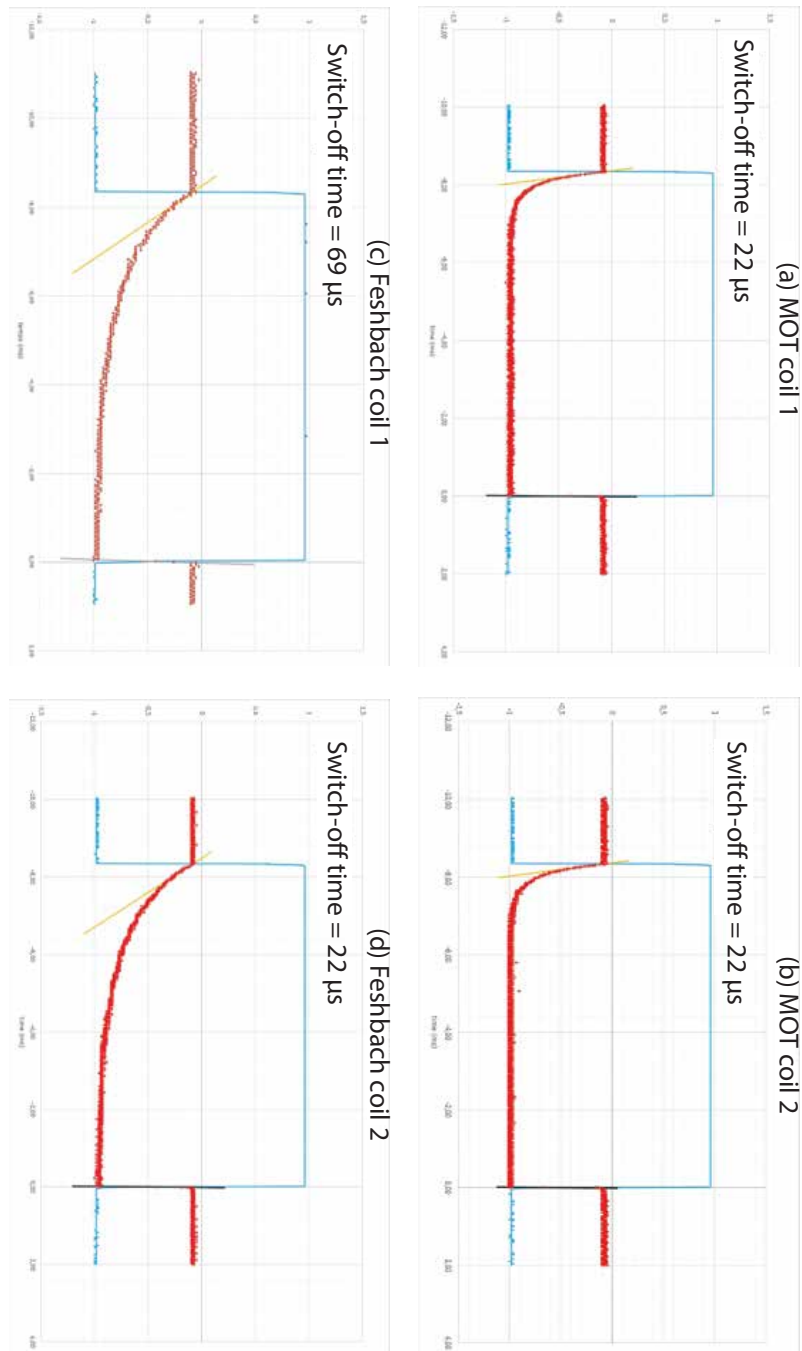


Figure 2.7: Current in the coils as a function of time during switch-off. The $1/e$ switch-off time of MOT coils is $\sim 22\mu\text{s}$, see. (a) and (b). Similarly the $1/e$ switch-off time of the Feshbach coils are $\sim 69\mu\text{s}$ and $\sim 22\mu\text{s}$, see (c) and (d)¹⁹.

¹⁹ Thanks to Alfred Hammond for the measurement of the switch-off time for the coils.

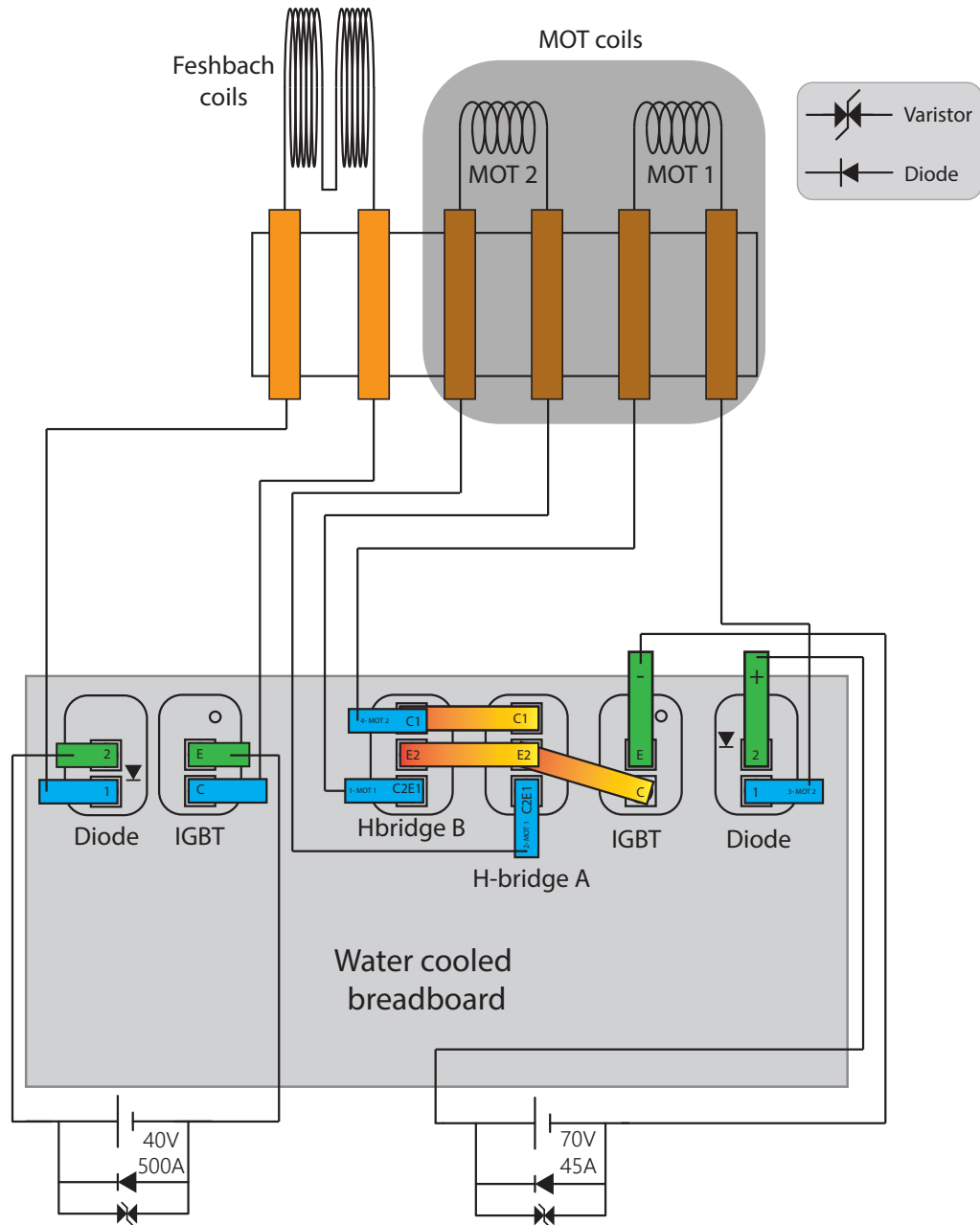


Figure 2.8: A schematic representation of electrical connections for the electro-magnetic coils. The MOT coils and the Feshbach coils are run on separate power supplies with completely independent circuits. Each electrical circuit contains both IGBT and diode modules for the control and unidirectional flow of current. The MOT coil circuit contains H-Bridge module which allows us to alternate the current flow in one of the MOT coils. Detailed circuit diagram can be found in figure 2.9. All these modules are mounted on water cooled breadboard for better heat dissipation. Varistors are used to protect the power supplies.

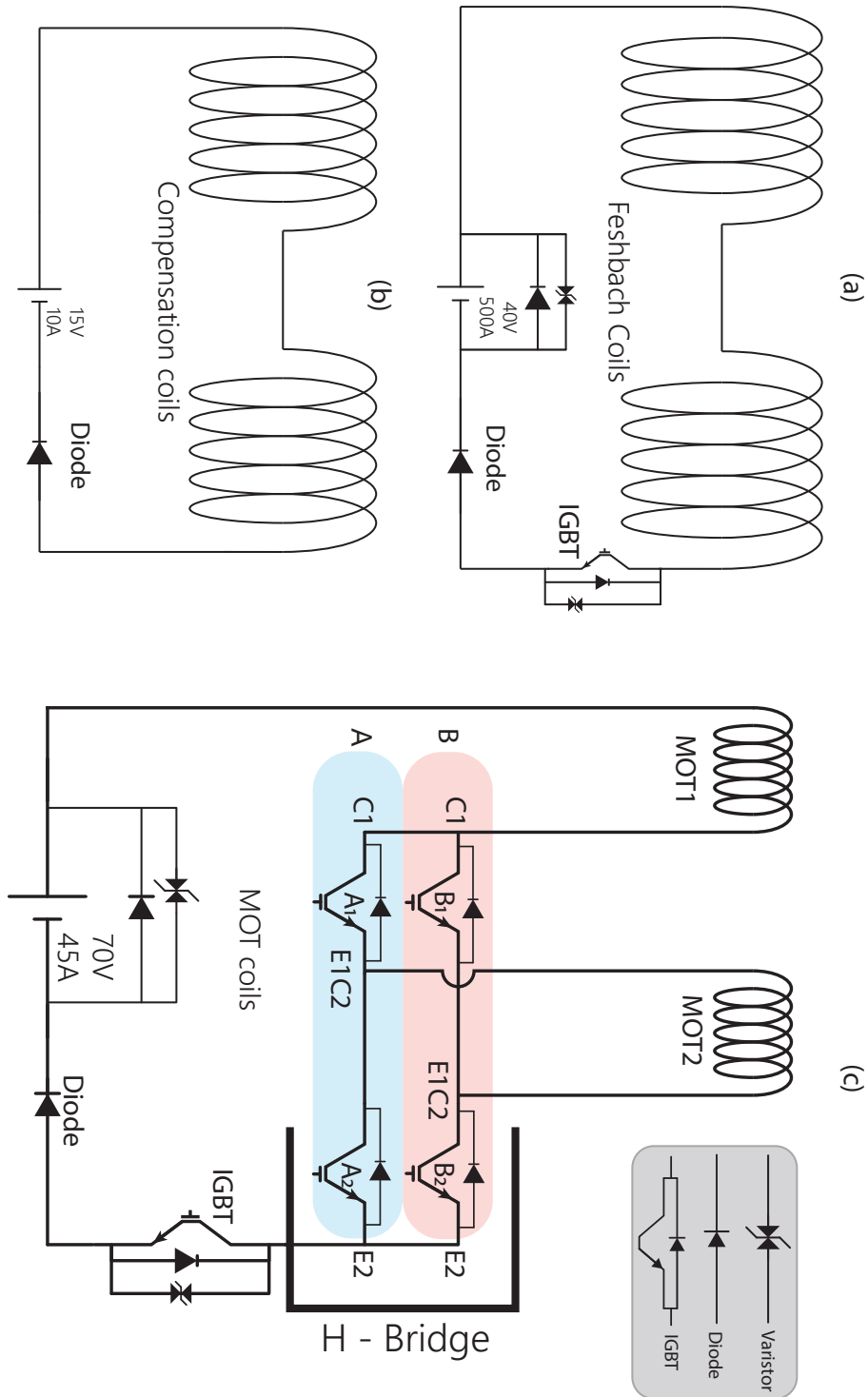


Figure 2.9: Circuit diagram for the electrical connections of figure 2.8. The H-Bridge has 4 internal IGBT modules represented by A1, A2, B1, B2. When A1, B2 are on and B1, A2 are off : the magnetic field produced by MOT1 and MOT2 are in the same direction and when B1, A2 are on and A1, B2 are off : the magnetic field produced by MOT1 and MOT2 are in the opposite directions.

2.4 Laser systems

In this section we discuss the new laser system that I have implemented during my PhD. The laser system is used in four stages of the experimental sequence, Zeeman slowing beams, MOT beams, molasses beams (both D2 molasses and D1 molasses beams) and imaging beams.

The wavelength corresponding to main optical transition in lithium is near 671 nm. Different types of laser source can produce this wavelength (dye laser, Ti-Sapphire laser, diode lasers, doubled solid-state laser[113]–[115] or fiber laser). We choose diode lasers because they are cheap and reliable, with a lot less maintenance requirements compared to other types of lasers. The only downside of diode lasers is that they produce moderate power at our required wavelength; typically 30 mW which is sometimes low for our purpose. Thus we had to implement intermediate amplification stage before we can use it for our purpose. We use the master-slave technique of injection locking to amplify the laser power (typically to 100 mW) while maintaining its spectral purity. The injection locking will be discussed in more details in section 2.4.3. We also use tapered amplifiers (TA) when we need more power. TAs typically produce 500 mW at the output facet, but after optical isolator, and spatial filtering by an optical fiber we usually get no more than 150 to 200 mW.

The lowest S and P states of both lithium isotopes are shown in fig 2.10. For both ${}^7\text{Li}$ and ${}^6\text{Li}$ the slowing and the MOT laser beams operate on the D2 transitions. The excited state hyperfine structure of both ${}^7\text{Li}$ and ${}^6\text{Li}$ is unresolved since the splitting is of the same order as the natural linewidth (5.8 MHz). While addressing the cooling transition other states in this hyperfine structure can also be excited, and these states can decay into the lower hyperfine states. For this reason we need repumping lasers from this lower hyperfine states.

For ${}^7\text{Li}$ the transition from $|F = 2\rangle \rightarrow |F' = 3\rangle$ is used as the cooling transition (principal beam), and $|F = 1\rangle \rightarrow |F' = 2\rangle$ for repumping (repumping beam). However for ${}^6\text{Li}$ while the principal beam is tuned to D2 transition ($|F = 3/2\rangle \rightarrow |F' = 5/2\rangle$) it is repumped on the D1 transition ($|F = 1/2\rangle \rightarrow |F' = 3/2\rangle$) and not on D2 transition because the D2 transition ($|F = 1/2\rangle \rightarrow |F' = 3/2\rangle$) for ${}^6\text{Li}$ is very close to the D1 transition for ${}^7\text{Li}$ ($|F = 2\rangle \rightarrow |F' = 1\rangle$). This accidental closeness of atomic transition is deteriorating for the ${}^7\text{Li}$ MOT and D2 molasses. On the other hand we will take advantage of this closeness in order to produce the D1 beam for ${}^7\text{Li}$ from ${}^6\text{Li}$ D2 principal transition (see 2.4.5).

As mentioned before we have 3 different laser sources which undergo various stages of amplification and frequency shifts before it can be used for cooling and trapping the atoms. In this section I will describe the different setups in details one by one. First I will start with the Master laser system then I will discuss the principle of lithium spectroscopy and the frequency locking technique. Then I will describe the master/slave laser system and discuss the injection locking technique. We will briefly talk about the slowing beams used in the Zeeman slower. Next I

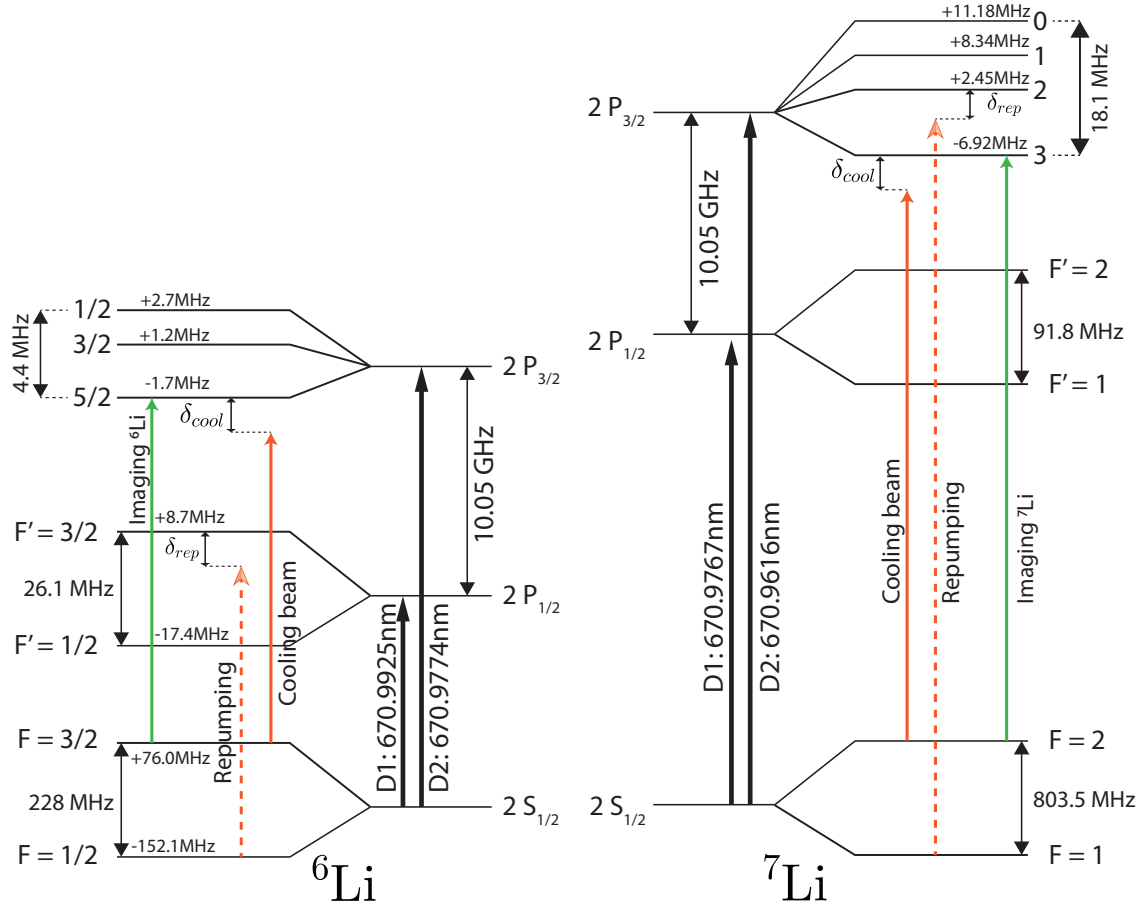


Figure 2.10: Energy level diagram for the S and P levels of ${}^6\text{Li}$ and ${}^7\text{Li}$ [116]. The transitions corresponding to the respective MOT beams are shown in red and the laser beams for imaging are shown in green.

will describe the D1 cooling setup for both ${}^7\text{Li}$ and ${}^6\text{Li}$, how the beams are derived and what are the challenges we encountered for these setups. We will then describe the probe beams and how they are mixed and sent to image the cloud in the absorption imaging setup. At the end of this section I will describe how various beams are mixed on the experiment table and sent to the vacuum chamber where the experiments take place.

2.4.1 Master laser system

After many years of successful operations we decided to replace the home-made Master lasers with commercial Toptica lasers because of high stability, higher power output, long durability and better lock systems. As mentioned before, due to the coincidence of the ${}^7\text{Li}$ D1 line with ${}^6\text{Li}$ D2 lines we repump ${}^6\text{Li}$ on D1 line of ${}^6\text{Li}$. Therefore we require 3 different master lasers. Fig 2.11 and fig 2.12

depict the master laser system for both ${}^7\text{Li}$ and ${}^6\text{Li}$ respectively. These master laser systems are placed on a dedicated optical table (laser table). With the use of double pass AOMs we are able to tune the frequency of these master lasers to the desired value at various steps of the experimental sequence. The output of these master laser systems are on the order of a few mW and are coupled to respective polarisation maintaining fibers (PMFs). The output of these fibers are used to seed the corresponding slave lasers resulting in frequency selective amplification of the beams required for our experiments (see 2.4.3).

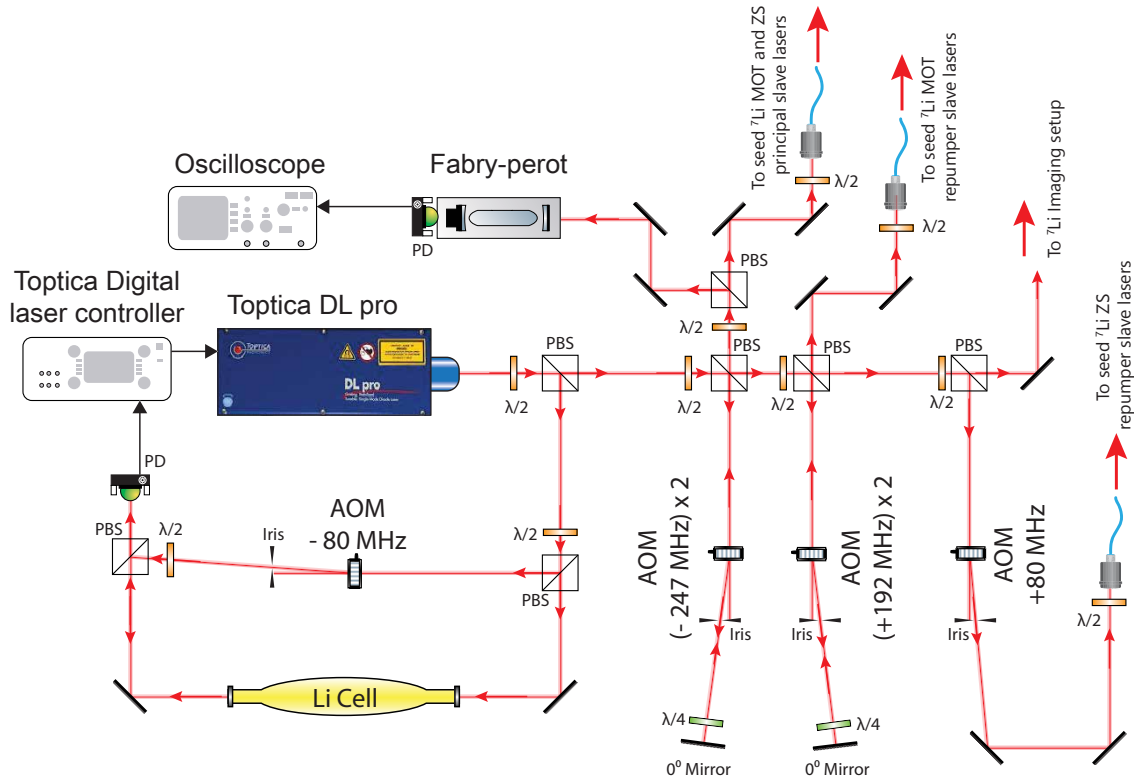


Figure 2.11: Setup for ${}^7\text{Li}$ master laser system. The Toptica master laser is stabilized by saturated absorption spectroscopy (see 2.4.2) and is locked to the cross-over line between ($|F = 2\rangle \rightarrow |F'\rangle$) and ($|F = 1\rangle \rightarrow |F'\rangle$) (see fig 2.15). The principal and repumping beams are derived from the same master laser by the respective double pass acousto-optic modulators (AOM's) and are sent to the slave laser system (see fig 2.18) through the injecting fibers (F1,F2,F3). Part of the master laser beam is sent to the Fabry-Perot interferometer (FPI) in order to check the lock frequency position and stability of the lock.

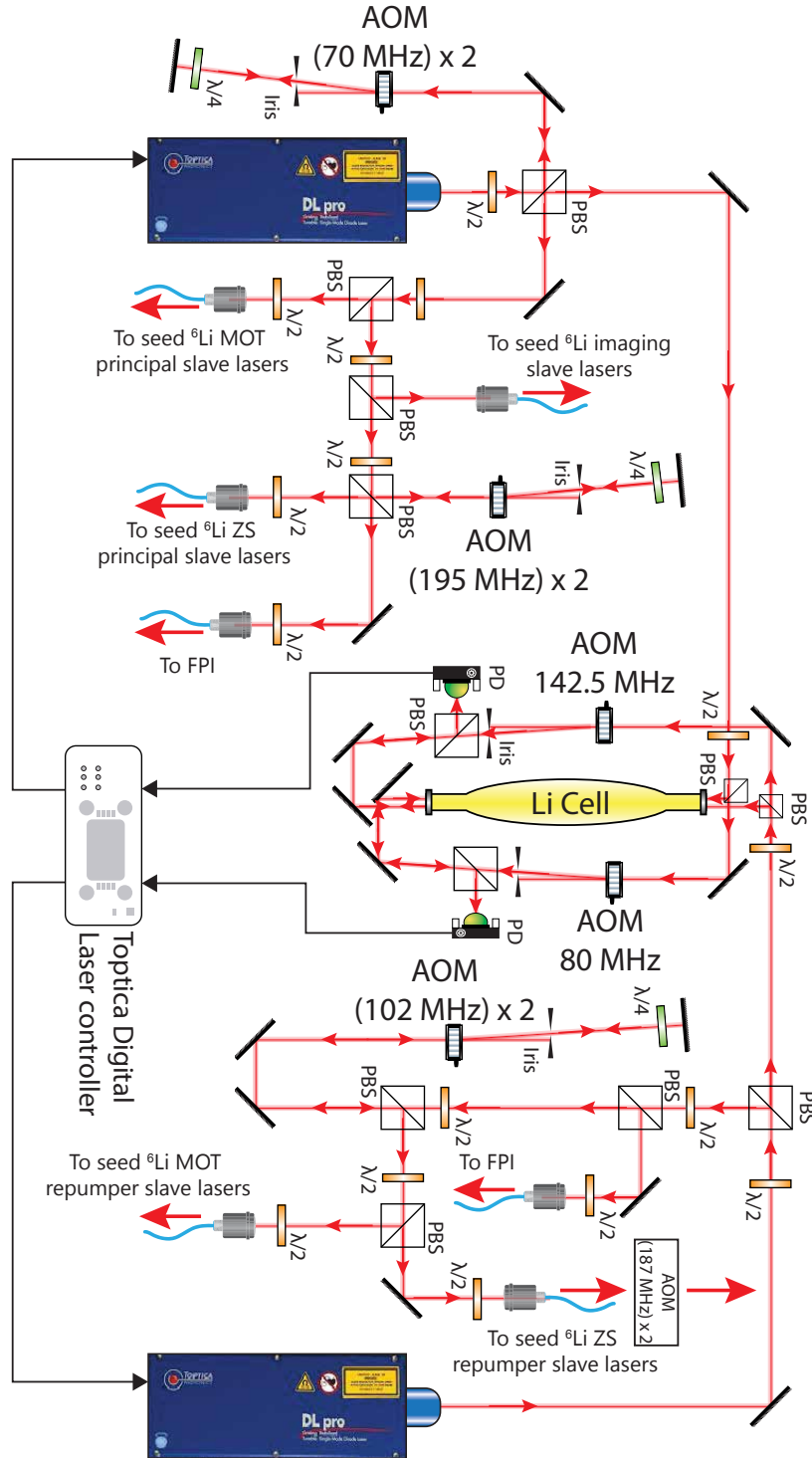


Figure 2.12: Setup for ^6Li master laser system. We have two master lasers one for the ^6Li principal laser beam and the other for the ^6Li repumping laser beam. Both the master lasers are sent to the same spectroscopy cell and are stabilized by saturated absorption spectroscopy (see 2.4.2). The ^6Li principal master is locked to the cross over line between ($|F = 3/2\rangle \rightarrow |F'\rangle$) and ($|F = 1/2\rangle \rightarrow |F'\rangle$) (see fig 2.16). The outputs of this setup are low power injection seeds for the slave lasers as shown in fig 2.18.

2.4.2 Lithium spectroscopy and frequency locking

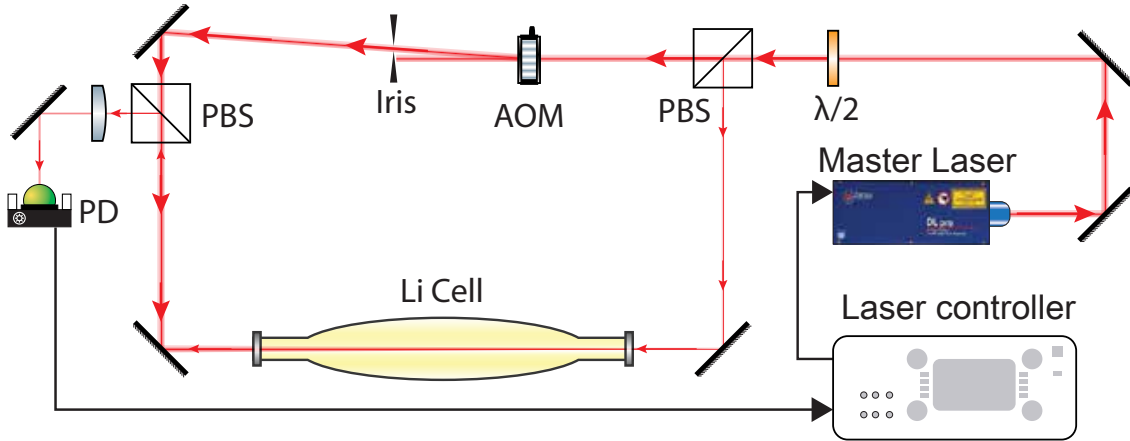


Figure 2.13: Pump-probe Doppler free saturation spectroscopy for frequency stabilization of the master lasers. A 47 kHz modulation is applied to the pump beam through the AOM. The transfer of modulation to the probe is detected by the photodiode and sent to the lock-in system. The error signal is fed to the piezo controller of the master laser. This provides master lasers with ~ 500 kHz laser emission linewidth (see fig 2.14)

The laser frequencies are stabilized using Doppler free spectroscopy on lithium vapor. The spectroscopy cell consists of a metal tube of ~ 30 cm long and the sides of this metal tube are closed by CF40 flanges with BK-7 windows. This tube is heated in the middle by a thermocoax coil up to 300° . The tube ends are water cooled, so that the glass windows do not get over heated and the hot lithium vapour cools down from the middle to the edge. Lithium atoms adsorb on the side of the tube and do not get deposited on the glass windows. The tube is also filled with argon at a pressure of a few 100 mbar. Argon helps to reduce the mean free path of the lithium gas and helps the windows not to get opaque. When the lithium is deposited on the walls it is transported back to the middle of the tube by capillary action produced by the temperature gradient. A steel mesh is introduced inside the tube to increase this capillary action.

The Doppler free spectroscopy[117] is done in a counter-propagating pump-probe configuration (see fig. 2.13). In this method the pump frequency is modulated by an AOM and the probe beam intensity is measured by a photo-diode using a lock-in amplifier. The error signal generated by this method has a very small offset. We have 3 such systems for ^7Li and ^6Li as shown in the fig 2.11 and 2.12.

We used a beat note technique to characterize the line-width of each laser. The two beams are mixed and sent to a fast photo-diode²⁰ of bandwidth 1 GHz. In the figure 2.14 the width of the beat note frequency was ~ 1 MHz. Assuming the spectrum is lorentzian for each laser this corresponds to a single laser linewidth of ~ 500 kHz.

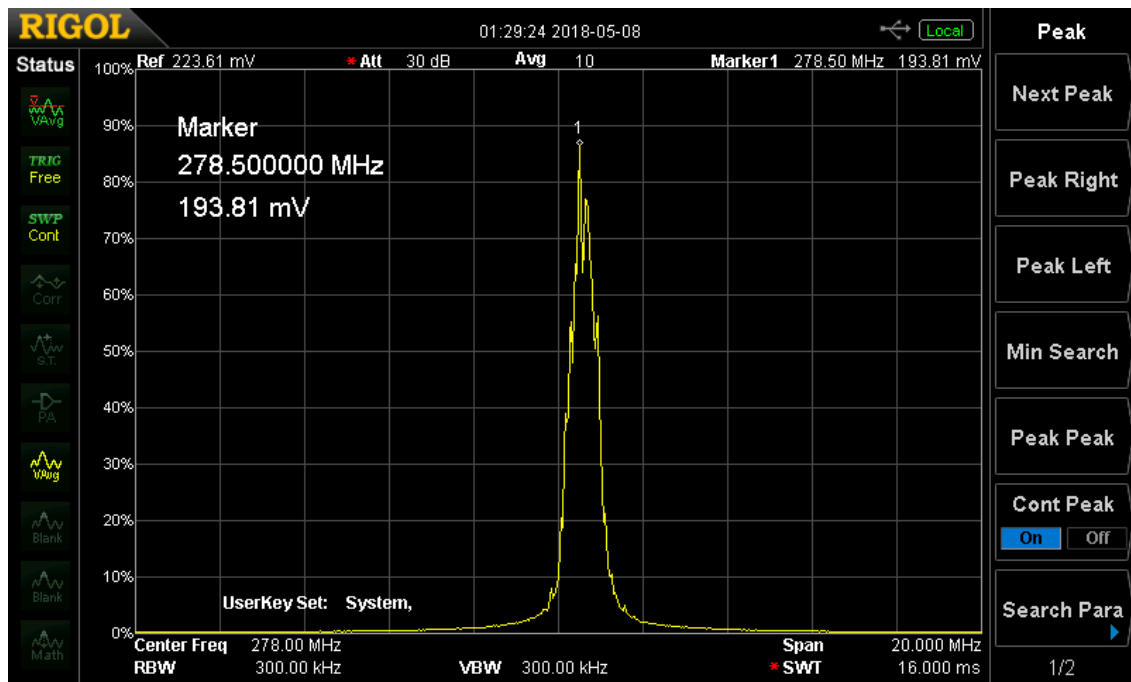


Figure 2.14: Beat note of the two Toptica master lasers. The full width at half maximum (FWHM) is ~ 1 MHz. Assuming a lorentzian profile for each laser this corresponds to an individual laser linewidth of ~ 500 kHz.

²⁰Thorlabs photodiode

As mentioned before we need the laser frequencies corresponding to the transitions shown in figure 2.10. However for the ${}^6\text{Li}$ D2 principal beam we lock the master laser onto the crossover between ($|F = 3/2\rangle \rightarrow |F'\rangle$ and $|F = 1/2\rangle \rightarrow |F'\rangle$), and for ${}^7\text{Li}$ D2 we lock the master laser onto the cross over between ($|F = 2\rangle \rightarrow |F'\rangle$ and $|F = 1\rangle \rightarrow |F'\rangle$). With the help of double pass AOMs we are able to generate the appropriate frequencies for our experiment and to tune them rapidly. Figure 2.16 and figure 2.15 show the respective spectroscopy signals and represent the relative frequency shifts caused by the AOMs in order to achieve the desired frequency of the laser beams during various stages of the experiment.

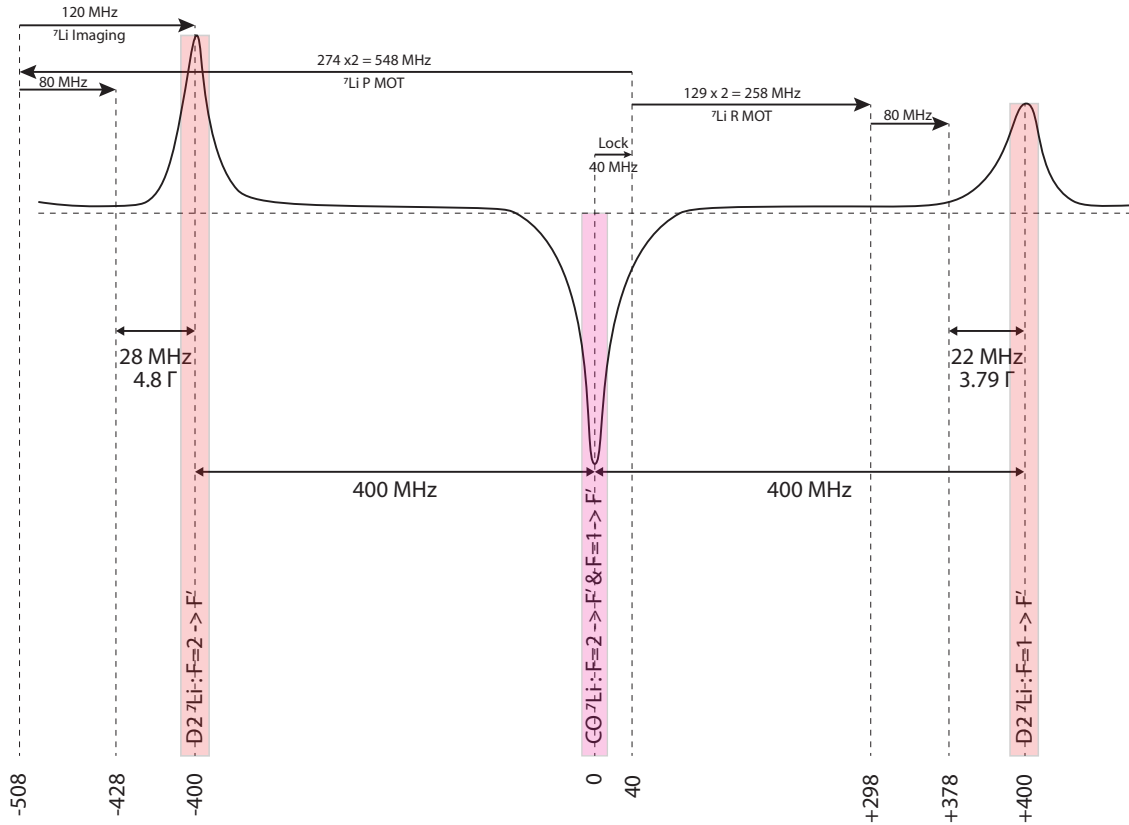


Figure 2.15: Spectroscopy signal for ${}^7\text{Li}$ master laser system. The master laser is locked to the crossover line between $|F = 2\rangle \rightarrow |F'\rangle$ and $|F = 1\rangle \rightarrow |F'\rangle$ and is represented by the magenta line. Due to the single pass AOM in the saturated absorption spectroscopy (see fig 2.11) the lock position is shifted by 40 MHz. The ${}^7\text{Li}$ principal MOT beam is red-detuned from the $|F = 2\rangle \rightarrow |F'\rangle$ by 28 MHz (4.8 Γ) and the ${}^7\text{Li}$ repumper MOT beam is red-detuned from the $|F = 1\rangle \rightarrow |F'\rangle$ by 22 MHz (3.79 Γ)

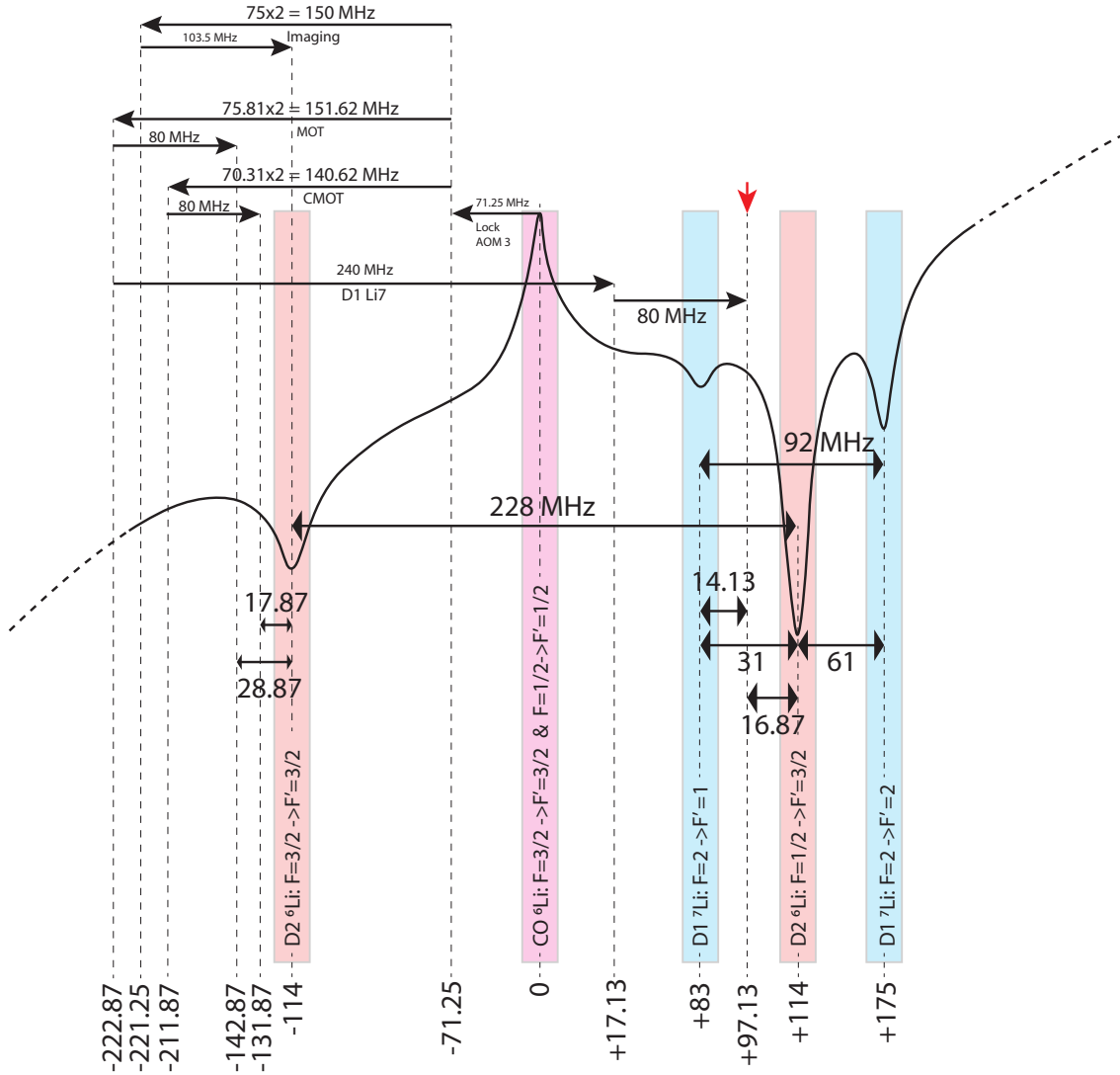


Figure 2.16: Spectroscopy signal for ${}^6\text{Li}$ master laser (principal beam). The master laser is locked to the cross-over line (shown in magenta). Due to the presence of a single pass AOM in the saturated absorption spectroscopy we have a shift of 71.5 MHz in the lock signal. Various atomic transition lines are shown in red (D2 transitions) and blue (D1 transitions). The ${}^7\text{Li}$ D1 laser beams are derived from ${}^6\text{Li}$ D2 principal MOT beam which is 240 MHz frequency shifted by a single pass AOM. Note the close proximity of ${}^7\text{Li}$ D1 beam (red arrow on top) and the D2 transition for ${}^6\text{Li}$ ($|F = 1/2\rangle \rightarrow |F' = 3/2\rangle$) which are just ~ 17 MHz away from each other.²¹

²¹ Initially we made a mistake in thinking that we were doing D1 cooling for ${}^7\text{Li}$ on $|F = 2\rangle \rightarrow |F' = 2\rangle$ transition. But later it turned out we were blue detuned to $|F = 2\rangle \rightarrow |F' = 1\rangle$ transition instead of $|F = 2\rangle \rightarrow |F' = 2\rangle$. I thank Dr. Tarik Yefsah, Dr. Tim de Jongh and Maxime Dixmieras for pointing it out to us.

2.4.3 Injection locking and slave lasers

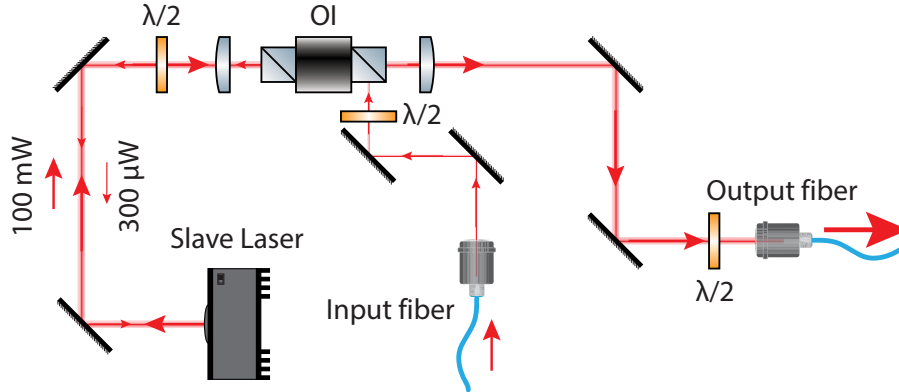


Figure 2.17: Principle of injection locking. About $300 \mu\text{W}$ to $500 \mu\text{W}$ are injected through the output polarizing cube of the optical isolator. This light has the correct polarization for injection locking of the slave diode laser. With the diode HL6545MG we get typically 120 mW of output power. The coupling efficiency of this output beam in the single mode fiber ranges between 40% to 50%.

Though the master laser has a narrow linewidth, one of the disadvantages of master laser diodes at lithium wavelength is that they typically deliver only about 25 mW of output power. The slave lasers are diode lasers originally built for DVD drives which have a spectrum centered at $\sim 660 \text{ nm}$. To obtain light on the transition of lithium ($\sim 671 \text{ nm}$) we heat the diodes up to 60° without reducing the diode's performance significantly. These slave lasers have a higher output power of 120 mW (compared to master lasers $\sim 25 \text{ mW}$) under normal conditions, but free running, the slave lasers have a broad emission linewidth.

Therefore we use the well-known injection locking technique to get sufficient power and narrow linewidth[118] see figure 2.17. One could also use Tapered Amplifiers (TA) to amplify the power but TAs are quite expensive and have a relatively poor output mode quality. We chose to implement the master-slave configuration where the individual diode cost is around 30€. The diodes also have a better mode quality enabling more than 50% coupling into single mode fibers.

We have 8 such slave laser amplification stages (4 for the MOT beams and 4 for the Zeeman slower beams). The slave laser systems for the MOT beams are shown in fig 2.18. We have AOMs for such slave laser systems which act as a switch for the MOT beams. The first order of the AOM is coupled to the respective polarization maintaining fibers which brings the light onto the experiment table where they are mixed onto 4 non polarizing beam splitters (NPBS) (see fig. 2.23).

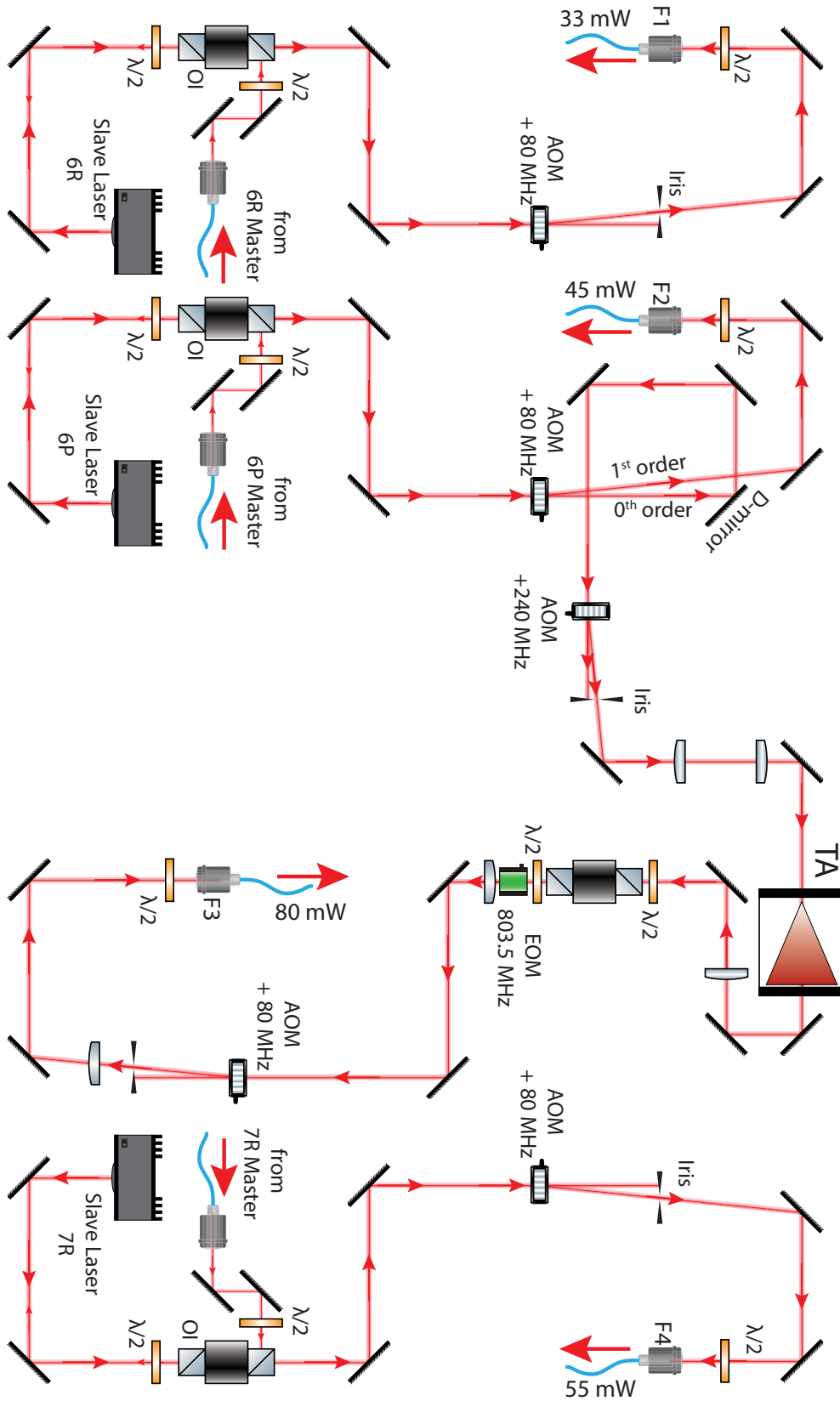


Figure 2.18: Slave laser systems for MOT beams (${}^6\text{Li}$ principal, ${}^6\text{Li}$ repumper and ${}^7\text{Li}$ repumper). The 0th order of the AOM for ${}^6\text{Li}$ principal slave laser is frequency shifted and injected into the TA and this produces ${}^7\text{Li}$ D1 beam.

2.4.4 Zeeman slowing beams

The counter-propagating Zeeman slowing beams consist of four frequencies. See figure 2.10.

- ${}^6\text{Li}$ - cooling beam on D_2 line from $F = 3/2$ to $F' = 5/2$ is used to slow down ${}^6\text{Li}$ atoms
- ${}^6\text{Li}$ - repumping beam on D_1 line from $F = 1/2$ to $F' = 3/2$ is used to recycle ${}^6\text{Li}$ atoms falling on $F = 1/2$ level of ground state($2S_{1/2}$)
- ${}^7\text{Li}$ - cooling beam on D_2 line from $F = 2$ to $F' = 3$ is used to slow down ${}^7\text{Li}$ atoms
- ${}^7\text{Li}$ - repumping beam on D_2 line from $F = 1$ to $F' = 2$ is used to recycle ${}^7\text{Li}$ atoms falling on $F = 1$ level of ground state($2S_{1/2}$). Due to the close proximity of transitions between ${}^6\text{Li}-D_2$ and ${}^7\text{Li}-D_1$ we are using ${}^7\text{Li}-D_2$ as a repumper instead of ${}^7\text{Li}-D_1$.
- Detunings of all the Zeeman light are given in table 2.2.

	Detuning	Output power
${}^6\text{Li}$ cooling	-390 MHz	26 mW
${}^6\text{Li}$ repumper	-375 MHz	23 mW
${}^7\text{Li}$ cooling	-390 MHz	31 mW
${}^7\text{Li}$ repumper	-400 MHz	24 mW

Table 2.2: Detuning and output power of the Zeeman slave lasers with respect to the corresponding main transitions as shown in figure 2.10.

The Zeeman slowing beams are further frequency shifted to the red by a set of four 200 MHz double pass AOMs. The resulting beams are amplified using slave lasers. The slave lasers consist of temperature stabilized 30 mW laser diodes of the same type as the diodes used in the master lasers. The injection is done through the sideport of isolators placed after each slave laser. The four beams for the Zeeman slower are geometrically superimposed under a slight angle. A telescope expands the beam size and a converging beam is sent through the vacuum chamber against the atomic beam, and focused on the oven collimation tube. The power in each frequency component is about 20 mW and at the entrance window the beam full size is about 4 cm.

2.4.5 D1 cooling setup

^7Li D1 laser setup

We can see in Fig. 2.19 the D2 line of ^6Li is very close to the D1 line of ^7Li . We can use this accidental coincidence and derive the required frequency from the already implemented setup for ^6Li MOT. Since the ^7Li D1 line is only 197 MHz away from the ^6Li D2 transition, we use an AOM in order to generate the frequency of ^7Li D1 beams.

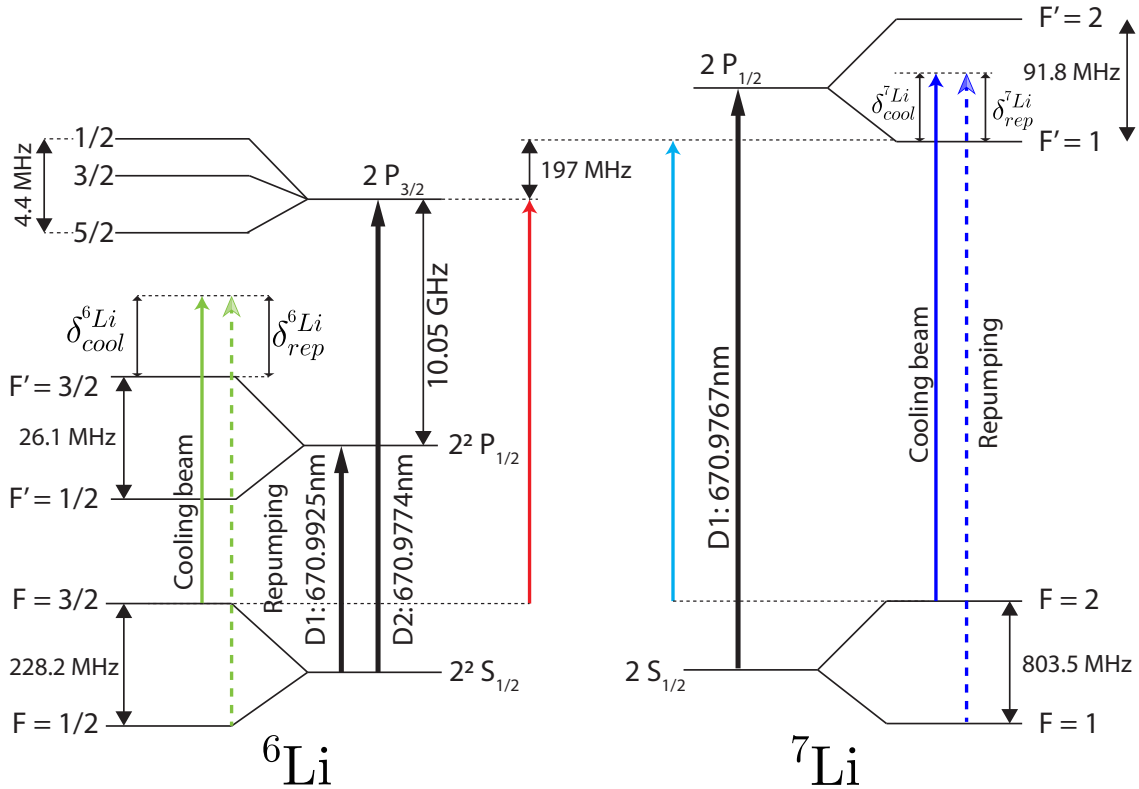


Figure 2.19: Transitions in ^6Li and ^7Li used for D1 molasses. Note the close proximity of ^6Li $|F=3/2\rangle \rightarrow |F'\rangle$ transitions (red arrow) and ^7Li transition ($|F'=2\rangle \rightarrow |F'=1\rangle$) involved in D1 cooling (cyan arrow) that lies +197 MHz above the ^6Li transition.

As shown in figure 2.20 the ^7Li D1 beams are generated from the 6P slave laser. The zeroth order of the +80 MHz AOM is carefully sent to a +240 MHz AOM. Since the spatial mode of the beam coming out of the AOM is not very good this beam is then passes through a couple of cylindrical lens in order to shape the spatial mode of this beam suitably matched for injecting into a Tapered amplifier (TA). The mode shaping of the seeding beam is very important for a TA, it significantly affects the amplification efficiency of the TA. The typical output power of this TA

is ~ 450 mW and lifetime is on the order of 2 years²². The output beam of the TA has asymmetric divergence along vertical and horizontal axis. In order to have a collimated beam we use a combination of cylindrical and spherical lenses. The beam is then passed through an Electro-optic modulator²³ (EOM) where it produces two weak sidebands at ± 803.5 MHz from the carrier. The purpose of this EOM is to generate the repumper beam for the ${}^7\text{Li}$ D1 cooling beam. Unlike the AOM, one of the main advantages of using an EOM is that the shifted frequency and the main frequency are spatially overlapping. Finally there is a +80 MHz AOM which acts as a switch for the ${}^7\text{Li}$ D1 beams. The beams are then coupled to a polarization maintaining fiber and the output of this fiber brings the ${}^7\text{Li}$ D1 beams on to the experiment table, where it is mixed to other beams with mixing cubes and follow the MOT beams path.

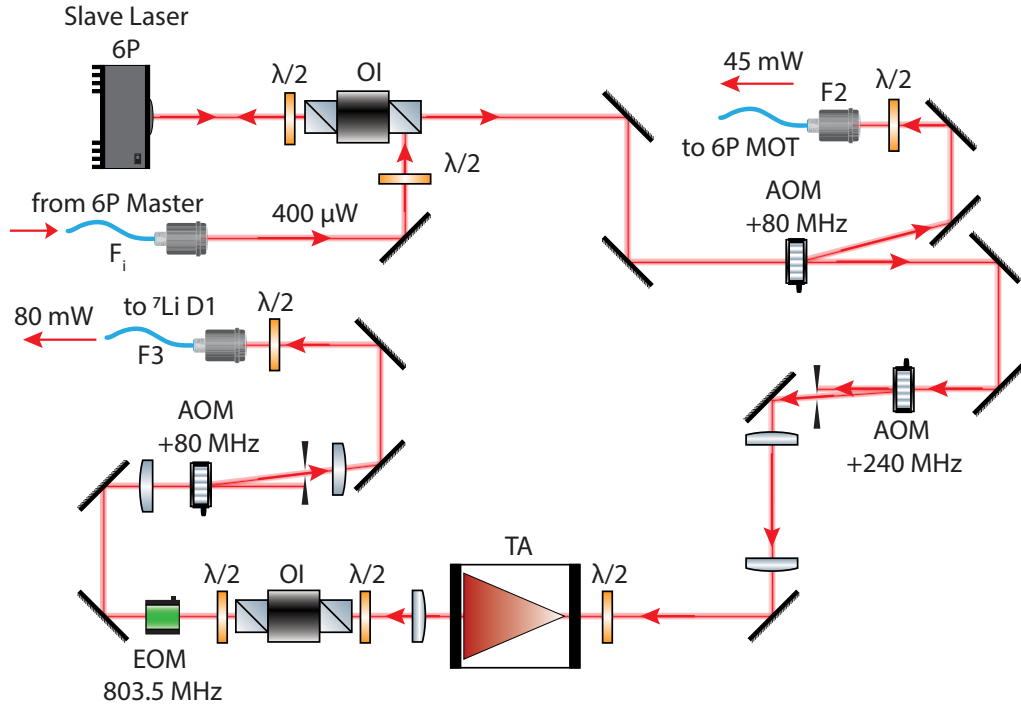


Figure 2.20: ${}^7\text{Li}$ D1 laser setup. ${}^7\text{Li}$ D1 beams are generated from a slave laser locked to the crossover lines between $|2S_{1/2}, F = 3/2\rangle \rightarrow |2P_{3/2}, F'\rangle$ and $|2S_{1/2}, F = 1/2\rangle \rightarrow |2P_{3/2}, F'\rangle$ (see Fig. 2.16). This setup generates 80 mW of switchable ${}^7\text{Li}$ D1 power out of the fiber F2. The first order of the +80 MHz AOM produces 45 mW of ${}^6\text{Li}$ D2 laser power out of fiber F3 for the MOT and D2 molasses beams.

²² The TA chips are designed in a such a way that it amplifies the seeding light in a specific direction. We should always prevent any light injecting the TA from the front facet (otherwise it will burn the TA chip).

²³ from QUBIG

^6Li D1 laser setup

In contrast to the setup for ^7Li D1 beams the ^6Li D1 beams are generated entirely from a new master laser source. The setup uses a Toptica TA pro laser and is locked to $|F = 3/2\rangle \rightarrow |F' = 3/2\rangle$ line of the D1 optical transition (see Fig. 2.19). The output of the TA is splitted by a 4% transmitting mirror (which acts as a beam splitter) and the transmitted part goes to the saturated absorption setup for the lock of the laser (see Fig. 2.21). Unlike any other saturated absorption spectroscopy setup we use in our experiment, this setup uses an EOM with a modulation frequency of 19 MHz to modulate the pump beam, instead of an AOM. The reflected part of the output beam passes through an EOM operating at 228 MHz which generates the repumping beam frequency for the ^6Li D1 beams. An AOM is used as a switch in order to rapidly modulate the ^6Li D1 beams. The beams are then coupled to a polarisation maintaining fiber (PMF) and the output of this fiber brings the ^6Li D1 beams on to the experiment table. This setup provides 120 mW of switchable power at the output of the coupling fiber. Later these beams are then mixed with the ^7Li D1 beams and then sent to the atoms.

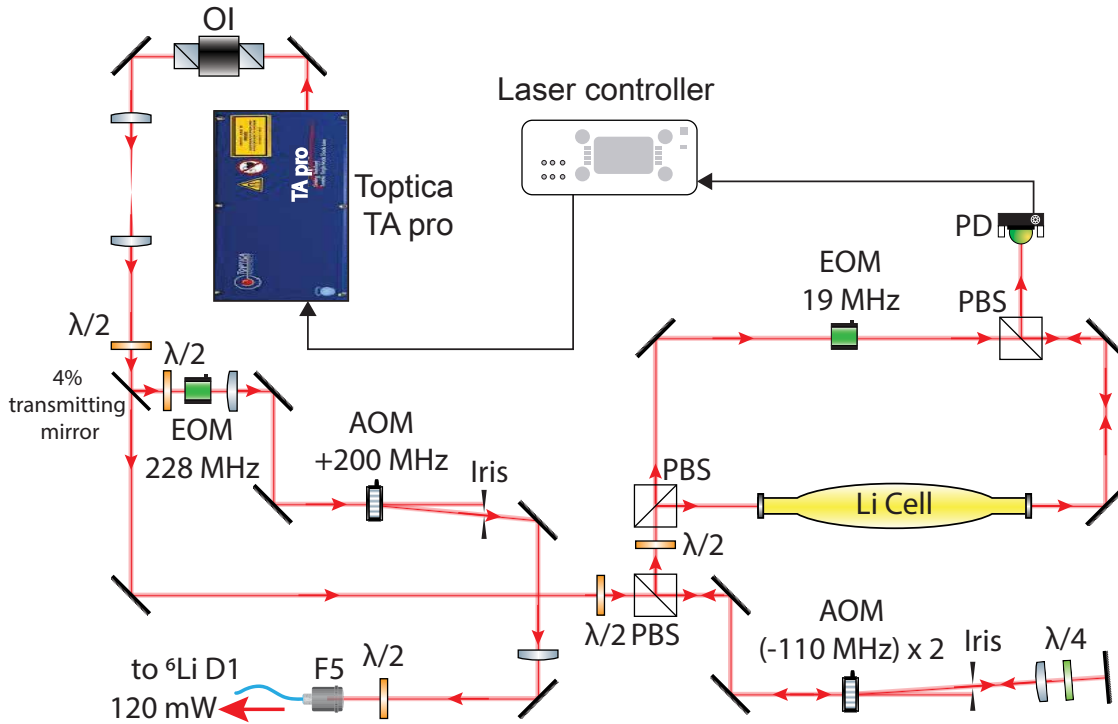


Figure 2.21: ^6Li D1 laser setup. Toptica TA pro is locked to $|F = 3/2\rangle \rightarrow |F' = 3/2\rangle$ line of the D1 optical transition (see Fig. 2.19). This setup generates 120 mW of power at the output of fiber F1.

2.4.6 Probe beams

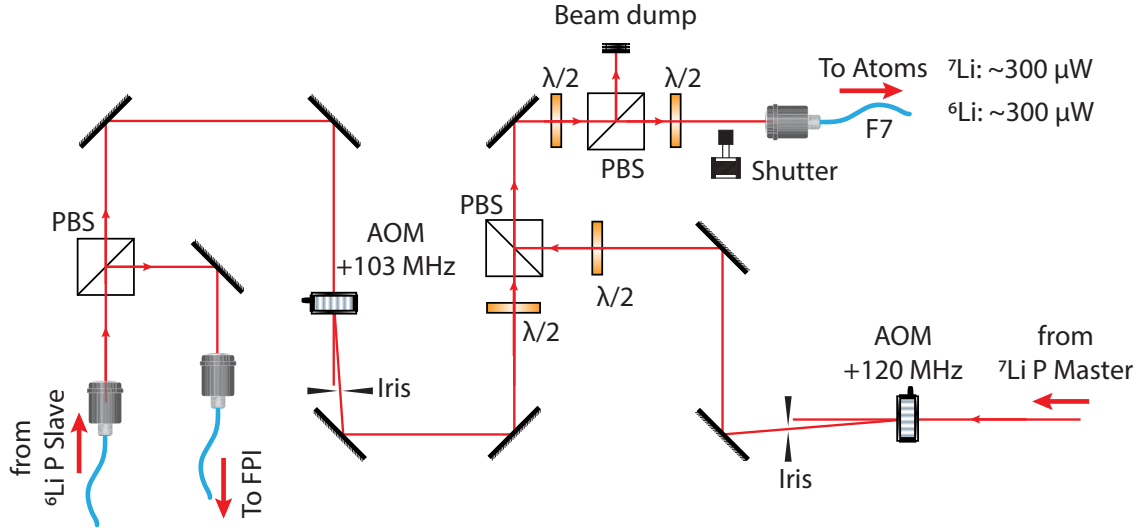


Figure 2.22: Imaging beam setup. Both ${}^7\text{Li}$ and ${}^6\text{Li}$ imaging beams are frequency shifted to the right frequency by their respective AOMs and are mixed on the PBS.

The ${}^7\text{Li}$ probe beam is derived directly from the master laser, whereas the ${}^6\text{Li}$ probe beam is derived after the injection into a slave laser. The ${}^7\text{Li}$ master laser is frequency shifted by a single pass 120 MHz AOM to bring the laser transition on resonance to the D2 atomic transition on ($|F = 2\rangle \rightarrow |F' = 3\rangle$). For ${}^6\text{Li}$ the laser is +103 MHz shifted by the AOM to bring the laser onto the ${}^6\text{Li}$ D2 atomic transition from $|F = 3/2\rangle \rightarrow |F' = 5/2\rangle$ (see fig 2.10). The AOMs also act as a light-switch which is used to pulse the imaging beam during the experimental sequence.

Since the ${}^7\text{Li}$ and ${}^6\text{Li}$ imaging beams have initially very different power (${}^7\text{Li}$: $700 \mu\text{W}$ and ${}^6\text{Li}$: 20 mW) they are mixed through a polarizing beam splitter (PBS) rather than a non polarizing beam splitter (NPBS). This in turn makes the polarisation of the imaging beam orthogonal with each other which is not appropriate because we want the imaging beams to pass through the same path until the camera. Thus we use another PBS as a polarisation filtering cube before injecting it into the fiber. We inject nearly equal proportions of power of both the imaging beams into the fiber. The output of this fiber gives $\sim 500 \mu\text{W}$ power for both lithium isotopes imaging beams (see fig 2.28).

2.4.7 Beam mixing

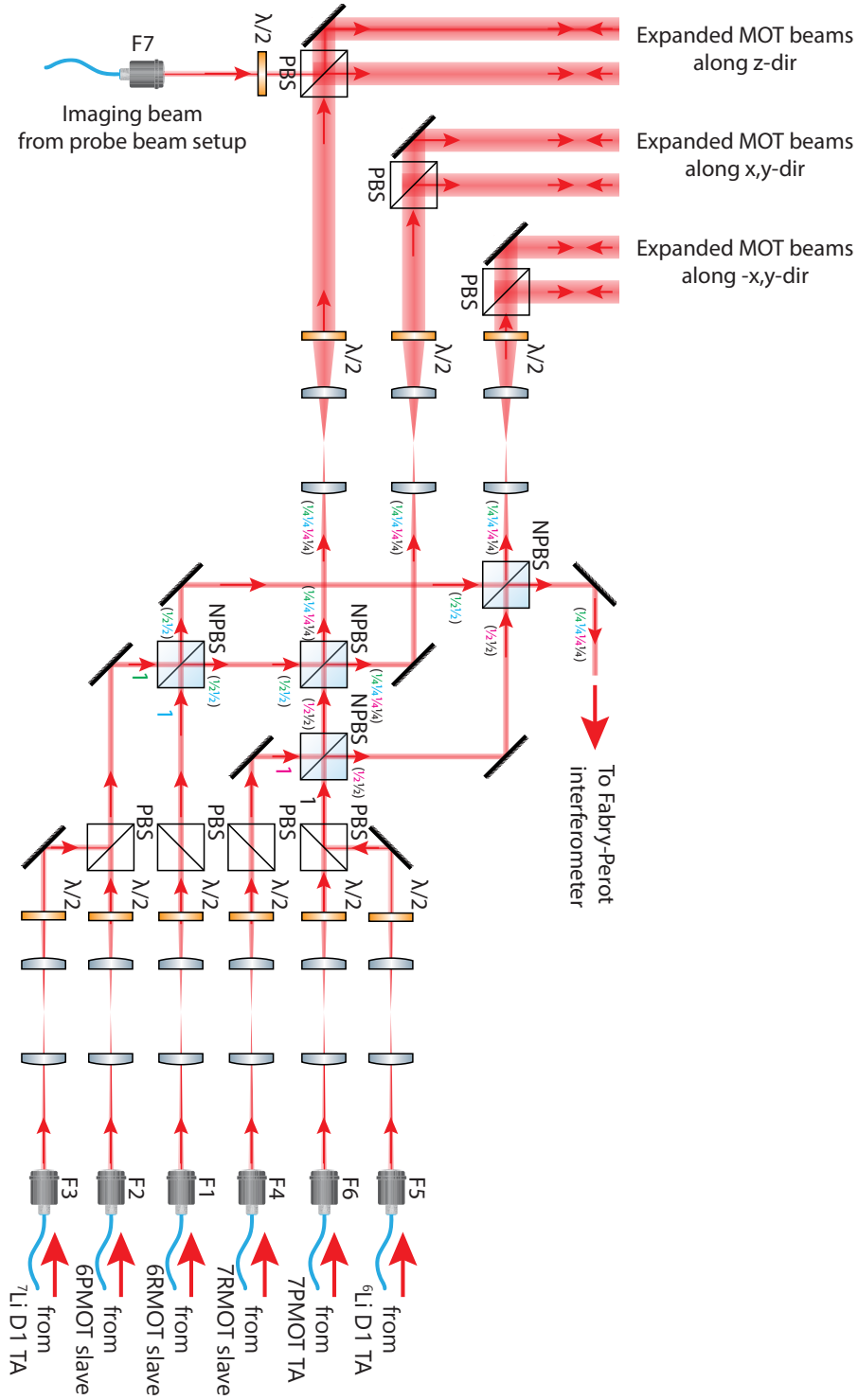


Figure 2.23: Setup for beam mixing.

All the MOT and D1 molasses beams are brought on to the experiment table by their respective polarization maintaining fibers. The MOT beams are then expanded individually using telescopes with a pair of lenses, and their polarization is rectified by PBS cubes. The beams are then mixed with each other with the help of NPBS cubes. Then the beams pass through another pair of telescopes and are expanded to a MOT beam diameter of 2.5 cm. Then they go through 3 PBS where they are split into 6 independent beams counter-propagating along 3 orthogonal axis. Since the atoms are trapped in the center of the overlapping volume of these six independent beams, the D1 beams are then mixed with the existing MOT beams and follow the same path and have a $1/e^2$ waist radius of ~ 3 mm about 3 times larger than the typical MOT cloud size.

2.5 Experiment control and data acquisition

A typical ultra cold Fermi gas experiment go through a series of complex experimental sequences each time we produce a cold atomic cloud. At the end of a cycle an absorption image of the atomic cloud is recorded on a CCD camera and the data is analyzed. A general outlook of the control system is depicted in fig. 2.24. In our experiment we use three computers, one controls the experiment, the second receives the pictures, evaluates the optical density of the cloud and automatically stores the data to an output file; and the third one is used as a snippet server which interacts between the above two computers.

2.5.1 Experiment control

We use Cicero Word Generator²⁴ as the user interface to control our experiment. This is an open source control software designed by A. Keshet[107]. Cicero word generator has two parts. Cicero is the user interface for adding and editing sequences. Atticus translates the sequences to output buffers and sends these buffers to the PXI²⁵ system by National Instruments. This PXI system contains the digital (TTL), analog and GPIB cards. These cards provide the necessary output channels to control various pieces of the experiment, such as VCO drivers, shutters, power supplies etc. The digital cards²⁶ have 32 channels and give 0 V or 5 V, the analog cards²⁷ have also 32 channels and deliver 0 V to 10 V and up to 10 mA current . The PXI system operates at low voltage and low current, but some of the device (IGBTs and Power supplies) require more current than what the National Instrument cards provide. We also need to protect the National Instruments cards

²⁴ <http://akeshet.github.io/Cicero-Word-Generator/>

²⁵ Chassis: [PXIe-1078](#)

²⁶ Digital cards: [NI PXIe-6535](#)

²⁷ Analog cards: [NI PXIe-6738](#)

from voltage spikes, wrong ground connection, and induced back currents from high current circuits. Thus opto-coupled buffer stage amplifiers are inserted in between the NI cards and the controlled device.

The relevant time scales in our experiment vary from seconds to microseconds, during one experimental sequence. The MOT loading takes several seconds, during which none of the digital or analog channels have changing values. On the other hand the duration of an imaging pulse is typically $\sim 10\text{-}30\ \mu\text{s}$. We synchronize the output cards with a variable FPGA clock²⁸. It generates the buffer (clock pulses) only when the output needs to change. All the digital and analog cards use this clock as the variable time base as their sample clock.

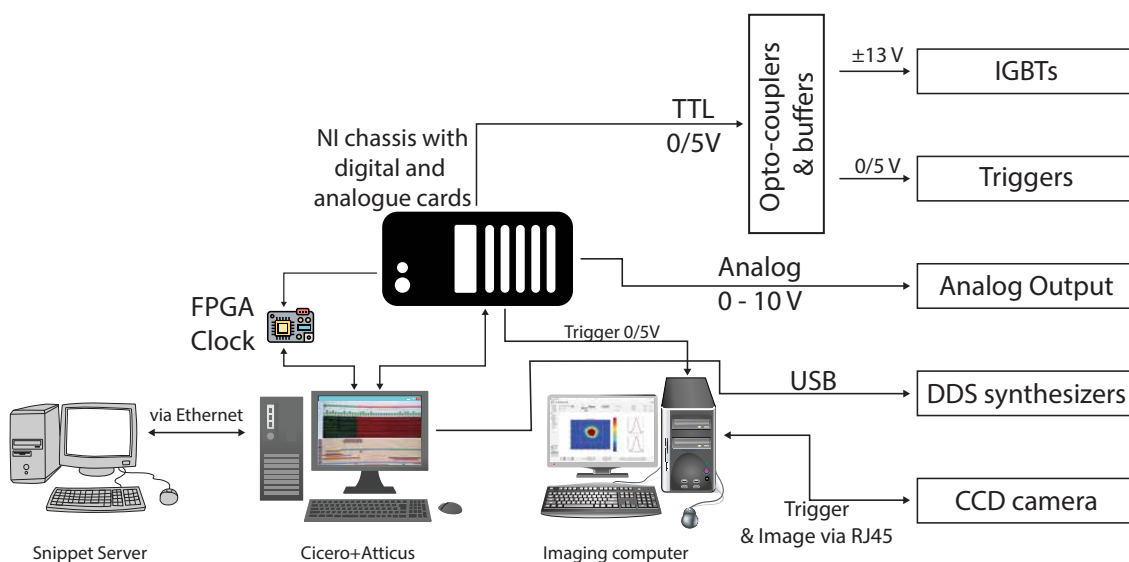


Figure 2.24: **Overview of the hardware control.** The NI PXI system is connected to the computer running Cicero and to the FPGA clock. This NI PXI is connected to different digital and analog output through opto-coupled buffers. The Cicero computer also controls the direct digital synthesis (DDS)²⁹ signal generators connected via USB. The imaging computer is connected to a Pixelfly CCD camera through RJ45 cable and is used for data acquisition and data analysis. A snippet server on a third computer is used to capture all the parameter used in Cicero sequence and transmits this data to the data analysis program on the imaging computer.³⁰

²⁸ Opal Kelly XEM 3001

³⁰ DS instruments, SG4400L. Thanks to Lithium 3 group for providing the DDS to us.

³⁰ Thanks to Julian Struck and Fermix group for providing the FPGA clock, multiple NI cards, its drivers and the snippet server to us.

2.5.2 Data acquisition

At the end of an experimental sequence we take an absorption imaging picture with a Pixelfly CCD camera. The camera is programmed in a double-shutter mode which means we can take two images at a very short period of time. In a double shutter mode the camera's CCD chip is exposed to light for the second picture while it is still processing and transmitting the data for the first image. This way we minimize the delay between the two consecutive images. Of course there is some jitter time for the CCD chip which is on a negligible time scale. Figure 2.25 depicts the various delays and exposure time for the Pixelfly CCD camera.

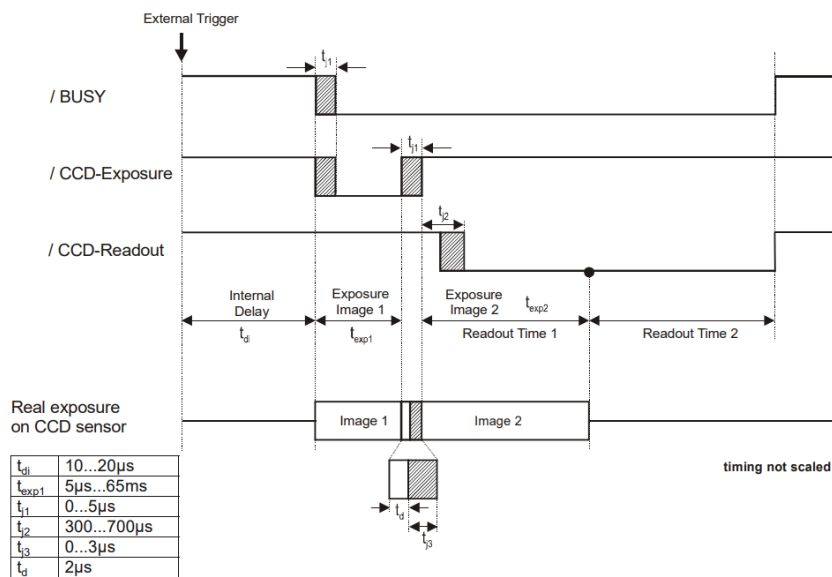


Figure 2.25: Time sequence³¹ of the Pixelfly CCD camera in the double shutter mode.

The image recorded by the camera is then sent to the imaging computer where it is stored and analyzed. We are using an image acquisition and analysis software which has been developed by the Fermix group at LKB³². This software is very user friendly, it can capture up to four pictures for a single experimental cycle and it calculates the optical density of the atomic cloud (OD) (see. section 2.6.2). It also fits a gaussian profile on the OD, and calculates the size of the cloud and gives the value of the atom number along x and y directions. It has a lot of other functionalities such as improving the image quality by using the “defringe” option. In this method an actual image is compared with a database of several tens of images with fringes and an algorithm removes the dominant fringes without distorting the image [119].

³¹ Figure taken from Pixelfly website.

³² Thanks to Clément De Daniloff for helping me in setting up the software

2.6 Detection system

The atomic clouds can be detected in many ways. In our lab we use the following techniques:

- The fluorescence of atoms in the presence of a resonant light can be captured by a photodiode or a camera.
- The absorption of light from a near resonant probe beam passing through the atomic cloud can be measured using a CCD camera.

2.6.1 Fluorescence detection

We continuously monitor part of the fluorescence emitted by the MOT with a high gain photodiode to estimate the atom number. The fluorescence is proportional to the number of atoms in the MOT and it depends on the MOT beam detunings and intensities. We also have an analogue video camera connected to a TV-screen to monitor the size, shape and position of the MOT. Both information are useful in optimizing the MOT and CMOT phase of the sequence.

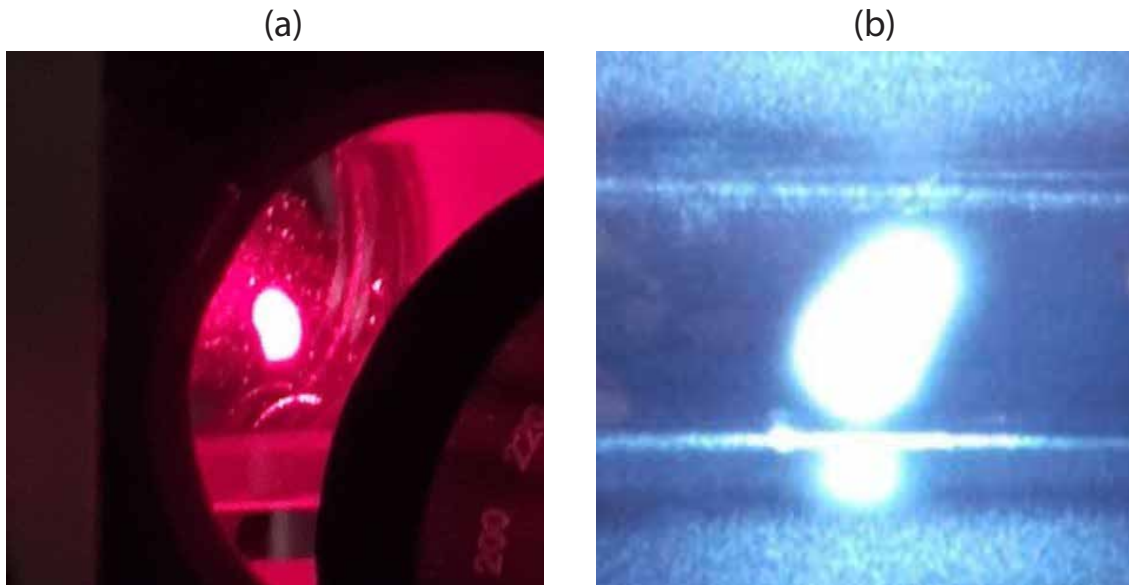


Figure 2.26: MOT fluorescence. (a) The Lithium MOT can be seen by the naked eye, (b) MOT seen by a video camera from top. The two horizontal lines are the internal edges of the glass cell appendix, 5 mm apart.

2.6.2 Absorption imaging technique

The absorption technique is the simplest of all the techniques and only a camera system is used for the detection of the atoms.

Principle of absorption imaging

We use standard absorption imaging either in in-situ or after a time of flight (TOF) to image the atomic cloud. The width of the beam has to be at least the size of the cloud after expansion. The atoms absorb the photon from the probe light and cast a shadow; this shadow is then captured by the camera. This image is called the “absorption image”. Another image is taken after a wait time of 30 ms when the atoms are sufficiently far from the observation region. This image is called the “reference image”.

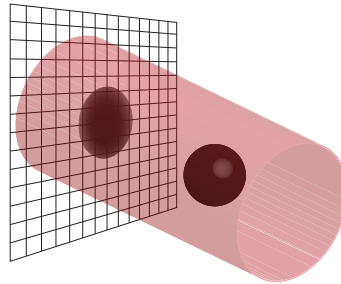


Figure 2.27: Schematic representation of imaging process. The near resonant light falls on the atoms and these atoms absorb and emit photons in all directions thus casting a shadow on the CCD camera chip. The CCD chip camera is shown as rectangular grid, the cloud is shown in black and the imaging beam is shown in red.

Imaging optics

Our imaging system (see figure 2.28) allows us to image along the axial direction of the MOT coils. The imaging system consists of 2 lenses of 300 mm focal length in $4-f$ imaging configuration giving a magnification of 0.95(5). We have placed an iris at the focus of the first lens which functions as a spatial filter and is used to remove any unwanted fringes on the camera detector plane caused by the multiple reflection by the inner and outer walls of the glass cell. We are using a Pixelfly QE camera. The Pixelfly QE has 1392×1024 pixels with each pixel size of $6.45\mu\text{m} \times 6.45\mu\text{m}$ and quantum efficiency $\sim 45\%$. We are using this camera in the double shutter mode (see figure 2.25) with the help of an external trigger from NI digital output. We used this imaging system to take in-situ or time-of-flight measurement of ${}^7\text{Li}$ and ${}^6\text{Li}$.

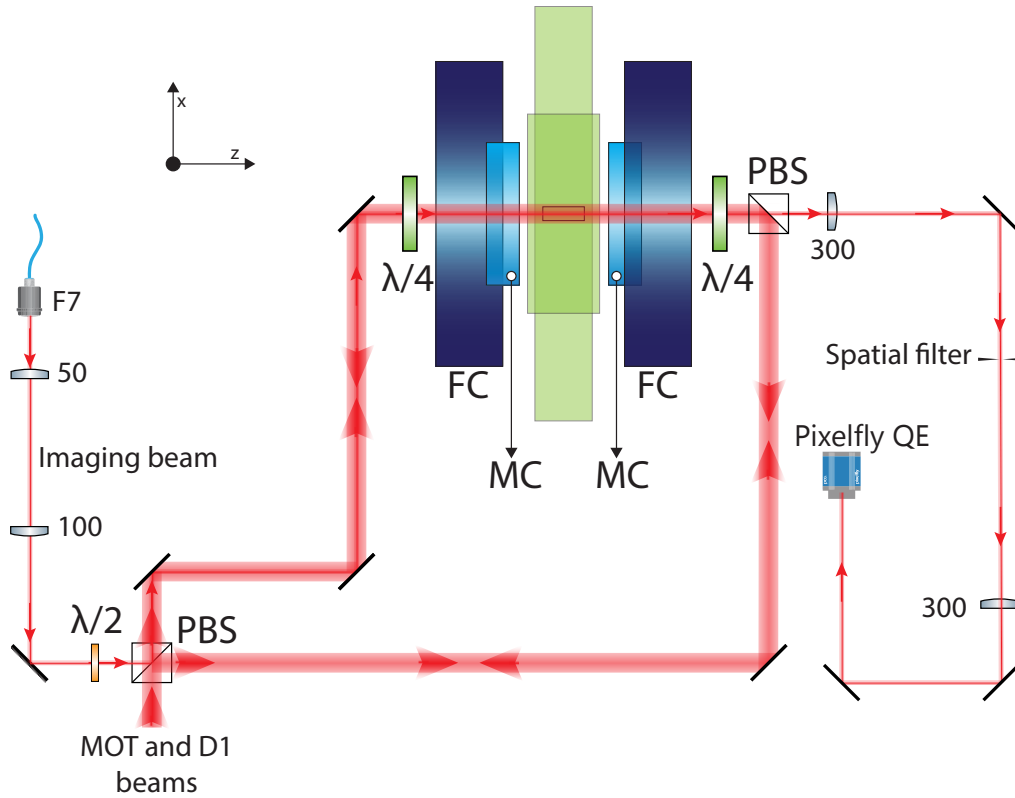


Figure 2.28: Setup for absorption imaging. The imaging beam is mixed with the MOT beams by the PBS. The imaging beam follows the path of the mot beam and is separated by another PBS. Since the beam passes through a $\lambda/4$ wave plate the polarization of the imaging beam is $\sigma+$ at the center of the glass cell. We use an iris pin hole as a spatial filter of diameter ~ 1 mm to remove the unwanted fringes on the image due to the multiple reflection of the imaging beam caused by inner and outer surface of the glass cell. FC: Feshbach coils, MC: MOT coils.

Image processing

As mentioned before we take absorption images to obtain information about the atoms. The Pixelfly³³ camera records the transmission profile of the probe beam. Since the probe beam is a near resonant pulsed ($30 \mu\text{s}$) light with low intensity ($I \ll I_{sat}$) we see a shadow in the presence of atoms (figure 2.29a). One of the main source of noise is the presence of fringe on the absorption image due to the interference with multiple back reflection from the glass cell. In order to reduce the effect of these fringes a reference image (figure 2.29b) is taken with a delay 30 ms when there are no atoms present in the vicinity giving us the un-absorbed intensity profile. A background picture (figure 2.29c) is taken with no imaging beam in order to compensate the offset.

³³ PCO imaging Pixelfly QE

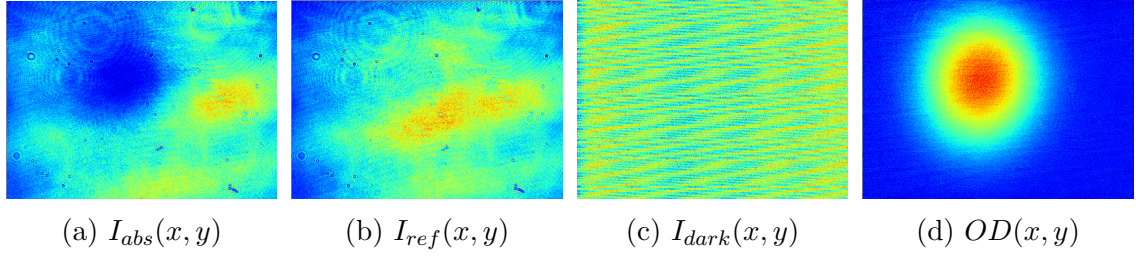


Figure 2.29: Absorption imaging technique (a) Absorption image, (b) Reference image, (c) Background image, (d) Optical density.

If z is the imaging direction then $I_{abs}(x, y)$ is the intensity of the absorption image in the x - y plane, $I_{ref}(x, y)$ is the intensity of the reference image, $I_{dark}(x, y)$ is the intensity of the background. The normalized transmission profile is then given by:

$$T(x, y) = \frac{I_{abs}(x, y) - I_{dark}(x, y)}{I_{ref}(x, y) - I_{dark}(x, y)}. \quad (2.1)$$

and the Optical density $OD(x, y)$ is given by:

$$OD(x, y) = -\ln(T(x, y)) \quad (2.2)$$

We know the optical density is related to the density of atoms as:

$$OD(x, y) = \sigma \int n(x, y, z) dz \quad (2.3)$$

where $n(x, y, z)$ is the atomic density of the cloud and σ is the absorption cross-section of one atom. For low intensity the absorption cross-section can be calculated from the Clebsch-Gordan coefficients, probe beam intensity and detuning as:

$$\sigma = C^2 \frac{3\lambda^2}{2\pi} \frac{1}{1 + (2\Delta\omega_{img}/\Gamma)^2}. \quad (2.4)$$

Here C and λ are Clebsch-Gordan coefficients and the wavelength of the atomic transition, respectively. $\Delta\omega_{img} = \omega_{laser} - \omega_0$ is the detuning of the imaging beam from resonance and $\Gamma = 2\pi \times 5.8$ MHz is the linewidth for lithium transition.

Atom number measurement

The atom number of the cloud can be found out by integrating the optical density.

$$N = \int dx \int dy \int dz n(x, y, z) = \int dx \int dy OD(x, y)/\sigma \quad (2.5)$$

where $n(x, y, z)$ is the density of the cloud, $OD_{x,y}$ is the optical density of the cloud which can be calculated from the equation 2.2, and σ is the absorption cross section which can be found in equation 2.4.

Detection parameters

The quality of the image captured on the camera depends on the intensity and detuning of probe beam and on the exposure time of the camera. We detect the absorption of a σ^+ polarized beam on the transition $|2S_{1/2}, F = 3/2\rangle \rightarrow |2P_{3/2}, F' = 5/2\rangle$ for ${}^6\text{Li}$. We note in figure 2.10 the excited state hyperfine structure is inverted and is very narrow; ~ 4.4 MHz ($< \Gamma$) for ${}^6\text{Li}$. There is a significant probability that the excitation of $|2S_{1/2}, F = 3/2\rangle$ transition may decay into other hyperfine states. For this reason we use a repumping beam tuned to the $|2S_{1/2}, F = 1/2\rangle \rightarrow |2P_{1/2}, F' = 3/2\rangle$ transition with a detuning of -1.5Γ . The repumping is done in all six direction to cancel radiation pressure effects.

The probe beam and the repumping beams establish an equilibrium between the population in the higher hyperfine structure and the lower hyperfine structure. This equilibrium is dependent on the intensity ratio between the two beams. In order to have a good absorption image we shift this equilibrium position towards the higher hyperfine structure by having a much higher intensity in the repumping beam (nearly 2.5 mW/cm^2) compared to the probe beam intensity.

Calculating precisely the absorption cross-section (σ) in the equation 2.4 is therefore difficult. In addition after the cooling phase the atoms are usually spread over the various Zeeman states in $|F = 3/2\rangle$ and the direction of the small residual magnetic field with respect to the σ^+ polarized beam is not known. A reasonable assumption is to assume equipartition of the population on the $|F = 3/2\rangle$ Zeeman states and thus for the excitation matrix elements we take an average of the square of the Clebsch-Gordan coefficient of the σ^+ transitions and this average is $1/2$. As noted above the excited state hyperfine structure is very narrow. Therefore we can also include the $|F = 3/2\rangle \rightarrow |F = 3/2\rangle$ and $|F = 3/2\rangle \rightarrow |F = 1/2\rangle$ transitions in our calculation of the absorption cross-section. In this case the average of the squared Clebsch-Gordan coefficients for σ^+ light is $2/3$ under the assumption of perfect degeneracy between these transitions. In summary a good approximation of the absorption cross-section is $3\lambda^2/4\pi$.

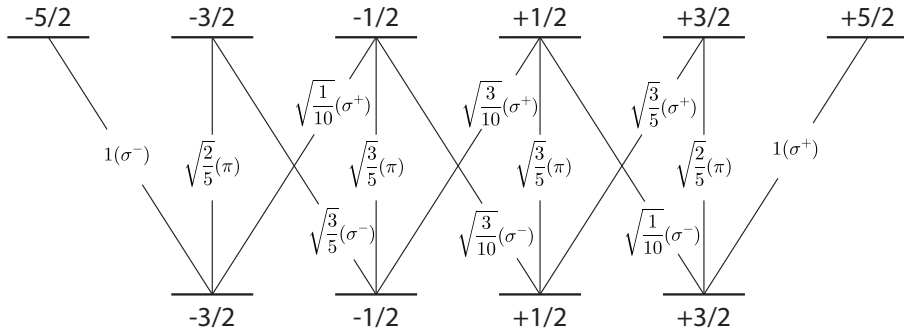


Figure 2.30: Electric dipole transition matrix element for ${}^6\text{Li}$ on the D2 transition line from $|2S_{1/2}, F = 3/2\rangle \rightarrow |2P_{3/2}, F' = 5/2\rangle$.

Furthermore the mass of lithium is very light and the radiation pressure of the probe beam pushes quickly the atoms out of resonance a simple estimate of the Doppler shift can be calculated as follows. In the absorption imaging process the atoms absorb the resonant photons from the imaging beam. These photons are then spontaneously re-emitted. The recoil velocity for ${}^6\text{Li}$ is 9.88 cm/s and the imparted Doppler shift per photon is $v/\lambda = 147$ kHz. With the parameters shown in table 2.3, during a 30 μs imaging pulse the lithium atoms absorb a maximum of 20 photons from the imaging beam. The corresponding Doppler shift is ~ 3 MHz (equivalent to 0.5Γ). This results in a reduction of the cross-section.

Similarly for ${}^7\text{Li}$, the imaging beam is tuned to $|2S_{1/2}, F = 2\rangle \rightarrow |2P_{3/2}, F' = 3\rangle$ transition (see figure 2.10). The excited state hyperfine structure for ${}^7\text{Li}$ is also inverted and is spread over $\sim 18.1\text{MHz}$. The distance between $|2P_{3/2}, F' = 3\rangle$ and $|2P_{3/2}, F' = 2\rangle$ is only 9.4 MHz. Although the excited state hyperfine splitting is not as narrow as for ${}^6\text{Li}$ there is still a significant probability that the excitation of $|2S_{1/2}, F = 2\rangle$ transition may decay into the lower hyperfine state $|2s_{1/2}, F = 1\rangle$. Therefore we repump on the $|2S_{1/2}, F = 1\rangle \rightarrow |2P_{3/2}, F' = 2\rangle$ transition with a detuning of -1.5Γ and in all six directions.

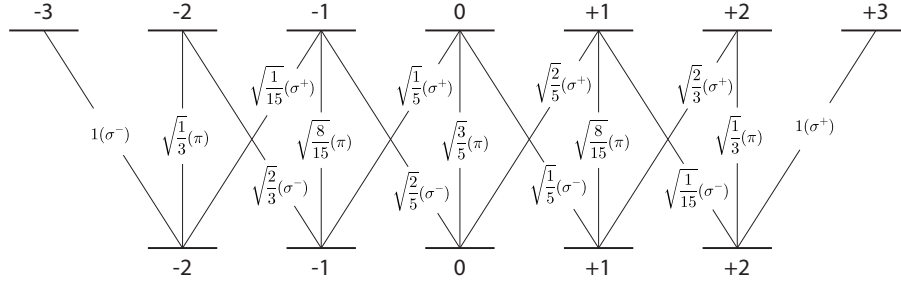


Figure 2.31: Electric dipole transition matrix element for ${}^7\text{Li}$ on the D2 transition line from $|2S_{1/2}, F = 2\rangle \rightarrow |2P_{3/2}, F' = 3\rangle$. The average of the squared Clebsch-Gordan coefficients for σ^+ light is $7/15$.

Parameters	Values
Repumping time	50 μs
Probe beam intensity	$\sim 200 \mu\text{W}/\text{cm}^2$
Imaging pulse time	30 μs
CCD exposure time	50 μs
absorption cross-section correction factor (C^2) for ${}^6\text{Li}$	$1/2$
absorption cross-section correction factor (C^2) for ${}^7\text{Li}$	$7/15$

Table 2.3: Values of different parameters used for ${}^6\text{Li}$ and ${}^7\text{Li}$ absorption imaging.

Temperature measurement

The temperature is measured by a time of flight (TOF) method. Atoms are released abruptly from the molasses and are allowed to expand freely. We take absorption images at specific time intervals and measure the expansion of these atomic clouds. The velocity distribution of the atoms is a Maxwell-Boltzmann distribution (Gaussian). Since the density is very dilute there are rarely any collisions between two atoms. Assuming a Gaussian initial position distribution in the molasses, the Gaussian waist of the atomic cloud evolves as a function of time as:

$$\sigma_{x,y}(t_{\text{TOF}}) = \sqrt{\sigma_{x,y}^2(t_{\text{TOF}} = 0) + \frac{k_B T}{m} t_{\text{TOF}}^2} \quad (2.6)$$

where $\sigma_{x,y}$ is the size of the cloud along x or y direction, T is the temperature of the cloud and m is the mass of the atoms. Note that the assumption of an initial Gaussian distribution is only valid at small atom numbers. For large numbers, the MOT atomic density saturates and the in-situ density profile departs strongly from a Gaussian. The Gaussian approximation is inadequate. However for large free-flight times the error on the initial position distribution becomes negligible.

2.7 Summary of chapter 2

In this chapter we have presented an overview of the Lithium 1 machine, where we discussed briefly about the vacuum system and the Zeeman slower. We have discussed about the lithium oven and various associated issues such as oven un-clogging procedure and the process to replace the oven. We have discussed in detail about various electrical coils. We have described their structure and configurations, electrical and hydro dynamical resistances, their assembly and finally the electrical connections. In the operational part of these coils we have characterized their magnetic properties such as their switch-off time and the magnetic field produced by the coils.

In the second part of the chapter we have discussed the newly implemented laser system, where we discussed about the master lasers and the principle of frequency locking by saturated absorption technique. We have discussed about the master-slave injection locking technique used in our lab to amplify the laser output while maintaining spectral purity as good as a master laser. We have discussed the new D1 cooling setup for both ^6Li and ^7Li .

In the third part of the chapter we have discussed about the newly implemented experiment control and data acquisition setup used to manipulate the experiment. This involves the setup of a new National Instruments PC and various digital and analog cards, and integration of all the electronics (AOMs/EOMs, switches, power supplies and the cameras) in to the newly installed Cicero program.

And finally we concluded this chapter with the description of our detection system where we discussed about the imaging setup, image processing and calculation of atom number and temperature measurement by the time of flight method.

This page intentionally left blank

Chapter 3

Overview of Laser cooling methods

Contents

3.1 Doppler cooling	58
3.2 Sub-Doppler cooling	60
3.3 Sub-recoil cooling techniques	62
3.4 Gray molasses cooling	66
3.5 Summary of chapter 3	68

When shining coherent light to an ensemble of atoms, one can cool them down to very low temperatures. Until the end of the 1980s, it was expected that the limit for laser cooling would be the Doppler temperature. However experiments have revealed temperatures much lower than the Doppler limit. New cooling mechanisms below the Doppler limit and even below the recoil limit have been proposed in the 1990's and exploited in various situations. Thus by using different strategies or a combination of them one can cool the atoms to the desired temperatures.

In this chapter we briefly recall the concepts and the results of different laser cooling methods.

3.1 Doppler cooling

Doppler cooling was the first optical mechanism proposed to cool atoms[20], [120]. The cooling scheme is based on a Doppler induced imbalance between opposite radiation pressure forces.

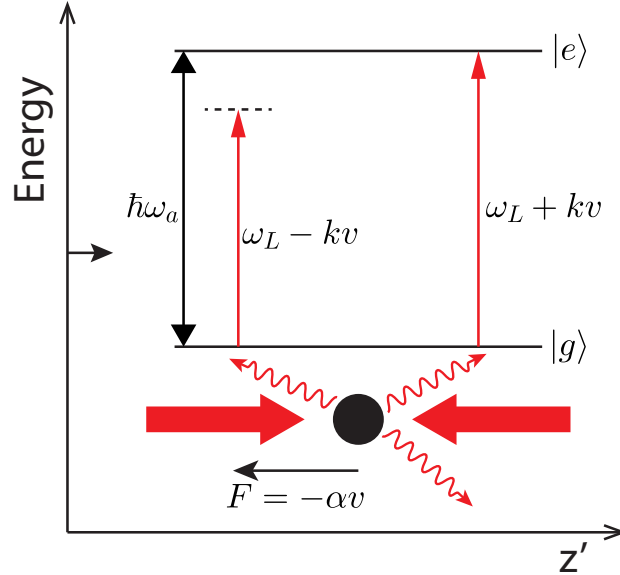


Figure 3.1: Schematic representation of optical molasses in 1D. The atom is moving along z -direction. In the moving frame of the atom the frequencies of the laser seen by the atoms are Doppler shifted. Due to Doppler effect more photons are scattered in the direction opposite to the atom's velocity resulting a net damping force opposite the atom's velocity. Figure adapted from[121].

To illustrate the principle of this mechanism, consider a moving two-level atom with ground state $|g\rangle$ and excited state $|e\rangle$ separated by $\hbar\omega_a$ and velocity \vec{v} . The atom is illuminated by a counter-propagating laser beam with wave vector \vec{k}_L , frequency ω_L and Rabi frequency Ω . The laser beam is red detuned $\omega_L < \omega_a$ and has a small intensity. The Doppler effect changes the detuning $\delta = \omega_L - \omega_a$ by $\vec{k}_L \cdot \vec{v}$. The radiative force \mathcal{F} exerted on the atom is therefore velocity dependent. The radiative force is maximum when the Doppler shift compensates the detuning, i.e. when $\vec{k}_L \cdot \vec{v} = \omega_a - \omega_L$.

If we add a second laser beam with same intensity and frequency propagating in the opposite direction, the Doppler shift has different signs for the two beams. The resultant total force \mathcal{F}_D , of the low intensity standing wave, is the sum of the forces created by the two beams. The two beams create a friction force for small velocities. The cooling is efficient between the two extreme of \mathcal{F}_D , where $v = \pm\delta/k_L$ (see fig. 3.2).

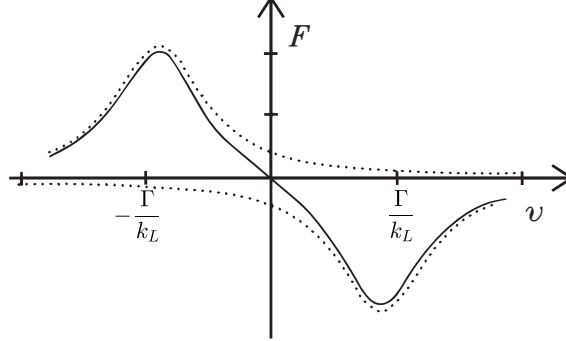


Figure 3.2: Force vs velocity for a laser detuning $\delta = -\Gamma$.

In laser cooling there are also heating process due to spontaneous emission. The spontaneous emission is a random process in time and the recoil momentum communicated to the atom is in a random direction. Take an atom at rest in the excited state. After spontaneous emission process the atom will gain an energy, the recoil energy given by

$$E_{recoil} = \frac{\hbar^2 k^2}{2m} \quad (3.1)$$

To this energy we associate a temperature, the recoil temperature given by;

$$T_{recoil} = \frac{\hbar^2 k^2}{2mk_B} \quad (3.2)$$

where m is the atomic mass and k is the wavevector of the spontaneously emitted photon and k_B is the Boltzmann constant. For heavy atoms the recoil temperature ranges from hundreds of nano-Kelvins to a few micro-Kelvins for different atomic species.

The balance between the friction force and heating due to spontaneous emission leads to an equilibrium temperature. At low intensity the Doppler temperature is;

$$k_B T_{Doppler} = \frac{\hbar\Gamma}{4} \left(\frac{\Gamma}{2|\delta|} + \frac{2|\delta|}{\Gamma} \right) \quad (3.3)$$

where $1/\Gamma$ is the lifetime of the excited state. The minimum Doppler cooling temperature is then achieved when $\delta = -\Gamma/2$ and is given by:

$$k_B T_{Doppler}^{min} = \frac{\hbar\Gamma}{2} \quad (3.4)$$

in the limit where $E_{recoil} \ll \hbar\Gamma$ the Doppler limit is simply proportional to the excited state linewidth. For Lithium isotopes on the main optical transitions with

$\Gamma = 2\pi \times 5.87$ MHz, the theoretical minimum Doppler cooling temperature is approximately $140 \mu\text{K}$. However in practice we measure temperature on the order of 1-2 mK. This is because the $2P_{3/2}$ hyperfine level structures are not well resolved compared to the linewidth Γ , and furthermore at high density multiple photon scattering occurs within the atomic cloud.

An obvious way to reduce the temperature is to cool the atoms on a narrower transition (with a longer excited state lifetime). For instance there is a near-UV transition for lithium at 323 nm with an effective linewidth of $2\pi \times 754$ kHz and a temperature of $59 \mu\text{K}$ has been obtained in [122], [123]. However cooling on this transition is challenging as this requires a coherent laser source at 323 nm wavelength and laser power is a limiting factor at this wavelength. This approach also requires special UV optics which can be expensive.

3.2 Sub-Doppler cooling

Polarization gradient cooling

The Doppler cooling theory was based on a two-level atom approximation. In general most atoms have Zeeman and hyperfine structures. Presence of these sub-levels makes the cooling mechanism more complex than for a simple two-level atom. In reality, the first experimental results showed that the temperature attained in this configuration was lower than expected by one to two orders of magnitude [124]. This effect was explained as being a consequence of another cooling mechanism: the Sisyphus or polarization gradient cooling [125].

We now consider a 1D laser configuration where the two counter-propagating laser beams have orthogonal linear polarization, have low intensities and are red-detuned. Figure 3.3 (a) shows how the polarization of the total field varies along the z -direction. The polarization is $\sigma+$ and $\sigma-$ in planes separated by a distance $\lambda/4$. In between, it is linear at $\pm 45^\circ$ or elliptical.

Let us consider the simplest case of a $F_g = 1/2$ ground state having only two Zeeman sublevels and an excited state $F_e = 3/2$ with a red-detuned laser. Since the laser is not resonant, for red-detuning the ground state energies are light-shifted down. Polarization gradients spatially modulate these light shifts with a period $\lambda/2$ as shown in figure 3.3 (b).

For a moving atom in a given Zeeman sublevel the probability to be optically pumped in the other sublevel is highest at the top of the potential hill. The atom is pumped to the bottom of the valley of this sublevel. The repetition of this process makes the atom moving uphill more frequently than downhill. This Sisyphus effect arises because of correlation between the spatial modulation of light shift and optical pumping rate. Figure 3.3 (b) shows the principle of Sisyphus cooling for bright optical molasses in the lin \perp lin configuration.

On one hand, the friction force emerging from Sisyphus cooling damps the

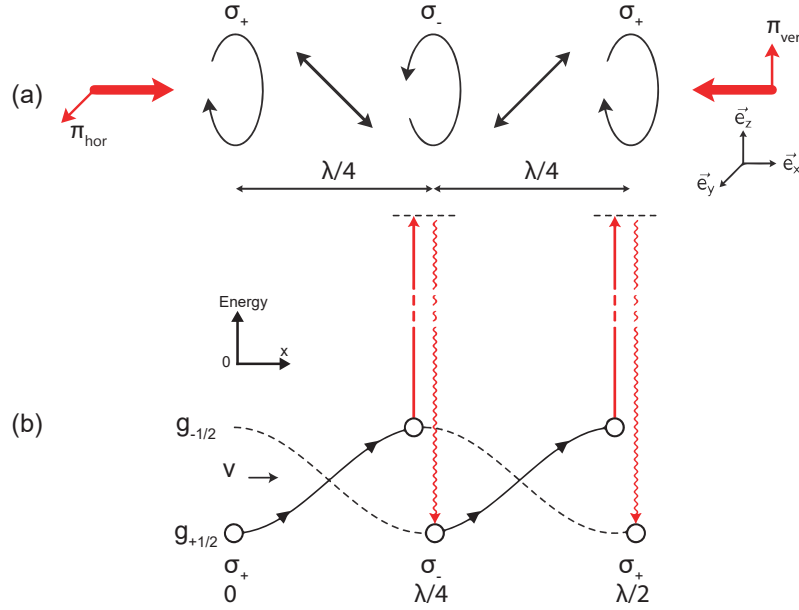


Figure 3.3: **Schematics of low intensity Sisyphus cooling.** An atom initially in $g_{+1/2}$ state moves up along the light shift potential to the top where it is optically pumped in to the $g_{-1/2}$ sublevel at the bottom of the valley. The atom continues to repeat the similar cycles and hereby loses energy in each cycle[125].

atomic momenta. On the other hand the fluctuations of the radiative forces lead to a momentum diffusion. In Sisyphus cooling we have fluctuation of the dipole forces as well as fluctuation related to the random spontaneous emission processes. It can be shown that the energy of the atom decreases step by step until the atom gets trapped in the optical potential wells. An equilibrium temperature on the order of a fraction of the light-shift potentials is obtained:

$$T_{sub-Doppler} \sim \hbar\delta_{ls} \sim \frac{\hbar\Omega^2}{4|\delta|k_B} \quad (3.5)$$

where the light shift of the ground states is denoted by δ_{ls} and with the assumption of large detuning ($|\delta| \gg \Gamma$) and low intensity ($s \ll 1$), with s being the saturation parameter. The proportionality of temperature and light shift dependence of formula 3.5 has been checked in heavy alkalis like Cs[126] and Rb as well as Na. At low intensity a minimum temperature is experimentally found. It corresponds to $v_{r.m.s} = (2k_B T/m)^{1/2} = 3.6 v_{recoil}$ along any axis. For Cs this is typically $2.5 \mu\text{K}$ [126]. For lithium isotopes standard polarization gradient cooling is not very efficient and the lowest temperature observed is the order of $300\text{-}400 \mu\text{K}$ [105]. We will show in chapter 3 and 4 that we can gain nearly one order of magnitude in temperature over these values by using blue-detuned gray molasses cooling.

3.3 Sub-recoil cooling techniques

As mentioned above, to achieve a temperature below the recoil limit the momentum spread of the atoms Δp should be smaller than the single photon momentum. So one should have a situation where the atoms with very small velocity do not absorb light. This would circumvent the single photon recoil problem achieving a temperature lower than the steady state recoil temperature.

The basic mechanism is to create a system where the photon scattering rate, $R(p)$ is dependent on the velocity of the atoms and vanishes at $v = 0$ (Fig. 3.4(a)). Therefore an atom with a velocity $v = 0$ neither absorb nor emit photon with spontaneous emission and hence it does not have any associated random recoils, while the atoms with non-zero velocity can absorb and re-emit the photons. These random changes in the velocity of the atoms due to the spontaneous emission may succumb them into the region near $v = 0$ (see Fig. 3.4(b))[127].

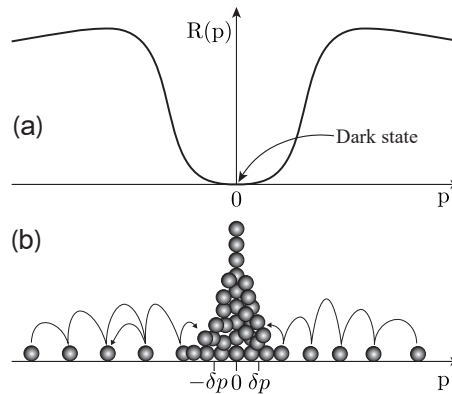


Figure 3.4: The sub-recoil cooling technique can be modeled as a random walk process in momentum space where the atoms gets trapped in a small volume δp near $\mathbf{p} = \mathbf{0}$. Since the photon scattering rate is reduced drastically as $\mathbf{p} \rightarrow \mathbf{0}$, thus the random walk process slows down and the atom stays in the confined volume for a long period of time. At $\mathbf{p} = \mathbf{0}$ the photon scattering rate vanishes completely so it can not absorb any photon from the light field and thus the atom is trapped in a dark state with $\mathbf{p} = \mathbf{0}$. Figure adapted from[127].

It is interesting to note that in this process the width of the velocity distribution (δp) now depends on the interaction time θ between the atoms and the light field[128]. If $R(p)$ varies as p^2 near $p = 0$ then it can be shown that;

$$\delta p \propto 1/\sqrt{\theta} \quad (3.6)$$

For long enough θ we can have $\delta p < \hbar k$, and this achieves a sub-recoil temperature. There is no real steady-state temperature for sub-recoil cooling as the longer the interaction time θ the lower the temperature we get.

This process of trapping the atom in a velocity selected dark state can be achieved by Velocity selective coherent population trapping (VSCPT) which uses quantum interference effect to make the absorption of photons velocity dependent[129] or by Raman resonance process which take advantages of velocity selective excitation of the atoms[130].

Velocity selective coherent population trapping (VSCPT)

Before we discuss VSCPT lets try to understand *coherent population trapping*. Let's consider a 3-level system having two ground state sub-levels (g_1 and g_2) and one excited state sub-level e (Fig. 3.5). Two lasers excite the transition $g_1 \rightarrow e$ and $g_2 \rightarrow e$ are denoted by $\vec{E}_1 e^{i(\vec{k}_1 \cdot \vec{r} - \omega_1 t)} + c.c$ and $\vec{E}_2 e^{i(\vec{k}_2 \cdot \vec{r} - \omega_2 t)} + c.c$ respectively. The corresponding light-atom interaction is characterized by their Rabi frequencies.

$$\Omega_i = -\mathbf{D}_{eg_i} \cdot \mathbf{E}_i / \hbar, \quad i = 1, 2 \quad (3.7)$$

where \mathbf{D}_{eg_i} is the matrix element of the dipole moment operator between e and g_i . The atom in g_1 can go to e with an amplitude Ω_1 by absorbing a photon ω_1 . It can also absorb another photon ω_2 and go from g_2 to e with an amplitude Ω_2 . The detuning Δ is the detuning from the Raman condition and is represented as

$$\hbar\Delta = \hbar\omega_1 - \hbar\omega_2 + (E_{g_1} - E_{g_2}) \quad (3.8)$$

where E_{g_1} and E_{g_2} represent the energy of the sub-level g_1 and g_2 respectively.

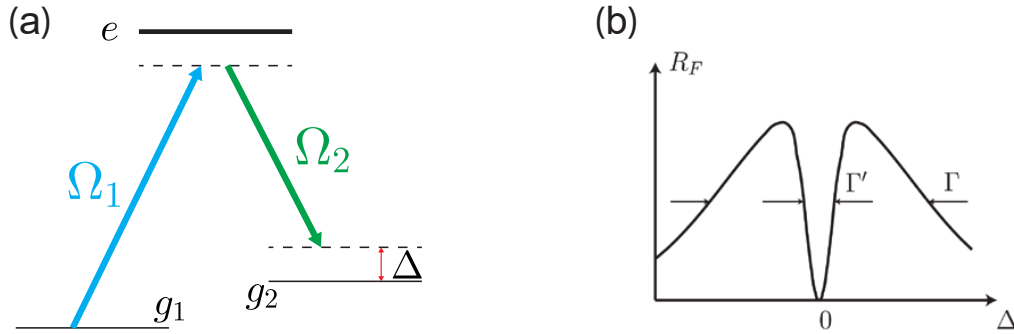


Figure 3.5: (a) Three level system having g_1 and g_2 as ground states and e as an excited state. Two lasers are represented in blue and green for the transition corresponding to $g_1 \rightarrow e$ with Rabi frequency Ω_1 and $g_2 \rightarrow e$ with Rabi frequency Ω_2 . (b) The variation of fluorescence rate (R_F) with respect to the detuning from the Raman resonance condition (Δ).

Now for a three level system (fig. 3.5(a)) the interaction operator is given by $\hat{V} = \hbar\Omega_1/2 |e\rangle \langle g_1| + \hbar\Omega_2/2 |e\rangle \langle g_2| + h.c..$ For this interaction we can introduce a

new basis for the ground state as

$$|\psi_D\rangle = \frac{1}{\Omega}(\Omega_2 |g_1\rangle - \Omega_1 |g_2\rangle) \quad (3.9)$$

$$|\psi_B\rangle = \frac{1}{\Omega}(\Omega_1 |g_1\rangle + \Omega_2 |g_2\rangle), \quad (3.10)$$

with $\Omega = \sqrt{\Omega_1^2 + \Omega_2^2}$. At $\Delta = 0$ when the Raman condition is satisfied and if the atom is in a superposition state of g_1 and g_2 such that the two absorption amplitudes interfere destructively ($\hat{V}|\psi_D\rangle = 0$), the excited state population vanishes and the atom occupies a state which does not absorb light. This state is called a dark state and is represented as $|\psi_D\rangle$. Conversely $|\psi_B\rangle$ is called the bright state since it puts the atom in the excited state with a probability $\langle e|\hat{V}|\psi_B\rangle = \hbar\Omega/2$. The Raman condition 3.8 ensures that if the atom is in a dark state at some point in time it remains in the dark state all the times. This is represented in Fig.3.5(b) where R_F is zero for $\Delta = 0$. If $\Delta \neq 0$ then atom in a dark state may absorb a photon and does not remain in the dark state at a later time. This is why $R_F \neq 0$ for $\Delta \neq 0$ in Fig.3.5(b).

Now that we have summarized what *coherent population trapping* is, lets briefly discuss how to make coherent population trapping velocity selective[129]. Let's consider the semi-classical treatment of atoms moving in one dimension with a velocity \vec{v} . Suppose the Raman condition is satisfied when $\vec{v} = 0$. Now if $\vec{v} \neq 0$ the two laser frequency seen by the atoms will be doppler shifted by $\vec{k}_1 \cdot \vec{v}$ and $\vec{k}_2 \cdot \vec{v}$ respectively in the center-of-mass frame of the atom. Thus the Raman detuning condition will change as $\Delta \rightarrow \Delta + (\vec{k}_1 \cdot \vec{v} - \vec{k}_2 \cdot \vec{v})$. Now if $\vec{k}_1 \cdot \vec{v} \neq \vec{k}_2 \cdot \vec{v}$ the Raman detuning condition is non zero and hence becomes velocity dependent. Thus the fluorescence rate in Fig.3.5(b) becomes velocity dependent and the atoms which are having $v = 0$ will remain in dark state.

The absorption from g_1 and g_2 interfere only if they end up in the same excited state $|e, \vec{p}\rangle$. Taking the momentum conservation in to account they can reach the excited state $|e, \vec{p}\rangle$ if they have the ground state as $|g_1, \vec{p} - \hbar\vec{k}_1\rangle$ and $|g_2, \vec{p} - \hbar\vec{k}_2\rangle$ and when we include the external kinetic term in the internal energy of the ground state; the corresponding Raman condition is modified as

$$E_{g_1} + \frac{(\vec{p} - \hbar\vec{k}_1)^2}{2m} + \hbar\omega_1 = E_{g_2} + \frac{(\vec{p} - \hbar\vec{k}_2)^2}{2m} + \hbar\omega_2 \quad (3.11)$$

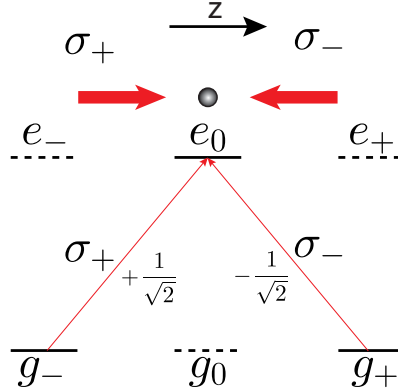


Figure 3.6: $g = 2^3S_1 \rightarrow e = 2^3P_1$ transition is excited by two counter propagating laser beams with $\sigma+$ and $\sigma-$ polarization. This forms a Λ transition.

An interesting case is the $2^3S_1 \rightarrow 2^3P_1$ transition in Helium 4 (see fig. 3.6). Two counter propagating laser beams are used with $\sigma+$ and $\sigma-$ polarization. In this configuration the atoms are optically pumped out of g_0 and because the selection rules forbid the $e_0 \leftrightarrow g_0$ the atom can not come back to g_0 and a pure three level Λ system is realized. In this system since the static magnetic field is assumed to be zero $E_{g_1} = E_{g_2}$, and the Raman resonance condition (equation 3.11) gives $p = 0$ in the excited state e_0 . The corresponding dark state reads $\frac{1}{\sqrt{2}}(|g_-, -\hbar\vec{k}\rangle + |g_+, +\hbar\vec{k}\rangle)$ and displays a double peak structure separated by $2\hbar\vec{k}$ as first observed in[129].

Raman cooling

Raman cooling works on a three level system with two long lived ground states like in alkali atoms[130]. It uses stimulated Raman transitions to transfer atoms from the lower hyperfine state to the upper hyperfine state in a velocity selective manner. When the Raman beams are in a counter-propagating configuration, atoms with positive velocity ($v > 0$) are transferred from the lower ground state level ($|g_1\rangle$) to upper ground state level ($|g_2\rangle$) with a change in the momentum by an amount $-2\hbar k$ (see Fig. 3.7(a)). This change reduces the atom's velocity. Now with a second laser beam the atoms are then optically pumped back to the lower hyperfine structure and in the process they undergo a random spontaneous emission, changing momentum by either $+\hbar k$ or $-\hbar k$ with equal probabilities in a simplified 1D model. These atoms when they are put back in the $|g_1\rangle$ state have a velocity smaller than their initial velocity. Repeating these Raman transition/optical pumping cycles, the atom reduces its momentum in this process.

Reversing the direction of the Raman beams, the same is true for atoms having negative velocity ($v < 0$), these atoms after the completion of the full cycle come back to $|g_1\rangle$ state with velocity greater than their initial velocity. This way the velocity distribution is compressed towards $v = 0$.

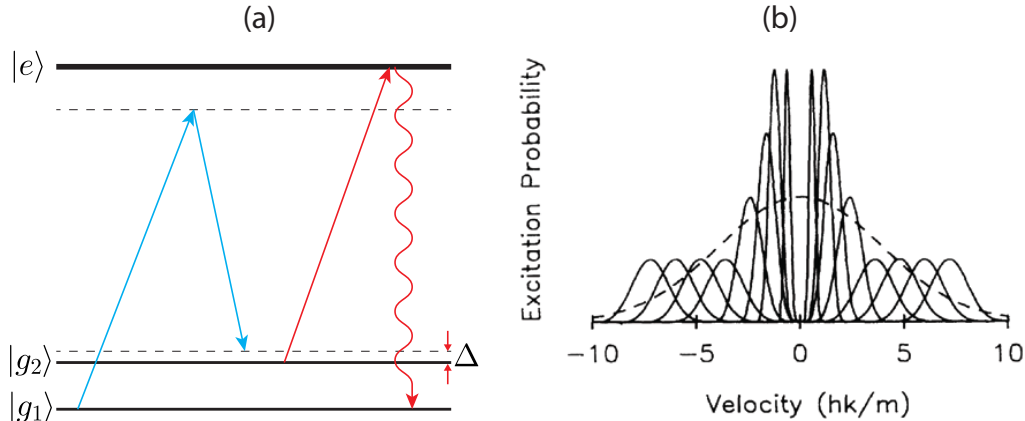


Figure 3.7: (a) Raman cooling process. The two counter-propagating stimulated Raman pulses are represented in blue. The optical pumping pulse is represented by red. (b) Velocity dependence of the excitation probability (also the fluorescence rate). A sequence of pulses are applied to push the atoms towards zero velocity. Figure adapted from[130].

However the atoms that have a velocity smaller than the recoil velocity in a small interval $\delta v \sim \hbar k/m$ around $v = 0$ should not be excited. Practically this is done by using Raman pulses of longer duration (narrower Fourier widths) precisely located at $\pm v_{rec}$ see figure 3.7(b). This small velocity interval plays as an accumulation region of the atoms. As the atoms undergo random spontaneous emission processes there is a finite chance that some of the atoms may end up inside this zone where they stay much longer before being re-excited, See Fig. 3.7(b).

3.4 Gray molasses cooling

Gray molasses cooling was proposed by Grynberg and Courtois[131], Weidemüller et al.[132], and was experimentally realized in a three dimensional configuration on the D2 transitions of Cesium and Rubidium[133]–[135]. The gray molasses technique combines the principles of polarization gradient cooling with velocity selective coherent population trapping. Gray molasses cooling operates with blue detuning on a $|g, J\rangle \rightarrow |e, J\rangle$ or $|g, J\rangle \rightarrow |e, J-1\rangle$ transitions having respectively one or two dark states. These transitions ensure that there will always be a dark state irrespective of the polarisation of the light whether it is $\sigma+$, $\sigma-$, π or elliptical[136]. The gray molasses cooling mechanism relies on the existence of dark and bright ground states (see eq. 3.9) for the atom in the presence of the radiation field.

Because of the counter propagating nature of the light field and the existence of polarization gradient, the energy of the atom in bright state manifold is spatially modulated, whereas the energy of the atom when it is in the dark state does not

change with position because of the non-coupled nature of the state (see Fig. 3.8). The energy of this bright state is positive for a positive light detuning and as mentioned above spatially modulated since the light shift depends on the light intensity (and hence on polarization of the field at a given point) variations.

Normally when the atom is at rest the $|\psi_D\rangle$ and $|\psi_B\rangle$ are not coupled, however when the atom moves there is a coupling between the dark state and the bright state due to the kinetic term in the atomic hamiltonian[137].

$$\langle\psi_B(p)|\frac{\hat{p}^2}{2m}|\psi_D(p)\rangle = -\frac{2\Omega_1\Omega_2}{\Omega^2}\hbar k\frac{p}{m} \quad (3.12)$$

where the Ω_i are the Rabi frequencies of the respective transitions as shown in figure 3.5(a) and are defined in 3.7.

The motional coupling from the dark state to the bright state predominantly occurs at the valleys of the bright state energy potential where the energy difference between the dark and bright state is smallest. The atom when transferred to the bright state climbs up the potential and hence loses its kinetic energy. From this bright state the atom is then optically pumped back to the dark state with the highest probability at the top of the potential. On average the atom moves more uphill than downhill in the light shift potential of the bright state. Multiple repetition of such cycles ultimately lead to the decrease of kinetic energy and hence the temperature of the atomic ensemble (see fig. 3.8).

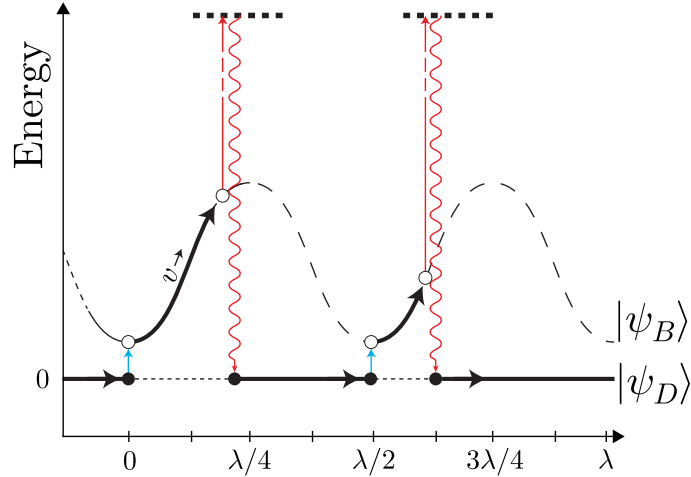


Figure 3.8: Schematics of gray molasses cooling for $|J\rangle \rightarrow |J' = J\rangle$ transition in the simple one dimensional σ^+ , σ^- case. The energy of the atom in the bright states are spatially modulated with a period of $\lambda/2$ where in the dark state it remains unchanged. The atom is represented by a black or a white circle depending on whether it is in dark or bright state respectively. The motional coupling is represented by the blue arrows and the wavy lines represent the spontaneous emission process.

From the equation 3.12 the probability of the atoms to go to the bright state from the dark state is proportional to the square of atomic speed. This results from a non-adiabatic following of the dark internal state when the atom moves. Thus atoms with low speed (colder) will preferably stay in the dark state, while atoms with high speed will be transferred to the bright state. Therefore the probability of the atom getting trapped in the dark state increases in each Sisyphus cycle thus enabling the production of cold atomic samples.

The main advantage of gray molasses arises from the strong reduction of light scattering and light-induced losses. Gray molasses cooling has been implemented for many atomic species and typically achieves minimum temperatures of ~ 15 times the single photon recoil limit, $k_B T \sim 15 \times E_R$ where k_B is the Boltzmann constant, and $E_R = \hbar^2 k^2 / 2m$ is the single photon recoil energy for an atom of mass m cooled by light with wave vector \mathbf{k} [99], [100], [104], [134], [138], [139]. For Lithium isotopes, this temperature is $\sim 50 \mu\text{K}$. Recently a blue detuned magneto optical trap based on this principle has also been realized[140].

In the context of quantum degenerate Bose and Fermi gases the gray molasses technique has been particularly useful for atoms with narrow excited states structure such as ^{40}K , ^6Li , ^7Li , ^{23}Na and molecules for which Sisyphus cooling does not work well[99], [100], [104], [138], [141]. For instance, loading of optical dipole traps (ODT) for Li or K with 1-2 mK atoms produced in standard MOT's is very inefficient unless one uses resonant power enhancement optical cavity for the ODT[142], [143]. With gray molasses temperatures, the requirement on the depth of the ODT trapping potential can be relaxed by one order of magnitude, and all-optical production of a ^6Li Fermi superfluid has been achieved in[101]. Finally in the field of quantum simulation with Rydberg atoms in optical tweezers, gray molasses have been applied to individual ^{87}Rb atoms[139].

3.5 Summary of chapter 3

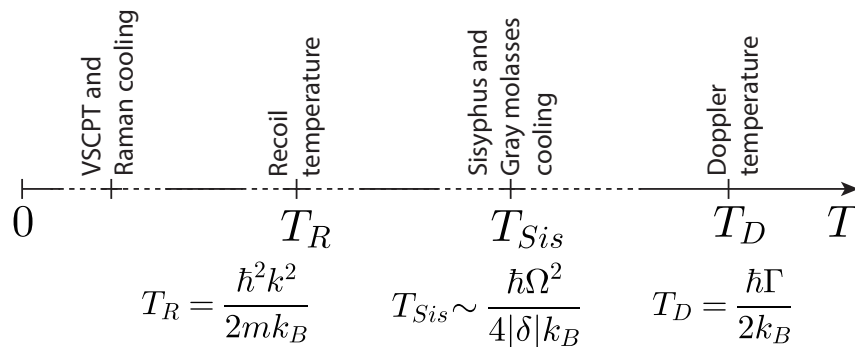


Figure 3.9: Temperature limit associated with various cooling techniques.

In this chapter we reviewed various laser cooling mechanisms. The different cooling schemes have different characteristic cooling limits. The Doppler temperature limit is simply proportional to the excited state linewidth. We have observed that the presence of several Zeeman sublevels in the ground state gives rise to interesting Sisyphus cooling. The Sisyphus cooling temperature varies as a function of light shift and thus for lower and lower light shift it can be way below the Doppler cooling temperature. Experimentally a light shift threshold has been found leading to r.m.s velocities on the order of $\sim 3 \times v_{rec}$ corresponding to temperatures on the order of $\sim 10 \times T_R$. Theoretically this minimum temperature is not easy to obtain as a full quantum treatment of the internal and external atomic degrees of freedom is required [144].

The recoil temperature limit of the atoms can be overcome with the introduction of velocity dependent Electromagnetic induced transparency (EIT), using a three level Λ -system around atomic momentum $p = 0$. There are two proven sub recoil techniques namely VSCPT and Raman cooling. In both methods the atoms perform random walks in the velocity space and eventually end-up in a trap region around $p = 0$. There is no lower limit to the effective temperature in the sub-recoil cooling techniques. It depends on the interaction time, θ . The longer the interaction time the lower is the temperature. In VSCPT temperature varies as $\theta^{-1/2}$. In standard Raman cooling with Blackman pulses the temperature varies as $\theta^{-1/4}$. With optimized square pulses Raman cooling temperature can also vary as $\theta^{-1/2}$ as in VSCPT[145]. Finally the Gray molasses cooling scheme is a hybrid of polarization gradient Sisyphus cooling and the VSCPT. It is efficient for alkali atoms and very useful for atoms with narrow excited state hyperfine structure.

Now that we have described the experimental apparatus and a brief overview of the different cooling mechanisms, in the next chapter I will present the results obtained in the experiment on simultaneous D1 cooling of Lithium isotopes.

This page intentionally left blank

Chapter 4

Simultaneous D1 sub-Doppler cooling of ${}^6\text{Li}$ and ${}^7\text{Li}$ isotopes

Contents

4.1 Experiment sequence	72
4.2 D2 molasses results	75
4.3 Individual D1 molasses in CW mode	78
4.4 The problem of simultaneous D1 cooling	79
4.4.1 Estimate of the differential light shifts of ${}^6\text{Li}$ ground states	80
4.4.2 Off-resonant excitation estimate	81
4.5 Pulsed D1 scheme	83
4.6 Model for D1 molasses cooling and heating	86
4.7 Optimization of pulsed sequence	88
4.7.1 D1 molasses in the optimized pulse sequence	89
4.8 Lifetime measurements	92
4.9 Molasses center of mass drift	93
4.10 TOF peak drift	94
4.11 Data Analysis method and error estimates	95
4.12 Improvements	98

In the previous chapters I have given a brief overview of the Lithium 1 machine and of the various laser cooling mechanisms. In this chapter I will present the main results of the thesis, the simultaneous D1 sub-Doppler cooling of ${}^6\text{Li}$ and ${}^7\text{Li}$ isotopes.

This chapter is organized as follows. First I will describe a typical time sequence for one experimental cycle of the experiment. Then we will characterize the MOT and D2 molasses in terms of atom number and temperature. Turning on simultaneously the D1 molasses for ${}^6\text{Li}$ on $|S_{1/2}, F = 3/2\rangle \rightarrow |P_{1/2}, F' = 3/2\rangle$ and for ${}^7\text{Li}$ on $|S_{1/2}, F = 2\rangle \rightarrow |P_{1/2}, F' = 1\rangle$ we observed a rapid loss in ${}^6\text{Li}$ atoms. We then present a novel pulse scheme method to circumvent the ${}^6\text{Li}$ loss problem. The optimization of this pulsed D1 molasses method enables us to gain one order of magnitude in temperature compared to the D2 molasses temperature for both isotopes. We then discuss the sources of uncertainties in the data analysis and we give the obtained phase space densities for both isotopes. Finally we present some of the latest results obtained by T. Yefsah, T. De Jongh and M. Dixmier on the machine after I left the experiment to write the PhD manuscript.

4.1 Experiment sequence

MOT loading

After the atomic beam is slowed down by the Zeeman slower the atoms reach the lower part of the science cell (see fig. 2.5). In this region the atoms are magneto-optically trapped. The four frequencies of the MOT beams which are mixed on the non-polarizing beam splitters are splitted by 3 polarizing beamsplitters and constitute the six independent arms of the MOT beams each having a diameter of 2.5 cm as shown in figure 2.23. Each beam has a peak intensity of about 2 mW/cm^2 corresponding to $I = 0.8 I_{sat}$. These beams intersect each other perpendicularly and form an overlapping volume which is centered to both the MOT chamber and the MOT coils. We load the MOT for 8 seconds and we obtain 7×10^7 atoms of ${}^7\text{Li}$ and 9×10^7 atoms of ${}^6\text{Li}$ in the MOT with $3\lambda^2/2\pi$ as the resonant cross-section.

CMOT

Once the atoms are captured in the MOT we perform a compressed-MOT (CMOT) phase. The CMOT phase is done in two steps. In the first step (CMOT1) the cooling beams are brought closer to the resonances ($\delta_{6P} = -1.5\Gamma$ and $\delta_{7P} = -3\Gamma$) in 1 ms. In the next step which lasts about 1 ms the beam intensity of the ${}^7\text{Li}$ and ${}^6\text{Li}$ principal beams are gradually reduced to 75%. The magnetic field gradient is kept constant as it was for the MOT phase. This phase increases the peak density of the cloud. Details of the detunings are given in table 4.1.

Detuning	MOT	CMOT	D2 molasses
^6Li cooling	-5.4Γ	-2.0Γ	-2.0Γ
^6Li repumper	-2.0Γ	-1.5Γ	-1.5Γ
^7Li cooling	-6.7Γ	-3.0Γ	-3.0Γ
^7Li repumper	-5.9Γ	-3.5Γ	-3.5Γ
Magnetic field gradient	25G/cm	25G/cm	0

Table 4.1: Magnetic field gradient and detuning of the laser beams in MOT phase and in CMOT phase and the D2 molasses phase, with respect to the corresponding resonant transitions as shown in figure 2.10.

D2 molasses

After the CMOT phase, we perform a 500 μs D2 molasses phase on the atoms. In this phase the magnetic field of the coils are switched off and the temperatures are reduced to about 900 μK as shown in figure 4.3a and 4.4a. The fast switch-off of the coils and reduced Eddy currents near the glass cell enables us to reach low enough residual magnetic field for the proper operation of the D1 molasses. Later in the chapter we discuss the results of D2 molasses in section 4.2.

D1 molasses

After the D2 molasses phase the atoms are subjected to D1 gray molasses. These beams are derived from the setup described above in 2.20 and 2.21. As in the previous works[99]–[101] the D1 molasses is usually done in two steps. In a first step the D1 beams are shone on the atoms typically for 1 ms with maximum power to optimize the capture efficiency of the atoms from D2 molasses. In a second step the D1 beam intensity is reduced to optimize the temperature.

Imaging

An absorption image is taken at the end of an experimental sequence. Typically we take multiple absorption images with a variable time of flight. The details of the imaging can be found in section 2.6.2 of this thesis.

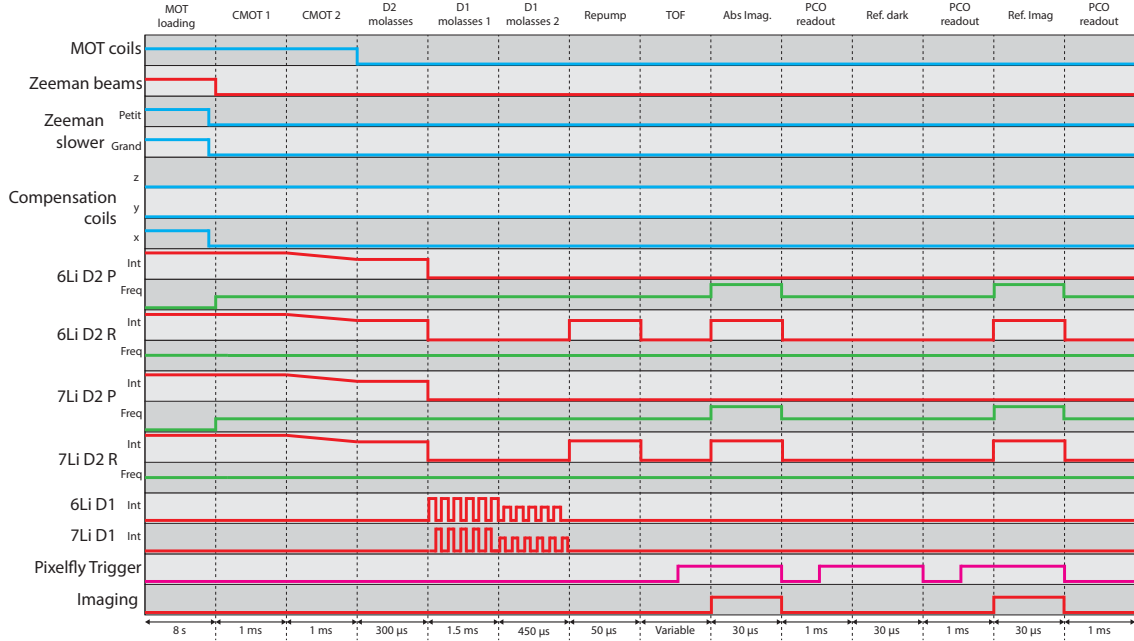


Figure 4.1: A simple representation of a typical experiment sequence. Multiple parameters are changed at different time of the sequence. The current in the electromagnetic coils are represented by the blue line, the laser power outputs represented by the red lines, the frequencies of the laser beams are represented by the green lines and the Pixelfly camera trigger is represented by the pink line. The sequence usually starts with loading the MOT followed by CMOT, D2 molasses, D1 molasses, hyperfine pumping of the atoms, time of flight and then absorption imaging. One experimental cycle lasts about 10 seconds.

The sketch of a typical experimental time sequence is depicted in the figure 4.1. In this figure we represent the various experimental steps and their duration in chronological order. Multiple experimental parameters change their values during the course of a single cycle. For simplicity a few important parameters and a relative change¹ in their values are represented in the figure 4.1.

¹ Please note this is just a diagrammatic representation of a typical sequence and the coordinates are not to scale.

4.2 D2 molasses results

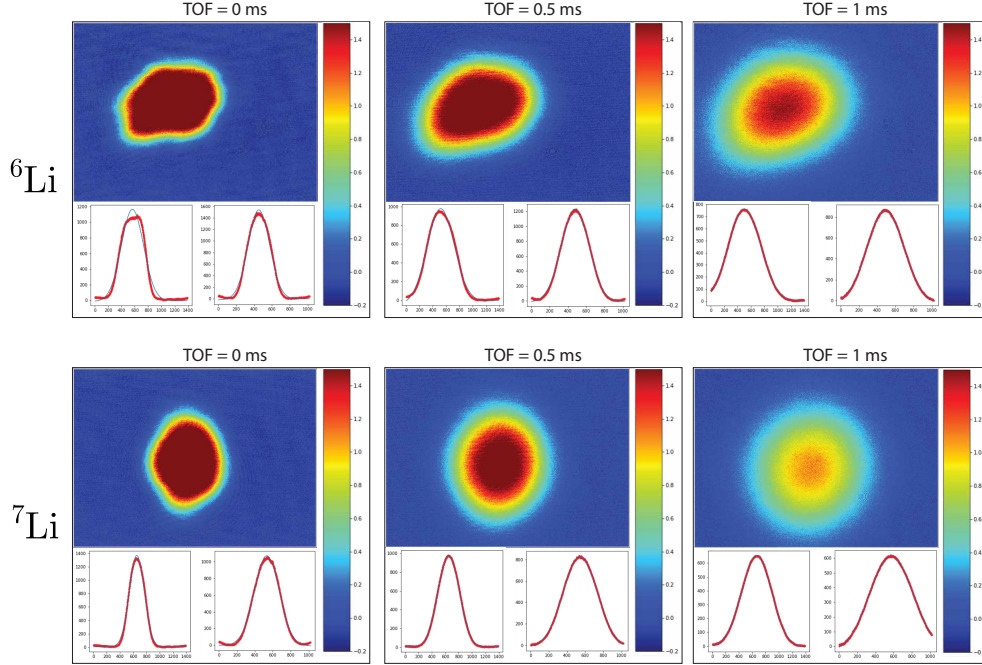


Figure 4.2: TOF images for D2 molasses. In the top row we see the in-situ (TOF=0) optical density (OD) profile of the ${}^6\text{Li}$ atomic cloud as well as at multiple 0.5 ms and 1 ms TOF interval. In the bottom we see the in-situ (TOF=0) OD profile for ${}^7\text{Li}$ and also at multiple TOF interval of 0.5 ms and 1 ms. In the bottom of each OD profile we see the Gaussian fit along x and y direction respectively. From the fit we can calculate the atom number and temperature of the cloud.

The optical density of expanding atomic cloud at different time of flight (TOF) is shown in figure 4.2. As described in equation 2.6 we observe in figure 4.3a at long time of flight the square of the cloud size expands linearly with respect to the time. From the rate of expansion of the cloud we can extract the temperature of the cloud. The temperature along one direction is calculated as $1/2 k_B T = 1/2 m v^2$. The slope of σ^2 vs TOF^2 gives the square of velocity (v^2). Putting the numbers in the above equation we get the temperature of ${}^6\text{Li}$ around 0.97(5) mK along x direction and 0.81(3) mK along y direction. The temperatures along x and y direction are very similar as we expect the cloud expands nearly isotropically in all three directions.

Similarly as described in section 29 the number of atoms captured in D2 molasses can be evaluated by integrating the optical density profile with the correct Clebsch-Gordan coefficient (see equation 2.5). In 4.3b the atom number² for ${}^6\text{Li}$ is found to be nearly $\sim 1 \times 10^8$.

² under the assumption of the resonant cross-section $3\lambda^2/2\pi$.

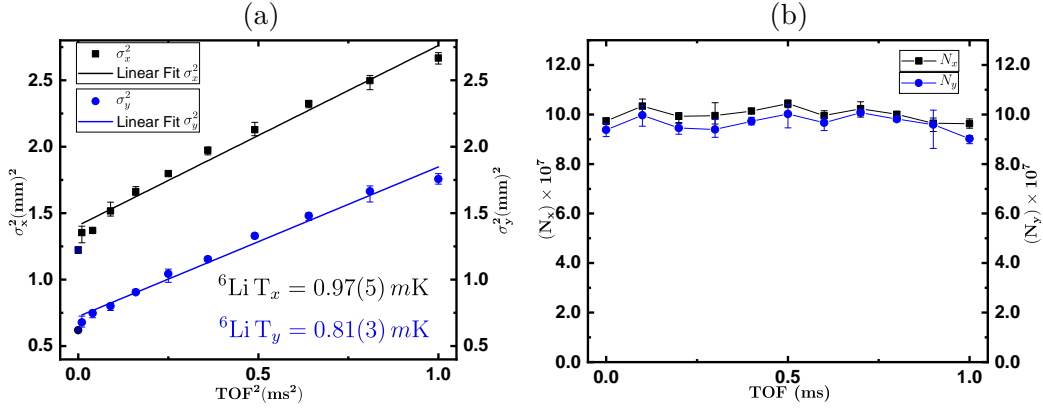


Figure 4.3: (a) Temperature measurement of ${}^6\text{Li}$ atomic cloud after $500 \mu\text{s}$ D2 molasses. Square of Gaussian waist in x and y direction σ_x^2 and σ_y^2 respectively are plotted as a function of square of TOF; the black solid squares and the blue solid circles represent the expansion of the cloud along the x and y direction respectively. The vertical lines represent the statistical error in σ^2 . The black and blue solid lines represent the respective linear fit of cloud expansion. The slope of the linear fit gives the temperature of the expanding atomic cloud which is shown at the bottom of the figure. (b) The average number of ${}^6\text{Li}$ atoms in D2 molasses as a function of TOF after $500 \mu\text{s}$ D2 molasses. The black solid squares and the blue solid circles represent the atom number after integration of OD along x and y direction respectively and the corresponding vertical lines represent the statistical error in the atom number measurement. As expected we see a constant atom number at various TOF.

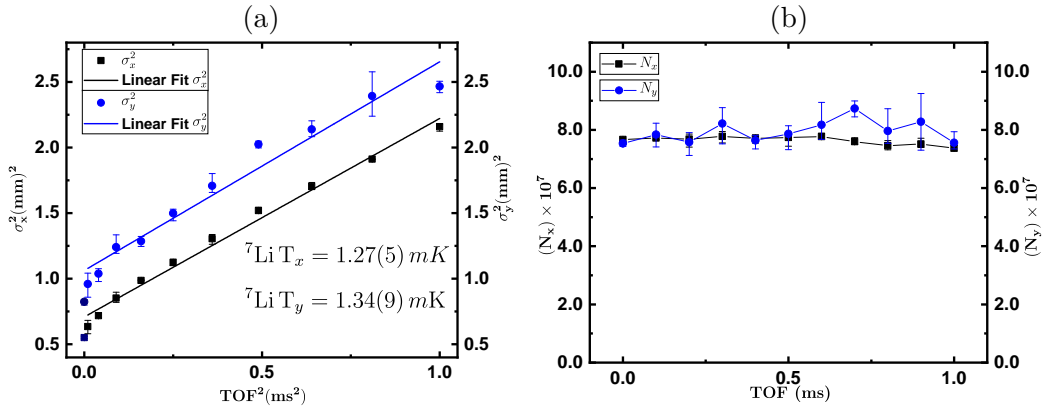


Figure 4.4: (a) Temperature measurement of ${}^7\text{Li}$ atomic cloud after $500 \mu\text{s}$ D2 molasses. (b) ${}^7\text{Li}$ Atom number as a function of TOF after $500 \mu\text{s}$ D2 molasses. Black points and black line: measurements along x direction. Blue: measurements along y direction.

Similar measurements of temperature and atom number for ${}^7\text{Li}$ are shown in figure 4.4. We observe for ${}^7\text{Li}$ that the temperature of the cloud is a little bit hotter (1.27(5) mK along x and 1.34(9) mK along y) than that for ${}^6\text{Li}$. The atom number³ captured in D2 molasses is approximately $\sim 8 \times 10^7$.

Apart from the temperature and atom number we also measured the center of mass position of both isotopes as a function of time of flight (see figure 4.5b). We observe a drift velocity of 0.32 m/s ($3.2 v_{recoil}$) and 0.25 m/s ($2.5 v_{recoil}$) along x and y direction respectively for ${}^6\text{Li}$ and 0.05 m/s ($0.6 v_{recoil}$) and 0.2 m/s ($2.3 v_{recoil}$) along x and y direction respectively for ${}^7\text{Li}$. This drift velocity is negligible compared to the rms velocity at the measured temperatures. It results from intensity imbalance of the laser beams during the D2 molasses phase.

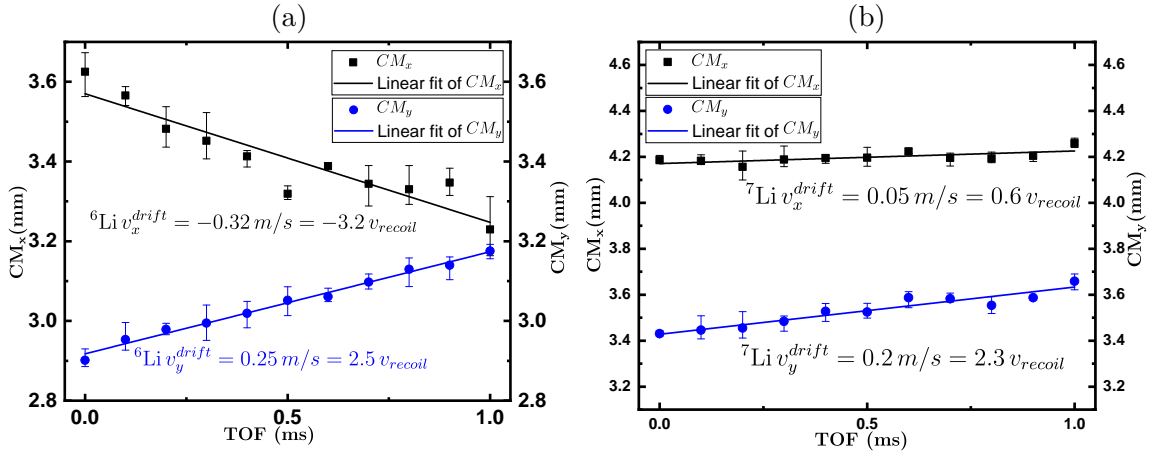


Figure 4.5: Displacement of center of mass of the (a) ${}^6\text{Li}$ and (b) ${}^7\text{Li}$ atomic clouds in the transverse plane perpendicular to the imaging axis direction as a function of time of flight. The black solid squares and blue solid circles represents the motion of center of mass along x and y direction respectively. The black and blue lines are the linear fit of the respective data points and the slopes of the fit gives the velocity along x and y direction respectively. The corresponding vertical lines represents the statistical error in measurement.

³ under the assumption of the resonant cross-section $3\lambda^2/2\pi$.

4.3 Individual D1 molasses in CW mode

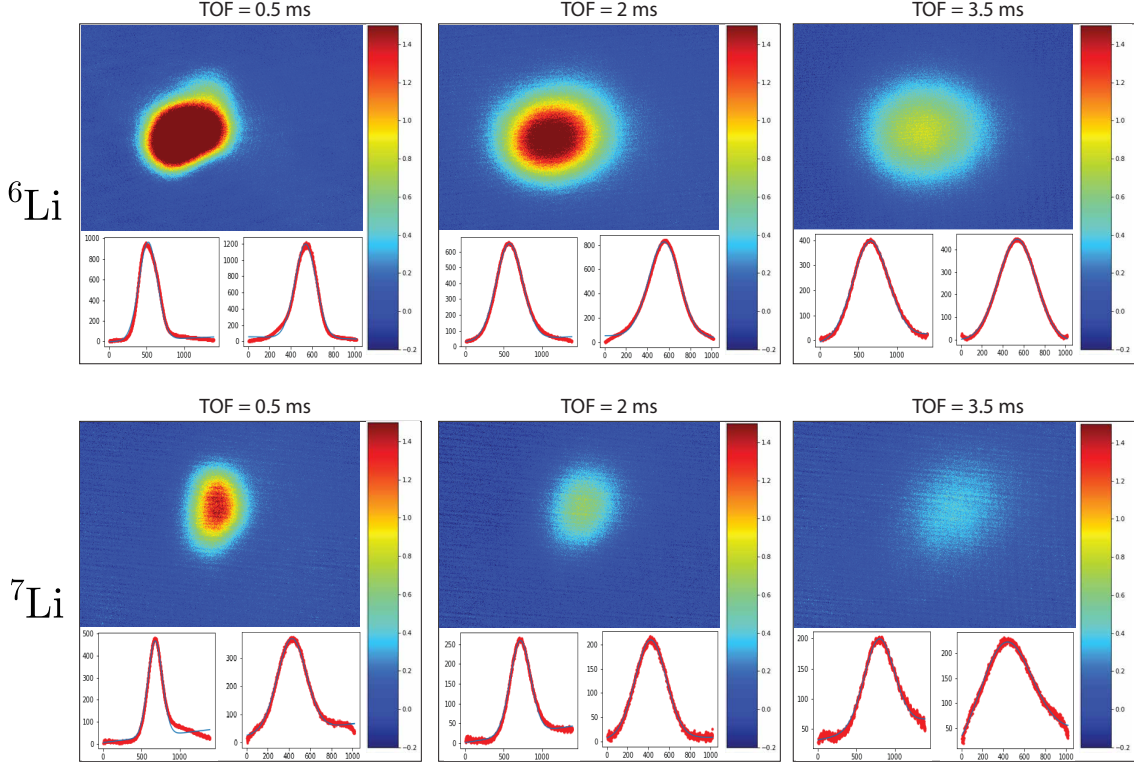


Figure 4.6: OD profile as a function of TOF for ${}^6\text{Li}$ and ${}^7\text{Li}$ D1 molasses in the continuous mode for 1 ms. This data is taken for each isotope individually without the presence of the other isotope and the corresponding D1 beams.

In the first D1 molasses runs we tried to cool ${}^6\text{Li}$ and ${}^7\text{Li}$ individually and independently without the presence of the other isotopes. The TOF images can be seen in figure 4.6 for 1 ms molasses time. As expected from previous works[99]–[101], our setup for D1 molasses works well for both isotopes individually. We were able to cool them individually from $\sim 900 \mu\text{K}$ to $\sim 93(15) \mu\text{K}$ and from $\sim 1.3 \text{ mK}$ to $\sim 90(10) \mu\text{K}$ for ${}^6\text{Li}$ and ${}^7\text{Li}$ respectively. The capture efficiency of ${}^6\text{Li}$ is about 40% and for ${}^7\text{Li}$ is about 20% in this data set. We will see later that these capture efficiencies can be improved by better alignment and beam intensity balance.

4.4 The problem of simultaneous D1 cooling

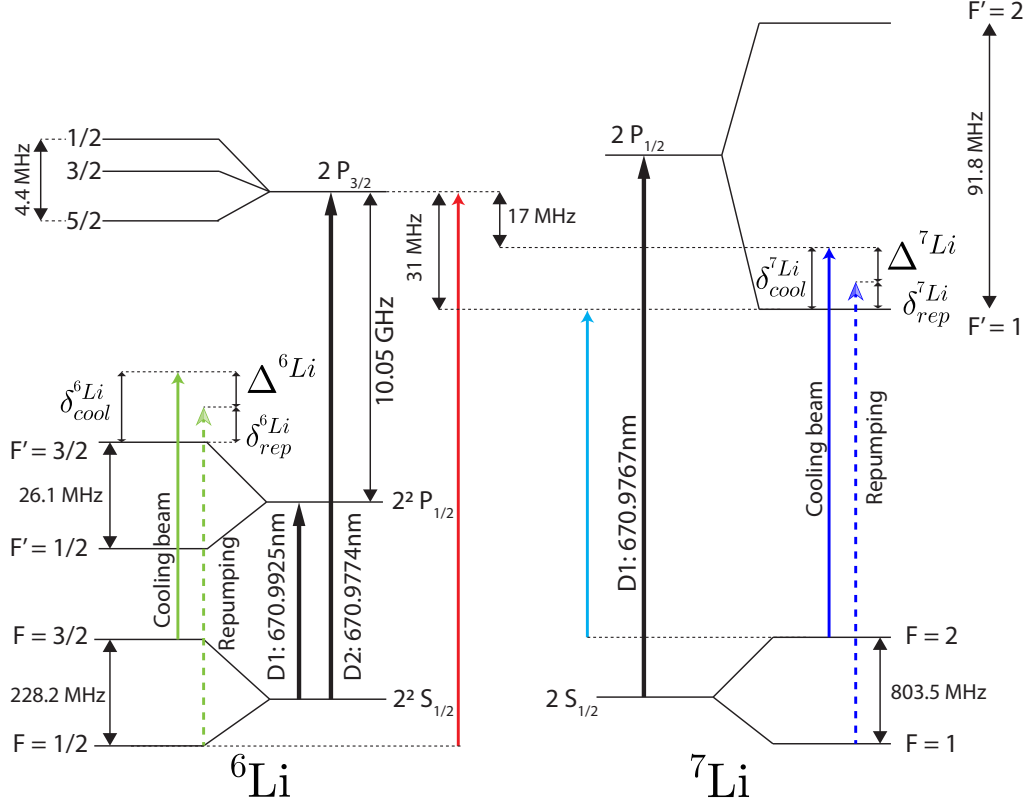


Figure 4.7: Energy level diagrams and relevant transitions for D1 cooling of ${}^6\text{Li}$ and ${}^7\text{Li}$. Note the close proximity of ${}^6\text{Li}$ $|F = 1/2\rangle \rightarrow |F' = 3/2\rangle$ transition (red arrow) and ${}^7\text{Li}$ transition ($|F = 2\rangle \rightarrow |F' = 1\rangle$) involved in D1 cooling (cyan arrow) that lies 31 MHz ($\sim 5.3 \Gamma$) below ${}^6\text{Li}$ D2 transition $|F = 1/2\rangle \rightarrow |F' = 3/2\rangle$. The Zeeman and hyperfine Raman conditions are fulfilled when $\delta_{cool} = \delta_{rep}$ i.e. $\Delta = 0$ for both ${}^6\text{Li}$ and ${}^7\text{Li}$.

When simultaneously applying D1 beams on the Lithium isotopes we observed that the ${}^7\text{Li}$ temperature drops quickly (< 1 ms) from 1 mK to less than 100 μK indicating proper operation of D1 molasses. However for ${}^6\text{Li}$ we observed heating and rapid disappearance of the cold atoms.

We attribute this phenomenon to the ${}^7\text{Li}$ D1 beams causing both differential light shifts of ${}^6\text{Li}$ $S_{1/2}$ hyperfine ground states and off-resonant excitation ($|2s_{1/2}, F = 1/2\rangle \rightarrow |2P_{3/2}, F' = 3/2\rangle$) breaking the correlation between light shifts and optical pumping in polarization gradient cooling process. We note in figure 4.7 the ${}^7\text{Li}$ D1 beam corresponding to the transition $|F = 2\rangle \rightarrow |F' = 1\rangle$ and the D2 transition for ${}^6\text{Li}$ ($|F = 1/2\rangle \rightarrow |F' = 3/2\rangle$) are at a very close proximity of only 31 MHz. We believe these ${}^7\text{Li}$ D1 beams break the velocity selective Raman condition ($|F = 3/2\rangle \rightarrow |F' = 3/2\rangle$ and $|F = 1/2\rangle \rightarrow |F' = 3/2\rangle$) required for cooling atoms into the dark states and also produces off-resonant excitation (fig. 3.8).

4.4.1 Estimate of the differential light shifts of ${}^6\text{Li}$ ground states

For a detuning large compared to Γ , a simple estimate of ${}^6\text{Li}$ ground state light shifts $U_{1/2}$ and $U_{3/2}$ is as follows:

$$U_{1/2} = \frac{\hbar\Omega_R^2(r)}{4\Delta_1} \quad (4.1)$$

$$U_{3/2} = \frac{\hbar\Omega_R^2(r)}{4\Delta_2} \quad (4.2)$$

where $\Delta_1 = \omega_{D1}^7 - \omega_{D2,R}^6 = -2\pi \times 16.7$ MHz is the detuning between the ${}^7\text{Li}$ D1 cooling beam and the $|S_{1/2}, F = 1/2\rangle \rightarrow |P_{3/2}, F' = 3/2\rangle$ ${}^6\text{Li}$ D2 repumping transition (subscript R) and $\Delta_2 = \omega_{D1}^7 - \omega_{D2,P}^6 = +2\pi \times 211.1$ MHz is the detuning between the ${}^7\text{Li}$ D1 cooling beam and the $|S_{1/2}, F = 3/2\rangle \rightarrow |P_{3/2}, F' = 3/2\rangle$ ${}^6\text{Li}$ principal D2 transition (subscript P)⁴.

With the parameters given in table 4.2 we found an estimate for the light shift $U_{1/2} \sim -5\hbar\Gamma/8$ and $U_{3/2} \sim 5\hbar\Gamma/96$ for a single beam resulting in an overall differential light shift of $\sim -65\hbar\Gamma/96$ for a single beam. Adding the light shift of six D1 molasses beams we get the differential light shift on the order of $\sim -65/16 \hbar\Gamma$. Note that this is an order of magnitude estimate as we have six molasses beams and the polarization pattern in 3D depends on the relative phases of the beams which are uncontrolled. This overall differential light shift, which is negative, position dependent, and of order 4Γ severely affects the Raman condition for the ${}^6\text{Li}$ 228 MHz hyperfine ground state splitting. The ground state coherence responsible for the efficiency of the D1 cooling process is reduced.

Parameters	${}^6\text{Li}$ D1	${}^7\text{Li}$ D1
Total power per beam pair	20 mW	12 mW
1/e beam diameter	6.4 mm	6.3 mm
Peak I/I _{sat} per beam	~ 25	~ 15
Detuning	$+3\Gamma$	$+2.3\Gamma$

Table 4.2: Parameters of D1 beams for simultaneous D1 molasses of ${}^6\text{Li}$ and ${}^7\text{Li}$.

Conversely the light shifts of ${}^7\text{Li}$ ground states due to ${}^6\text{Li}$ D1 beams are negligible because of the large detuning (10 GHz) of ${}^6\text{Li}$ D1 cooling light from the ${}^7\text{Li}$ atomic transition lines.

The heating phenomenon due to the differential light shift has previously been observed by mistuning the D1 beams from the exact Raman condition as shown in Sievers et al.[99] on Potassium (${}^{40}\text{K}$) and lithium (${}^6\text{Li}$).

⁴ we can safely neglect the light shifts induced by the ${}^7\text{Li}$ repumping beam because of 803.5 MHz additional detuning and factor 10 lower beam intensity

4.4.2 Off-resonant excitation estimate

The second adverse effect is the off-resonant excitation out of the ${}^6\text{Li}$ $F = 1/2$ state. As shown in figure 4.7 the $|2S_{1/2}, F = 1/2\rangle \rightarrow |2P_{3/2}, F = 3/2\rangle$ transition is only 17 MHz blue of the ${}^7\text{Li}$ D1 beams. Direct excitation to $F=1/2$ or $3/2$ breaks the dark state and produces heating by spontaneous emission. Let us now give an estimate of this process. The photon scattering rate R_{scatt} for a two-level atom is given by:

$$R_{scatt} = \frac{\Gamma}{2} \frac{\Omega^2/2}{\delta^2 + \Omega^2/2 + \Gamma^2/4} \quad (4.3)$$

where $\Gamma = 2\pi \times 5.8$ MHz is the natural line width of lithium transition, Ω is the ${}^6\text{Li}$ Rabi frequency corresponding to the ${}^7\text{Li}$ D1 beam and δ is the detuning of ${}^7\text{Li}$ D1 beam from D2 transitions of ${}^6\text{Li}$.⁵

In reality the atomic system is more complex than a simple two-level atom. Let's assume we can model the problem as a three level system as shown in figure 4.8. With the values given in table 4.2 and the average Clebsch-Gordan coefficient (4/9) corresponding to the σ^+ light for the transition $|S_{1/2}, F = 1/2\rangle \rightarrow |P_{3/2}, F' = 3/2, 1/2\rangle$ and a detuning of $\delta = -10.4\Gamma^6$, the off-resonant excitation rate R_{scatt_1} is found to be ~ 1.6 photons/ μs . After a few photons atoms are quickly optically pumped into $|S_{1/2}, F = 3/2\rangle$ state. This optical pumping then leads to a second, weaker, off-resonant photon scattering between the state $|S_{1/2}, F = 3/2\rangle \rightarrow |P_{3/2}, F' = 5/2, 3/2, 1/2\rangle$ with the average Clebsch-Gordan coefficient 2/3. With the values given in table 4.2 and a detuning of $\delta = +35.3\Gamma^7$, the off-resonant photon scattering rate R_{scatt_2} is found to be ~ 0.22 photons/ μs . This scattering rate leads to heating in ${}^6\text{Li}$ atoms, which we will discuss in section 4.6.

⁵ The presence of ${}^7\text{Li}$ D1 beams also increases the linewidth of ${}^6\text{Li}$ D2 transitions (power broadening) and is given by: $\Gamma' = \Gamma \sqrt{1 + \frac{I/I_{sat}}{1 + 4\frac{\delta^2}{\Gamma^2}}}$. With the parameters given in table 4.2 the power-broadened linewidth is found to be $\Gamma' = 1.01 \times \Gamma$.

⁶ Light shift of $|S_{1/2}, F = 1/2\rangle$ (-7.5Γ) was taken into account for the value of detuning.

⁷ Light shift of $|S_{1/2}, F = 3/2\rangle$ ($+0.6\Gamma$) was taken into account for the value of detuning.

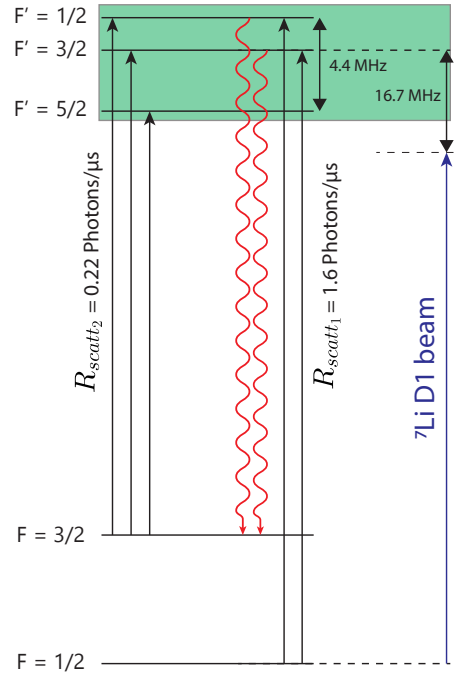


Figure 4.8: Off-resonant photon scattering of $|S_{1/2}, F = 1/2\rangle$ and $|S_{1/2}, F = 3/2\rangle$ due to the ${}^7\text{Li}$ D1 beams. The ${}^7\text{Li}$ D1 beams are represented by the blue arrow and the ${}^6\text{Li}$ D2 transitions are represented by black arrows. Due to the ${}^7\text{Li}$ D1 beams the atoms are optically pumped into $|S_{1/2}, F = 3/2\rangle$ state (represented by curvy red lines).

To conclude this section both the ${}^7\text{Li}$ beam light shifts and excitation from $|F = 1/2\rangle$ sub-level are detrimental to D1 cooling of ${}^6\text{Li}$.

4.5 Pulsed D1 scheme

We have developed an efficient way of overcoming this atom loss problem during D1 cooling by introducing a pulsed D1 cooling scheme.

As shown in figure 4.9 we alternate the D1 beams for ${}^6\text{Li}$ and ${}^7\text{Li}$. We shine the ${}^6\text{Li}$ D1 beams for $100\ \mu\text{s}$ and during the next $100\ \mu\text{s}$ only ${}^7\text{Li}$ D1 beams are present. We repeat this pulse sequence for a variable time. During the first $100\ \mu\text{s}$ the ${}^6\text{Li}$ gets cooled whereas the ${}^7\text{Li}$ is in free flight. In the following $100\ \mu\text{s}$ the ${}^7\text{Li}$ gets cooled and the ${}^6\text{Li}$ is in free flight. In this way the ${}^7\text{Li}$ D1 beams do not destroy the Raman condition required for the D1 cooling of ${}^6\text{Li}$ isotopes at any point in time. Repeating this alternate cooling pulses enables us to cool both isotopes simultaneously and efficiently to sub-Doppler temperatures. The duration of the pulse results from an optimum between two extremes. If the pulse duration is too short the cooling efficiency is reduced, as a result of too short dark state lifetime (see figure 4.27). On the other hand if the pulse duration is too long, as the atomic cloud of the other isotope expands freely in the absence of its cooling beams the cloud density is reduced. We empirically found an optimum in the $50 - 100\ \mu\text{s}$ range. The average speed at $100\ \mu\text{K}$ is $0.3\ \text{m/s}$ for ${}^6\text{Li}$. During the $100\ \mu\text{s}$ free flight, the molasses expansion is $\sim 30\ \mu\text{m}$, much less than the initial molasses size of $\sim 700\ \mu\text{m}$. We will discuss the cooling dynamics in more detail in section 4.6.

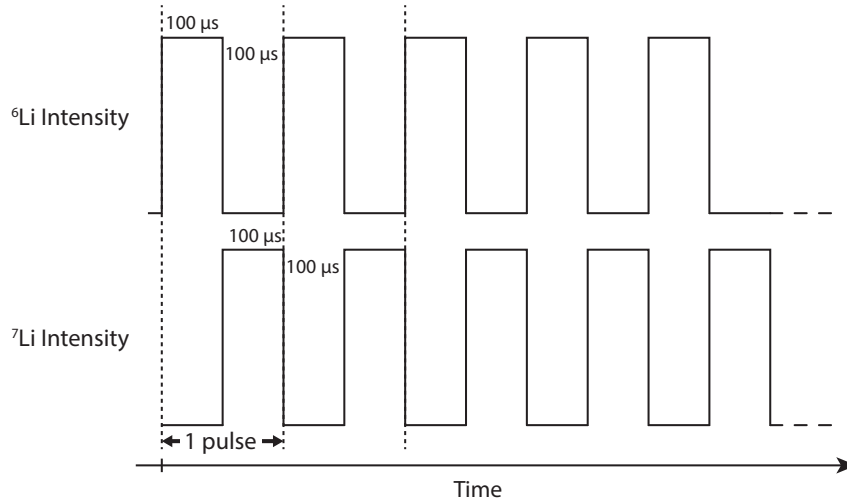


Figure 4.9: Pulse sequence for the operation of ${}^6\text{Li}$ and ${}^7\text{Li}$ dual D1 molasses. The number of pulses is typically varied from 6 to 13 pulses. Each pulse is divided in two parts. In the first part of a pulse we shine ${}^6\text{Li}$ D1 beams for $100\ \mu\text{s}$ and in the second part we shine ${}^7\text{Li}$ D1 beams for $100\ \mu\text{s}$. We modulate the two beams with a phase difference of π so that the D1 beams of one isotope do not cause any perturbation of the D1 cooling of the other isotope.

We also observe in figure 4.10 that, in about 2 to 3 D1 pulses, the temperature drops by one order of magnitude to $\sim 100 \mu\text{K}$ for both isotopes, reaching then a steady state. An exponential decay curve provides a temperature damping time of $0.33(2) \text{ ms}$ and 0.24 ms for ${}^6\text{Li}$ and ${}^7\text{Li}$ respectively in this dual pulsed mode D1 cooling.

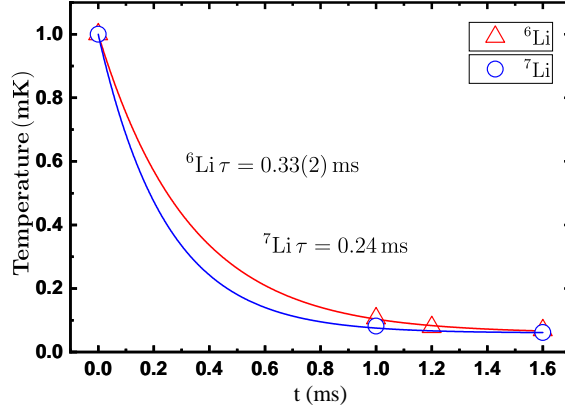


Figure 4.10: Temperature decay of ${}^6\text{Li}$ and ${}^7\text{Li}$ as function of time. The initial temperature is that of D2 molasses near 1 mK for both isotopes. After 1 ms of pulsed dual D1 molasses as shown in figure 4.9 the temperatures drop by one order of magnitude.

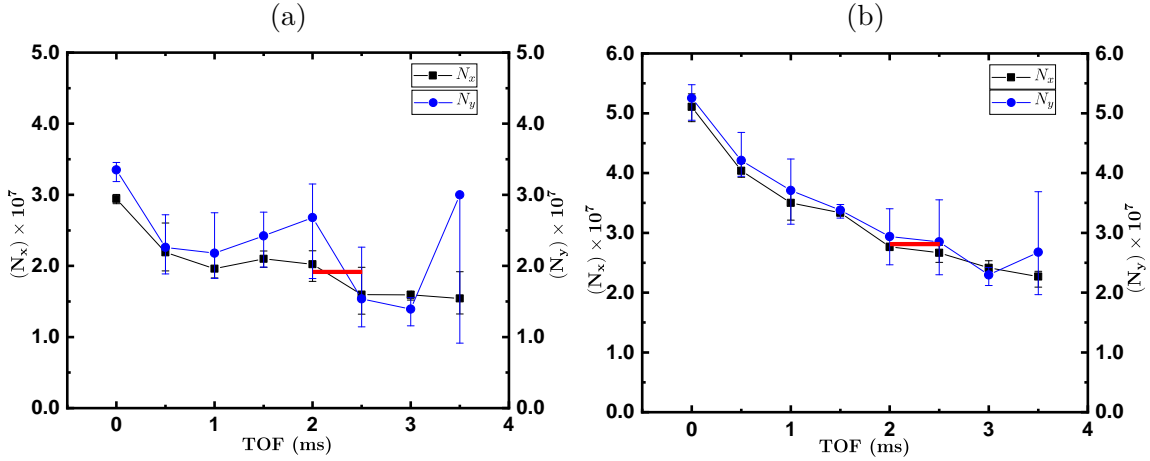


Figure 4.11: Atom number of (a) ${}^6\text{Li}$ and (b) ${}^7\text{Li}$ as a function of TOF for the dual D1 molasses of 1.6 ms . A loss of atoms is observed during the first 2 ms which corresponds to uncaptured atoms from the D2 molasses into D1 molasses. After 2 ms TOF we observe a plateau in the atom number which represents the average D1 molasses number. We thus take the average of 2 ms and 2.5 ms TOF numbers for estimating the D1 molasses capture efficiency (red horizontal lines). Each point is the mean of 3 consecutive measurements and the error bar the standard deviation to the mean.

As shown in figure 4.11 we observe that the atom number for both ${}^6\text{Li}$ and ${}^7\text{Li}$ decay as a function of time of flight. This strange behavior should not occur unless non-captured atoms from the D2 molasses are detected by the probe beam while flying away.

However for a longer D1 molasses time (3 ms and above) we do not see this phenomenon, figure 4.12. We observe the D1 atom number stays constant as function of time of flight with normal shot to shot technical fluctuations. From this figure we infer that the atoms in D2 molasses which were not captured by D1 molasses beams have completely escaped from the observation plane and thus we do not detect a rapid loss of atom number as a function of TOF. Thus a reasonable assumption is to take the average atom number measured at 2 ms and 2.5 ms time of flight (as shown in red horizontal line in figure 4.11) in order to calculate the capture efficiency of D1 molasses.

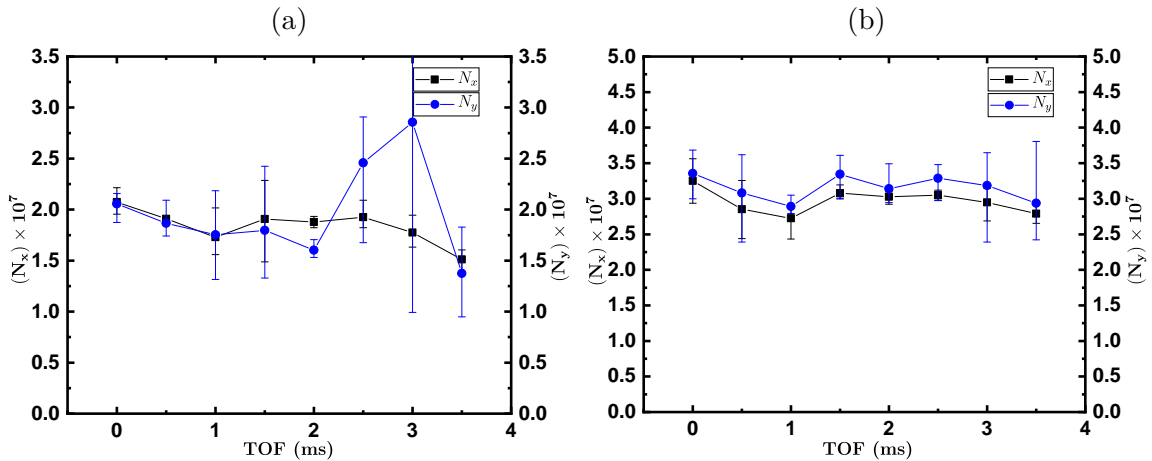


Figure 4.12: Atom number of (a) ${}^6\text{Li}$ and (b) ${}^7\text{Li}$ as a function of TOF for 3 ms of dual D1 molasses. In this measurement we do not observe the atom number decay as contrast to the fig. 4.11.

In figure 4.13 we examine in more detail the temperature evolution of the respective D1 molasses as a function of number of pulses. First for ${}^7\text{Li}$ (blue and red circles) the temperature reaches 67 (10) μK after typically 6 to 8 pulses irrespective of the presence or absence of ${}^6\text{Li}$ D1 beams. As usual the number in parenthesis is the 1σ standard deviation from the mean. This temperature is very close to that reported previously[100]. The ${}^7\text{Li}$ capture efficiency is 25-30%⁸. Conversely the

⁸ The capture efficiency is a trade off between available laser intensity that determines the capture velocity, D2 molasses temperature, D1 molasses beam diameter and local beam intensity balance. The efficiency could benefit from larger D1 laser power[99], [100]

temperature of ${}^6\text{Li}$ atoms is about 160 (69) μK i.e. 1.7 times higher in presence of ${}^7\text{Li}$ D1 beams than in its absence. The capture efficiency of ${}^6\text{Li}$ D1 molasses is only 20% after 6 pulses and after the disappearance of un-captured D2 molasses atoms.

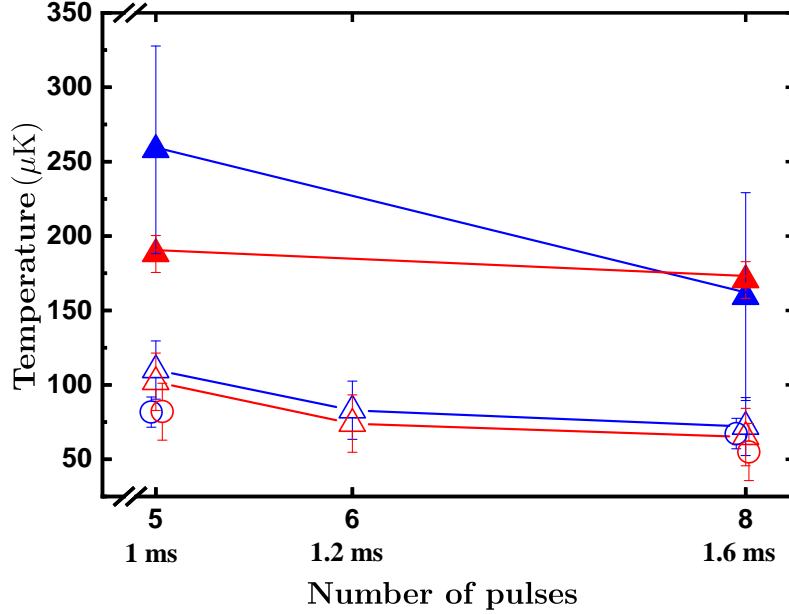


Figure 4.13: Temperature of D1 molasses as a function of number of pulses. Filled triangles: ${}^6\text{Li}$ temperature along X direction (blue) and Y direction (red) in presence of ${}^7\text{Li}$ D1 beams. Open triangles: ${}^6\text{Li}$ temperature in absence of ${}^7\text{Li}$ D1 beams. The presence of ${}^7\text{Li}$ D1 beams degrades the ${}^6\text{Li}$ D1 molasses temperature. Open circles: conversely ${}^7\text{Li}$ temperature remains unchanged in presence or absence of ${}^6\text{Li}$ D1 beams.

4.6 Model for D1 molasses cooling and heating

To understand the pulsed cooling we now take a simple theoretical model of the sequence. In figure 4.14 we see an alternating D1 molasses pulse with 50 % duty cycle. Each pulse sequence contains a ${}^6\text{Li}$ D1 molasses phase of time t_2 (represented by blue region) followed by a ${}^7\text{Li}$ D1 molasses phase of time t_1 (represented by red region). A ${}^6\text{Li}$ atom during the ${}^6\text{Li}$ D1 molasses phase gets cooled and during the ${}^7\text{Li}$ D1 molasses phase it gets heated up as discussed in section 4.4.

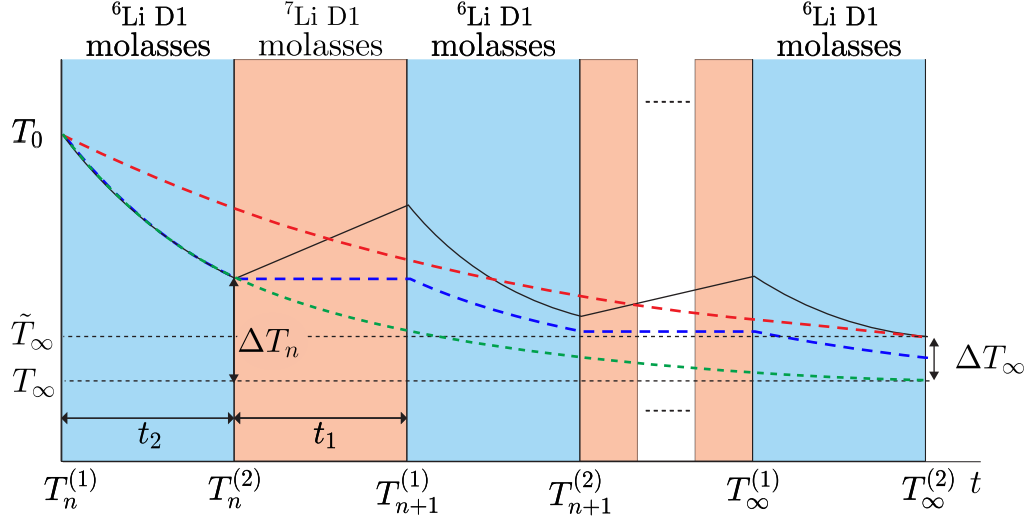


Figure 4.14: Schematic representation of cooling and heating cycle for ${}^6\text{Li}$ isotope during pulsed D1 molasses scheme. The blue region represent the interval where only ${}^6\text{Li}$ D1 beams are present, the orange region represent the interval where ${}^7\text{Li}$ D1 beams are present. The dotted exponential curve in green represent the temperature decay as a function of time with ${}^6\text{Li}$ D1 beams in the CW mode. The dotted blue line represent the temperature of ${}^6\text{Li}$ when only pulsed ${}^6\text{Li}$ D1 beams are present. The solid black line represent the periodic cooling and heating process as a result of pulsed D1 cooling scheme. The red dotted exponential represent the time average temperature decay as a function of temperature due to the pulsed D1 cooling scheme.

Now let T_∞ be the steady state temperature of ${}^6\text{Li}$ in the continuous mode, and \tilde{T}_∞ be the steady state temperature of ${}^6\text{Li}$ when there is an alternating cooling and heating phase. Let $T_n^{(1)}$ and $T_n^{(2)}$ be the temperature of ${}^6\text{Li}$ at the starting and ending of n_{th} cooling pulse. And we define the difference in temperature at n_{th} pulse from its steady state value as $\Delta T_n = T_n - T_\infty$. Thus the temperature difference at $(n+1)_{th}$ pulse can be written as:

$$\begin{aligned}\Delta T_{n+1}^{(1)} &= \Delta T_n^{(2)} + \gamma t_1 \\ \Delta T_{n+1}^{(2)} &= (\Delta T_n^{(2)} + \gamma t_1)e^{-rt_2}\end{aligned}\quad (4.4)$$

where γ is the heating rate of ${}^6\text{Li}$ atoms in the presence of ${}^7\text{Li}$ D1 beams, r is the time constant of ${}^6\text{Li}$ D1 molasses cooling. As $n \rightarrow \infty$ we have:

$$\begin{aligned}\Delta T_\infty^{(2)} &= (\Delta T_\infty^{(2)} + \gamma t_1)e^{-rt_2} \\ \Delta T_\infty^{(2)} &= \frac{\gamma t_1}{(ert_2 - 1)}\end{aligned}\quad (4.5)$$

As a result of heating the new steady state temperature of ${}^6\text{Li}$ will be \tilde{T}_∞ which is shown in figure 4.14.

We notice this increase in temperature is due to the significant heating phase during the ${}^7\text{Li}$ D1 molasses phase. Reducing the ${}^7\text{Li}$ D1 pulse length will result in less heating and this will reduce ΔT_∞ . As an attempt for optimization of the pulse sequence we shorten the ${}^7\text{Li}$ D1 pulse length to $50\mu\text{s}$ resulting $t_1 = 100\mu\text{s}$ and $t_2 = 50\mu\text{s}$. The result of this pulse sequence is described in the next section.

4.7 Optimization of pulsed sequence

We have observed that the cooling of ${}^7\text{Li}$ was more efficient than that of ${}^6\text{Li}$ for an equal pulse length. As discussed above ${}^7\text{Li}$ D1 beams do produce heating of the ${}^6\text{Li}$ cloud. In order to improve the ${}^6\text{Li}$ temperature and the capture efficiency of the D1 molasses we optimized the pulse sequence as shown in figure 4.15. Here we use an asymmetric pulse sequence where the ${}^7\text{Li}$ D1 molasses duration is divided by two resulting in a single pulse length of $150\mu\text{s}$.

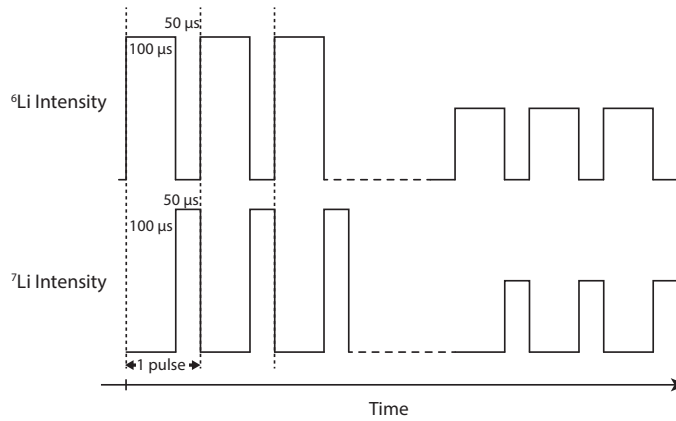


Figure 4.15: Optimized pulse sequence for the operation of ${}^6\text{Li}$ D1 and ${}^7\text{Li}$ D1 molasses. In contrast to figure 4.9 first we shine ${}^6\text{Li}$ D1 beams for $100\mu\text{s}$ and then we shine ${}^7\text{Li}$ D1 beams for $50\mu\text{s}$. The intensity of the last 3 pulses is reduced by $1/2$ for both D1 cooling beams.

We apply between 6 and 13 repetitions of this $150\mu\text{s}$ pulse sequence. In figure 4.19 we see that with 9 or 10 asymmetric pulses the ${}^6\text{Li}$ cools down to $\sim 120\mu\text{K}$ instead of $160\mu\text{K}$ which is summarized in the table 4.3.

	CW	$t_1 = t_2 = 100\mu\text{s}$	$t_1 = 100\mu\text{s}, t_2 = 50\mu\text{s}$
Temperature of ${}^6\text{Li}$ (μK)	93(15)	160 (15)	120 (15)

Table 4.3: Comparison between the symmetric and asymmetric pulse modes. The model described in section 4.4 predicts a temperature of $113\mu\text{K}$ for asymmetric pulse sequence, which is in good agreement with the measured value.

Furthermore as the molasses temperature increases with the D1 beam intensity we reduce the intensity by 1/2 for the last 3 pulses to optimize the final temperature for ${}^6\text{Li}$ and ${}^7\text{Li}$. With this optimized pulse sequence we have increased the capture efficiency of ${}^6\text{Li}$ to $\sim 45\%$ and the temperature of ${}^6\text{Li}$ in the presence of ${}^7\text{Li}$ D1 beams at the end of the sequence drops to $103(10) \mu\text{K}$ as shown in figure 4.19 with the filled triangles.

4.7.1 D1 molasses in the optimized pulse sequence

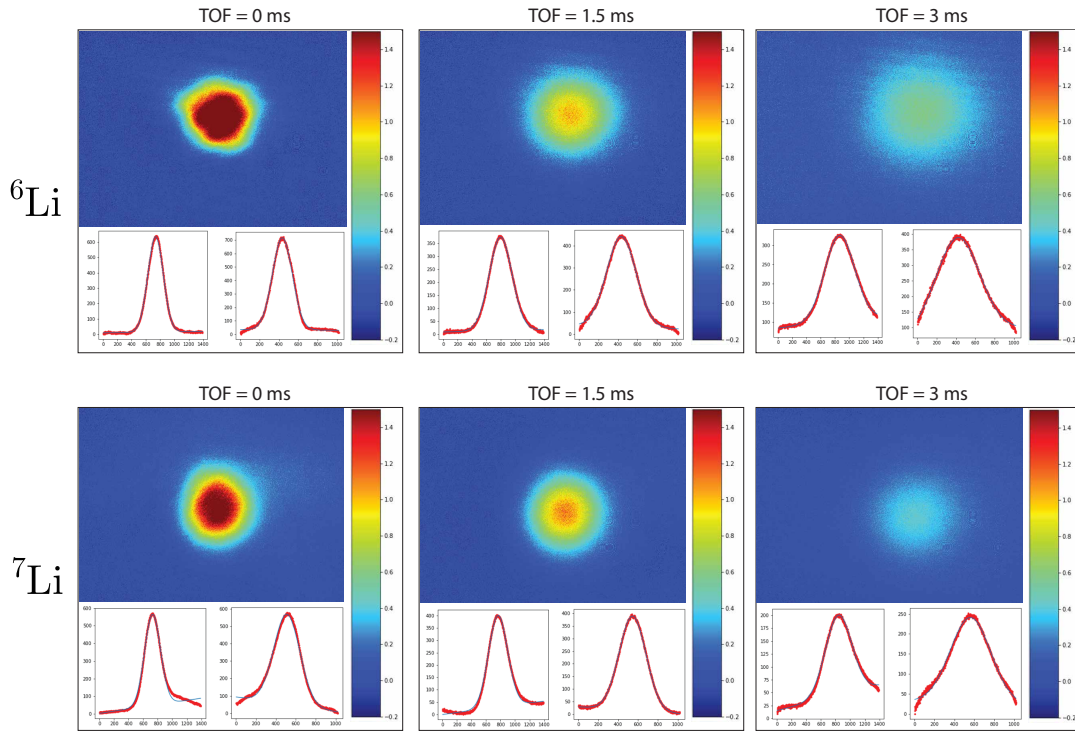


Figure 4.16: Optical density profile of ${}^6\text{Li}$ and ${}^7\text{Li}$ at different TOF in the optimized pulse sequence. These measurements are taken with the optimized pulse sequence described in figure 4.15 with a total D1 molasses time of 1.95 ms.

A typical temperature and atom number measurements of ${}^6\text{Li}$ and ${}^7\text{Li}$ in the optimized pulsed dual D1 molasses sequence is represented in figure 4.17 and 4.18 respectively. In figure 4.17a we observe the temperature of ${}^6\text{Li}$ is $\sim 103(14) \mu\text{K}$, with $\sim 5.0(5) \times 10^7$ atoms in the D1 molasses. For ${}^7\text{Li}$ we have approximately $\sim 4.2(5) \times 10^7$ atoms with an average temperature of $\sim 80(10) \mu\text{K}$ (see fig. 4.18a). These atom numbers are calculated with the correct Clebsch-Gordan factors in the absorption cross-section. From now on in the manuscript we use the best estimate of the atom number with the correction factor of 2 for ${}^6\text{Li}$ and 15/7 for ${}^7\text{Li}$ cross-sections (see the discussions in section 2.6.2).

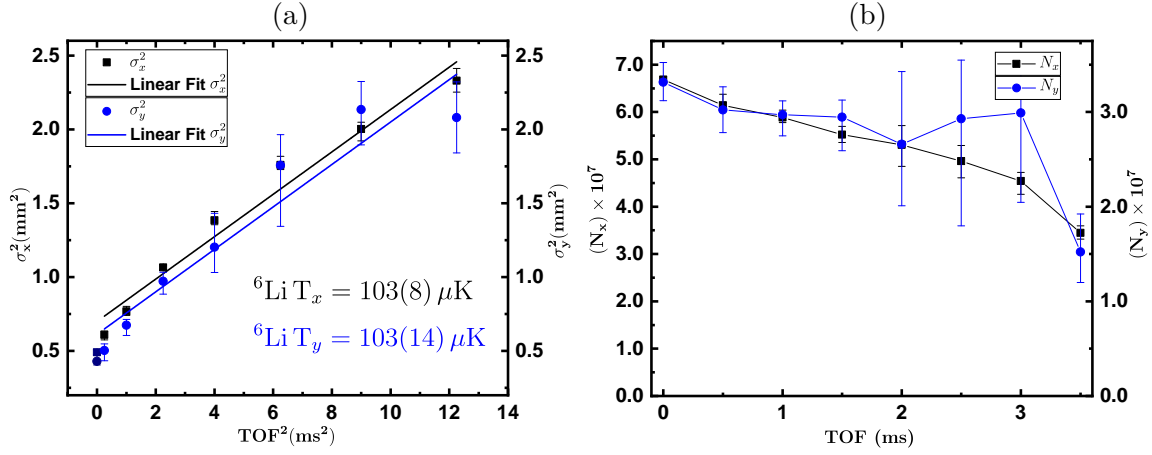


Figure 4.17: ${}^6\text{Li}$ temperature (a) and atom number (b) measurement in the optimized dual D1 molasses sequence of 13 pulses (1.95 ms).

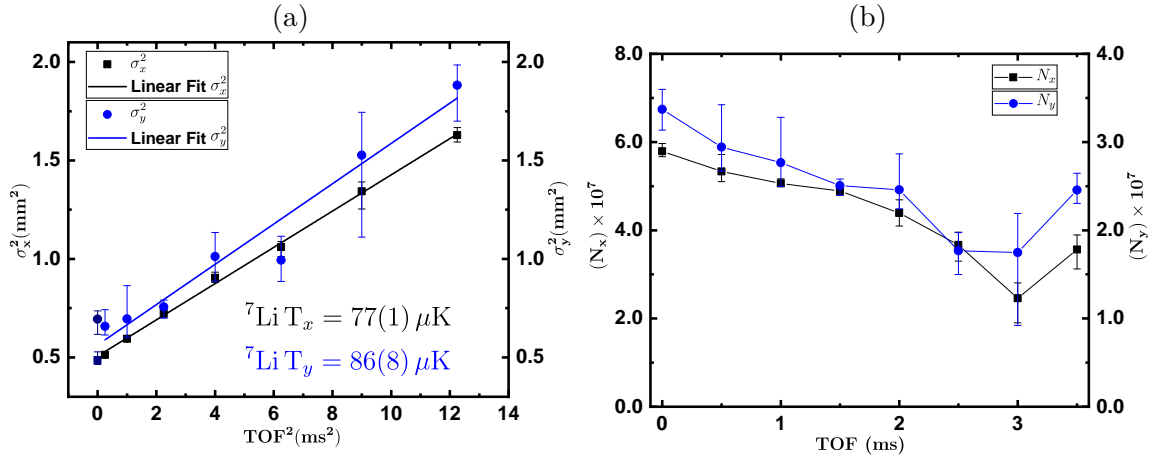


Figure 4.18: ${}^7\text{Li}$ temperature (a) and atom number (b) measurement in the optimized dual D1 molasses sequence of 13 pulses (1.95 ms).

Temperature measurements vs number of pulses are plotted in figure 4.19. The filled solid triangles represent the ${}^6\text{Li}$ temperature in the presence of ${}^7\text{Li}$ D1 beams. Compared to the previous cooling scheme, the temperature has improved from $160(69) \mu\text{K}$ to $103(10) \mu\text{K}$ in this optimized sequence. This temperature is only $18 \mu\text{K}$ above that of ${}^6\text{Li}$ without ${}^7\text{Li}$ D1 beams present. This excess temperature is due to off-resonant scattering of ${}^7\text{Li}$ D1 beams by the ${}^6\text{Li}$ atoms during the $50 \mu\text{s}$ time interval of a single pulse. The ${}^7\text{Li}$ temperature is $64(16) \mu\text{K}$ nearly identical to the temperature of $67(10) \mu\text{K}$ which was obtained by the $100\mu\text{s}+100\mu\text{s}$ pulse scheme.

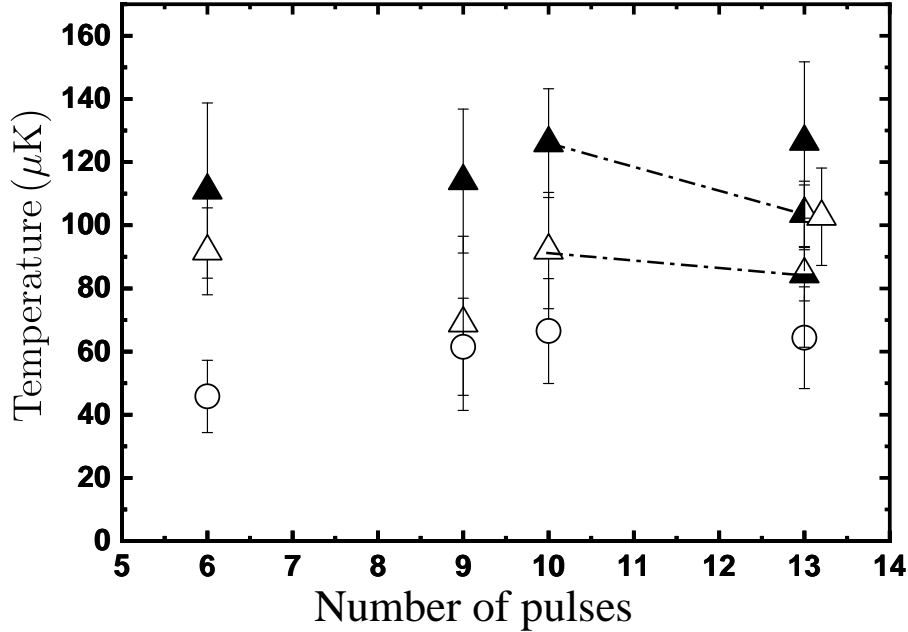


Figure 4.19: Optimized cooling sequence with $100 \mu\text{s}$ ${}^6\text{Li}$ and $50 \mu\text{s}$ ${}^7\text{Li}$ pulses, as shown in figure 4.15. Open triangles: ${}^6\text{Li}$ temperature in absence of ${}^7\text{Li}$ D1 beams with full intensity for all pulses. Filled triangles: ${}^6\text{Li}$ temperature in presence of ${}^7\text{Li}$ D1 beams with full intensity for all pulses. In the optimized sequence the last 3 pulses have half the intensity for both ${}^6\text{Li}$ and ${}^7\text{Li}$ D1 beams which is represented by the half-filled triangles at pulse 13 and the dashed lines. Open circles: ${}^7\text{Li}$ temperature in presence of ${}^6\text{Li}$ D1 beams with reduced intensity for the last 3 pulses. The error bars correspond to the statistical average of individual time-of-flight temperature measurements spread over several days of measurements. In this optimized cooling sequence the difference in temperature between ${}^6\text{Li}$ alone ($\sim 85(8) \mu\text{K}$) and ${}^6\text{Li}$ in presence of ${}^7\text{Li}$ D1 beams ($\sim 103(10) \mu\text{K}$) amounts to $\sim 18 \mu\text{K}$.

From the temperature measurement for $t_1 = t_2 = 100 \mu\text{s}$ pulse mode we calculated the Heating rate to be $\sim 0.4 \mu\text{K}/\mu\text{s}$. It is natural to assume the heating rate is proportional to the pulse duration and the intensity of the beam. Thus when we reduced the pulse length for ${}^7\text{Li}$ D1 beams to half in the optimized pulse sequence the heating is reduced $0.2 \mu\text{K}/\mu\text{s}$ and in the last 3 pulses since the intensity of beam is also reduced to one-half of the full intensity the heating rate becomes $0.1 \mu\text{K}/\mu\text{s}$. With the help of our model using the equation 4.5 we predict a temperature of $96 \mu\text{K}$ which is quite close to the measured temperature of $103(14) \mu\text{K}$. So the predicted value is in good agreement with the measured value and thus it supports the validity of our model which is summarized in the table 4.4.

	$t_1 = t_2 = 100 \mu\text{s}$	$t_1 = 100 \mu\text{s}, t_2 = 50 \mu\text{s}$
Temperature of ${}^6\text{Li}$ without ${}^7\text{Li}$ D1 beams (measured)	72(10) μK	85(8) μK
Temperature of ${}^6\text{Li}$ with ${}^7\text{Li}$ D1 beams (measured)	160(15) μK	103(14) μK
Heating rate ($\mu\text{K}/\mu\text{s}$)	0.4	0.2 (0.1 for last 3 pulses)
Temperature of ${}^6\text{Li}$ with ${}^7\text{Li}$ D1 beams (predicted)	-	96 μK

Table 4.4: The model described in section 4.4 predicts a temperature of $96\mu\text{K}$ for asymmetric pulse sequence, which is in good agreement with the measured value of $103(14) \mu\text{K}$.

4.8 Lifetime measurements

We have measured the D1 molasses lifetime of ${}^6\text{Li}$ and ${}^7\text{Li}$ individually and simultaneously in the optimized cooling sequence (fig. 4.15). In optical molasses atoms are not confined and experience a spatial Brownian motion within the volume defined by the intersection of the six laser beams. If the beam intensities are perfectly balanced the molasses cloud stays fixed in space and its radius expands in a diffusive manner as a square root of time. When atoms reach the edges of the laser beams they leave the molasses, creating atom losses. In case of beam intensity imbalance the molasses cloud drifts. Some atoms reach the edges of the beams earlier than in the intensity balanced case. Experimentally it is therefore particularly crucial to have large diameter molasses beams and well balanced local intensities. Here we use D1 beams with $1/e$ diameters of ~ 6 mm and the initial $1/e$ molasses diameter is ~ 1.5 mm. Light atoms like lithium have faster molasses dynamics compared to heavier alkalis like Rb or Cs.

The results are presented in figure 4.20. As noticed before during the first 2 ms some ${}^7\text{Li}$ atoms of the D2 molasses are detected while escaping the D1 molasses beams. Therefore we present two exponential fits for ${}^7\text{Li}$. In figure 4.20 (a), ${}^7\text{Li}$ alone, in red a single exponential fit with a time constant of $6.21(25)$ ms that shows systematic deviations at short and long times. In blue a single exponential fit starting at 3 ms molasses time, which provides much better agreement with the data and a life time of $8.26(77)$ ms.

The comparison of the plots 4.20 (a) and (c) shows that the ${}^7\text{Li}$ molasses lifetime is not affected by the presence of ${}^6\text{Li}$ D1 beams with $1/e$ decay time of $\sim 8.26(77)$ ms and $\sim 9.7(1.4)$ ms respectively in the absence or presence of ${}^6\text{Li}$ beams (blue curves). Turning our attention to ${}^6\text{Li}$ we observe that a single exponential fit represents the data well. The ${}^6\text{Li}$ molasses lifetime figure (b) and (d) shows a slight reduction from ~ 5.38 ms to ~ 4.07 ms in presence of ${}^7\text{Li}$ D1 beams. In summary these lifetimes are sufficient to efficiently load the ${}^6\text{Li}$ and ${}^7\text{Li}$ mixture into an optical dipole trap.

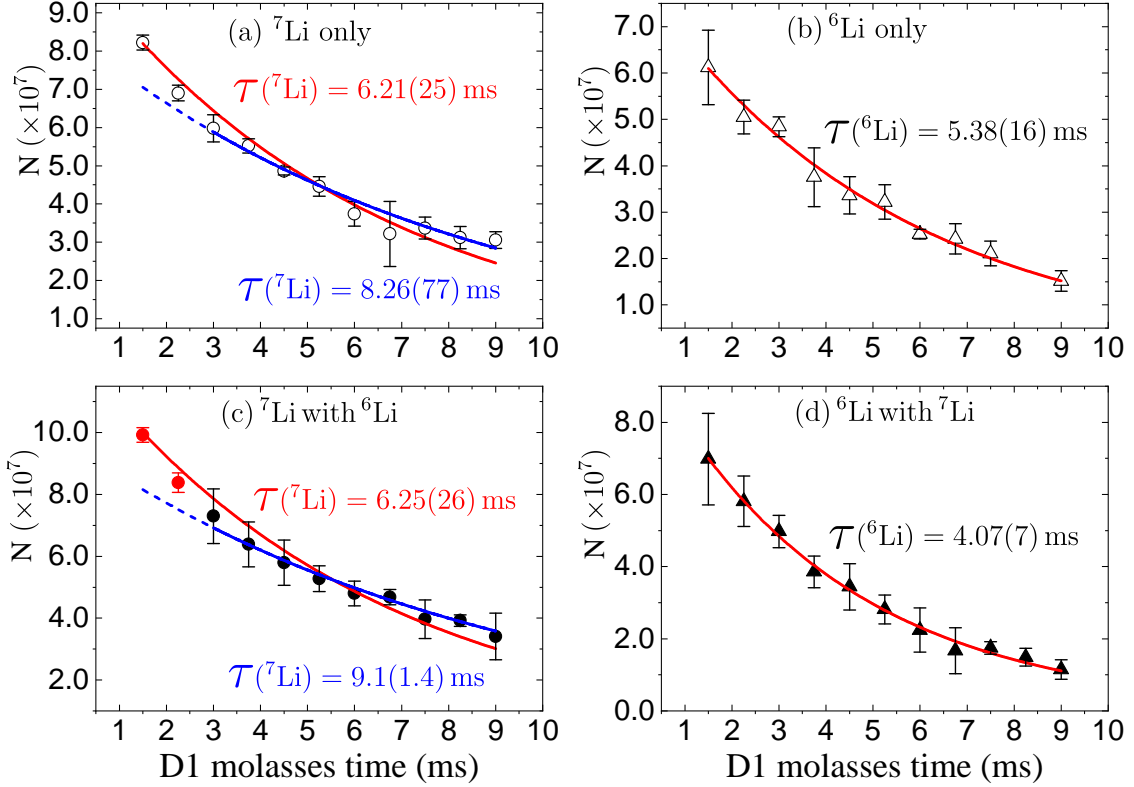


Figure 4.20: D1 molasses lifetime in the optimized pulse sequence of fig. 4.15 for single species (a) and (b) and dual species mode (c) and (d). In red single exponential fits for ${}^7\text{Li}$. In blue single exponential fits of the data removing the points at 1 and 2 ms. While the lifetime of ${}^7\text{Li}$ D1 molasses remains unchanged, the ${}^6\text{Li}$ molasses lifetime is slightly affected by ${}^7\text{Li}$ beams.

4.9 Molasses center of mass drift

During the D1 molasses phase we also observed a small drift of the center of mass of ${}^6\text{Li}$ and ${}^7\text{Li}$ clouds in the imaging plane. This drift velocity of the center of mass for ${}^6\text{Li}$ are $v_x^{drift} = 0.04$ m/s and $v_y^{drift} = -0.02$ m/s along x and y direction respectively. These drift velocities are small compared to ${}^6\text{Li}$ single photon recoil velocity and are $0.4 v_{recoil}$ and $-0.2 v_{recoil}$ respectively for x and y direction (see fig. 4.21a).

A similar drift is also observed for ${}^7\text{Li}$ (see fig. 4.21b) during the D1 molasses phase, with $v_x^{drift} = 0.08$ m/s and $v_y^{drift} = 0.06$ m/s corresponding to $0.93 v_{recoil}$ and $0.7 v_{recoil}$ respectively along x and y direction. These drifts are a result of residual intensity imbalance of the D1 beams along x and y directions for the respective isotopes.

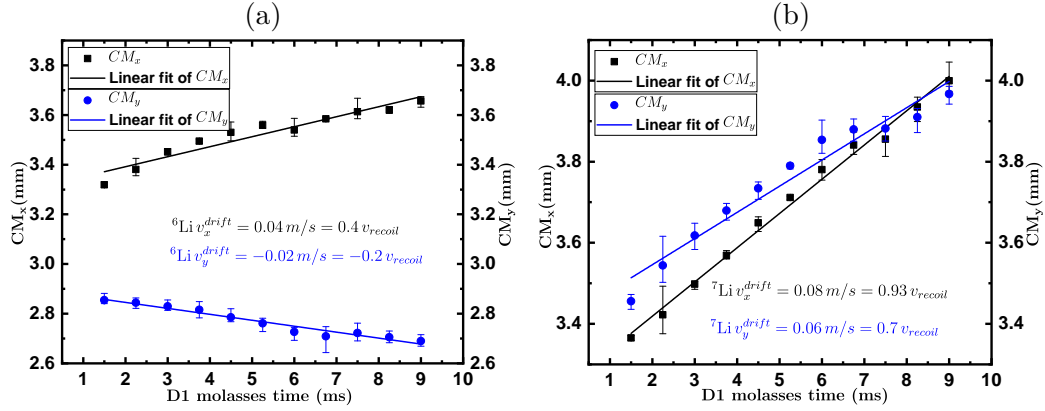


Figure 4.21: Center of mass drift of (a) ${}^6\text{Li}$ and (b) ${}^7\text{Li}$ atomic clouds during the pulsed dual D1 molasses. The position of center of mass of the clouds are measured at TOF=0.

4.10 TOF peak drift

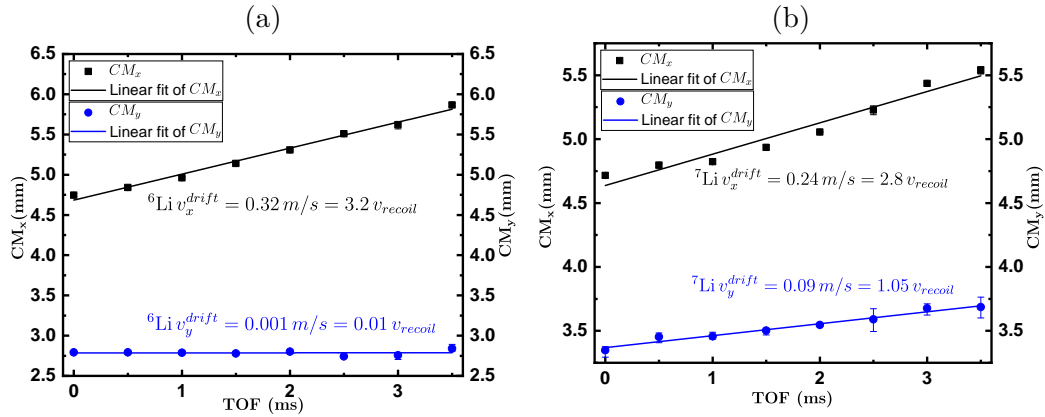


Figure 4.22: Center of mass drift of (a) ${}^6\text{Li}$ and (b) ${}^7\text{Li}$ during the time of flight after 1.9 ms of D1 molasses in the optimized pulsed dual D1 molasses sequence.

Apart from the drift of center of mass during the D1 molasses phase, we also observed a drift in the peak position of the atomic cloud density during the time of flight expansion. Figure 4.22 represent the peak position as a function of time of flight for both ${}^6\text{Li}$ and ${}^7\text{Li}$ isotopes. We observed a drift of $v_x^{drift} = 0.32 \text{ m/s} \sim 3.2 v_{recoil}$ and $v_y^{drift} = 0.001 \text{ m/s} \sim 0.01 v_{recoil}$ along x and y direction respectively for ${}^6\text{Li}$ and $v_x^{drift} = 0.24 \text{ m/s} \sim 2.8 v_{recoil}$ and $v_y^{drift} = 0.09 \text{ m/s} \sim 1.05 v_{recoil}$ along x and y direction respectively for ${}^7\text{Li}$. We note this drift velocity is larger than the molasses drift velocity as shown in figure 4.21. We have not been able to explain this difference.

4.11 Data Analysis method and error estimates

As described in section 2.6.2 the atom number in the atomic cloud along a specific axis can be calculated by integrating the optical density (OD) with the proper absorption cross-section as represented by equation 2.5. When the atoms are released from the trap or form the molasses the size of the cloud can be properly described as a Gaussian distribution along x and y axis. We sometime observe a tilted background on the images resulting from technical imperfections in the imaging. This makes it difficult to fit a perfect Gaussian function on the observed OD. Therefore we fit the data with a Gaussian and an adjustable tilted baseline as shown in fig 4.23 (a). This procedure leads to a systematic error on the area (atom number) and width (temperature) that we now estimate. We calculate the atom number and temperature by enforcing an horizontal baseline for the Gaussian fit to the left (or to the right) of the Gaussian peak as shown in fig. 4.23 (b) and (c).

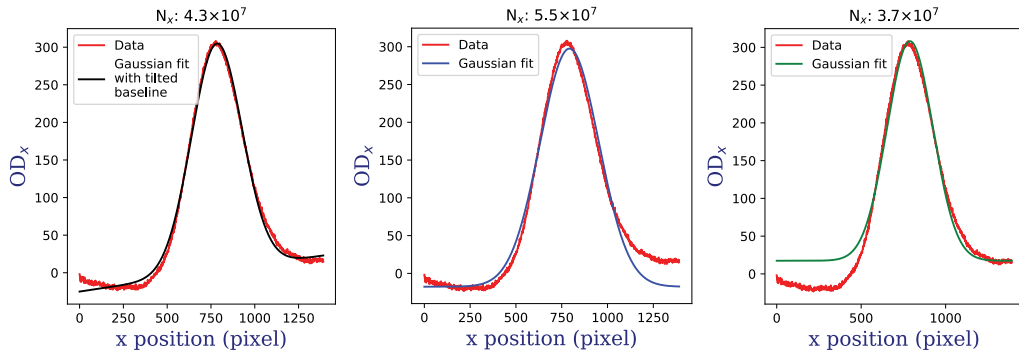


Figure 4.23: Summation of optical density (OD) along x direction as a function of pixel position is represented in red curves. (a) Gaussian fit of the data is represented in black curve with a tilted baseline, (b) Gaussian fit of the same data is represented in blue curve with the baseline of the fit enforced on the left of the peak, (c) Gaussian fit of the same data is represented in green curve with the baseline of the fit enforced on the right of the peak. The respective atom number for ${}^7\text{Li}$ with the resonant absorption cross-section of $\frac{15}{7} \frac{3\lambda^2}{2\pi}$ is presented on the top of each figure.

As an example in figure 4.23 for ${}^7\text{Li}$ atoms with $\text{TOF} = 2$ ms, we observe a tilt of 16% of the Gaussian peak maximum along the x direction. The corresponding atom number is 4.3×10^7 . With the left baseline we get an upper bound of 5.5×10^7 and with the right baseline a lower bound of 3.7×10^7 . We thus take these two extreme values as an estimate of the systematic error due to the tilt which corresponds to an uncertainty of $\sim 21\%$.

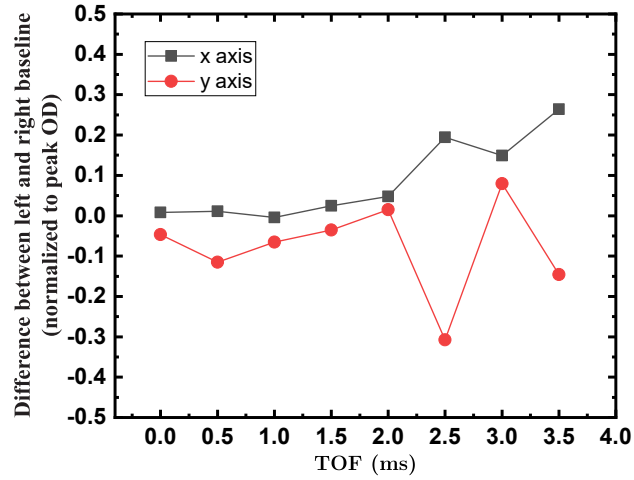


Figure 4.24: The difference between the right horizontal baseline fit and the left horizontal baseline fit as a function of time of flight. This difference is normalized by the OD peak. As the cloud expands for longer TOF's the difference between the left and right horizontal baselife fits increases and part of the absorption image of the atomic cloud falls outside the CCD chip of camera. This leads to systematic errors in estimating the width and area under the Gaussian fit.

We also see from figure 4.23 enforcing the baseline to the left or right of the Gaussian peak not only we make a possible error in the area under the curve but also we get a different width of the Gaussian fit which leads to different temperature measurements. As an example for ${}^6\text{Li}$ in figure 4.25 we observe that by enforcing the baseline to the left or right of the Gaussian peak we get different temperatures.

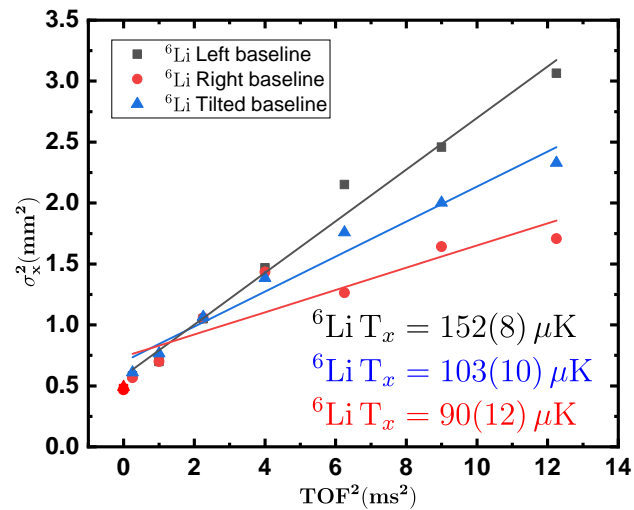


Figure 4.25: Different temperature measurements by enforcing the baseline to the left of the Gaussian peak (black), right of the Gaussian peak (red) and taking a tilted baseline (blue).

This procedure for the temperature determination leads to the upper and lower bound in the temperature which are presented below in table 4.5.

	Tilted baseline	Horizontal baseline to left	Horizontal baseline to right
⁶ Li	103(10) μ K	152(8) μ K	90(12) μ K
⁷ Li	77(1) μ K	117(10) μ K	64(6) μ K

Table 4.5: Temperature measurements corresponding to different baseline corrections in the Gaussian fits. These corrections lead to systematic errors on the temperature measurements. Numbers in parenthesis are the statistical errors in the fits.

As shown in table 4.5 the systematic error is much larger than the statistical error appearing in the table. We take the half of the difference between the temperature obtained by horizontal baseline to the left or to the right as an estimate of the systematic error for the tilted baseline fits used throughout this chapter. In summary the temperature in this data set is 103(10)(30) μ K for ⁶Li and 77(1)(25) μ K for ⁷Li where the first and second parenthesis refer to the statistical and systematic error estimates respectively. Similarly the atoms numbers are $\sim 5(1) \times 10^7$ and $\sim 4.2(9) \times 10^7$ for ⁶Li and ⁷Li respectively.

4.12 Improvements

After I stopped working on the machine to write my PhD manuscript, Dr. Tim de Jongh and Dr. Tarik Yefsah with Maxime Dixmieras continued to run the experiment. In addition to detecting the AOM frequency error which led us to operate ${}^7\text{Li}$ D1 cooling on the $|F_g = 2\rangle \rightarrow |F_e = 1\rangle$ transition, they have made improvements of the experimental setup. Below I present a few results obtained from their experiments. In particular, they have added additional degrees of freedom for optimizing the D1 beam alignments which resulted in significantly larger lifetime for both ${}^6\text{Li}$ and ${}^7\text{Li}$ D1 molasses as shown in figure 4.26.

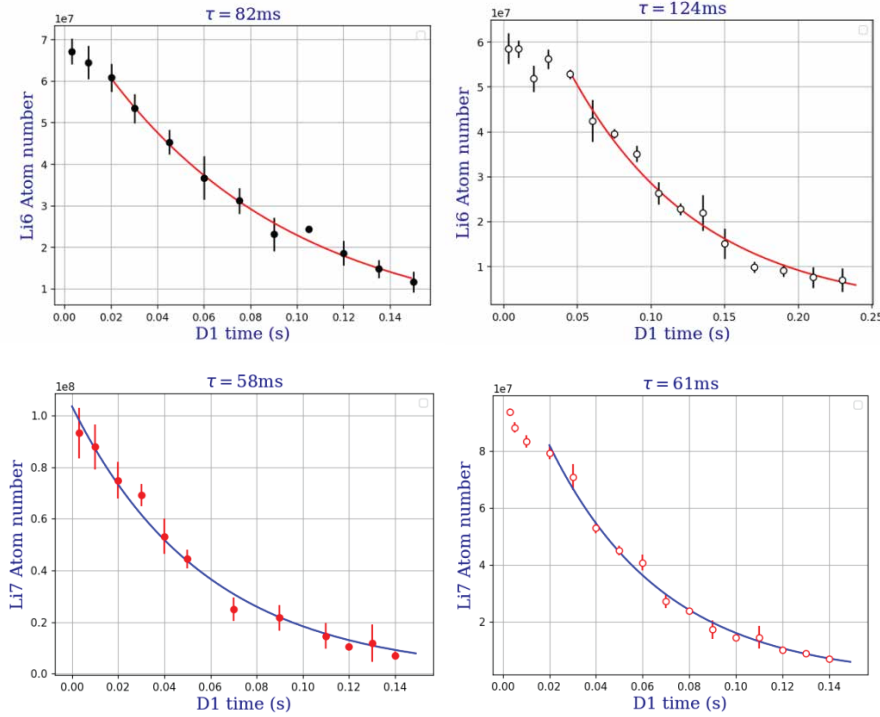


Figure 4.26: Lifetime of ${}^6\text{Li}$ (black) and ${}^7\text{Li}$ (red) D1 molasses after the optimization of D1 beams. The black solid circles represent the lifetime of ${}^6\text{Li}$ in the presence of ${}^7\text{Li}$ D1 beams and the open circles represent the ${}^6\text{Li}$ lifetime in the absence of ${}^7\text{Li}$ D1 beams. The red solid circles represent the lifetime of ${}^7\text{Li}$ in the presence of ${}^6\text{Li}$ D1 beams and the open circles represent the ${}^7\text{Li}$ lifetime in the absence of ${}^6\text{Li}$ D1 beams. The initial data points are a manifestation of atoms which are not leaking out of molasses and are excluded from the exponential decay fits.

It was also observed that the temperature of ${}^6\text{Li}$ D1 molasses strongly depends upon the ending of the pulse sequence (see figure 4.27). Ending the pulse sequence with ${}^7\text{Li}$ D1 pulse leads to heating in ${}^6\text{Li}$ atoms. The heating rate was measured to be $0.69 \mu\text{K}/\mu\text{s}$. This heating rate is consistent with our heating estimate of $0.78 \mu\text{K}/\mu\text{s}$ due to off-resonant photon scattering (see section 4.4). This heating can be minimized by ending the pulse sequence with ${}^6\text{Li}$ D1 molasses beams. Further

improvements in the temperature was also made possible by discretely decreasing the intensities of the last few pulses of the pulse sequence.

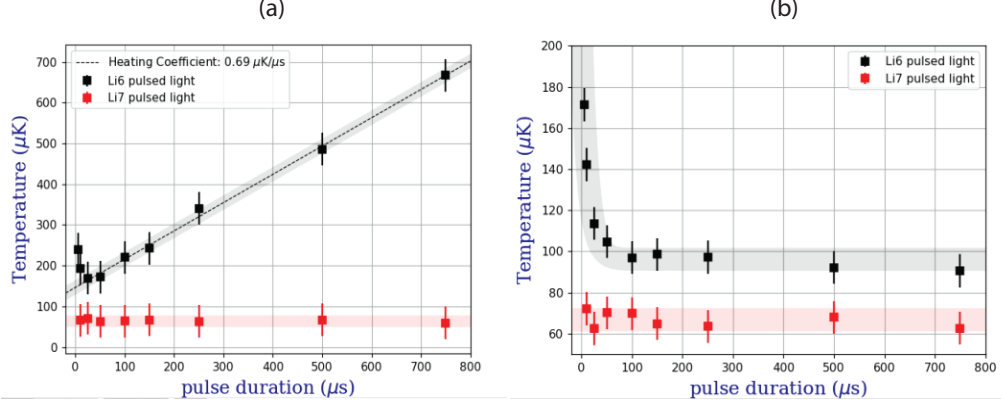


Figure 4.27: Temperature of ${}^6\text{Li}$ and ${}^7\text{Li}$ as function of pulse duration. The total D1 time is kept constant to $\sim 3 \text{ ms}$ and the duration of each pulse is varied. (a) The pulse sequence ends with a ${}^7\text{Li}$ D1 pulse. The temperature of ${}^7\text{Li}$ remains constant whereas we observe heating in ${}^6\text{Li}$ as we increase the pulse duration. The dotted line represents the linear fit for pulse duration $\geq 50 \mu\text{s}$. The corresponding heating rate is $\sim 0.69 \mu\text{K}/\mu\text{s}$ which is in fair agreement with the calculated heating rate of section 4.7.1. (b) The pulse sequence ends with a ${}^6\text{Li}$ D1 pulse. The temperature of ${}^7\text{Li}$ remains unaffected and, as we increase the last pulse duration, the ${}^6\text{Li}$ temperature quickly drops to a steady state.

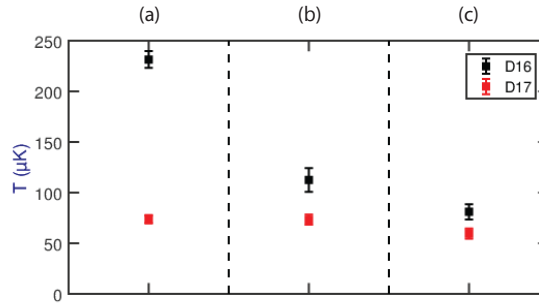


Figure 4.28: Temperature ${}^6\text{Li}$ and ${}^7\text{Li}$ obtained by different cooling strategies. (a) Pulse scheme ending with ${}^7\text{Li}$ D1 beam. (b) Pulse scheme ending with ${}^6\text{Li}$ D1 beam. (c) Pulse scheme ending with ${}^6\text{Li}$ D1 beam with a discrete intensity ramp.

A summary of temperature obtained by various pulse sequence is represented in figure 4.28. This data shows it is better to end the sequence with a ${}^6\text{Li}$ pulse.

Tarik Yefsah and his team also investigated D1 cooling on the ${}^7\text{Li}$ $|F = 2\rangle \rightarrow |F' = 2\rangle$ together with ${}^6\text{Li}$ $|F = 3/2\rangle \rightarrow |F' = 3/2\rangle$ transition and found that temperatures comparable to the one reported in this chapter are reached without pulsing. The results obtained on both transitions with or without pulsing are reported in a publication in Phys Rev A [106].

Summary of Chapter 4

In this chapter we have achieved simultaneous D1 gray molasses cooling of ${}^6\text{Li}$ and ${}^7\text{Li}$. We have operated the ${}^7\text{Li}$ molasses on the transition $|F = 2\rangle \rightarrow |F' = 1\rangle$. We have shown that the close proximity of ${}^7\text{Li}$ D1 beams to the D2 optical transition for ${}^6\text{Li}$ is detrimental for ${}^6\text{Li}$ D1 gray molasses cooling. We have developed a pulsed cooling sequence to circumvent the above mentioned problem. We have observed that after a few D1 molasses pulses the temperature of the atoms quickly drops from ~ 1 mK to ~ 100 μK .

After the optimization of the D1 pulse sequence we were finally able to achieve a temperature of $\sim 103(30)$ μK with $\sim 5(1) \times 10^7$ atoms for ${}^6\text{Li}$ and $\sim 77(25)$ μK with $\sim 4.2(9) \times 10^7$ atoms for ${}^7\text{Li}$. The uncertainties are conservatively taken with horizontal baseline fits.

One important parameter in cold atom experiments is the phase-space density (PSD) and is given by:

$$PSD = n_{peak} \lambda_{dB}^3$$

$$n = \frac{N}{(2\pi)^{3/2} \sigma_x \sigma_y \sigma_z} \quad (4.6)$$

Here n_{peak} is called the peak atomic density of the cloud, N is the total number of captured atoms in D1 molasses, $\sigma_{x,y,z}$ are the half-widths of gaussian fit at $1/e^2$ value of the maximum for the respective OD profiles along x,y and z directions. We expect the D1 molasses to be symmetric along x,y and z direction thus it is reasonable to assume $\sigma_z = (\sigma_x + \sigma_y)/2$. In equation 4.6 λ_{dB} is the thermal de Broglie wavelength and is given by $\lambda_{dB} = h/\sqrt{2\pi mk_B T}$, h is the Plank's constant, m is the mass of the atoms, k_B is the Boltzmann's constant and T is the temperature of the cloud. The simultaneous gray molasses cooling of ${}^6\text{Li}$ and ${}^7\text{Li}$ improves the PSD by one order of magnitude for both ${}^6\text{Li}$ and ${}^7\text{Li}$ and is given in table 4.6. These values are comparable to previously reported ones[99], [101].

	D2	D1
${}^6\text{Li}$	$\sim 2.5 \times 10^{-7}$	$\sim 2.5 \times 10^{-6}$
${}^7\text{Li}$	$\sim 1 \times 10^{-7}$	$\sim 2.5 \times 10^{-6}$

Table 4.6: Gain in PSD from D2 to D1 molasses.

Chapter 5

Perspectives

In this chapter we first show how the D1 cooling of Lithium isotopes can be used to efficiently load a high power optical dipole trap. And finally we give a few perspectives for utilization of ultracold ^6Li and ^7Li isotopes.

Loading of Dipole trap for evaporative cooling

After the sub-Doppler cooling phase the next step towards BEC or superfluid Fermi gases is to achieve evaporative cooling. In order to have an efficient evaporation we need to load the atoms into a trap with sufficient collision rate and where we can manipulate the trap depth to allow the atoms with highest energy to escape the trap resulting in evaporative cooling.

In this section we will focus on optical dipole traps (ODT) which enables to trap atoms regardless of their internal states. The intensity profile for a Gaussian laser beam in the position space is given by:

$$I(r, z) = \frac{2P}{\pi w_0^2(1 + z^2/z_R^2)} \exp\left[-\frac{2r^2}{w_0^2(1 + z^2/z_R^2)}\right] \quad (5.1)$$

where the distance from the center of the beam is represented by (r, z) in cylindrical coordinate system. w_0 is called the beam waist. $z_R = \pi w_0^2/\lambda$ is the Rayleigh length of the beam corresponding to the given wavelength (λ) and a beam waist (w_0) for the ODT beam.

The optical dipole trap operates with a far detuned wavelength. If the difference between the frequency of the laser ω and the atomic transition ω_0 , given by $\Delta = \omega - \omega_0$, is large compared to Γ , the electron motion can be treated as a classical oscillator and the dipole potential acting on the atom is given by[98]:

$$U_{dip}(\mathbf{r}) = -\frac{3\pi c^2}{2\omega_0^3} \left(\frac{\Gamma}{\omega_0 - \omega} + \frac{\Gamma}{\omega_0 + \omega} \right) I(\mathbf{r}) \quad (5.2)$$

where Γ is the linewidth of the given atomic transition, $I(\mathbf{r})$ is the intensity of the laser beam and c is the speed of light. Now in the limit of $\Delta \ll \omega_0$ we can use the Rotating wave approximation and neglect the second term of the expression 5.2 which results as:

$$U_{dip}(\mathbf{r}) = \frac{3\pi c^2 \Gamma}{2\omega_0^3 \Delta} I(\mathbf{r}) \quad (5.3)$$

We use a high power laser at $\lambda = 1064$ nm resulting $\Delta = 0.3 \omega_0$. In this case we can no longer use the Rotating wave approximation and the the second term will contribute in equation 5.2 will also contribute in the dipole potential. From equation 5.3 we find the optical dipole potential U_{dip} is proportional to the intensity of the laser. Using equation 5.1 the depth of the dipole trap (at $r = 0, z = 0$) is given by:

$$U_{dip}(r, z) = \frac{3\pi c^2 \Gamma}{2\omega_0^3 \Delta} \frac{2P}{\pi w_0^2 (1 + z^2/z_R^2)} \exp\left[-\frac{2r^2}{w_0^2 (1 + z^2/z_R^2)}\right] \quad (5.4)$$

This potential behaves as a harmonic potential close to the bottom of the trap. Efficient loading of the atoms into the dipole trap depends on the depth of the ODT and the volume overlap between the dipole trap and the D1 molasses. The depth of ODT will impose a cut in the momentum distribution of the captured cloud.

Let's take an example and estimate the capture efficiency of the ODT. For a D1 cloud at a temperature $T = 100 \mu\text{K}$ it is reasonable to take a trap depth (U_0) of 4 - 5 $k_B T$ to ensure good loading in momentum space.

The atoms with mass m which are cooled to a temperature T follows the Maxwell-Boltzmann distribution given by:

$$f(\vec{r}, \vec{p}) = A e^{-\beta(\frac{p^2}{2m} + \frac{m\omega^2}{2} r^2)} \quad (5.5)$$

where A is a constant, $\beta = 1/k_B T$ and k_B is the Boltzmann's constant. $p^2/2m$ is the kinetic energy of the atoms and $m\omega^2 r^2/2$ is the potential energy of the atom. Now we define scaling factors as given below:

$$\sqrt{\frac{k_B T}{m\omega^2}} = \Delta R, \quad (5.6)$$

$$\sqrt{mk_B T} = \Delta P \quad (5.7)$$

with the above scaling factors the equation 5.5 becomes:

$$\begin{aligned} f(\vec{r}, \vec{p}) &= A e^{-\left(\frac{p^2}{2(\Delta P)^2} + \frac{r^2}{2(\Delta R)^2}\right)} \\ &= A e^{-\left(\frac{p^2}{2} + \frac{r^2}{2}\right)} \quad (\text{in normalized units}) \end{aligned} \quad (5.8)$$

With the above expression one can find the total number of atoms by integrating the distribution function $f(\vec{r}, \vec{p})$. Thus the total atom number is given by:

$$\begin{aligned} N &= \int d^3r d^3p f(\vec{r}, \vec{p}) \\ &= \int d^3r d^3p A e^{-(\frac{p^2}{2} + \frac{r^2}{2})} \end{aligned} \quad (5.9)$$

Now let's define the depth of the ODT as U_0 with:

$$U_0 = \frac{U_{dip}(r=0, z=0)}{k_B T} \quad (5.10)$$

With the above scaling factors the dipole trap potential can be expressed as:

$$U = U_0 e^{-\frac{\rho^2}{\sigma^2}} \quad (5.11)$$

where $\rho^2 = x^2 + y^2$ is expressed in cylindrical coordinate and $\sigma = w_0/\Delta R$. The number of atoms captured in this optical trap is then given by:

$$N_c = \int d^3r \int_{\frac{p^2}{2m} < U(\rho)} d^3p A e^{-(\frac{p^2}{2} + \frac{r^2}{2})} \quad (5.12)$$

The captured efficiency thus can be defined as $\eta = N_c/N$ which is given by:

$$\eta = \frac{N_c}{N} = \frac{\int d^3r \int_{\frac{p^2}{2m} < U(\rho)} d^3p A e^{-(\frac{p^2}{2} + \frac{r^2}{2})}}{\int d^3r \int d^3p A e^{-(\frac{p^2}{2} + \frac{r^2}{2})}} \quad (5.13)$$

Due to the cylindrical symmetry of the optical trap potential, it is natural to perform this integration in cylindrical coordinate as given below:

$$\eta = \frac{\int d^2\rho e^{-\rho^2/2} \int_{\frac{p^2}{2m} < U(\rho)} d^3p e^{-p^2/2}}{\int d^2\rho e^{-\rho^2/2} \int d^3p e^{-p^2/2}} \quad (5.14)$$

The integral of the denominator in equation 5.14 can be easily evaluated and it is $(\sqrt{2\pi})^5$. In the numerator we first evaluate $\int_{\frac{p^2}{2m} < U(\rho)} d^3p e^{-p^2/2}$. Using the cylindrical symmetry and normalizing with respect to the mass of the atoms ($m = 1$) we can write this integral as

$$\int_{\frac{p^2}{2} < U(\rho)} 4\pi p^2 e^{-p^2/2} dp \quad (5.15)$$

We define a variable t such that:

$$t = \frac{p^2}{2}, \quad t < U(\rho) \quad (5.16)$$

$$dt = pdp \quad (5.17)$$

substituting t in equation 5.15 we get,

$$4\pi\sqrt{2} \int_0^{U(\rho)} \sqrt{t} e^{-t} dt \quad (5.18)$$

The integral in equation 5.18 is

$$\int_0^{U(\rho)} \sqrt{t} e^{-t} dt = \frac{\sqrt{\pi}}{2} - \Gamma(3/2, U(\rho)) \quad (5.19)$$

Thus equation 5.14 simplifies as:

$$\eta = \frac{4\pi\sqrt{2} \int d^2\rho \left(\frac{\sqrt{\pi}}{2} - \Gamma(3/2, U(\rho)) \right) e^{-\rho^2/2}}{(2\pi)^{5/2}} \quad (5.20)$$

Using radial symmetry $\int d^2\rho$ can be written as $\int 2\pi\rho d\rho$. Thus

$$\eta = \frac{2}{\sqrt{\pi}} \int \rho d\rho \left(\frac{\sqrt{\pi}}{2} - \Gamma(3/2, U(\rho)) \right) e^{-\rho^2/2} \quad (5.21)$$

We define a variable u such that

$$u = \frac{\rho^2}{2}, \quad (5.22)$$

$$du = \rho d\rho \quad (5.23)$$

substituting u in equation 5.21 we get

$$\eta = \frac{2}{\sqrt{\pi}} \int_0^\infty du e^{-u} \left(\frac{\sqrt{\pi}}{2} - \Gamma(3/2, U(\rho)) \right) \quad (5.24)$$

$$= \frac{2}{\sqrt{\pi}} \int_0^\infty du e^{-u} \left(\frac{\sqrt{\pi}}{2} - \Gamma\left(\frac{3}{2}, U_0 e^{-\frac{2u}{\sigma^2}}\right) \right) \quad (5.25)$$

Now for an ODT with a depth of $5 k_B T$, $U_0 = 5$ and a waist of $w_0 = 100 \mu\text{m}$, $\sigma = 0.136$ the capture efficiency from equation 5.25 is $\sim 1.4\%$ for ${}^6\text{Li}$ and $\sim 1.6\%$ for ${}^7\text{Li}$.

Today we find lasers with sufficiently low amplitude and frequency noise suitable for atom trapping with power exceeding 200 W at a wavelength $\lambda = 1064 \text{ nm}$ [146]. With this laser wavelength, the available power and the desired trap depth the desired waist of the trapping beam is calculated to be $\sim 100 \mu\text{m}$. This beam waist is small compared to the D1 molasses size ($700 \mu\text{m} - 800 \mu\text{m}$). With this beam waist and the corresponding Rayleigh length (29.52 mm) we expect from formula 5.25 to load 1.4% ($\sim 7 \times 10^5$ atoms) of the ${}^6\text{Li}$ D1 molasses, and 1.6% ($\sim 7 \times 10^5$ atoms) of the ${}^7\text{Li}$ D1 molasses. In this calculation we assume no active cooling during the capture phase of the atoms in the ODT. We note that D1 cooling of ${}^6\text{Li}$

has also been shown to be efficient in a far detuned optical dipole trap by [101]. Therefore the above capture efficiency numbers are probably lower bounds.

At the bottom of this dipole potential (equation 5.4) the atoms experience a quasi-harmonic potential, and thus when we expand the above exponential as a Taylor series around $r = 0, z = 0$, we get the frequency of the trap along the radial (ω_r) and axial (ω_z) direction as:

$$\omega_r = \sqrt{\frac{4U_0}{mw_0^2}} \quad (5.26)$$

and

$$\omega_z = \sqrt{\frac{2U_0}{mz_R^2}} \quad (5.27)$$

where U_0 is the minimum of the dipole potential given in the equation 5.4, m is the mass of the atoms, w_0 and z_R are the beam waist and the Rayleigh range for the corresponding dipole trap. For the above mentioned dipole trap with 200 W power and a beam waist of $w_0 = 100 \mu\text{m}$ the trapping frequencies along radial (ω_r) and axial (ω_z) directions are $2\pi \times 3.26 \text{ kHz}$ and $2\pi \times 7.82 \text{ Hz}$ for ${}^6\text{Li}$ and $2\pi \times 3.02 \text{ kHz}$ and $2\pi \times 7.24 \text{ Hz}$ for ${}^7\text{Li}$.

The efficiency of the evaporation cooling depends on the collision rate Γ_{coll} of the atoms in the dipole trap. In order to have an efficient evaporation the collision rate should be as high as possible. We now take an example, where ${}^6\text{Li}$ are prepared in equal amounts in $|F = 1/2, m_F = 1/2\rangle$ and $|F = 1/2, m_F = -1/2\rangle$ Zeeman states in a magnetic field of 832 G corresponding to the peak of a Feshbach resonance where the collision rate is unitary. We also take ${}^7\text{Li}$ prepared in state $|F = 1, m_F = 0\rangle$ which displays two Feshbach resonances at 845.5 G and 894 G as shown in figure 5.1. For atoms having a peak density n_{peak} , scattering cross-section σ and the r.m.s thermal velocity $v_{r.m.s} = \sqrt{8k_B T / \pi m}$, the collision rate can be expressed as[147]:

$$\Gamma_{coll} = \frac{n_{peak} \sigma v_{r.m.s}}{2} \quad (5.28)$$

For an identical Bose gas $\sigma = 8\pi a^2$ where a is the scattering length, typically 80 Bohr for ${}^7\text{Li}$. For a gas in two spin states $\sigma = 4\pi a^2$, but for an unitary gas $|a| \rightarrow \infty$ and the scattering length between the two fermions can be replaced by the de Broglie wavelength $a \sim \lambda_{dB}$. Thus for a temperature T the collision rate for fermions at unitarity in equation 5.28 can be expressed as[148]:

$$\Gamma_{coll} = \frac{(2\pi)^{3/2} N \hbar^2 \bar{\omega}^3}{16(k_B T)^2} \quad (5.29)$$

where $\bar{\omega} = (\omega_{radial}^2 \times \omega_{axial})^{1/3}$ is the geometric mean trapping frequency and N is the number of atoms in the optical dipole trap in spin up (\uparrow) or down (\downarrow) state.

Now using the above two equation and the atom number and trapping frequencies which are given above we have estimated the collision rate for ${}^6\text{Li}$, ${}^7\text{Li}$ and a mixture of ${}^6\text{Li}+{}^7\text{Li}$ at 832 G (red spot in figure 5.1), which is summarized below in table 5.1.

Atomic species	Scattering length	Single ODT Γ_{coll} (s^{-1})	Crossed ODT Γ_{coll} (s^{-1})	Hybrid trap Γ_{coll} (s^{-1})
${}^6\text{Li}$	λ_{dB}	~ 60	~ 10500	~ 195
${}^7\text{Li}$	$80 a_0$	~ 4	~ 970	~ 17
${}^6\text{Li}+{}^7\text{Li}$	$40.8 a_0$	~ 1.3	~ 270	~ 5

Table 5.1: Initial collision rate for Lithium isotopes at $T = 100 \mu\text{K}$ in a $100 \mu\text{m}$ waist single beam dipole trap and in a crossed dipole trap with identical waists. This collision rate is calculated near unitarity for ${}^6\text{Li}$ at 832 G. Scattering length is shown in the unit of Bohr radius a_0 . The hybrid trap is described in Annex B

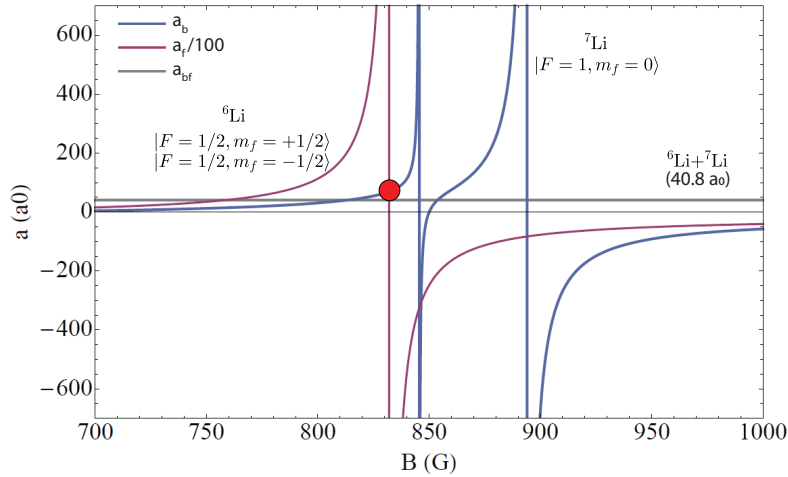


Figure 5.1: Scattering length for ${}^6\text{Li}$ (red), ${}^7\text{Li}$ (blue) and ${}^6\text{Li}+{}^7\text{Li}$ (grey) as a function of magnetic field. The ${}^6\text{Li}$ is prepared in state $|1_f\rangle$ and $|2_f\rangle$ which connects to $|F = 1/2, m_F = 1/2\rangle$ and $|F = 1/2, m_F = -1/2\rangle$ Zeeman states respectively at low magnetic field. The ${}^7\text{Li}$ is prepared in state $|2_b\rangle$ which connects to $|F = 1, m_F = 0\rangle$ at low field. Please note the scattering length of ${}^6\text{Li}$ is in $(1/100)$ scale. We observe a resonance at 832.18 G (red dot) for ${}^6\text{Li}$. For ${}^7\text{Li}$ we observe two resonance at 845.5 G and 894 G. The scattering length between ${}^6\text{Li}$ and ${}^7\text{Li}$ does not vary in this magnetic field range and is equal to $40.8 a_0$ [111].

With the initial collision rate given in table 5.1 the evaporation can start with the single beam ODT but during the evaporation phase when we lower the intensity of the ODT the axial frequency becomes small and so does the collision rate. Therefore it is highly preferable to use a crossed dipole trap geometry. For

instance with a crossed dipole trap of $\sim 100 \mu\text{m}$ waist, our trapping frequencies along both radial and axial directions improve to $\sim 2\pi \times 4.6 \text{ kHz}$ for ${}^6\text{Li}$ and $\sim 2\pi \times 4.2 \text{ kHz}$ for ${}^7\text{Li}$, the loading efficiency becomes $\sim 0.30\%$ (1.5×10^5) atoms for ${}^6\text{Li}$ and $\sim 0.33\%$ (1.4×10^5) atoms for ${}^7\text{Li}$, and the collision rate improves significantly with the use of a crossed dipole trap as indicated in table 5.1.

We have given here the estimates for the initial collision rates in two simple geometries (single or crossed dipole trap). These rates indicate that evaporation should be very efficient. However a full theoretical model of evaporation is beyond the scope of this chapter. When performing evaporation at unitarity for ${}^6\text{Li}$, atoms cool rapidly and ${}^7\text{Li}$ atoms cool sympathetically by collisions with the unitary Fermi gas. Based on this collision rate and previous results reported in [65] it should be possible to produce a ${}^6\text{Li}$ Fermi superfluid with $\sim 2 \times 10^4$ atoms mixed with a ${}^7\text{Li}$ BEC with a similar atom number.

As a final remark, it is worthwhile to note that for a constant scattering length, evaporation in ODT leads to a decrease in collision rate when the trap depth is reduced as $\Gamma_{coll} \propto U_0^{1/2}$. On the contrary for a unitary Fermi gas $\sigma \propto \lambda_{dB}^2$ and thus the collision rate does increase as $\Gamma_{coll} \propto U_0^{-1/2}$ when the trap depth is reduced.

Further directions

As a conclusion of this thesis we have shown that dual species gray molasses are very useful for improving the PSD of Lithium isotope mixtures. The pulsed D1 cooling method that we have presented in this thesis can also find its application in mixtures of other species where light-induced losses limit the MOT density and temperature. As discussed above an immediate perspective is to perform evaporative cooling in a crossed optical dipole trap in order to produce samples in the superfluid regime. The further decrease of temperature by 2-3 orders of magnitude below the gray molasses temperature may also find interesting applications in atom interferometry [149], [150], measurement of h/m and of the fine structure constant α [151]. The light mass of Lithium and high recoil energy is very favourable for such an experiment. And finally, a test of the Einstein's equivalence principle with Lithium isotopes is an appealing direction of research.

This page intentionally left blank

Appendix A

Oven operation and unclogging procedure

The oven has 3 heating coils. One along the body, one wrapped around the collimation tube and one on the top flange of the oven (see figure 2.2 (a)). In normal operation we use only 2 heating coils the one on the body and the the one wrapped on the collimation tube. Depending on how much current we provide on each of the heating coil different parts of the oven are heated to different temperatures. For a normal operation the bottom of the oven is kept at around $\sim 450^\circ$ C and the corresponding temperatures at different part of the oven is shown in the figure 2.3. This differential heating leads to a temperature gradient along different parts of the oven. This gradient should be such that the Lithium liquid deposited on the collimation tube is recycled by capillary action towards the oven reservoir. This minimizes the lithium consumption and prevents oven clogging. The surface tension of liquid lithium decreases with temperature which allows the liquid lithium to flow from cold to hot surfaces. Thus it is very important to keep a consistent temperature gradient along the collimation tube. In addition the stainless steel mesh inside the collimation tube (see figure 2.2 (b)) enhances this capillary action of liquid lithium and helps in the recycling process.

Failure in maintaining proper temperature gradient at different parts of the oven (specially inside the collimation tube) leads to disruption of the recycling process of Lithium inside the oven. If this disruption is persistent then this leads to deposition of lithium along the side walls of the collimation tube. As a result the effective diameter of the collimation tube is reduced and this leads to low flux in the atomic beam. We should be very careful about this side wall deposition. If this deposition continues to grow we will eventually clog the collimation tube and then there will not be an atomic beam to begin with.

There have been several instances during my PhD when the collimation tube of the oven got clogged¹. In such scenarios we have empirically developed a method to remove the clog from the collimation tube which I present below.

The clogs happen in the collimation tube from time to time, mostly due to irregular heating and different temperature gradients. Fortunately with the 3 heating coils we can manipulate the temperature gradients along different parts of the oven. In order to remove the clog we need to heat the coils in a rather unnatural way to obtain required temperature inside the collimation tube to melt the lithium deposit. We have to be careful in maintaining the temperature gradient because a wrong gradient might lead to formation of another clog in the collimation tube at a different position. Unfortunately we cannot predict the exact spot of clog in the collimation tube, so we have to heat the tube empirically.

We heat the coils slowly so that the temperature does not rapidly increase and cause damage to the nickel gasket attached to each of the flanges. The slow heating procedure also ensures the current in the Ion pump does not suddenly exceed its critical value (30mA). We usually heat up the collimation tube to $\sim 700^\circ\text{C}$ while maintaining the bottom of the reservoir to $\sim 400^\circ\text{C}$. It usually takes 4-5 hours to unclog the collimation tube depending on the clog(s) position, and size of the clog.

We usually look for a sudden change of pressure in the attached ion pump² while observing the fluorescence of the lithium gas in the view port. In case of unclogging we can clearly see a sudden increase of flux through the view port. In order to observe the fluorescence it is advised to scan the master laser (7P) around the locking point. In this method if the slave lasers are properly injected and if we have some atomic beam we would see fluorescence emitted from different positions along the atomic beam direction because of the beam divergence and the Doppler effect. In addition we monitor the fluorescence signal of the MOT³. A sudden jump in fluorescence signal indicates a successful unclogging procedure.

There could also be multiple clogs in the collimation tube. Some times when we remove one clog we see a burst of fluorescence which quickly dissipates. The lithium we observe in this case is a result of partial melting of the one clog while the collimation tube is still clogged.

¹ mostly due to malfunction in the temperature sensors which destroyed the temperature gradient in the collimation tube

² we monitor the current of the ion pump which is proportional to the pressure

³ in this case the MOT lasers should be properly locked to the respective MOT transitions

Appendix B

Hybrid trap

In order to maintain a sufficient axial frequency for the optical dipole trap along the trap axis, an elegant solution is to create a magnetic curvature along this axis, realizing an hybrid optical/ magnetic trap. One way to do it is to use the MOT coils which are away from the Helmholtz configuration and therefore produce a weak curvature near $z = 0$. The advantage of such a trap is that the axial frequency is of magnetic origin, thus it is very smooth and free of optical dipole trap potential defects. Since the radial confinement is given by the ODT, it easily compensates for the expulsion forces of the curvature coils in the radial directions.

We are interested in trapping the states $|1\rangle$ and $|2\rangle$ as they show an useful Feshbach resonance around 832 G. These states are high field seeking states around 832 G and thus we need a magnetic maximum to trap these atoms in the ODT direction (z axis) where the ODT confinement is weak.

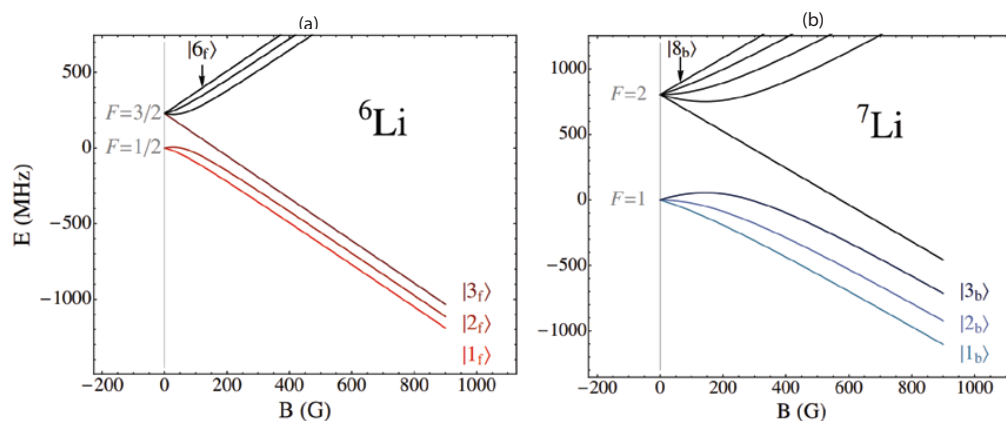


Figure B.1: Energy levels as a function of the magnetic field for the hyperfine ground states of ${}^6\text{Li}$ and ${}^7\text{Li}$. States $|1_f\rangle, |2_f\rangle, |3_f\rangle$ of ${}^6\text{Li}$ and $|1_b\rangle, |2_b\rangle, |3_b\rangle, |4_b\rangle$ of ${}^7\text{Li}$ are the high-field seeking states at large fields. Figure adapted from Ferrier-Barbut PhD thesis [111].

We use the previously stated MOT coils in a parallel current configuration in our hybrid trap. The MOT coils create a magnetic field curvature in this setup. On top of this curvature, a set of Feshbach coils is employed to produce a magnetic field bias. Figure B.2 depicts the variation of the magnetic field along the axial direction (z axis). The combined magnetic field of the MOT coils and the Feshbach coils has a curvature of 30 Hz and a bias field of 832 G along the axial direction.

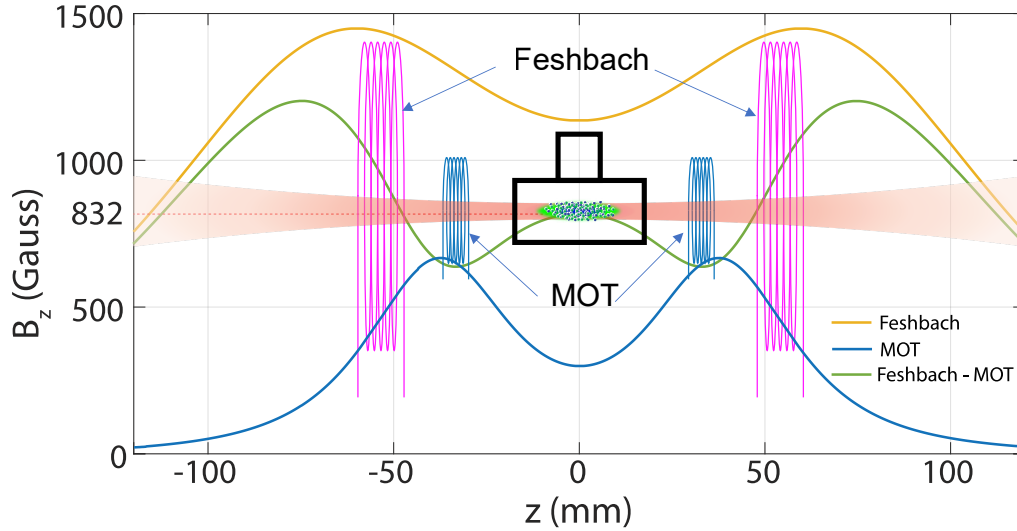


Figure B.2: Magnetic field variation along the axial direction in a hybrid trap. In a parallel current configuration the spatial variation of magnetic field produced by the MOT coils (with 190 A current) along the z axis is represented in blue curve. The Feshbach field (with 390 A current) is represented in yellow curve and the sum of both field is represented in green curve. We note the combined magnetic field near the center is 832 G and high field seeking states can be magnetically confined along z .

Appendix C




Abbreviations

AOM	: Acousto-Optic Modulator
BCS	: Bardeen-Cooper-Schrieffer
BEC	: Bose Einstein Condensate
CCD	: Charge Coupled Device
CMOT	: Compressed Magneto Optical Trap
CW	: Continuous Wave
DDS	: Direct Digital Synthesis
EIT	: Electromagnetic Induced Transparency
EOM	: Electro-Optic Modulator
FET	: Field Effect Transistor
FFLO	: Fulde-Ferrell-Larkin-Ovchinnikov
FPGA	: Field-Programmable Gate Array
FPI	: Fabry-Perot Interferometer
FWHM	: Full Width at Half Maximum
IGBT	: Insulated-Gate Bipolar Transistor
MOT	: Magneto Optical Trap
NPBS	: Non Polarizing Beam Splitters
OD	: Optical Density
ODT	: Optical Dipole Trap
PBS	: Polarizing Beam Splitters
PMF	: Polarisation Maintaining Fibers
PSD	: Phase Space Density
RGA	: Residual Gas Analyzer
TA	: Tapered Amplifiers
TOF	: Time of Flight
TTL	: Transistor-Transistor Logic
QE	: Quantum Efficiency
VSCPT	: Velocity Selective Coherent Population Trapping
USB	: Universal Serial Bus

Appendix D

Publication

Simultaneous sub-Doppler laser cooling of ${}^6\text{Li}$ and ${}^7\text{Li}$ isotopes

Gentle Dash, Tim de Jongh , Maxime Dixmierias , Christophe Salomon, and Tarik Yefsah *

Laboratoire Kastler Brossel, ENS-Université PSL, CNRS, Sorbonne Université, Collège de France, 24 rue Lhomond, 75005 Paris, France



(Received 8 June 2022; accepted 19 August 2022; published 12 September 2022)

We report on the simultaneous sub-Doppler laser cooling of ${}^6\text{Li}$ and ${}^7\text{Li}$ isotopes using gray molasses operating on their respective D_1 atomic transitions. For ${}^7\text{Li}$ we show that the sub-Doppler cooling can be achieved with two distinct Λ -type transitions, where the upper level can be either of the two $2^2 P_{1/2}$ hyperfine states. We obtain temperatures of $\sim 85 \mu\text{K}$, with atom numbers of $\sim 10^8$, and phase-space densities in the range of 10^{-6} – 10^{-5} for both isotopes. These conditions provide a good starting point for loading the mixture into an optical dipole trap and performing evaporative cooling to quantum degeneracy. Our work provides a valuable simplification for the preparation of ultracold ${}^6\text{Li}$ - ${}^7\text{Li}$ mixtures, which were proven to be a successful system for the study of impurity physics and Bose-Fermi superfluids.

DOI: [10.1103/PhysRevA.106.033105](https://doi.org/10.1103/PhysRevA.106.033105)

I. INTRODUCTION

The study of ultracold atomic mixtures offers the possibility to explore a wide scope of quantum phenomena ranging from few-body to many-body physics [1,2]. Such mixtures provide the starting point for a variety of systems, from immersed impurities [3–7] to Efimov states [8–10], ground-state molecules [11–14], and degenerate Bose-Fermi mixtures [15–18]. A prominent example in the field of many-body physics is the observation of dual Bose-Fermi superfluidity, which was achieved for the first time using an ultracold mixture of lithium-6 (${}^6\text{Li}$) and lithium-7 (${}^7\text{Li}$) isotopes [19], unlocking a new area of ultracold physics. Soon after, other Bose-Fermi superfluids were observed with mixtures of ${}^6\text{Li}$ - ${}^{41}\text{K}$ [20] and ${}^6\text{Li}$ - ${}^{174}\text{Yb}$ [21]. These experimental advances have intensified the interest in superfluid mixtures, triggering a renewed theoretical effort on the topic and raising a series of novel conceptual questions [22–26].

From the quantum simulation perspective, dual superfluid experiments represent promising platforms where interisotope or interspecies interactions can be tuned. Moreover, the available realizations of such mixtures allow exploration of the role of the mass difference between the bosonic and fermionic particles, ranging from weak mass imbalance for ${}^6\text{Li}$ - ${}^7\text{Li}$, to intermediate for ${}^6\text{Li}$ - ${}^{41}\text{K}$, to extreme for ${}^6\text{Li}$ - ${}^{174}\text{Yb}$. However, in practice, the benefits of such platforms are limited by the significant technical overhead in development and maintenance. Even in the case of ${}^6\text{Li}$ - ${}^7\text{Li}$, which is technologically the simplest owing to the ability to use solid-state diode lasers at 671 nm for both isotopes, the preparation of an ultracold mixture has historically been tedious. The difficulty with the existing approach for ${}^6\text{Li}$ - ${}^7\text{Li}$ [7,19,27] resides in bringing the temperature of the mixture from the millikelvin range, typically achieved in magneto-optical traps, to the $\lesssim 100 \mu\text{K}$ range necessary to load the mixture in an optical dipole trap

of reasonable power, where evaporative cooling to quantum degeneracy and double superfluidity can be performed.

Here, we propose a significant simplification of this critical stage by demonstrating the simultaneous sub-Doppler cooling of ${}^6\text{Li}$ and ${}^7\text{Li}$. The method is based on gray-molasses cooling operating on the respective D_1 atomic transitions ($2^2 S_{1/2} \rightarrow 2^2 P_{1/2}$) of the two isotopes. While D_1 gray-molasses cooling was already achieved for ${}^7\text{Li}$ [28] and ${}^6\text{Li}$ [29] independently, the feasibility of their simultaneous operation is not evident given the proximity of the D_1 transition of ${}^7\text{Li}$ to the D_2 transition ($2^2 S_{1/2} \rightarrow 2^2 P_{3/2}$) of ${}^6\text{Li}$, as illustrated in Fig. 1. In this work, we explore this simultaneous cooling for two distinct Λ -type transitions of ${}^7\text{Li}$ by using either of the two hyperfine levels $|2^2 P_{1/2}, F_e = 1\rangle$ and $|2^2 P_{1/2}, F_e = 2\rangle$ as the excited state, with F_e being the hyperfine angular momentum quantum number of the upper electronic state.

When the D_1 cooling of ${}^7\text{Li}$ is performed via the $|2^2 P_{1/2}, F_e = 2\rangle$ hyperfine level, such that the proximity of the transitions is best evaded, we obtain efficient simultaneous cooling of both isotopes to temperatures $\lesssim 100 \mu\text{K}$ on a millisecond timescale. We find that the main adverse effect of the ${}^7\text{Li}$ cooling light on the ${}^6\text{Li}$ atoms is a reduced molasses lifetime to a few tens of milliseconds, which is, nonetheless, much larger than the timescale needed for the molasses to reach its equilibrium temperature (~ 1 ms) and to subsequently load the mixture into a dipole trap. On the contrary, when the D_1 cooling of ${}^7\text{Li}$ is performed via the $|2^2 P_{1/2}, F_e = 1\rangle$ hyperfine level, we observe rapid destruction of the ${}^6\text{Li}$ cloud due to the near coincidence between the ${}^7\text{Li}$ cooling beam's frequency and the D_2 transition frequency for ${}^6\text{Li}$. We circumvent this detrimental effect by applying an alternating pulse sequence of the molasses beams and achieve concurrent cooling to temperatures $\lesssim 100 \mu\text{K}$ for both isotopes.

In both cases we thus reach the desired temperature range. The achieved phase-space densities (PSDs) are on the order of 10^{-6} – 10^{-5} , offering a good starting point for loading the atoms into an optical dipole trap and evaporatively cooling

*Corresponding author: tarik.yefsah@lkb.ens.fr

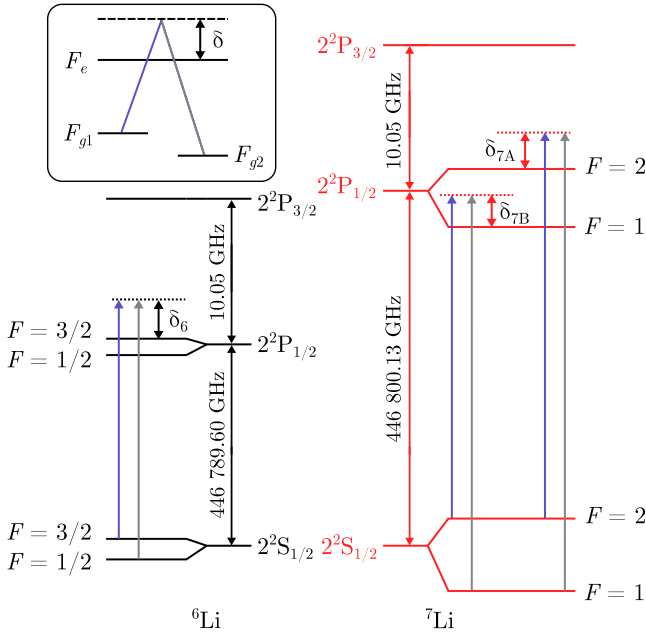


FIG. 1. Energy-level scheme showing the D_1 transitions for the ${}^6\text{Li}$ and ${}^7\text{Li}$ isotopes. The upper electronic state involved in the D_2 transition is also shown. The blue and gray arrows indicate the two frequencies of the D_1 gray-molasses cooling beams, which we refer to as the strong and weak arms, respectively, due to their relative laser intensity. The one-photon detuning for the ${}^6\text{Li}$ molasses is indicated by δ_6 , while the one-photon detuning for the ${}^7\text{Li}$ molasses is indicated by δ_{7A} (δ_{7B}) for the configuration with $F_e = 2$ ($F_e = 1$) as the upper state. The Raman condition is ensured for all transitions. These laser-cooling configurations can be represented by a Λ scheme, as displayed in the inset, with one-photon detuning δ . See the text for details on the addressed transitions.

the mixture to quantum degeneracy. This work shows that this simultaneous gray-molasses cooling method is robust and provides a substantial simplification for the preparation of superfluid Bose-Fermi mixtures of ${}^6\text{Li}$ and ${}^7\text{Li}$.

II. EXPERIMENTAL PROTOCOL

A. Overview

Our experiment starts with a dual magneto-optical trap (MOT) of ${}^6\text{Li}$ and ${}^7\text{Li}$ inside a glass cell, loaded from a Zeeman-slowed atomic beam of lithium enriched in ${}^6\text{Li}$. After loading the MOT for typically 8 s, we apply a simple compression stage (CMOT) in which the laser detunings are reduced. We subsequently turn off the magnetic quadrupole field while keeping the MOT laser beams on for 0.5 ms to hold the atoms until all transient magnetic fields have fully decayed ($\sim 250 \mu\text{s}$) and only residual static magnetic fields remain. We will refer to this stage as the D_2 optical molasses phase, although transient magnetic gradients are still present for the first half of this phase. In the last stage of the preparation sequence, we switch off all the MOT beams and turn on the D_1 laser-cooling beams for 1.5 to 3 ms to create gray molasses.

D_1 gray molasses is a bichromatic laser-cooling technique that applies to atoms with a well-resolved Λ -type three-level structure, typically connecting two nondegenerate hyperfine

ground states F_{g1} and F_{g2} to an upper state F_e via strong- and weak-coupling lasers, respectively [28]. This is shown schematically in Fig. 1. Each frequency component is blue detuned with respect to either the $F_{g1} \rightarrow F_e$ or $F_{g2} \rightarrow F_e$ transition. In such molasses, two mechanisms—both involving dark states—work in tandem to provide sub-Doppler cooling of the atoms: Sisyphus-like cooling on a $F_{g1} \rightarrow F_e$ transition with either $F_e = F_{g1}$ or $F_e = F_{g1} - 1$ [30–32] and a two-photon effect similar to velocity-selective coherent population trapping via a (coherent) Raman process connecting the two hyperfine ground states according to the Λ structure [28]. This cooling method has been successfully applied to and proven to be efficient for several alkali atoms such as ${}^6\text{Li}$ [29,33], ${}^7\text{Li}$ [28,34], ${}^{23}\text{Na}$ [35], ${}^{39}\text{K}$ [36,37], ${}^{40}\text{K}$ [38], ${}^{41}\text{K}$ [39], and ${}^{87}\text{Rb}$ [40].

For ${}^6\text{Li}$, we use the $F_{g1} = 3/2 \rightarrow F_e = 3/2$ and $F_{g2} = 1/2 \rightarrow F_e = 3/2$ transitions of the D_1 line. Gray-molasses cooling could, in principle, also be applied using the $F_e = 1/2$ state, but the small hyperfine splitting within the $2^2P_{1/2}$ electronic state of $26 \text{ MHz} \sim 4\Gamma$, with $\Gamma = 2\pi \times 5.87 \text{ MHz}$ being the excited state linewidth, is not sufficient to prevent competing effects between the two hyperfine levels. For ${}^7\text{Li}$, the hyperfine splitting is sufficient that we can explore the two possible Λ schemes on the D_1 transition: (i) $F_{g1} = 2 \rightarrow F_e = 2$ and $F_{g2} = 1 \rightarrow F_e = 2$ and (ii) $F_{g1} = 2 \rightarrow F_e = 1$ and $F_{g2} = 1 \rightarrow F_e = 1$.

The energy-level diagram in Fig. 1 shows the D_1 and D_2 lines of the ${}^6\text{Li}$ and ${}^7\text{Li}$ isotopes, which are the four lines relevant to the present work. In the following we will refer to these four lines as L_{16} , L_{26} , L_{17} , and L_{27} , with the first digit of the subscript referring to the electronic transition (D_1 or D_2) and the second digit referring to the mass of the isotope, and we will use a superscript of the form $F_g \rightarrow F_e$ to specify the hyperfine transition when needed. Table I displays the frequency difference among various hyperfine transitions among these lines, where we note a close proximity of the $L_{26}^{1/2 \rightarrow 1/2}$ and $L_{26}^{1/2 \rightarrow 3/2}$ transitions of ${}^6\text{Li}$ with $L_{17}^{2 \rightarrow 1}$, on the one hand ($\sim 5\Gamma$), and with $L_{17}^{2 \rightarrow 2}$, on the other hand ($\sim 10\Gamma$). Note that the situation is particularly problematic in the former case, as the strong D_1 cooling beam of ${}^7\text{Li}$ is required to be typically 3Γ – 5Γ blue detuned from $L_{17}^{2 \rightarrow 1}$. This proximity raises the question of whether it is possible to perform D_1 cooling on ${}^7\text{Li}$ without altering the ${}^6\text{Li}$ cloud. This issue is addressed throughout this paper.

B. Laser setup

All laser beams are derived from four distinct extended-cavity diode lasers at 671 nm, each being independently frequency locked on the relevant lines (two of them on L_{16} , one on L_{17} , and one on L_{27}). Each laser provides about 20 mW of laser power, which undergoes a single or multiple amplification stages via injection of tapered amplifiers or seeding of high-power diodes through injection locking, providing sufficient power at all required frequencies for Zeeman slowing, laser cooling, and imaging.

For each isotope, the MOT operates with two frequencies: one cooling frequency and one repumper frequency. The cooling beam is red detuned by 4.4Γ (3.9Γ) from the transition $L_{26}^{3/2 \rightarrow 5/2}$ for ${}^6\text{Li}$ ($L_{27}^{2 \rightarrow 3}$ for ${}^7\text{Li}$). The MOT repumper

TABLE I. Hyperfine transitions of the D_1 and D_2 lines of both lithium isotopes. Frequencies are taken from [41]. The rightmost column gives the frequency difference $\Delta\nu$ between each transition and the $L_{17}^{2\rightarrow 1}$ transition.

	Transition $F_g \rightarrow F_e$	Label	Frequency ν (MHz)	$\Delta\nu$ (MHz)
^6Li D_2 line (L_{26})	$3/2 \rightarrow 5/2$	$L_{26}^{3/2\rightarrow 5/2}$	446 799 571	-200 (-34.1 Γ)
	$3/2 \rightarrow 3/2$	$L_{26}^{3/2\rightarrow 3/2}$	446 799 574	-197 (-33.6 Γ)
	$3/2 \rightarrow 1/2$	$L_{26}^{3/2\rightarrow 1/2}$	446 799 576	-195 (-33.3 Γ)
	$1/2 \rightarrow 3/2$	$L_{26}^{1/2\rightarrow 3/2}$	446 799 802	31.1 (5.3 Γ)
	$1/2 \rightarrow 1/2$	$L_{26}^{1/2\rightarrow 1/2}$	446 799 804	32.8 (5.6 Γ)
^7Li D_1 line (L_{17})	$2 \rightarrow 1$	$L_{17}^{2\rightarrow 1}$	446 799 771	
	$2 \rightarrow 2$	$L_{17}^{2\rightarrow 2}$	446 799 863	91.9 (15.6 Γ)
	$1 \rightarrow 1$	$L_{17}^{1\rightarrow 1}$	446 800 575	803 (137 Γ)
	$1 \rightarrow 2$	$L_{17}^{1\rightarrow 2}$	446 800 666	895 (152 Γ)

frequency is red detuned by 2.9Γ (2.2Γ) from the transition $L_{16}^{1/2\rightarrow 1/2}$ for ^6Li ($L_{27}^{1\rightarrow 2}$ for ^7Li). Note here that the ^6Li MOT repumper operates near the D_1 line instead of D_2 in order to avoid losses of ^7Li due to the vicinity of L_{26} and L_{17} [42]. Four laser beams, each at one of these four frequencies, are generated and spatially superimposed to follow the same optical path where they are each split into six independent beams to create pairs of $\sigma^+ - \sigma^-$ counterpropagating beams along three orthogonal directions. The same 24 beams are used for the CMOT and D_2 molasses phases, where their frequencies are shifted (typically by a few Γ) to optimal detunings.

For the gray molasses we use laser beams with two frequency components, which we obtain by generating a low-amplitude (approximately 8%) sideband via an electro-optic modulator. This ensures phase coherence of the (high-amplitude) carrier and (low-amplitude) sideband, which is essential to obtain Λ enhancement of the gray-molasses cooling [28,40]. For each isotope the sideband is generated at a frequency corresponding to the hyperfine splitting of the ground states: +228 MHz (+803.5 MHz) for ^6Li (^7Li). The laser frequencies are blue detuned from the relevant D_1 transitions as depicted in Fig. 1.

For ^6Li , the strong (weak) amplitude component of the molasses beams is blue detuned by $\delta_6 = 5.2\Gamma$ from $L_{16}^{3/2\rightarrow 3/2}$ ($L_{16}^{1/2\rightarrow 3/2}$). For ^7Li , as indicated, we investigate two possible Λ schemes: configuration A, where we use $|2^2 P_{1/2}, F_e = 2\rangle$ as the upper state, and configuration B, for which the upper state is $|2^2 P_{1/2}, F_e = 1\rangle$. In configuration A, the detuning of the strong (weak) amplitude component from $L_{17}^{2\rightarrow 2}$ ($L_{17}^{1\rightarrow 2}$) is denoted by δ_{7A} . We study the effects of δ_{7A} on both the ^7Li and ^6Li atoms in order to assess whether the proximity between L_{26} and L_{17} is detrimental to the simultaneous cooling. In configuration B, the strong (weak) amplitude component of the molasses beams is detuned from $L_{17}^{2\rightarrow 1}$ ($L_{17}^{1\rightarrow 1}$) by $\delta_{7B} = 2.5\Gamma$. This value of δ_{7B} sets the two frequencies at over 10Γ red detuned from the transitions involving the $|2^2 P_{1/2}, F_e = 2\rangle$ state of ^7Li , making the off-resonant scattering due to this level negligible.

The D_1 cooling beams follow the same optical path as the MOT beams and form three pairs of counterpropagating beams in a $\sigma^+ - \sigma^-$ configuration. At the science cell, each of the six resulting gray-molasses beams has a power of 9.0

and 4.5 mW and a waist ($1/e^2$ width) of approximately 3 and 2 mm for ^6Li and ^7Li , respectively, resulting in peak intensities in the range of $I \approx 3I_{\text{sat}} - 6I_{\text{sat}}$ and $I \approx 7I_{\text{sat}} - 11I_{\text{sat}}$, with $I_{\text{sat}} = 7.6 \text{ mW/cm}^2$ being the saturation intensity for the D_1 transition.

C. Detection

Following the gray-molasses stage, we switch off all laser beams and let the atoms expand freely. After a certain time of flight (TOF) we detect the atoms through low-saturation absorption imaging using a $10\text{-}\mu\text{s}$ pulse of circularly polarized probe beams that are resonant with the respective D_2 lines $L_{26}^{3/2\rightarrow 5/2}$ and $L_{27}^{2\rightarrow 3}$. For each isotope, we shine a repumper beam (tuned to $L_{27}^{1/2\rightarrow 3/2}$ and $L_{27}^{1\rightarrow 2}$) for $10\text{ }\mu\text{s}$ before imaging in order to transfer all atoms to the upper hyperfine ground state ($F_g = 3/2$ for ^6Li and $F_g = 2$ for ^7Li), and then during the imaging phase, we apply a second repumping pulse to compensate for pumping effects into the lower hyperfine ground states. These repumping beams are directed along the two axes perpendicular to the imaging direction. The absorption shadow of the atoms is then collected by a CCD camera and converted to an optical density profile.

We convert the optical densities into atomic densities using absorption cross sections of $0.59\sigma_0$ and $0.48\sigma_0$ for ^6Li and ^7Li , respectively, where $\sigma_0 = \frac{3\lambda^2}{2\pi}$, with λ being the wavelength of the resonant imaging light. These values correspond to the theoretical values computed at zero magnetic field by assuming that for each isotope all atoms occupy the upper hyperfine ground state ($F_g = 3/2$ for ^6Li and $F_g = 2$ for ^7Li) with equal populations in the m_F levels, with m_F being the quantum number associated with projection of the hyperfine angular momentum onto a quantization axis. In practice, the magnetic field is nonzero, and we measured it to be $0.4(2) \text{ G}$ using ^7Li hyperfine absorption spectra as a magnetometer, yielding a reduction in the absorption cross sections stated above by about 5% and 10%, respectively, according to our calculations. For simplicity, we will, however, deliberately ignore this reduction, which implies that the atom numbers stated throughout the paper are slightly underestimated.

The resulting atomic density profiles are fitted with a two-dimensional Gaussian function yielding peak density n_0 ,

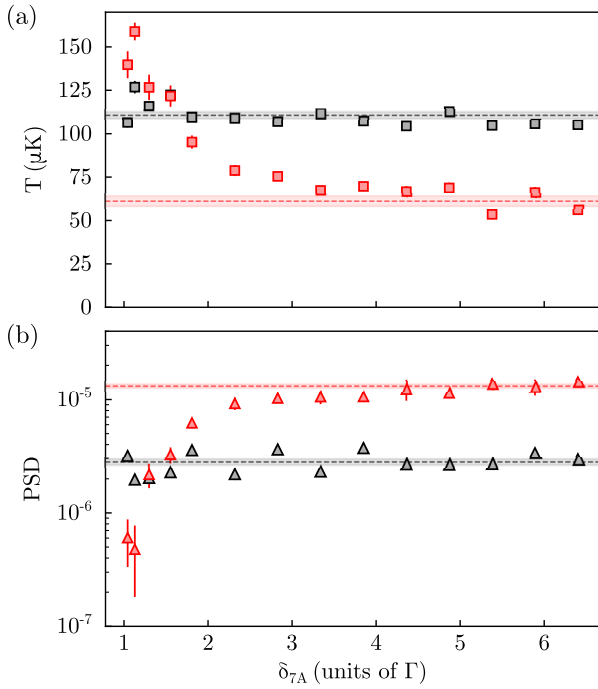


FIG. 2. (a) Temperatures and (b) PSDs of the clouds after 1.5 ms of simultaneous gray-molasses cooling in configuration A as a function of δ_{7A} . Black (red) data points correspond to values of ^6Li (^7Li). Error bars represent statistical uncertainties at one standard deviation determined with the bootstrap method [43]. Dashed lines show average temperatures and phase-space densities for the respective isotopes for $\delta_{7A} > 4\Gamma$, and the shaded regions indicate the corresponding standard error.

atom number, and cloud sizes. By varying the TOF we determine the ballistic expansion rate of the atoms and extract temperatures T of the clouds. Finally, we determine the peak PSD $n_0 \Lambda_T^3$, where $\Lambda_T = \frac{h}{\sqrt{2\pi m k_B T}}$ is the thermal de Broglie wavelength. Note that the uncertainty of the imaging system magnification was measured to be 2.3%, resulting in systematic relative errors of 4.6% and 9.2%, respectively, for temperatures and PSDs reported in this paper.

III. RESULTS

When loading the MOT for 8 s, we routinely capture $9(1) \times 10^7$ ^6Li atoms and $13(2) \times 10^7$ ^7Li atoms in the D_2 molasses and obtain temperatures of approximately 0.7 mK for both isotopes. All atoms present at the D_2 stage are captured in the gray molasses. Optimization and characterization of the gray molasses for each cooling configuration are discussed below.

A. Cooling on the $F_e = 2$ state of ^7Li

In configuration A, where ^7Li is cooled via the $F_e = 2$ upper state, the ^7Li transition is 10Γ blue detuned from the $L_{26}^{1/2 \rightarrow 1/2, 3/2}$ lines of ^6Li . Additional blue detuning of the ^7Li gray-molasses beams (given by δ_{7A}) moves the cooling lasers further away from the ^6Li resonance. In Fig. 2, we report ^6Li and ^7Li temperatures for 1.5-ms simultaneous gray-molasses

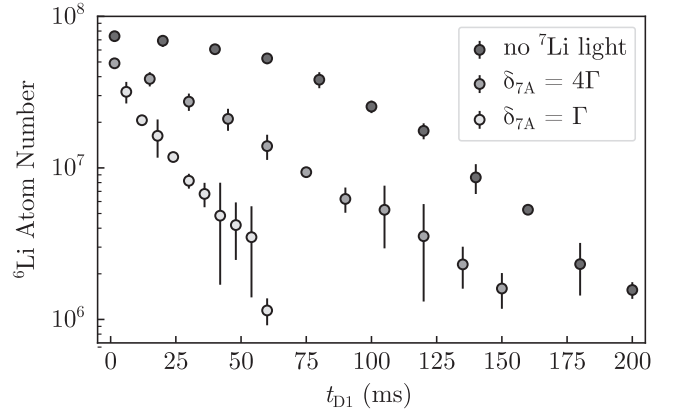


FIG. 3. Semilogarithmic plot of the ^6Li atom number as a function of D_1 molasses duration t_{D1} for three distinct situations: in the absence of ^7Li molasses light (dark gray circles), in the presence of ^7Li molasses light with $\delta_{7A} = 4\Gamma$ (medium gray circles), and in the presence of ^7Li molasses light with $\delta_{7A} = \Gamma$ (light gray circles). Error bars represent statistical uncertainties at one standard deviation.

cooling at several values of δ_{7A} while maintaining the respective Raman conditions.

We observe that the ^7Li gray-molasses cooling is efficient for a broad range of one-photon detunings, becoming less effective only for $\delta_{7A} < 3\Gamma$, and that for this entire range the influence of the ^7Li cooling light on the ^6Li temperatures and atom numbers is negligible. We readily obtain temperatures of $T_6 = 105(2) \mu\text{K}$ and $T_7 = 56(2) \mu\text{K}$ and phase-space densities of $3.0(1) \times 10^{-6}$ and $1.4(1) \times 10^{-5}$ for ^6Li and ^7Li , respectively, which are well within the range of parameters for efficient loading into a dipole trap, although the factor of 2 between T_6 and T_7 could be unpractical. Upon intensity ramp of the D_1 molasses laser beams, we were able to obtain a better compromise, with $T_6 = 90(3) \mu\text{K}$ and $T_7 = 83(3) \mu\text{K}$, leading to phase-space densities of $3.1(2) \times 10^{-6}$ and $9.0(7) \times 10^{-6}$, respectively. These ^6Li temperatures are slightly higher than reported in previous experiments [19,29,33,44], which we ascribe to imperfect magnetic field cancellation in our setup where the residual magnetic field is ~ 0.4 G. Nonetheless, this simultaneous cooling method still provides a good starting point for loading the cloud into a dipole trap and initiating evaporation.

While the ^6Li clouds are hardly affected by the ^7Li cooling beams for D_1 molasses durations of a few milliseconds, we observe a marked effect at longer times, which is revealed in the lifetime of the ^6Li atoms in the molasses. Figure 3 displays the number of ^6Li atoms as a function of hold time in the molasses in the absence and in the presence of ^7Li molasses light for two distinct values of δ_{7A} . We observe a faster decay of the atom number in the presence of ^7Li molasses light that gets stronger as the ^7Li cooling light frequency is shifted towards the ^6Li resonance, as is expected from the enhanced photon scattering rate. Overall, the main adverse effect of the ^7Li cooling light on the ^6Li atoms is thus a reduced molasses lifetime from ~ 150 ms to a few tens of milliseconds. This relatively short lifetime is, nonetheless, much larger than the timescale needed for the molasses to reach its equilibrium

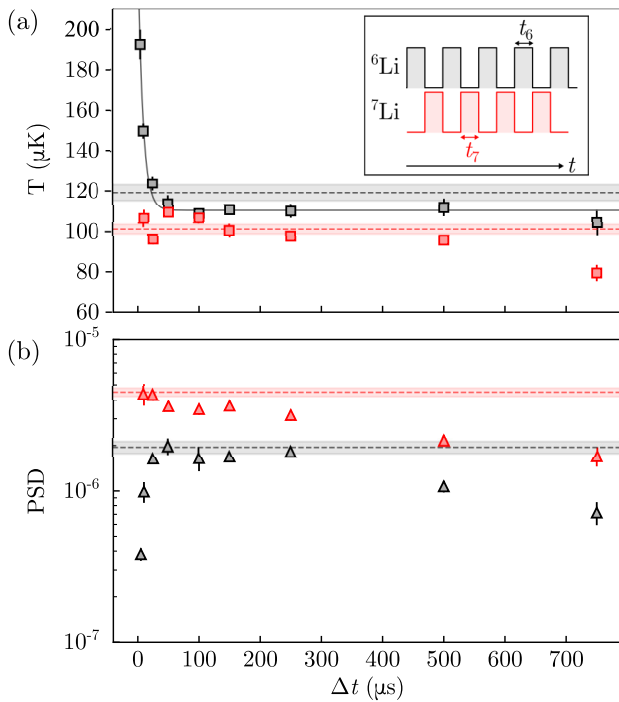


FIG. 4. Optimization of the individual pulse duration for gray-molasses cooling in the alternating cooling sequence of configuration B. Black (red) data points correspond to values of ${}^6\text{Li}$ (${}^7\text{Li}$). (a) Temperatures after 3 ms of pulsed gray-molasses cooling. Dashed lines show temperatures obtained when cooling each isotope individually with a continuous pulse of 1.5 ms, with the shaded areas indicating the statistical error at one standard deviation. The solid gray line shows an exponential fit of the ${}^6\text{Li}$ temperatures to guide the eye. The inset shows a schematic representation of the pulse sequence. (b) PSDs for ${}^6\text{Li}$ and ${}^7\text{Li}$. Dashed lines represent PSDs for individual cooling.

temperature (~ 1 ms) and to subsequently load the mixture into a dipole trap.

B. Cooling on the $F_e = 1$ state of ${}^7\text{Li}$

In configuration B, where cooling of ${}^7\text{Li}$ is performed via the $F_e = 1$ upper state, the spectral-line proximity does hinder the simultaneous cooling of the two isotopes: At $\delta_{7B} = 2.5\Gamma$ the ${}^7\text{Li}$ cooling beam that acts on the $L_{17}^{2 \rightarrow 1}$ transition is only 3Γ red detuned from the $L_{26}^{1/2 \rightarrow 1/2, 3/2}$ lines. At such a detuning the ${}^7\text{Li}$ light is expected to considerably heat up the ${}^6\text{Li}$ cloud, which we confirmed experimentally. Moreover, we observe that simultaneous operation of both molasses leads to stronger detrimental effects with a rapid destruction of the ${}^6\text{Li}$ cloud (see Sec. IV). To circumvent this, we employ a temporally alternating pulse sequence by shining the ${}^6\text{Li}$ and ${}^7\text{Li}$ molasses in successive pulses (see the inset in Fig. 4). This technique is very similar to earlier work on atom tweezers [45], single-atom imaging of ${}^6\text{Li}$ [46], and molecule experiments [47–49], in which adverse effects of laser light are circumvented via periodic amplitude modulation. Here, we aim to find an optimal pulsed scheme in which we alternate between cooling and heating cycles on the ${}^6\text{Li}$ atoms such

that the heating due to the ${}^7\text{Li}$ molasses beams is largely compensated by the cooling power of the ${}^6\text{Li}$ molasses. This additionally prevents the rapid destruction of the ${}^6\text{Li}$ cloud observed when simultaneously operating both molasses.

We therefore employ a pulse sequence for which the ${}^6\text{Li}$ and ${}^7\text{Li}$ molasses beams are exactly out of phase. We refer to t_6 and t_7 as the pulse durations of ${}^6\text{Li}$ and ${}^7\text{Li}$, respectively. The pulsed sequence always starts with a ${}^6\text{Li}$ light pulse but can end with either a ${}^6\text{Li}$ or ${}^7\text{Li}$ light pulse. Typically, the total D_1 gray-molasses duration is 3 ms to obtain effective cooling periods similar to those in configuration A (~ 1.5 -ms molasses time). In order to optimize the pulse sequence we first explore the situation where $t_6 = t_7 = \Delta t$, with a final pulse of ${}^6\text{Li}$ light. The results are shown in Fig. 4, where we observe that for $\Delta t \gtrsim 50 \mu\text{s}$ we obtain temperatures $\lesssim 100 \mu\text{K}$, which are comparable to those obtained for separate cooling of each isotope with continuous molasses of 1.5 ms. The cooling of ${}^6\text{Li}$ atoms, however, is seen to be less efficient at smaller values of Δt . From this we infer that at these shorter pulse widths the ${}^6\text{Li}$ molasses is not able to compensate for the heating induced by the ${}^7\text{Li}$ beams. Note that we restricted the pulse duration to $\Delta t \leq 750 \mu\text{s}$ in order to limit the free expansion of the cloud when the cooling light is off. Indeed, the characteristic velocity of atoms at $100 \mu\text{K}$ is approximately 0.37 m/s, yielding a size of 0.37 mm after a free expansion of 1 ms, which should be compared to the initial size of the molasses clouds of $\lesssim 1$ mm and the laser beam waists of ~ 2 – 3 mm.

In order to improve further the performances of the pulsed scheme we varied a number of parameters. First, we investigated the role of the duty cycle by fixing t_6 to $100 \mu\text{s}$ while varying t_7 from 25 to $200 \mu\text{s}$, which did not show any influence on the final temperatures. Second, we also explored the situation where the pulse sequence ends on ${}^7\text{Li}$ light, which we found to yield systematically higher temperatures and lower PSDs (see below), as expected from the proximity of the $L_{17}^{2 \rightarrow 1}$ and $L_{26}^{1/2 \rightarrow 1/2, 3/2}$ lines. Finally, we implemented diverse schemes of intensity ramp down, which we found to yield the best results. In Fig. 5 we present an overview of three different pulse sequences (I, II, and III). In sequence I, we use $t_6 = t_7 = \Delta t = 100 \mu\text{s}$ and end on a ${}^7\text{Li}$ light pulse. In sequence II, we use $t_6 = 100 \mu\text{s}$ and $t_7 = 50 \mu\text{s}$ while ending on a ${}^6\text{Li}$ light pulse. Finally, sequence III corresponds to ramped pulse sequences (ending on ${}^6\text{Li}$ light) in which intensities are reduced by half over the total molasses duration of 3 ms.

The results summarized in Fig. 5 show that it is most favorable to combine ending the sequence on a pulse of ${}^6\text{Li}$ light together with an intensity ramp, yielding PSDs on the order of $\sim 4 \times 10^{-6}$ and temperatures of approximately $85 \mu\text{K}$ for both isotopes. These temperature and PSD values are obtained at the cost of a reduction in the atom numbers by only 18% (16%) for ${}^6\text{Li}$ (${}^7\text{Li}$). With this optimized pulsed scheme we are thus able to not only circumvent destruction of the ${}^6\text{Li}$ cloud due to the near-resonant light of the ${}^7\text{Li}$ molasses beams but also reach PSDs which are suitable for loading the atoms into an optical dipole trap but lower than PSDs obtained in configuration A for ${}^7\text{Li}$.

To understand the effect of the ${}^7\text{Li}$ molasses light on the ${}^6\text{Li}$ atoms, we repeat the temperature measurements in Fig. 4, altering the sequence by adding a final pulse of ${}^7\text{Li}$ light of

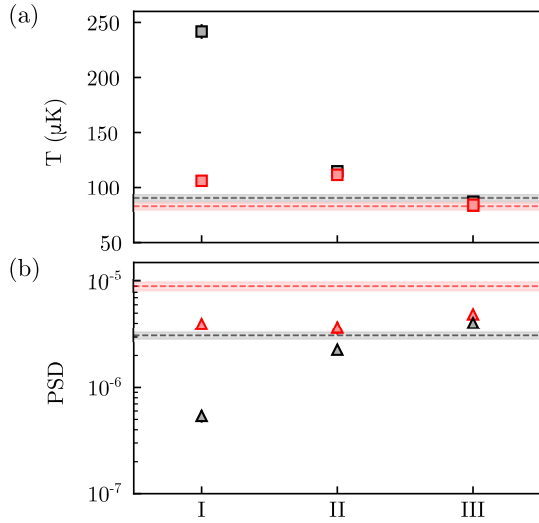


FIG. 5. (a) Temperatures and (b) phase-space densities for different pulse sequences employed for the alternating cooling of ${}^6\text{Li}$ (black) and ${}^7\text{Li}$ (red) for the configuration in which ${}^7\text{Li}$ is cooled via the $F_e = 1$ state with $\delta_{7B} = 2.5\Gamma$. Sequences ending on a ${}^7\text{Li}$ light pulse (I) lead to higher temperatures of the ${}^6\text{Li}$ cloud compared to a sequence ending on a ${}^6\text{Li}$ light pulse (II). For a ramped sequence (III) higher PSDs are obtained for both isotopes. See text for details on the sequences. Dashed lines represent the optimal temperatures and phase-space densities reached in configuration A, as shown in Fig. 2. Shaded areas correspond to the statistical error at one standard deviation.

width Δt , deliberately heating the ${}^6\text{Li}$ cloud. Figure 6 shows the obtained temperatures. First, we observe the occurrence of an optimum at $\Delta t \sim 50 \mu\text{s}$ with a ${}^6\text{Li}$ temperature of $\approx 180 \mu\text{K}$ that is substantially higher than the lowest temperatures reported above.

At short pulse duration, the ${}^6\text{Li}$ laser pulse cannot compensate the heating induced by the ${}^7\text{Li}$ light, similar to what was observed in Fig. 4. For longer pulse durations ($\Delta t \geq 50 \mu\text{s}$) we observe a linear increase of temperature, signaling a heating mechanism with a steady heating rate of $0.82(4) \text{ K/s}$. This heating can be explained by analyzing the photon scattering of ${}^6\text{Li}$ atoms exposed to ${}^7\text{Li}$ molasses light. The coupling of the carrier ${}^7\text{Li}$ molasses light to the ${}^6\text{Li}$ atoms via the $L_{26}^{1/2 \rightarrow 1/2, 3/2}$ and $L_{26}^{3/2 \rightarrow 1/2, 3/2, 5/2}$ transitions yields successive photon scattering cycles with two characteristic scattering rates of $\approx \Gamma/5$ and $\approx \Gamma/400$, respectively. Taking into account the combined effect of these photon scattering processes, we quantify the resulting momentum diffusion and obtain a heating rate of $\sim 0.9 \text{ K/s}$, in agreement with the measured value.

IV. DISCUSSION

In addition to the heating observed in Fig. 6, there are two other detrimental effects one may consider as a result of the proximity of the ${}^7\text{Li}$ molasses light to the L_{26} transitions: light shifts and net radiation pressure forces resulting from an imperfect intensity balance of the molasses beams. Light shifts induced by the ${}^7\text{Li}$ beams can, indeed, alter the Raman condition for the Λ scheme of the ${}^6\text{Li}$ molasses. However,

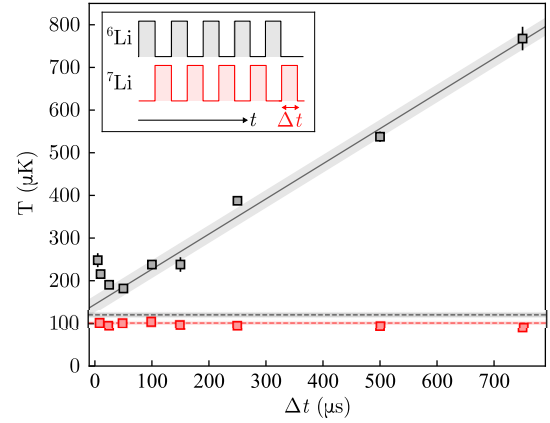


FIG. 6. Heating effects of the ${}^7\text{Li}$ gray-molasses cooling light on the ${}^6\text{Li}$ atoms. The same pulse sequences are used as for the data in Fig. 4, but a final pulse of ${}^7\text{Li}$ cooling light is added. Black (red) data points correspond to temperatures for ${}^6\text{Li}$ (${}^7\text{Li}$). The dashed lines represent temperatures obtained for individual cooling of each isotope using a continuous 1.5-ms pulse, with the surrounding shaded areas indicating the statistical error at one standard deviation. The solid gray line represents a linear fit of the ${}^6\text{Li}$ temperatures taken for $\Delta t \geq 50 \mu\text{s}$, yielding a heating rate of $0.82(4) \text{ K/s}$. The inset shows a schematic representation of the pulse sequence.

we estimate these light shifts to be only on the order of $\hbar\Gamma$ and negative, such that the resulting change in the Raman condition merely leads to less efficient cooling; it would still allow us to reach temperatures of $\sim 100 \mu\text{K}$, as observed in previous studies [28,29,44]. Furthermore, the light shifts cannot account for the fact that, when both ${}^6\text{Li}$ and ${}^7\text{Li}$ act on the ${}^6\text{Li}$ cloud, the latter is rapidly expelled with an overall center-of-mass velocity of 10 times the recoil velocity.

On the other hand, a net radiation pressure resulting from an intensity imbalance among the molasses beams can have an important effect. Indeed, for scattering rates on the order of those discussed in Sec. III B, one would expect extremely high radiation pressure forces in the case of a cycling transition. When only the ${}^7\text{Li}$ light acts on the ${}^6\text{Li}$ cloud, this effect is transient and not dominant due to the noncycling nature of the $L_{26}^{1/2 \rightarrow 1/2, 3/2}$ and $L_{26}^{3/2 \rightarrow 1/2, 3/2, 5/2}$ transitions. However, when the ${}^6\text{Li}$ and ${}^7\text{Li}$ molasses beams are shone simultaneously, the effect of an intensity imbalance becomes dominant. In this case the strong ${}^6\text{Li}$ molasses light plays the role of a repumper for the $L_{26}^{1/2 \rightarrow 1/2, 3/2}$ transitions, making them effectively cycling with a scattering rate that we estimate to be $\approx \Gamma/10$. For such a high scattering rate, an intensity imbalance of only 1% would lead the atoms to experience an acceleration of 3 km/s^2 , which can, indeed, explain our observations. The pulsed scheme employed in configuration B therefore not only serves to alternate between cooling and heating cycles on the ${}^6\text{Li}$ atoms; it also prevents the large radiation pressure which causes the observed rapid destruction of the ${}^6\text{Li}$ cloud.

V. CONCLUSION

In this work we have demonstrated simultaneous D_1 gray-molasses cooling of ${}^6\text{Li}$ and ${}^7\text{Li}$. Two possible cooling configurations were explored. In the first configuration, in which we cool ${}^7\text{Li}$ via the upper hyperfine state ($F_e = 2$) of the $2^2P_{1/2}$ level, simultaneous cooling is straightforward and readily allows us to reach temperatures of $\sim 85\ \mu\text{K}$, with atom numbers of $\sim 10^8$ and phase-space densities of $\sim 5 \times 10^{-6}$ for both isotopes. When operating simultaneous cooling in which we cool ${}^7\text{Li}$ via the lower hyperfine state ($F_e = 1$) of the $2^2P_{1/2}$ level, we find that the proximity of the ${}^7\text{Li}$ cooling light to the D_2 transition of ${}^6\text{Li}$ leads to the destruction of the ${}^6\text{Li}$ cloud. We resolved this issue by employing an alternating pulsed sequence of the cooling light, with which we were able to reach performances comparable to those above. In

conclusion, we have shown that ${}^6\text{Li}$ and ${}^7\text{Li}$ can be simultaneously laser cooled to temperatures $\lesssim 100\ \mu\text{K}$, thus providing a significant simplification in the preparation of degenerate Bose-Fermi mixtures of these isotopes.

ACKNOWLEDGMENTS

We thank K. Dai, C. de Daniloff, S. Dhar, A. Hammond, J. Lis, S. Jin, J. Struck, and J. Verstraten for experimental assistance at various stages of this project. This work has been supported by Agence Nationale de la Recherche (Grant No. ANR-21-CE30-0021), the European Research Council (Grant No. ERC-2016-ADG-743159), CNRS (Tremplin@INP 2020), and Région Ile-de-France in the framework of DIM SIRTEQ (Super2D and SISCO).

-
- [1] C. Ospelkaus and S. Ospelkaus, *J. Phys. B* **41**, 203001 (2008).
- [2] C. Chin, R. Grimm, P. Julienne, and E. Tiesinga, *Rev. Mod. Phys.* **82**, 1225 (2010).
- [3] A. Schirotzek, C.-H. Wu, A. Sommer, and M. W. Zwierlein, *Phys. Rev. Lett.* **102**, 230402 (2009).
- [4] N. Spethmann, F. Kindermann, S. John, C. Weber, D. Meschede, and A. Widera, *Phys. Rev. Lett.* **109**, 235301 (2012).
- [5] M.-G. Hu, M. J. Van de Graaff, D. Kedar, J. P. Corson, E. A. Cornell, and D. S. Jin, *Phys. Rev. Lett.* **117**, 055301 (2016).
- [6] N. B. Jørgensen, L. Wacker, K. T. Skalmstang, M. M. Parish, J. Levinsen, R. S. Christensen, G. M. Bruun, and J. J. Arlt, *Phys. Rev. Lett.* **117**, 055302 (2016).
- [7] S. Laurent, M. Pierce, M. Delehaye, T. Yefsah, F. Chevy, and C. Salomon, *Phys. Rev. Lett.* **118**, 103403 (2017).
- [8] R. S. Bloom, M.-G. Hu, T. D. Cumby, and D. S. Jin, *Phys. Rev. Lett.* **111**, 105301 (2013).
- [9] R. Pires, J. Ulmanis, S. Häfner, M. Repp, A. Arias, E. D. Kuhnle, and M. Weidemüller, *Phys. Rev. Lett.* **112**, 250404 (2014).
- [10] S.-K. Tung, K. Jiménez-García, J. Johansen, C. V. Parker, and C. Chin, *Phys. Rev. Lett.* **113**, 240402 (2014).
- [11] K.-K. Ni, S. Ospelkaus, M. H. G. de Miranda, A. Pe'er, B. Neyenhuis, J. J. Zirbel, S. Kotochigova, P. S. Julienne, D. S. Jin, and J. Ye, *Science* **322**, 231 (2008).
- [12] L. D. Carr, D. DeMille, R. V. Krems, and J. Ye, *New J. Phys.* **11**, 055049 (2009).
- [13] P. K. Molony, P. D. Gregory, Z. Ji, B. Lu, M. P. Köppinger, C. R. Le Sueur, C. L. Blackley, J. M. Hutson, and S. L. Cornish, *Phys. Rev. Lett.* **113**, 255301 (2014).
- [14] J. W. Park, S. A. Will, and M. W. Zwierlein, *Phys. Rev. Lett.* **114**, 205302 (2015).
- [15] B. J. DeSalvo, K. Patel, J. Johansen, and C. Chin, *Phys. Rev. Lett.* **119**, 233401 (2017).
- [16] R. S. Lous, I. Fritsche, M. Jag, B. Huang, and R. Grimm, *Phys. Rev. A* **95**, 053627 (2017).
- [17] R. S. Lous, I. Fritsche, M. Jag, F. Lehmann, E. Kirilov, B. Huang, and R. Grimm, *Phys. Rev. Lett.* **120**, 243403 (2018).
- [18] B. J. DeSalvo, K. Patel, G. Cai, and C. Chin, *Nature (London)* **568**, 61 (2019).
- [19] I. Ferrier-Barbut, M. Delehaye, S. Laurent, A. T. Grier, M. Pierce, B. S. Rem, F. Chevy, and C. Salomon, *Science* **345**, 1035 (2014).
- [20] X.-C. Yao, H.-Z. Chen, Y.-P. Wu, X.-P. Liu, X.-Q. Wang, X. Jiang, Y. Deng, Y.-A. Chen, and J.-W. Pan, *Phys. Rev. Lett.* **117**, 145301 (2016).
- [21] R. Roy, A. Green, R. Bowler, and S. Gupta, *Phys. Rev. Lett.* **118**, 055301 (2017).
- [22] R. Zhang, W. Zhang, H. Zhai, and P. Zhang, *Phys. Rev. A* **90**, 063614 (2014).
- [23] T. Ozawa, A. Recati, M. Delehaye, F. Chevy, and S. Stringari, *Phys. Rev. A* **90**, 043608 (2014).
- [24] Y. Castin, I. Ferrier-Barbut, and C. Salomon, *C. R. Phys.* **16**, 241 (2015).
- [25] M. Abad, A. Recati, S. Stringari, and F. Chevy, *Eur. Phys. J. D* **69**, 126 (2015).
- [26] Y. Jiang, R. Qi, Z.-Y. Shi, and H. Zhai, *Phys. Rev. Lett.* **118**, 080403 (2017).
- [27] M. Delehaye, S. Laurent, I. Ferrier-Barbut, S. Jin, F. Chevy, and C. Salomon, *Phys. Rev. Lett.* **115**, 265303 (2015).
- [28] A. T. Grier, I. Ferrier-Barbut, B. S. Rem, M. Delehaye, L. Khaykovich, F. Chevy, and C. Salomon, *Phys. Rev. A* **87**, 063411 (2013).
- [29] A. Burchianti, G. Valtolina, J. A. Seman, E. Pace, M. De Pas, M. Inguscio, M. Zaccanti, and G. Roati, *Phys. Rev. A* **90**, 043408 (2014).
- [30] G. Grynberg and J.-Y. Courtois, *Europhys. Lett.* **27**, 41 (1994).
- [31] D. Boiron, C. Triché, D. R. Meacher, P. Verkerk, and G. Grynberg, *Phys. Rev. A* **52**, R3425 (1995).
- [32] M. Weidemüller, T. Esslinger, M. A. Ol'shanii, A. Hemmerich, and T. W. Hänsch, *Europhys. Lett.* **27**, 109 (1994).
- [33] F. Sievers, N. Kretzschmar, D. R. Fernandes, D. Suchet, M. Rabinovic, S. Wu, C. V. Parker, L. Khaykovich, C. Salomon, and F. Chevy, *Phys. Rev. A* **91**, 023426 (2015).
- [34] D. S. Barker, E. B. Norrgard, N. N. Klimov, J. A. Fedchak, J. Scherschligt, and S. Eckel, *Opt. Express* **30**, 9959 (2022).

- [35] G. Colzi, G. Durastante, E. Fava, S. Serafini, G. Lamporesi, and G. Ferrari, *Phys. Rev. A* **93**, 023421 (2016).
- [36] D. Nath, R. K. Easwaran, G. Rajalakshmi, and C. S. Unnikrishnan, *Phys. Rev. A* **88**, 053407 (2013).
- [37] G. Salomon, L. Fouché, P. Wang, A. Aspect, P. Bouyer, and T. Bourdel, *Europhys. Lett.* **104**, 63002 (2013).
- [38] D. R. Fernandes, F. Sievers, N. Kretzschmar, S. Wu, C. Salomon, and F. Chevy, *Europhys. Lett.* **100**, 63001 (2012).
- [39] H.-Z. Chen, X.-C. Yao, Y.-P. Wu, X.-P. Liu, X.-Q. Wang, Y.-X. Wang, Y.-A. Chen, and J.-W. Pan, *Phys. Rev. A* **94**, 033408 (2016).
- [40] S. Rosi, A. Burchianti, S. Conclave, D. S. Naik, G. Roati, C. Fort, and F. Minardi, *Sci. Rep.* **8**, 1301 (2018).
- [41] C. J. Sansonetti, C. E. Simien, J. D. Gillaspay, J. N. Tan, S. M. Brewer, R. C. Brown, S. Wu, and J. V. Porto, *Phys. Rev. Lett.* **107**, 023001 (2011).
- [42] M.-O. Mewes, G. Ferrari, F. Schreck, A. Sinatra, and C. Salomon, *Phys. Rev. A* **61**, 011403(R) (1999).
- [43] B. Efron, *Ann Stat.* **7**, 1 (1979).
- [44] C. L. Satter, S. Tan, and K. Dieckmann, *Phys. Rev. A* **98**, 023422 (2018).
- [45] N. R. Hutzler, L. R. Liu, Y. Yu, and K.-K. Ni, *New J. Phys.* **19**, 023007 (2017).
- [46] A. Bergschneider, V. M. Klinkhamer, J. H. Becher, R. Klemt, G. Zürn, P. M. Preiss, and S. Jochim, *Phys. Rev. A* **97**, 063613 (2018).
- [47] P. D. Gregory, J. A. Blackmore, S. L. Bromley, and S. L. Cornish, *Phys. Rev. Lett.* **124**, 163402 (2020).
- [48] Y. Liu, M.-G. Hu, M. A. Nichols, D. D. Grimes, T. Karman, H. Guo, and K.-K. Ni, *Nat. Phys.* **16**, 1132 (2020).
- [49] M. A. Nichols, Y.-X. Liu, L. Zhu, M.-G. Hu, Y. Liu, and K.-K. Ni, *Phys. Rev. X* **12**, 011049 (2022).

Acknowledgements

This manuscript is the result of four and half years of work. In this time period I faced a lot of challenges both personal and professional on top of a global pandemic and associated lockdowns. The successful completion of my PhD has only been possible thanks to the countless efforts of various personalities. Over the next few pages, I would like to personally thank all of the people who were part of this journey.

First of all, I would like to express my gratitude to Florian Schreck, Bruno Laburthe-Tolra, Thomas Bourdel, Juliette Billy and Michel Brune for being a part of my jury and for the evaluation of my work.

Second, I would like to thank my supervisor Christophe Salomon who gave me the opportunity to join the group as a PhD student. To get an opportunity like this for a master's student coming from a rural city in India was a very big deal for me even back in 2017. I am very grateful that Christophe trusted on my abilities and invited me to Paris to join Ultracold Fermi gases group. Working with Christophe was a great experience. I am truly amazed by his optimism and risk taking abilities. He has this aura in his stories which always motivate to keep going. His past experience in the lab as well as his adventures in the Alps are absolute delight.

I would like to thank Tarik Yefsah for his guidance in building the setup. I am very much inspired by his project management skills and his dedication for improvements of the lab. His planning skills to the last bit of detail are absolutely amazing, his contribution to the revival of lithium 1 machine will always be invaluable. After working 4.5 years in the lab with Christophe and Tarik I was not only able to grow as a physicist but also inculcated multiple aspects of project management skills.

I would also like to thank Frédéric Chevy for his immense support for me during my PhD on the experiment as well as in theoretical discussions. Frédéric's deep understanding of physical phenomena and its pedagogical analysis were very helpful for me to understand the physics behind the experiment.

I am grateful to the interns, Alfred Hammond, Sudipta Dhar, Anwesh Bhattacharya (mota), Joanna Lis who worked in the lab. Making the heavy magnetic field producing coils with Alfred and Sudipto was a memorable experience for me. Thanks to Anwesh's joyful personality and his never ending curiosity, working with Anwesh was always fun. However, biggest impact of Anwesh to my memory was his crazy activities outside the lab.

I am also extremely grateful to the several interns, PhDs and postdocs from the Lithium 3 and Fermix team for the fruitful discussions, help and fun during those years: Shuwei Jin, Ragheed Alhyder, Kunlun Dai, Darby Bates, Bruno Peaudecerf, Joris Verstraten, Clara Bachorz, Maxime Dixmerias, Tim de Jongh, Yann Kiefer, Mihail Rabinovic, Thomas Reimann, Markus Bohlen, Clément De Daniloff, Marin Tharrault, Julian Struck. Thanks to Clement and Julian for the essential help in setting up the computer control and the imaging software. Thanks to Tim and Maxime who helped me during the last phase of my PhD and with this much needed help we were able to finish the D1 project, and publish the results.

I am very thankful to my mentors Sylvain Nascimbène and Saïda Guellati-Khélifa who were always supportive in my PhD journey. I also thank Maria Chamorro and Etienne Reyssat from EDPIF alongwith Antoine Heidmann from LKB for their help and support during the last days of my PhD.

Similarly, I would like to thank the fellow PhDs and postdocs of LKB and in particular Mohamed Baghdad who was very kind to check upon me when ever I was working alone in the lab. I would also like to thank Gaurav Prabhudesai, and Vasu from LPENS for the joyful discussions on the corridor.

I would also like to express my gratitude to all the members of the workshops and the administration for their invaluable helps. In particular, I would like to thank Nabil Nabil Garroum, Arnaud Leclercq, Mathieu Sardin, Allan Hourdry, Didier Courtiade, Catherine Gripe, Théo Charpentier, Thierry Tradieu, Audrey Gohlke, Stephanie Dubois, Christelle Rio for their constant help with the experiment.

Additionally, over the last five years and even long before, I had the chance to benefit from the support of many friends. Unfortunately I will not be able to thank each of them as much as I would like to. Nevertheless, I would like to express my deep regards to:

- Dr. Amita Mohanty, for motivating me to do a PhD outside India. I must acknowledge that without her support and motivation my life would have been a very different from what it is now.

- My Friends from India (Kishan, Debashis, Abinash, Jaydeep, Biswa, Abhisekh, Aditya ...) for the awesome time since the first day of NISER and still continuing.
- My friends in Paris (Anand, Lennard, Nishit ...) for all the awesome moments to explore different parts of Paris.
- My various floor mate and friends at Indian House (Janhavi, Mageshi, Alaksh and Zoya, Shweta Dalal, Bijayalaxmi, Anshul, Amit ji, Shweta, Kartik and their little angle Thea, Komal and Sumit, Shreenath, Krishna Kanth, Saurabh, Nagesh, Yuvika and Maneesh.) I want to particularly thank to Shweta and Kartik who treated me as a member of their family. I also want to thank Yuvika, Maneesh, Saurabh, and Nagesh for all the weekend parties in second floor. I want to thank all of you who made my stay in India House a wonderful memory of my life.
- My seniors (Muna bhai, Abhash bhaiya, Baba, Nischaya bhaiya, Mukesh bhaiya, Samir bhaiya, Aroop bhaiya, Sony di, Rita di ...) juniors (Nilesh, Amit, Dipti, Biswajit, Sonam, Aroop, Sujit ...) and friends from NISER (Anupa, Tanim, Snigdha ...)
- Piyalee for the wonderful time we spent together in the NISER campus.

I would like to express my deepest gratitude to Nilesh for providing me the much needed accommodation in his apartment in Paris during the darkest time of my PhD journey.

I also would like to thank my family, especially my mom and dad for their everlasting love and support in my life. I have been truly blessed to have such a fantastic family.

Finally, I want to express my deepest gratitude to Rashmi Rekha, for her constant support in the last five years. I thank her for standing by my side through thick and thin.

This page intentionally left blank

Bibliography

- [1] P. Lebedew, “Untersuchungen über die druckkräfte des lichtes,” *Annalen der Physik*, vol. 311, no. 11, pp. 433–458, 1901 (cit. on p. 2).
- [2] W. D. Phillips, “Nobel lecture: Laser cooling and trapping of neutral atoms,” *Reviews of Modern Physics*, vol. 70, no. 3, p. 721, 1998 (cit. on p. 2).
- [3] J. J. Sakurai and E. D. Commins, *Modern quantum mechanics, revised edition*, 1995 (cit. on p. 2).
- [4] A. Einstein, *Quantentheorie des einatomigen idealen Gases* (Marilee E. Thomas and Robert C. Thomas Science and Related Subjects Collection v. 1). Verlag der Akademie der Wissenschaften, in Kommission bei Walter de Gruyter u. Company, 1924. [Online]. Available: <https://books.google.fr/books?id=uAsvwwEACAAJ> (cit. on p. 2).
- [5] S. N. Bose, “Plancks gesetz und lichtquantenhypothese,” 1924 (cit. on p. 2).
- [6] E. Fermi, “Zur quantelung des idealen einatomigen gases,” *Zeitschrift für Physik*, vol. 36, no. 11, pp. 902–912, 1926 (cit. on p. 3).
- [7] P. Kapitza, “Viscosity of liquid helium below the λ -point,” *Nature*, vol. 141, no. 3558, pp. 74–74, 1938 (cit. on p. 3).
- [8] J. F. Allen and A. Misener, “Flow of liquid helium ii,” *Nature*, vol. 141, no. 3558, pp. 75–75, 1938 (cit. on p. 3).
- [9] L. Tisza, “Transport phenomena in helium ii,” *Nature*, vol. 141, no. 3577, pp. 913–913, 1938 (cit. on p. 3).
- [10] F. London, “The λ -phenomenon of liquid helium and the bose-einstein degeneracy,” *Nature*, vol. 141, no. 3571, pp. 643–644, 1938 (cit. on p. 3).
- [11] L. Landau, “Theory of the superfluidity of helium ii,” *Physical Review*, vol. 60, no. 4, p. 356, 1941 (cit. on p. 3).
- [12] L. Tisza, “The theory of liquid helium,” *Physical Review*, vol. 72, no. 9, p. 838, 1947 (cit. on p. 3).
- [13] D. Osheroff, W. Gully, R. Richardson, and D. Lee, “New magnetic phenomena in liquid he 3 below 3 mk,” *Physical Review Letters*, vol. 29, no. 14, p. 920, 1972 (cit. on p. 3).

- [14] D. Osheroff, R. Richardson, and D. Lee, "Evidence for a new phase of solid he 3," *Physical Review Letters*, vol. 28, no. 14, p. 885, 1972 (cit. on p. 3).
- [15] A. J. Leggett, "A theoretical description of the new phases of liquid he 3," *Reviews of Modern Physics*, vol. 47, no. 2, p. 331, 1975 (cit. on p. 3).
- [16] L. N. Cooper, "Bound electron pairs in a degenerate fermi gas," *Physical Review*, vol. 104, no. 4, p. 1189, 1956 (cit. on pp. 3, 5).
- [17] J. Bardeen, L. N. Cooper, and J. R. Schrieffer, "Theory of superconductivity," *Physical review*, vol. 108, no. 5, p. 1175, 1957 (cit. on p. 3).
- [18] C. Ebner and D. O. Edwards, "The low temperature thermodynamic properties of superfluid solutions of 3he in 4he," *Physics Reports*, vol. 2, no. 2, pp. 77–154, 1971 (cit. on p. 4).
- [19] A. Ashkin, "Acceleration and trapping of particles by radiation pressure," *Physical review letters*, vol. 24, no. 4, p. 156, 1970 (cit. on p. 4).
- [20] T. W. Hänsch and A. L. Schawlow, "Cooling of gases by laser radiation," *Optics Communications*, vol. 13, no. 1, pp. 68–69, 1975 (cit. on pp. 4, 58).
- [21] W. D. Phillips and H. Metcalf, "Laser deceleration of an atomic beam," *Physical Review Letters*, vol. 48, no. 9, p. 596, 1982 (cit. on pp. 4, 20).
- [22] S. Chu, J. Bjorkholm, A. Ashkin, and A. Cable, "Experimental observation of optically trapped atoms," *Physical review letters*, vol. 57, no. 3, p. 314, 1986 (cit. on p. 4).
- [23] E. Raab, M. Prentiss, A. Cable, S. Chu, and D. E. Pritchard, "Trapping of neutral sodium atoms with radiation pressure," *Physical review letters*, vol. 59, no. 23, p. 2631, 1987 (cit. on p. 4).
- [24] A. L. Migdall, J. V. Prodan, W. D. Phillips, T. H. Bergeman, and H. J. Metcalf, "First observation of magnetically trapped neutral atoms," *Physical Review Letters*, vol. 54, no. 24, p. 2596, 1985 (cit. on p. 4).
- [25] M. H. Anderson, J. R. Ensher, M. R. Matthews, C. E. Wieman, and E. A. Cornell, "Observation of bose-einstein condensation in a dilute atomic vapor," *science*, vol. 269, no. 5221, pp. 198–201, 1995 (cit. on p. 4).
- [26] K. B. Davis, M.-O. Mewes, M. R. Andrews, *et al.*, "Bose-einstein condensation in a gas of sodium atoms," *Physical review letters*, vol. 75, no. 22, p. 3969, 1995 (cit. on p. 4).
- [27] C. C. Bradley, C. Sackett, J. Tollett, and R. G. Hulet, "Evidence of bose-einstein condensation in an atomic gas with attractive interactions," *Physical review letters*, vol. 75, no. 9, p. 1687, 1995 (cit. on p. 4).
- [28] B. DeMarco and D. S. Jin, "Onset of fermi degeneracy in a trapped atomic gas," *science*, vol. 285, no. 5434, pp. 1703–1706, 1999 (cit. on p. 4).

-
- [29] J. Ensher, D. S. Jin, M. Matthews, C. Wieman, and E. A. Cornell, “Bose-einstein condensation in a dilute gas: Measurement of energy and ground-state occupation,” *Physical Review Letters*, vol. 77, no. 25, p. 4984, 1996 (cit. on p. 4).
- [30] M. Andrews, C. Townsend, H.-J. Miesner, D. Durfee, D. Kurn, and W. Ketterle, “Observation of interference between two bose condensates,” *Science*, vol. 275, no. 5300, pp. 637–641, 1997 (cit. on p. 4).
- [31] M.-O. Mewes, M. Andrews, D. Kurn, D. Durfee, C. Townsend, and W. Ketterle, “Output coupler for bose-einstein condensed atoms,” *Physical Review Letters*, vol. 78, no. 4, p. 582, 1997 (cit. on p. 4).
- [32] I. Bloch, T. W. Hänsch, and T. Esslinger, “Atom laser with a cw output coupler,” *Physical Review Letters*, vol. 82, no. 15, p. 3008, 1999 (cit. on p. 4).
- [33] C. Raman, M. Köhl, R. Onofrio, *et al.*, “Evidence for a critical velocity in a bose-einstein condensed gas,” *Physical Review Letters*, vol. 83, no. 13, p. 2502, 1999 (cit. on p. 4).
- [34] M. Greiner, O. Mandel, T. Esslinger, T. W. Hänsch, and I. Bloch, “Quantum phase transition from a superfluid to a mott insulator in a gas of ultracold atoms,” *nature*, vol. 415, no. 6867, pp. 39–44, 2002 (cit. on p. 4).
- [35] J. Billy, V. Josse, Z. Zuo, *et al.*, “Direct observation of anderson localization of matter waves in a controlled disorder,” *Nature*, vol. 453, no. 7197, pp. 891–894, 2008 (cit. on p. 4).
- [36] G. Roati, C. D’Errico, L. Fallani, *et al.*, “Anderson localization of a non-interacting bose–einstein condensate,” *Nature*, vol. 453, no. 7197, pp. 895–898, 2008 (cit. on p. 4).
- [37] M. R. Matthews, B. P. Anderson, P. Haljan, D. Hall, C. Wieman, and E. A. Cornell, “Vortices in a bose-einstein condensate,” *Physical Review Letters*, vol. 83, no. 13, p. 2498, 1999 (cit. on p. 4).
- [38] K. W. Madison, F. Chevy, W. Wohlleben, and J. Dalibard, “Vortex formation in a stirred bose-einstein condensate,” *Physical review letters*, vol. 84, no. 5, p. 806, 2000 (cit. on p. 4).
- [39] J. R. Abo-Shaer, C. Raman, J. M. Vogels, and W. Ketterle, “Observation of vortex lattices in bose-einstein condensates,” *Science*, vol. 292, no. 5516, pp. 476–479, 2001 (cit. on p. 4).
- [40] S. Burger, K. Bongs, S. Dettmer, *et al.*, “Dark solitons in bose-einstein condensates,” *Physical Review Letters*, vol. 83, no. 25, p. 5198, 1999 (cit. on p. 4).

- [41] L. Khaykovich, F. Schreck, G. Ferrari, *et al.*, “Formation of a matter-wave bright soliton,” *Science*, vol. 296, no. 5571, pp. 1290–1293, 2002 (cit. on pp. 4, 14).
- [42] M. Randeria, “Pre-pairing for condensation,” *Nature Physics*, vol. 6, no. 8, pp. 561–562, 2010 (cit. on p. 4).
- [43] C. Chin, R. Grimm, P. Julienne, and E. Tiesinga, “Feshbach resonances in ultracold gases,” *Reviews of Modern Physics*, vol. 82, no. 2, p. 1225, 2010 (cit. on p. 4).
- [44] M. Bartenstein, A. Altmeyer, S. Riedl, *et al.*, “Collective excitations of a degenerate gas at the bec-bcs crossover,” *Physical review letters*, vol. 92, no. 20, p. 203 201, 2004 (cit. on p. 5).
- [45] T. Bourdel, L. Khaykovich, J. Cubizolles, *et al.*, “Experimental study of the bec-bcs crossover region in lithium 6,” *Physical Review Letters*, vol. 93, no. 5, p. 050 401, 2004 (cit. on pp. 5, 14).
- [46] C. Regal, M. Greiner, and D. S. Jin, “Observation of resonance condensation of fermionic atom pairs,” *Physical review letters*, vol. 92, no. 4, p. 040 403, 2004 (cit. on p. 5).
- [47] M. W. Zwierlein, C. A. Stan, C. H. Schunck, *et al.*, “Observation of bose-einstein condensation of molecules,” *Physical review letters*, vol. 91, no. 25, p. 250 401, 2003 (cit. on p. 5).
- [48] S. Nascimbène, N. Navon, K. Jiang, F. Chevy, and C. Salomon, “Exploring the thermodynamics of a universal fermi gas,” *Nature*, vol. 463, no. 7284, pp. 1057–1060, 2010 (cit. on pp. 5, 6, 7, 14).
- [49] N. Navon, S. Nascimbene, F. Chevy, and C. Salomon, “The equation of state of a low-temperature fermi gas with tunable interactions,” *Science*, vol. 328, no. 5979, pp. 729–732, 2010 (cit. on pp. 5, 6, 14).
- [50] M. J. Ku, A. T. Sommer, L. W. Cheuk, and M. W. Zwierlein, “Revealing the superfluid lambda transition in the universal thermodynamics of a unitary fermi gas,” *Science*, vol. 335, no. 6068, pp. 563–567, 2012 (cit. on pp. 5, 6).
- [51] T.-L. Ho, “Universal thermodynamics of degenerate quantum gases in the unitarity limit,” *Physical review letters*, vol. 92, no. 9, p. 090 402, 2004 (cit. on p. 5).
- [52] M. Horikoshi, S. Nakajima, M. Ueda, and T. Mukaiyama, “Measurement of universal thermodynamic functions for a unitary fermi gas,” *Science*, vol. 327, no. 5964, pp. 442–445, 2010 (cit. on p. 6).
- [53] Y.-i. Shin, “Determination of the equation of state of a polarized fermi gas at unitarity,” *Physical Review A*, vol. 77, no. 4, p. 041 603, 2008 (cit. on p. 6).

- [54] B. Chandrasekhar, “A note on the maximum critical field of high-field superconductors,” *Applied Physics Letters*, vol. 1, no. 1, pp. 7–8, 1962 (cit. on p. 6).
- [55] A. M. Clogston, “Upper limit for the critical field in hard superconductors,” *Physical Review Letters*, vol. 9, no. 6, p. 266, 1962 (cit. on p. 6).
- [56] F. Chevy, “Universal phase diagram of a strongly interacting fermi gas with unbalanced spin populations,” *Physical Review A*, vol. 74, no. 6, p. 063 628, 2006 (cit. on p. 6).
- [57] I. Bausmerth, A. Recati, and S. Stringari, “Chandrasekhar-clogston limit and phase separation in fermi mixtures at unitarity,” *Physical Review A*, vol. 79, no. 4, p. 043 622, 2009 (cit. on p. 6).
- [58] M. W. Zwierlein, A. Schirotzek, C. H. Schunck, and W. Ketterle, “Fermionic superfluidity with imbalanced spin populations,” *Science*, vol. 311, no. 5760, pp. 492–496, 2006 (cit. on p. 6).
- [59] G. B. Partridge, W. Li, R. I. Kamar, Y.-a. Liao, and R. G. Hulet, “Pairing and phase separation in a polarized fermi gas,” *Science*, vol. 311, no. 5760, pp. 503–505, 2006 (cit. on p. 6).
- [60] P. Fulde and R. A. Ferrell, “Superconductivity in a strong spin-exchange field,” *Physical Review*, vol. 135, no. 3A, A550, 1964 (cit. on p. 6).
- [61] A. Larkin and Y. N. Ovchinnikov, “Nonuniform state of superconductors,” *Soviet Physics-JETP*, vol. 20, no. 3, pp. 762–762, 1965 (cit. on p. 6).
- [62] F. Schreck, G. Ferrari, K. Corwin, *et al.*, “Sympathetic cooling of bosonic and fermionic lithium gases towards quantum degeneracy,” *Physical Review A*, vol. 64, no. 1, p. 011 402, 2001 (cit. on p. 6).
- [63] A. G. Truscott, K. E. Strecker, W. I. McAlexander, G. B. Partridge, and R. G. Hulet, “Observation of fermi pressure in a gas of trapped atoms,” *Science*, vol. 291, no. 5513, pp. 2570–2572, 2001 (cit. on pp. 6, 7).
- [64] F. Schreck, L. Khaykovich, K. Corwin, *et al.*, “Quasipure bose-einstein condensate immersed in a fermi sea,” *Physical Review Letters*, vol. 87, no. 8, p. 080 403, 2001 (cit. on pp. 6, 7, 14).
- [65] I. Ferrier-Barbut, M. Delehaye, S. Laurent, *et al.*, “A mixture of bose and fermi superfluids,” *Science*, vol. 345, no. 6200, pp. 1035–1038, 2014 (cit. on pp. 7, 10, 14, 107).
- [66] Z. Hadzibabic, C. Stan, K. Dieckmann, *et al.*, “Two-species mixture of quantum degenerate bose and fermi gases,” *Physical review letters*, vol. 88, no. 16, p. 160 401, 2002 (cit. on p. 7).
- [67] G. Roati, F. Riboli, G. Modugno, and M. Inguscio, “Fermi-bose quantum degenerate k 40- r 87 b mixture with attractive interaction,” *Physical Review Letters*, vol. 89, no. 15, p. 150 403, 2002 (cit. on p. 7).

- [68] C. Silber, S. Günther, C. Marzok, B. Deh, P. W. Courteille, and C. Zimmermann, “Quantum-degenerate mixture of fermionic lithium and bosonic rubidium gases,” *Physical review letters*, vol. 95, no. 17, p. 170 408, 2005 (cit. on p. 7).
- [69] J. McNamara, T. Jeltsov, A. Tychkov, W. Hogervorst, and W. Vassen, “Degenerate bose-fermi mixture of metastable atoms,” *Physical Review Letters*, vol. 97, no. 8, p. 080 404, 2006 (cit. on p. 7).
- [70] M. Taglieber, A.-C. Voigt, T. Aoki, T. Hänsch, and K. Dieckmann, “Quantum degenerate two-species fermi-fermi mixture coexisting with a bose-einstein condensate,” *Physical review letters*, vol. 100, no. 1, p. 010 401, 2008 (cit. on p. 7).
- [71] B. Deh, C. Marzok, C. Zimmermann, and P. W. Courteille, “Feshbach resonances in mixtures of ultracold li 6 and rb 87 gases,” *Physical Review A*, vol. 77, no. 1, p. 010 701, 2008 (cit. on p. 7).
- [72] B. Deh, W. Gunton, B. Klappauf, *et al.*, “Giant feshbach resonances in li 6-rb 85 mixtures,” *Physical Review A*, vol. 82, no. 2, p. 020 701, 2010 (cit. on p. 7).
- [73] M. K. Tey, S. Stellmer, R. Grimm, and F. Schreck, “Double-degenerate bose-fermi mixture of strontium,” *Physical Review A*, vol. 82, no. 1, p. 011 608, 2010 (cit. on p. 7).
- [74] S. Stellmer, R. Grimm, and F. Schreck, “Production of quantum-degenerate strontium gases,” *Physical Review A*, vol. 87, no. 1, p. 013 611, 2013 (cit. on p. 7).
- [75] H. Hara, Y. Takasu, Y. Yamaoka, J. M. Doyle, and Y. Takahashi, “Quantum degenerate mixtures of alkali and alkaline-earth-like atoms,” *Physical review letters*, vol. 106, no. 20, p. 205 304, 2011 (cit. on p. 7).
- [76] A. H. Hansen, A. Khramov, W. H. Dowd, A. O. Jamison, V. V. Ivanov, and S. Gupta, “Quantum degenerate mixture of ytterbium and lithium atoms,” *Physical Review A*, vol. 84, no. 1, p. 011 606, 2011 (cit. on p. 7).
- [77] S. Sugawa, K. Inaba, S. Taie, R. Yamazaki, M. Yamashita, and Y. Takahashi, “Interaction and filling-induced quantum phases of dual mott insulators of bosons and fermions,” *Nature Physics*, vol. 7, no. 8, pp. 642–648, 2011 (cit. on p. 7).
- [78] C.-H. Wu, I. Santiago, J. W. Park, P. Ahmadi, and M. W. Zwierlein, “Strongly interacting isotopic bose-fermi mixture immersed in a fermi sea,” *Physical Review A*, vol. 84, no. 1, p. 011 601, 2011 (cit. on p. 7).
- [79] M. Lu, N. Q. Burdick, and B. L. Lev, “Quantum degenerate dipolar fermi gas,” *Physical Review Letters*, vol. 108, no. 21, p. 215 301, 2012 (cit. on p. 7).

- [80] J. W. Park, C.-H. Wu, I. Santiago, *et al.*, “Quantum degenerate bose-fermi mixture of chemically different atomic species with widely tunable interactions,” *Physical Review A*, vol. 85, no. 5, p. 051 602, 2012 (cit. on p. 7).
- [81] M. Repp, R. Pires, J. Ulmanis, *et al.*, “Observation of interspecies 6 li-133 cs feshbach resonances,” *Physical Review A*, vol. 87, no. 1, p. 010 701, 2013 (cit. on p. 7).
- [82] B. Naylor, A. Reigue, E. Maréchal, O. Gorceix, B. Laburthe-Tolra, and L. Vernac, “Chromium dipolar fermi sea,” *Physical Review A*, vol. 91, no. 1, p. 011 603, 2015 (cit. on p. 7).
- [83] Z. Z. Yan, Y. Ni, C. Robens, and M. W. Zwierlein, “Bose polarons near quantum criticality,” *Science*, vol. 368, no. 6487, pp. 190–194, 2020 (cit. on p. 7).
- [84] F. Chevy and C. Mora, “Ultra-cold polarized fermi gases,” *Reports on Progress in Physics*, vol. 73, no. 11, p. 112 401, 2010 (cit. on p. 7).
- [85] M. Cetina, M. Jag, R. S. Lous, *et al.*, “Ultrafast many-body interferometry of impurities coupled to a fermi sea,” *Science*, vol. 354, no. 6308, pp. 96–99, 2016 (cit. on p. 7).
- [86] C. Kohstall, M. Zaccanti, M. Jag, *et al.*, “Metastability and coherence of repulsive polarons in a strongly interacting fermi mixture,” *Nature*, vol. 485, no. 7400, pp. 615–618, 2012 (cit. on p. 7).
- [87] F. Scazza, G. Valtolina, P. Massignan, *et al.*, “Repulsive fermi polarons in a resonant mixture of ultracold li 6 atoms,” *Physical review letters*, vol. 118, no. 8, p. 083 602, 2017 (cit. on p. 7).
- [88] M. Koschorreck, D. Pertot, E. Vogt, B. Fröhlich, M. Feld, and M. Köhl, “Attractive and repulsive fermi polarons in two dimensions,” *Nature*, vol. 485, no. 7400, pp. 619–622, 2012 (cit. on p. 7).
- [89] M. Delehaye, S. Laurent, I. Ferrier-Barbut, S. Jin, F. Chevy, and C. Salomon, “Critical velocity and dissipation of an ultracold bose-fermi counterflow,” *Physical review letters*, vol. 115, no. 26, p. 265 303, 2015 (cit. on p. 8).
- [90] Y. Castin, I. Ferrier-Barbut, and C. Salomon, “La vitesse critique de landau d’une particule dans un superfluide de fermions,” *Comptes Rendus Physique*, vol. 16, no. 2, pp. 241–253, 2015 (cit. on p. 8).
- [91] X.-C. Yao, H.-Z. Chen, Y.-P. Wu, *et al.*, “Observation of coupled vortex lattices in a mass-imbalance bose and fermi superfluid mixture,” *Physical review letters*, vol. 117, no. 14, p. 145 301, 2016 (cit. on p. 8).
- [92] D. Goldhaber-Gordon, H. Shtrikman, D. Mahalu, D. Abusch-Magder, U. Meirav, and M. Kastner, “Kondo effect in a single-electron transistor,” *Nature*, vol. 391, no. 6663, pp. 156–159, 1998 (cit. on p. 8).

- [93] S. M. Cronenwett, T. H. Oosterkamp, and L. P. Kouwenhoven, “A tunable kondo effect in quantum dots,” *Science*, vol. 281, no. 5376, pp. 540–544, 1998 (cit. on p. 8).
- [94] J. Bauer, C. Salomon, and E. Demler, “Realizing a kondo-correlated state with ultracold atoms,” *Physical review letters*, vol. 111, no. 21, p. 215304, 2013 (cit. on p. 8).
- [95] Y. Nishida, “Su (3) orbital kondo effect with ultracold atoms,” *Physical review letters*, vol. 111, no. 13, p. 135301, 2013 (cit. on p. 8).
- [96] B. Sundar and E. J. Mueller, “Proposal to directly observe the kondo effect through enhanced photoinduced scattering of cold fermionic and bosonic atoms,” *Physical Review A*, vol. 93, no. 2, p. 023635, 2016 (cit. on p. 8).
- [97] I. Kuzmenko, T. Kuzmenko, Y. Avishai, and K. Kikoin, “Model for over-screened kondo effect in ultracold fermi gas,” *Physical Review B*, vol. 91, no. 16, p. 165131, 2015 (cit. on p. 8).
- [98] R. Grimm, M. Weidemüller, and Y. B. Ovchinnikov, “Optical dipole traps for neutral atoms,” *Advances in atomic, molecular, and optical physics*, vol. 42, pp. 95–170, 2000 (cit. on pp. 9, 11, 101).
- [99] F. Sievers, N. Kretschmar, D. R. Fernandes, *et al.*, “Simultaneous sub-doppler laser cooling of fermionic li 6 and k 40 on the d 1 line: Theory and experiment,” *Physical review A*, vol. 91, no. 2, p. 023426, 2015 (cit. on pp. 10, 68, 73, 78, 80, 85, 100).
- [100] A. T. Grier, I. Ferrier-Barbut, B. S. Rem, *et al.*, “ Λ -enhanced sub-doppler cooling of lithium atoms in d 1 gray molasses,” *Physical Review A*, vol. 87, no. 6, p. 063411, 2013 (cit. on pp. 10, 68, 73, 78, 85).
- [101] A. Burchianti, G. Valtolina, J. Seman, *et al.*, “Efficient all-optical production of large li 6 quantum gases using d 1 gray-molasses cooling,” *Physical Review A*, vol. 90, no. 4, p. 043408, 2014 (cit. on pp. 10, 68, 73, 78, 100, 105).
- [102] D. Nath, R. K. Easwaran, G. Rajalakshmi, and C. Unnikrishnan, “Quantum-interference-enhanced deep sub-doppler cooling of 39 k atoms in gray molasses,” *Physical Review A*, vol. 88, no. 5, p. 053407, 2013 (cit. on p. 10).
- [103] G. Salomon, L. Fouché, P. Wang, A. Aspect, P. Bouyer, and T. Bourdel, “Gray-molasses cooling of 39k to a high phase-space density,” *EPL (Europhysics Letters)*, vol. 104, no. 6, p. 63002, 2014 (cit. on p. 10).
- [104] D. R. Fernandes, F. Sievers, N. Kretschmar, S. Wu, C. Salomon, and F. Chevy, “Sub-doppler laser cooling of fermionic 40k atoms in three-dimensional gray optical molasses,” *EPL (Europhysics Letters)*, vol. 100, no. 6, p. 63001, 2012 (cit. on pp. 10, 68).

- [105] P. Hamilton, G. Kim, T. Joshi, B. Mukherjee, D. Tiarks, and H. Müller, “Sisyphus cooling of lithium,” *Physical Review A*, vol. 89, no. 2, p. 023 409, 2014 (cit. on pp. 10, 61).
- [106] G. Dash, T. de Jongh, M. Dixmieras, C. Salomon, and T. Yefsah, “Simultaneous sub-doppler laser cooling of li 6 and li 7 isotopes,” *Physical Review A*, vol. 106, no. 3, p. 033 105, 2022 (cit. on pp. 11, 99).
- [107] A. Keshet and W. Ketterle, “A distributed, graphical user interface based, computer control system for atomic physics experiments,” *Review of Scientific Instruments*, vol. 84, no. 1, p. 015 105, 2013 (cit. on pp. 11, 45).
- [108] F. Schreck, “Mixtures of ultracold gases: Fermi sea and Bose-Einstein condensate of Lithium isotopes,” Theses, Université Pierre et Marie Curie - Paris VI, Jan. 2002. [Online]. Available: <https://tel.archives-ouvertes.fr/tel-00001340> (cit. on p. 14).
- [109] G. Ferrari, “Piégeage simultané des isotopes fermionique et bosonique du lithium, étude théorique de la relaxation collisionnelle dans un gaz de Fermi dégénéré,” Theses, Université Pierre et Marie Curie - Paris VI, Jul. 2000. [Online]. Available: <https://tel.archives-ouvertes.fr/tel-00006145> (cit. on p. 14).
- [110] L. Tarruell, “Superfluidité dans un gaz de fermions ultrafroids,” Theses, Université Pierre et Marie Curie - Paris VI, Jun. 2008. [Online]. Available: <https://tel.archives-ouvertes.fr/tel-00429181> (cit. on p. 14).
- [111] I. Ferrier-Barbut, “Mixtures of Bose and Fermi superfluids,” Theses, Ecole Normale Supérieure, Oct. 2014. [Online]. Available: <https://tel.archives-ouvertes.fr/tel-01087312> (cit. on pp. 14, 106, 111).
- [112] R. G. Hulet, J. H. Nguyen, and R. Senaratne, “Methods for preparing quantum gases of lithium,” *Review of Scientific Instruments*, vol. 91, no. 1, p. 011 101, 2020 (cit. on p. 17).
- [113] U. Eismann, F. Gerbier, C. Canalias, *et al.*, “An all-solid-state laser source at 671 nm for cold-atom experiments with lithium,” *Applied Physics B*, vol. 106, no. 1, pp. 25–36, 2012 (cit. on p. 29).
- [114] N. Kretzschmar, U. Eismann, F. Sievers, F. Chevy, and C. Salomon, “2.4-watts second-harmonic generation in ppzno: Ln ridge waveguide for lithium laser cooling,” *Optics express*, vol. 25, no. 13, pp. 14 840–14 855, 2017 (cit. on p. 29).
- [115] U. Eismann, A. Bergschneider, F. Sievers, N. Kretzschmar, C. Salomon, and F. Chevy, “2.1-watts intracavity-frequency-doubled all-solid-state light source at 671 nm for laser cooling of lithium,” *Optics express*, vol. 21, no. 7, pp. 9091–9102, 2013 (cit. on p. 29).

- [116] C. J. Sansonetti, C. Simien, J. D. Gillaspay, *et al.*, “Absolute transition frequencies and quantum interference in a frequency comb based measurement of the li 6, 7 d lines,” *Physical review letters*, vol. 107, no. 2, p. 023 001, 2011 (cit. on p. 30).
- [117] D. W. Preston, “Doppler-free saturated absorption: Laser spectroscopy,” *American Journal of Physics*, vol. 64, no. 11, pp. 1432–1436, 1996 (cit. on p. 33).
- [118] J.-P. Bouyer, C. Breant, and P. Schanne, “Injection-locking mechanisms in semiconductor lasers,” in *Frequency-Stabilized Lasers and Their Applications*, International Society for Optics and Photonics, vol. 1837, 1993, pp. 324–335 (cit. on p. 37).
- [119] B. Song, C. He, Z. Ren, E. Zhao, J. Lee, and G.-B. Jo, “Effective statistical fringe removal algorithm for high-sensitivity imaging of ultracold atoms,” *Physical Review Applied*, vol. 14, no. 3, p. 034 006, 2020 (cit. on p. 47).
- [120] W. M. Itano and D. Wineland, “Laser cooling of ions stored in harmonic and penning traps,” *Physical Review A*, vol. 25, no. 1, p. 35, 1982 (cit. on p. 58).
- [121] C. J. Foot, *Atomic physics*. OUP Oxford, 2004, vol. 7 (cit. on p. 58).
- [122] P. Duarte, R. Hart, J. Hitchcock, *et al.*, “All-optical production of a lithium quantum gas using narrow-line laser cooling,” *Physical Review A*, vol. 84, no. 6, p. 061 406, 2011 (cit. on p. 60).
- [123] D. McKay, D. Jervis, D. Fine, J. Simpson-Porco, G. Edge, and J. Thywissen, “Low-temperature high-density magneto-optical trapping of potassium using the open 4 s \rightarrow 5 p transition at 405 nm,” *Physical Review A*, vol. 84, no. 6, p. 063 420, 2011 (cit. on p. 60).
- [124] P. D. Lett, R. N. Watts, C. I. Westbrook, W. D. Phillips, P. L. Gould, and H. J. Metcalf, “Observation of atoms laser cooled below the doppler limit,” *Physical review letters*, vol. 61, no. 2, p. 169, 1988 (cit. on p. 60).
- [125] J. Dalibard and C. Cohen-Tannoudji, “Laser cooling below the doppler limit by polarization gradients: Simple theoretical models,” *JOSA B*, vol. 6, no. 11, pp. 2023–2045, 1989 (cit. on pp. 60, 61).
- [126] C. Salomon, J. Dalibard, W. Phillips, A. Clairon, and S. Guellati, “Laser cooling of cesium atoms below 3 μ k,” *EPL (Europhysics Letters)*, vol. 12, no. 8, p. 683, 1990 (cit. on p. 61).
- [127] F. Bardou, J.-P. Bouchaud, A. Aspect, and C. Cohen-Tannoudji, *Lévy statistics and laser cooling: how rare events bring atoms to rest*. Cambridge University Press, 2002 (cit. on p. 62).

- [128] F. Bardou, J. Bouchaud, O. Emile, A. Aspect, and C. Cohen-Tannoudji, “Subrecoil laser cooling and lévy flights,” *Physical review letters*, vol. 72, no. 2, p. 203, 1994 (cit. on p. 62).
- [129] A. Aspect, E. Arimondo, R. e. a. Kaiser, N. Vansteenkiste, and C. Cohen-Tannoudji, “Laser cooling below the one-photon recoil energy by velocity-selective coherent population trapping,” *Physical Review Letters*, vol. 61, no. 7, p. 826, 1988 (cit. on pp. 63, 64, 65).
- [130] M. Kasevich and S. Chu, “Laser cooling below a photon recoil with three-level atoms,” *Physical review letters*, vol. 69, no. 12, p. 1741, 1992 (cit. on pp. 63, 65, 66).
- [131] G. Grynberg and J.-Y. Courtois, “Proposal for a magneto-optical lattice for trapping atoms in nearly-dark states,” *EPL (Europhysics Letters)*, vol. 27, no. 1, p. 41, 1994 (cit. on p. 66).
- [132] M. Weidemüller, T. Esslinger, M. A. Ol’shanii, A. Hemmerich, and T. W. Hänsch, “A novel scheme for efficient cooling below the photon recoil limit,” *EPL (Europhysics Letters)*, vol. 27, no. 2, p. 109, 1994 (cit. on p. 66).
- [133] D. Boiron, C. Triché, D. Meacher, P. Verkerk, and G. Grynberg, “Three-dimensional cooling of cesium atoms in four-beam gray optical molasses,” *Physical Review A*, vol. 52, no. 5, R3425, 1995 (cit. on p. 66).
- [134] D. Boiron, A. Michaud, P. Lemonde, *et al.*, “Laser cooling of cesium atoms in gray optical molasses down to $1.1 \mu\text{k}$,” *Physical Review A*, vol. 53, no. 6, R3734, 1996 (cit. on pp. 66, 68).
- [135] T. Esslinger, F. Sander, A. Hemmerich, T. W. Hänsch, H. Ritsch, and M. Weidemüller, “Purely optical dark lattice,” *Optics letters*, vol. 21, no. 13, pp. 991–993, 1996 (cit. on p. 66).
- [136] M. Ol’Shanii and V. Minogin, “Three-dimensional velocity-selective coherent population trapping of a $(3+3)$ -level atom,” *Optics communications*, vol. 89, no. 5-6, pp. 393–398, 1992 (cit. on p. 66).
- [137] F. Papoff, F. Mauri, and E. Arimondo, “Transient velocity-selective coherent population trapping in one dimension,” *JOSA B*, vol. 9, no. 3, pp. 321–331, 1992 (cit. on p. 67).
- [138] G. Colzi, E. Fava, M. Barbiero, C. Mordini, G. Lamporesi, and G. Ferrari, “Production of large bose-einstein condensates in a magnetic-shield-compatible hybrid trap,” *Physical Review A*, vol. 97, no. 5, p. 053625, 2018 (cit. on p. 68).
- [139] M. M. Aliyu, L. Zhao, X. Q. Quek, K. C. Yellapragada, and H. Loh, “D 1 magic wavelength tweezers for scaling atom arrays,” *Physical Review Research*, vol. 3, no. 4, p. 043059, 2021 (cit. on p. 68).

- [140] K. N. Jarvis, J. Devlin, T. Wall, B. Sauer, and M. Tarbutt, “Blue-detuned magneto-optical trap,” *Physical review letters*, vol. 120, no. 8, p. 083 201, 2018 (cit. on p. 68).
- [141] L. Anderegg, B. L. Augenbraun, Y. Bao, *et al.*, “Laser cooling of optically trapped molecules,” *Nature Physics*, vol. 14, no. 9, pp. 890–893, 2018 (cit. on p. 68).
- [142] A. Mosk, S. Jochim, H. Moritz, T. Elsässer, M. Weidemüller, and R. Grimm, “Resonator-enhanced optical dipole trap for fermionic lithium atoms,” *Optics Letters*, vol. 26, no. 23, pp. 1837–1839, 2001 (cit. on p. 68).
- [143] K. Roux, V. Helson, H. Konishi, and J.-P. Brantut, “Cavity-assisted preparation and detection of a unitary fermi gas,” *New Journal of Physics*, vol. 23, no. 4, p. 043 029, 2021 (cit. on p. 68).
- [144] Y. Castin and K. Mølmer, “Monte carlo wave-function analysis of 3d optical molasses,” *Physical review letters*, vol. 74, no. 19, p. 3772, 1995 (cit. on p. 69).
- [145] J. Reichel, F. Bardou, M. B. Dahan, *et al.*, “Raman cooling of cesium below 3 nk: New approach inspired by lévy flight statistics,” *Physical review letters*, vol. 75, no. 25, p. 4575, 1995 (cit. on p. 69).
- [146] C. Dixneuf, G. Guiraud, Y.-V. Bardin, *et al.*, “Ultra-low intensity noise, all fiber 365 w linearly polarized single frequency laser at 1064 nm,” *Optics Express*, vol. 28, no. 8, pp. 10 960–10 969, 2020 (cit. on p. 104).
- [147] D. Guéry-Odelin, “Dynamique collisionnelle des gaz d’alcalins lourds : du refroidissement évaporatif à la condensation de Bose-Einstein,” Theses, Université Pierre et Marie Curie - Paris VI, Nov. 1998. [Online]. Available: <https://tel.archives-ouvertes.fr/tel-00001134> (cit. on p. 105).
- [148] M. Gehm, S. Hemmer, K. O’Hara, and J. Thomas, “Unitarity-limited elastic collision rate in a harmonically trapped fermi gas,” *Physical Review A*, vol. 68, no. 1, p. 011 603, 2003 (cit. on p. 105).
- [149] B. Décamps, J. Vigué, A. Gauguet, and M. Büchner, “Measurement of the 671-nm tune-out wavelength of li 7 by atom interferometry,” *Physical Review A*, vol. 101, no. 3, p. 033 614, 2020 (cit. on p. 107).
- [150] K. Cassella, E. Copenhaver, B. Estey, Y. Feng, C. Lai, and H. Müller, “Recoil-sensitive lithium interferometer without a subrecoil sample,” *Physical Review Letters*, vol. 118, no. 23, p. 233 201, 2017 (cit. on p. 107).
- [151] L. Morel, Z. Yao, P. Cladé, and S. Guellati-Khélifa, “Determination of the fine-structure constant with an accuracy of 81 parts per trillion,” *Nature*, vol. 588, no. 7836, pp. 61–65, 2020 (cit. on p. 107).

RÉSUMÉ

Cette thèse porte sur la construction d'une expérience de nouvelle génération sur un mélange de gaz quantiques bosons-fermions. Nous implémentons un refroidissement sub-Doppler D1 simultané sur les isotopes ${}^6\text{Li}$ et ${}^7\text{Li}$ de l'atome de lithium. Nous opérons une mélasse D1 sur la transition $|F_g = 2\rangle \rightarrow |F_e = 1\rangle$ du ${}^7\text{Li}$ et la transition $|F_g = 3/2\rangle \rightarrow |F_e = 3/2\rangle$ du ${}^6\text{Li}$ qui présentent des états noirs. En utilisant une nouvelle séquence pulsée, nous refroidissons les deux isotopes à partir d'une température de piège magnéto-optique (MOT) de ~ 1 mK à moins de $100 \mu\text{K}$ en 3 ms. Nous discutons de l'optimisation de la séquence de refroidissement pulsé.

Nous fournissons également une description détaillée du montage expérimental en nous concentrant en particulier sur le système de diode lasers, la conception des bobines de champ magnétique et le nouveau contrôle informatique de l'expérience.

Après refroidissement par mélasses grises, les densités dans l'espace des phases obtenues, de $\sim 2 \times 10^{-6}$ pour les deux isotopes, sont adaptées au chargement direct d'un piège dipolaire fortement désaccordé avec $\sim 7 \times 10^5$ atomes où un refroidissement par évaporation jusqu'à la double dégénérescence quantique pourrait être effectué. Nos résultats ouvrent la voie à l'étude des propriétés quantiques des mélanges Bose-Fermi à très basse température.

MOTS CLÉS

Gaz Ultrafroids - Refroidissement D1 - Refroidissement des mélasses grises

ABSTRACT

This thesis reports on the construction of a new generation Bose-Fermi quantum gas experiment. We implement simultaneous D1 sub-Doppler cooling on ${}^6\text{Li}$ and ${}^7\text{Li}$ isotopes. We operate D1 molasses on ${}^7\text{Li}$ $|F_g = 2\rangle \rightarrow |F_e = 1\rangle$ and on ${}^6\text{Li}$ $|F_g = 3/2\rangle \rightarrow |F_e = 3/2\rangle$ which display dark states. Using a novel pulsed sequence we cool both isotopes from a magneto optical trap (MOT) temperature of ~ 1 mK to less than $100 \mu\text{K}$ in 3 ms. We discuss the optimization of the pulsed cooling sequence.

We also provide a detailed description of the experimental set-up focusing in particular on the all-diode laser system, the magnetic field coil design and the new computer control system.

After D1 cooling, the obtained phase space densities of $\sim 2 \times 10^{-6}$ are suitable for directly loading a far detuned optical dipole trap with $\sim 7 \times 10^5$ atoms where evaporative cooling to dual quantum degeneracy could be performed. Our results pave the way towards the study of Bose-Fermi quantum many-body physics at low temperature.

KEYWORDS

Ultracold Quantum Gases - D1 cooling - Gray molasses cooling